Targeting Fusion Proteins of HIV-1 and SARS-CoV-2

Thesis by

Claudia A. Jette

In Partial Fulfillment of the Requirements for

the degree of

Biochemistry and Molecular Biophysics

CALIFORNIA INSTITUTE OF TECHNOLOGY

Pasadena, California

2022

(Defended April 6, 2022)

Claudia A. Jette
ORCID: 0000-0002-5085-8027

ACKNOWLEDGEMENTS

I am tremendously blessed to be surrounded by many people who have loved, supported, and pushed me. That I am finishing my PhD in a normal timeline for my program is truly a testament to the mentorship, willingness, and generosity everyone has shown me.

First, I'd like to thank Pamela Bjorkman. You took a chance on me and gave me the space to figure out how to be a scientist without judgement. One of the most formative moments of my career was when I sat in your office on the verge of joining your lab—so sure at that moment that I had somehow failed—and you told me I could do and be whatever I wanted to. In fact, you were shocked at the absurdity that I did not already know so. You've taught me so much about being a scientist and thinking critically. I know that besides my degree I walk away with just as much knowledge in other areas—about being a woman in science, about finding adventures and challenges, and about navigating the politics that underly science and academia.

Thank you to my committee, especially to Bil Clemons and Rebecca Voorhees. Conversations with both of you have helped me be on the path I am now.

I am so thankful to my Bjorklab family for the love, support, and camaraderie I've felt since the first moment I stepped into the lab. Alex Cohen, thank you for all of your unconditional support inside and outside the lab. I am honored to have had you cheering next to me through this crazy ride. Christopher Barnes, Marta Murphy, Jennifer Keefe, Andy DeLaitsch, Morgan Abernathy, Chengcheng Fan, Beth Huey-Tubman, Han Gao, Zhi Yang, Kate Radford, and everyone else in the Bjorkman Lab: I never knew it could be so awesome to go to work each day—even when work meant opening zoom on my computer at home.

To Ferdinand Huber, Karsten Thierbach, Jonas Weinrich, Daniel Lin, Sara Weaver, and of course Taylor Stevens. I don't know what I would have done without all those late nights, honest conversations, and funny moments. At the very least, I am graduating with lots of weird cat pictures and far too much knowledge about *The Office* than anyone who hasn't watched the show should ever have.

Elyse Verstelle, Emma Wrenn, Will Crago, and Kevin Kipp—working with you guys was the very start of this journey. You guys convinced me science was awesome. To Daniela Fera, thank you for teaching me how to set up a column right side up and for showing me how cool structural biology is.

George Mobbs, you've seen it all. What can I say—I guess I was building a life for myself? Thank you for all the coffee breaks, the much-needed hugs, and the science advice.

Roscoe Linstadt, I don't know anybody else whose brain works like yours. Thanks for feeding me steak tacos and asking me questions nobody else thinks about.

Stefan Petrovic, you are the best bay mate I could have asked for. I'm so thankful for all the scary smart and hilarious tidbits you've gifted me over the years—you have pushed me to be better and think deeper about science.

Jessica Slagle, I honestly don't know how we would have survived the worst of the pandemic without you. You are a bottomless well of reason and no-bullshit ready to help at a moment's notice with a book recommendation and a roast chicken.

Lucas Schaus, you are a bastion of support, kindness, and exceptionally detailed historical factoids. Thank you for loving me, feeding me good food, and helping me through all the moments, good or bad.

Paulie Jette and G Aron, thank you for taking me on the coolest of adventures and for always reminding me I am an actual human being and there is a whole wide world outside of the lab.

Thank you to my mom Claudia Jette and my grandmother Ivonne Ionescu for always challenging me to be stronger and loving me no matter what.

And finally, thank you to my amazing and brilliant sisters Daniela and Carina Jette. Your unconditional love and support has always let me know that I can do anything and that everything will be ok.

ABSTRACT

Viruses are disease-causing pathogenic agents that require host cells to replicate. Fusion of host and viral membranes is critical for the lifecycle of enveloped viruses. Studying viral fusion proteins can allow us to better understand how they shape immune responses and inform the design of therapeutics such as drugs, monoclonal antibodies, and vaccines. This thesis discusses two approaches to targeting two fusion proteins: Env from HIV-1 and S from SARS-CoV-2. The first chapter of this thesis is an introduction to viruses with a specific focus on HIV-1 CD4 mimetic drugs and antibodies against SARS-CoV-2. It discusses the architecture of these viruses and fusion proteins and how small molecules, peptides, and antibodies can target these proteins successfully to treat and prevent disease. In addition, a brief overview is included of the techniques involved in structural biology and how it has informed the study of viruses. For the interested reader, chapter 2 contains a review article that serves as a more in-depth introduction for both viruses as well as how the use of structural biology has informed the study of viral surface proteins and neutralizing antibody responses to them. The subsequent chapters provide a body of work divided into two parts. The first part in chapter 3 involves a study on conformational changes induced in the HIV-1 Env protein by CD4-mimemtic drugs using single particle cryo-EM. The second part encompassing chapters 4 and 5 includes two studies on antibodies isolated from convalescent COVID-19 donors. The former involves classification of antibody responses to the SARS-CoV-2 S receptor-binding domain (RBD). The latter discusses an anti-RBD antibody class that binds to a conserved epitope on the RBD and shows cross-binding and cross-neutralization to other coronaviruses in the *sarbecovirus* subgenus.

PUBLISHED CONTENT AND CONTRIBUTIONS

1. **Jette, C.A.**, Barnes, C.O., Kirk, S.M., Melillo, B., Smith, A.B., Bjorkman, P.J. Cryo-EM structures of HIV-1 trimer bound to CD4-mimetics BNM-III-170 and M48U1 adopt a CD4-bound open conformation. *Nat Commun* **12,** 1950 (2021). doi:10.1038/s41467-021-21816-x

   C.A.J. designed research, performed experiments, analyzed results, solved and analyzed cryo-EM structures, and wrote the manuscript.

2. Barnes, C.O., **Jette, C.A.**, Abernathy, M.E., Dam, K.-M.A., Esswein, S.R., Gristick, H.B., Malyutin, A.G., Sharaf, N.G., Huey-Tubman, K.E., Lee, Y.E., Robbiani, D.F., Nussenzweig, M.C., West, A.P., Bjorkman, P.J. SARS-CoV-2 neutralizing antibody structures inform therapeutic strategies. *Nature* **588,** 682–687 (2020). doi:10.1038/s41586-020-2852-1

   C.A.J. solved and analyzed various X-ray crystal structures and assisted in writing the manuscript.

3. **Jette, C.A.***, Cohen, A.A.*, Gnanapragasam, P.N.P., Muecksch, F., Lee, Y.E., Huey-Tubman, K.E., Schmidt, F., Hatziioannou, T., Bieniasz, P.D., Nussenzweig, M.C., West, A.P., Keeffe, J.R., Bjorkman, P.J. & Barnes, C.O. Broad cross-reactivity across sarbecoviruses exhibited by a subset of COVID-19 donor-derived neutralizing antibodies. *Cell Reports* **36,** 109760 (2021). doi:10.1016/j.celrep.2021.109760

   C.A.J. designed research, performed experiments, analyzed results, solved and analyzed structural data, and wrote the manuscript.

4. Abernathy, M.E.*, Dam, K.-M.A.*, Esswein, S.R.*, **Jette, C.A.***, Bjorkman, P.J. How Antibodies Recognize Pathogenic Viruses: Structural Correlates of Antibody Neutralization of HIV-1, SARS-CoV-2, and Zika. *Viruses* **13**, 2106 (2021). doi:10.3390/v13102106

   C.A.J. participated in the writing and editing of the review including designing and making figures and with particular emphasis on SARS-CoV-2 and HIV-1 material.

* Equal Contributions

TABLE OF CONTENTS

Chapter 1

INTRODUCTION

1: Introduction to the introduction

Viruses are small infectious agents defined by their reliance on a host for replication. All viruses share general features including (1) a genetic material that stores its genome, be it RNA or DNA, (2) a protective barrier to shield the genetic material, typically a protein capsid and in some cases also a membrane, (3) machinery designed to infect its target cell and allow the virus to replicate, and (4) mechanisms to assemble new viruses and allow them to exit their host cells. While the specifics change species to species, together these four conserved features allow viruses to go through their basic lifecycle of infection, replication, and production of new viruses.

In order to replicate, viruses must create an environment within a host organism to synthesize and package new progeny while evading host defenses. To this end, many different interactions occur between viral factors and host components, including viral entry, tamping down of anti-viral host responses, and hijacking of host replication machinery. Specialization of the viral factors involved in infection therefore constrain the scope of infection of a virus to a limited range of host organisms. This is known as the viral *tropism.* The exact range of cells within organisms that can serve as a host varies from virus to virus and is largely dependent on the interactions necessary for the virus's successful infection lifecycle. Within eukaryotes, a major determinant for cellular tropism is the infection machinery of a virus. Much like having the correct key to unlock a door, the attachment and fusion mechanisms of a virus must be compatible with a target cell for successful entry into the cell. Understanding entry mechanisms has become essential to understanding both natural infections and therapeutic targeting of viruses. Studies on viral fusion proteins have directly informed the discovery of effective treatments and therapeutics such as small molecules, antibodies, and vaccines. These inhibit viral infection through various mechanisms including blocking key

interactions, locking specific conformational states of viral fusion proteins, or engaging other components of the human immune system.

This thesis is divided into three sections related in their goal of understanding targeting of viral fusion proteins. The first part (chapter 2) is a short review presenting a comprehensive discussion of the role of structural biology in studying how antibodies target HIV-1, SARS-CoV-2, and Zika fusion proteins.

The second part (chapter 3) discusses the use of small molecules and peptide drugs to target the fusion protein envelope (Env) from HIV-1. This study focuses on promising therapeutic drugs designed to exploit the interactions of Env protein with its target host receptor, CD4.

The third part (chapters 4 and 5) discusses the effective targeting of the SARS-CoV-2 Spike (S) protein by convalescent human-derived antibodies. Chapter 4 presents a study early during the COVID-19 pandemic using structural biology to classify different epitopes on the S receptor binding domain (RBD). Chapter 5 contains a study identifying cross-reactive antibodies that bind to and neutralize a wide range of coronaviruses from the sub-clade *sarbecovirus*. Both stories were important milestones during the SARS-CoV-2 pandemic and helped us understand natural antibody responses in humans and identify targets on the S protein that can be exploited for future therapies.

2.1: HIV-1

In 1981, increasing numbers of young homosexual men succumbing to unusual opportunistic and rare infections led to the recognition of Acquired Immune Deficiency Syndrome (AIDS). Soon after, a retrovirus termed human immunodeficiency virus type 1 (HIV-1) was identified as the causative agent.[1] The HIV/AIDS epidemic quickly became one of the biggest in recent history, and as of 2021 there were an estimated 37.7 million people living with HIV-1.[2]

HIV-1 is a member of the retrovirus family and has a negative-sense RNA genome. Like other retroviruses, it begins its lifecycle by binding to a cellular receptor (the T cell protein CD4 in the case of HIV-1) and a co-receptor on the surface of host cells with its fusion protein

envelope (Env) (Figure 1). The viral membrane then fuses to the cell membrane and releases the capsid containing the viral RNA. Within the infected cell the viral RNA is uncoated and reverse transcribed into DNA using the HIV-1 enzyme reverse transcriptase. The newly transcribed viral DNA is stably integrated into the host cell genome within infected cells. Once active in the lytic cycle, the viral DNA is transcribed into new RNA molecules and viral components are produced. The viral components are packaged into new viruses, which are released through budding from the infected cells. The new viruses can then infect new target cells and continue the cycle.[3] After integration, in some cells the virus is also able to enter a latent phase in which the virus is inactive but can be re-triggered back into the cytopathic *lytic cycle*. The virus in this phase is known as the *latent reservoir* and results in long-lived viral populations within an infected individual even after undetectable viral loads in the blood are achieved through therapeutic means.[3,4]

2.2: The HIV-1 Envelope protein and entry into cells

HIV-1 infection begins with fusion of the HIV-1 viral membrane with the target cell membrane. This is mediated by the heavily-glycosylated HIV-1 envelope protein (Env), a 330kDa heterotrimeric transmembrane protein embedded in the viral membrane. Unlike other viruses that present a dense array of viral proteins on their surface, HIV-1 Env is only sparsely populated on the its membrane, with approximately 14 Env spikes per virus.[5] The native Env protein on the surface of the virus exists in a metastable, pre-fusion conformation that comprises a bundle of three gp41 subunits proximal to the membrane that are surrounded by three large lobes of the gp120 subunits and capped by folded and structured variable loops (Figure 2).[6]

Env directly attaches to the target host cell through interactions with the CD4 receptor and followed by co-receptor binding. This unleashes dramatic conformational changes that ultimately result in fusion of the viral and host cell membranes. CD4 binding is the first step in the HIV-1 fusion mechanism and hence poses an attractive target for therapeutic and vaccine designs. Structurally, CD4 has four extracellular immunoglobulin-like domains (D1-D4) connected to a transmembrane domain and a short cytoplasmic tail. Attachment begins

when the D1 domain of CD4 is bound by the gp120 subunits of Env.[7] At the center of the ~800Å^2 CD4 binding footprint on gp120, there is a deep hydrophobic pocket into which CD4 inserts residue Phe43 from its D1 domain (dubbed the "Phe43 pocket") (Figure 3A-B). At the entrance of the Phe43 pocket, CD4 makes additional backbone H-bond contacts with its beta hairpin and with the Arg59 side chain that forms an H-bond with the gp120 residue Asp368.[7] Attachment of CD4 to gp120 and insertion of the Phe43 results in a dramatic conformational change of the Env: the V1-V2 and V3 loops at the apex of the trimer become unstructured and open, exposing the co-receptor binding site, and the gp120 subunits swing away from the central axis and rotate counter-clockwise to expose the central gp41 helices.[8–11]

2.3: Clinical treatment of HIV-1

The CD4 receptor and co-receptors CXCR4 or CCR5 are primarily expressed on the surface of CD4+ T cells, an integral component of the adaptive immune system in humans. Among other roles, CD4+ T cells identify infected cells by binding peptides presented on the major histocompatibility complex class II (MHC II) proteins on the surface of antigen presenting cells and activate a targeted immune response against invading pathogens.[12] CD4+ T cells continue a progressive decline during an untreated, established HIV-1 infection until the adaptive immune system is completely crippled, progressing to AIDS.[3] Besides CD4+ T cells, HIV-1 also infects other CD4+ immune cells such as dendritic cells and macrophages that play necessary roles in antigen presentation and the adaptive immune response, further hindering the immune system.[4] Treatment is imperative for long-term survival of most HIV-1 individuals but the virus has proven very difficult to pin down.

HIV-1 has extremely high genetic diversity.[13] These variations arise due to faulty replication and high turnover of new virus, resulting in a large, widely diverse population of virus within a single infected individual. Dense glycan shields present on Env add an additional layer of diversity as the sugars can be modified quickly, obscuring vulnerable, conserved regions of Env that could be targeted either by the immune system or therapeutics.[14] Further complicating treatments, HIV-1 persists in an infected person because of its integration into the genome of infected cells (Figure 1, step 4), resulting in a stable, inactivated population

of virus that can be re-activated.[4] While a vaccine against HIV-1 is highly desirable, all of these features have led to more than 40 years of HIV-1 vaccine research without a single candidate successfully passing clinical trials.

Small molecules and other drugs focused on the treatment and prevention of HIV-1 have proven to be more fruitful. Azidothymidine (AZT) the first successful small molecule treatment against HIV-1 was approved by the Food and Drug Administration (FDA) in 1987.[15] This nucleotide analog binds the HIV-1 reverse transcriptase and inhibits viral replication. While patients treated with AZT initially showed a greatly decreased viral load, the speed at which HIV-1 developed resistance to the drug and its intense side effects for patients made it an ineffective long-term treatment.[16] In spite of AZT proving to be a poor treatment on its own, it marked the beginning of a massive push of research into small molecules and other drugs targeting various components of HIV-1.[15] Many new categories of anti-HIV-1 drugs have since been developed targeting vulnerable sites on HIV-1, effectively stunting the viral lifecycle at different steps by preventing necessary interactions (e.g. attachment) or mechanisms (e.g. reverse transcription, protease activity).

The availability of multiple drug options to treat HIV-1 catalyzed the development of highly active antiretroviral therapy (HAART). HAART refers to treatment regimens that include different categories of HIV-1 drugs taken in combination to reduce the circulating viral load in a patient.[17] Unlike use of a single drug as was the case with early AZT treatment, the use of multiple drugs at once can prevent the development of viral drug resistance[18] and availability of various HAART regimens offers alternative treatment plans in the event resistance does arise. Reactivation of the latent reservoir of HIV-1 in patients causes persistence of the virus even after undetectable viral loads are reached through therapeutic means. Consequently, a strict, lifelong adherence to HAART is required to prevent viral rebound.[4] The combination of access to care and testing, early prescription, and strict adherence to HAART can provide long-term management of HIV-1 in infected individuals and permit them to live normal lifespans.[19] This has led to the global reduction in both annual deaths of individuals with AIDS and new HIV-1 infections; from the peak in 2004 to 2020,

AIDS-related deaths were reduced by 52%; from the peak in 1997 to 2020, new HIV-1 infections were reduced by 52%.[2]

Historically, a combination of three oral drugs needed to be taken for successful HAART therapy. Recently, new options have been developed that reduce the drugs to fewer components and provide alternative administration methods. These include the first approval of an injectable, slow-release drug treatment approved in December 2021 named Cabenuva that is a combination of two inhibitors cabotegravir and rilpivirine.[20]

Drugs targeting of the Entry mechanism of HIV-1

There are currently four FDA-approved drugs designed to inhibit HIV-1 infection by blocking viral entry into cells. The earliest is the fusion inhibitor T-20 (Enfuvirtide, Fuzeon) that acts by preventing specific helices of gp41 from associating and was approved by the FDA in 2003.[20,21] Maraviroc, an antagonist small molecule, targets and prevents co-receptor (CCR5) attachment and was FDA approved in 2007.[20] The monoclonal antibody Ibalixumab binds to CD4 domain D2 on target cells and blocks co-receptor attachment to HIV-1 after gp120 binding.[20–22]

As of July 2020, the small molecule entry inhibitor named Rukobia was FDA approved for HIV-1 treatment.[20] Rukobia is a small molecule pro-drug compound developed by Bristol Myers Squibb known as fostemsavir tromethamine or BMS-663068 that is converted within the body to its active form called BMS-626529 (Figure 3B).[23] This compound marks the first drug directly targeting the CD4 binding site on gp120 that has been approved by the FDA. Unlike CD4, which binds directly into the Phe43 pocket on gp120, BMS-626529 binds orthogonally to the mouth of the Phe43 pocket and inserts into the base of the pocket by reaching underneath the β20 and β21 strands. Separation of these strands from the rest of the gp120 prevent Env from opening and inhibits infection.[24]

2.4: Development of CD4-mimetic drugs

Exploiting the key CD4-gp120 interaction has been of particular interest for developing new therapeutics beyond inhibitors like BMS-626529. Specifically, CD4-mimetic (CD4m) drugs,

or compounds directly mimicking the CD4-gp120 interaction and binding into the Phe43 pocket have become a promising avenue of research. While no CD4m is currently FDA approved, several CD4m have shown potential therapeutic value both alone or in combination with other treatments.

In particular, the CD4m small molecule BNM-III-170 and the CD4m miniprotein M48U1 have demonstrated valuable results in pre-clinical studies. Gp120 component vaccines are known to induce strong anti-gp120 antibodies but not strong anti-HIV-1 neutralizing antibodies.[25] Some CD4m small molecules that open Env have been reported to sensitize HIV-1 to neutralization by antibodies that are otherwise non-neutralizing. Combining one such vaccine with BNM-III-170 dosage in macaques showed increased protection in animals following challenge by simian HIV (SHIV).[26] Using macaque models of vaginal mucosal transmission, M48U1 showed effective HIV-1 inhibition when present in an antimicrobial hydrogel for use as an alternative to condoms.[27] Unfortunately, cross-linked M48U1 and gp120 immunogens have proven to have only short-lived protection in animals, although further development could lead to more successful vaccine candidates.[25] While the mechanisms of neutralization by CD4m inhibitors like BNM-III-170 and M48U1 are not fully understood, it is postulated to be related to (a) direct blocking of CD4 binding to gp120, (b) binding of a CD4m causing conformational changes of Env leading to an inactive conformation (c) inactivation by antibodies binding to epitopes exposed by CD4m binding, (d) sensitization to ADCC and (e) increasing gp120 shedding.[25,28]

Future studies including clinical trials will be necessary to determine the full scope of CD4m inhibitors and their use as human therapies.

The earliest example of a drug mimicking native CD4-Env interaction was a soluble version of CD4 (sCD4) (Figure 3A-B). sCD4, which binds and neutralizes HIV-1 *in vitro,* proved to be disappointing in clinical studies as sCD4 administration showed rapid viral rebound and could even enhance infection at low concentrations.[25] Despite poor clinical performance, these initial sCD4 proteins motivated development of other drugs that mimic the CD4-Env interaction—the group of compounds and proteins now known as CD4 mimetic (CD4m) drugs (Figure 3). Current CD4m drugs can be divided into three general categories: sCD4

protein mimics (including proteins like the original sCD4 fusion proteins), small molecules, and miniproteins (or peptides).

Small molecule CD4m

Small molecules have been successfully designed to bind into the Phe43 pocket. The original prototypes NBD-556 and NBD-557 were identified using screens testing for molecules that could inhibit binding of sCD4 to gp120.[29] Further experiments with NBD-556 and NBD-557 showed they were limited in potency and breadth and, similar to sCD4, could sensitize cells lacking CD4 and containing the correct co-receptor to HIV-1 infection.[25]

The structures of CD4m small molecules can generally be divided into three regions, with a halogenated aromatic ring and oxalamide linker (I and II) inserting into the Phe43 cavity and an external region made up of a substituted indane ring (III) binding outside at the mouth of the cavity.[30] Modifications to all three regions led to more potent CD4m small molecules with increased affinities and breadth, including the family of BNM-III-170 developed by the group of Amos Smith III and collaborators[31] (Figure 3B). Unlike their ancestral molecules, these more potent CD4m compounds behaved as antagonists against HIV-1 and effectively showed inhibition of HIV-1 at sufficiently high concentrations.[30]

Miniprotein CD4m

The first CD4m miniproteins were designed using the scorpion toxin scyllatoxin as a scaffold, a small mini protein that shared high structural homology with the CDR-2 loop of the D1 domain of CD4 that contains the Phe43 residue and a beta hairpin structure. Key CD4 residues were grafted onto this toxin, producing a drug that binds the Phe43 pocket in a close imitation to the CDR-2 loop of CD4.[32]

The first generation of successful CD4m miniproteins was the M9 family and since their conception these have been further improved to produce more potent series including the M48 family. Of the later generations of miniproteins, the most potent miniprotein is M48U1, in which the Phe43-equivalent residue at position 23 of the peptide has been modified into a

synthetic hydrophobic cyclohexylmethoxy phenylalanine sidechain which extends 3.5Å deeper into the hydrophobic cavity than the original phenyl sidechain[33] (Figure 3B).

Unlike CD4m small molecules that have very few interactions at the mouth of the Phe43 cavity, CD4m miniproteins contain additional regions outside of the pocket that mimic CD4-gp120 interactions including a β-strand that hydrogen bonds with the gp120 β15 strand at the mouth of the Phe43 cavity and an equivalent Arg residue at peptide position 5 to mimic the $Arg59_{CD4}$-$Asp368_{gp120}$ salt bridge interaction.[33] In contrast to larger sCD4 protein mimics that include most of the D1 domain of CD4, these miniproteins are only ~30 residues and have a smaller gp120 binding footprint more similar to those of small molecule CD4m.

Opening of Env by CD4m

It is important to note that while all CD4m bind at the Phe43 pocket, not all small molecule CD4m are able to open the Env trimer. Indeed, it was only after incorporating interactions at the mouth of the Phe43 pocket including engagement of gp120 residues Met 426 and Asp368 that the first CD4m small molecules appearing to open Env were reported[30,31] and experiments demonstrating binding of Env by these molecules showed sensitization to antibodies that can only bind open Env conformations.[34]

Crystal structures of M48U1 and related peptides or BNM-III-170 and related compounds in complex with Env gp120 cores (truncated subunits lacking the gp41 helices and the variable loops) confirmed important interactions that mimic the CD4 receptor binding were present when the compounds were bound to gp120.[31,33] Gp120 cores are known to adopt similar conformations as gp120s in CD4-bound trimeric Env this suggested that an open conformation of gp120 would be possible when the compounds are bound.

Despite these reports, the question of whether a trimeric Env opened by one of these CD4m looks like an Env opened by CD4 remained. Chapter 3 contains a study reporting two structures of trimeric Env bound by CD4m drugs BNM-III-170 and M48U1. The described

structures demonstrate that both large and small conformational changes in the CD4m-bound Env match those of a sCD4-bound Env.

3.1: Emergence of SARS-CoV-2

While many coronaviruses infect humans, not all infections produce the same severity of disease. Most human coronaviruses cause mild respiratory disease, including several species which are responsible for the common cold. In recent memory, the first instance of a lethal coronavirus was the Severe Acute Respiratory Syndrome-associated Coronavirus (SARS-CoV) epidemic of 2002. A second outbreak of similar scope by a related coronavirus Middle Eastern Respiratory Syndrome Coronavirus (MERS-CoV) occurred in 2012, signaling that coronaviruses were becoming an increasing global health concern and that emerging coronaviruses had the potential to cause large-scale, deadly infections.[35] Sequencing and sampling efforts suggest that both SARS-CoV and MERS-CoV originated in wild bat populations and likely spilled over into humans through an intermediary host.[35,36]

In late 2019, a novel coronavirus later named SARS-like Coronavirus-2 (SARS-CoV-2) was first reported in Wuhan, China.[37] It quickly spread to become a deadly worldwide pandemic that, at the time of this thesis being written, is still ongoing. Despite sharing high sequence similarity with SARS-CoV, this virus showed higher infection rate and a long incubation period, leading to fast and undetected spread of the virus through human populations across the globe.[38] While many cases of Coronavirus Disease 19 (COVID-19), the acute respiratory disease caused by SARS-CoV-2, are mild or asymptomatic, a subset of patients exhibit severe symptoms including respiratory distress can result in death.[38] Regardless of disease severity, another subset of convalescent SARS-CoV-2 patients have also exhibited long-term physiological effects that are less understood including fatigue and loss of concentration, a condition now termed Long Covid.[39] Research is still ongoing to better understand differences in disease severity and the underlying mechanisms that cause Long Covid.

3.2: The Spike Protein

Coronaviruses are large, enveloped, positive sense RNA viruses. They contain three main viral proteins on their surface: Spike (S), Envelope (E), and Membrane (M) (Figure 4A). S is responsible for membrane attachment and fusion. Unlike HIV-1 Env which is sparsely populated on the viral surface,[5] S is present in large quantities. Coronaviruses were named for the dense, corona-like appearance of S around the circumference of the virus visible in early electron microscopy micrographs from the pioneering work of Dr. June Almeida and Dr. David Tyrrell.[40,41]

S is produced as a trimer of three identical subunits, similar to other Type I fusion proteins, and must be cleaved by a protease at the junction of the S1 and S2 subcomponents of S to produce a fusion-competent trimer.[42] Three receptor binding domains (RBDs) sit atop the S trimer and are connected by flexible linkers to the rest of the S1 subunit and are able are able to adopt either a 'down' or 'up' conformation.[43,44] The entry receptor for SARS-CoV-2 is the Angiotensin converting enzyme-2 (ACE2), which is highly expressed on the surface of alveolar epithelial cells and capillary epithelial cells in the respiratory tract and lungs.[45] The ACE2 binding site is located at the top of the RBD on the receptor binding ridge and is occluded in the 'down' position, therefore the RBD must be flipped in the 'up' position for ACE2 to be able to bind[44] (Figure 5A).

3.3: Antibodies against SARS-CoV-2

Antibodies are soluble proteins that serve as an integral component of the adaptive immune system by binding to foreign molecules in an organism and tagging them for other immune cells.[12] In the special case of neutralizing antibodies (nAb)s, a bound target molecule, or antigen, such as a virus is neutralized by the direct binding of the antibody. Typically, this is a result of either blocking other interactions or preventing conformational changes of the antigen.

Antibodies are produced by B cells as a soluble form of their B-cell receptor. Class-switched IgG antibodies have a Y-shaped structure consisting of two identical heavy chains and two

identical light chains (Figure 4B). An antigen is recognized and bound by the variable domains located at the tips of the Y. The rest of the antibody structure consists of constant domains which have more conserved sequences and are responsible for signaling and other immunological functions such as antibody-dependent cell cytotoxicity (ADCC).[12]

The binding site of an antibody on an antigenic molecule is known as an epitope and each antibody is usually specific for its antigen; good antibodies are able to bind to their antigen with high affinity and high specificity. Over the course of an infection, the process of somatic hypermutation (SHM) mutates antibody genes to further mature them to be higher affinity binders.[12]

The primary target of nAbs in coronavirus infections is S; nAbs have been reported that target the N-terminal domain (NTD), the S2 subunit, and the S1 subunit including the RBD.[46] As the site of receptor binding, some of the most potent isolated antibodies directly target the RBD. Chapter 4 of this thesis discusses the characterization of various SARS-CoV-2 RBD-specific antibodies that, in combination with other published antibodies, enabled sorting their epitopes into four classes (Figure 5B). Class 1 and class 2 antibodies both overlap the ACE2 binding site, however only class 1 antibodies require the RBD to be in an 'up' conformation as with ACE2 binding. Both class 3 and class 4 antibodies bind outside of the ACE2 binding site. Similar to class 2, class 3 can bind either 'up' or 'down' RBDs since its epitope region is on the outer face of the RBD. Class 4 binds to a cryptic epitope at the base of the RBD facing the central axis of the S and is occluded in the 'down' position, therefore requiring an 'up' RBD to accommodate binding.[47]

3.4 SARS-CoV-2 variants of concern and emerging *sarbecoviruses*

Throughout the course of the pandemic, new mutations have arisen in SARS-CoV-2 as the virus changed in response to evolutionary pressures from human immunity obtained naturally or through immunization.[48] It is important to note that most mutated strains of SARS-CoV-2 are isolates—versions of the virus with small genetic changes that still behave the same way as the original strain. With enough time and the correct mutations, versions of

the virus with increased apparent fitness from the original strain known as variants of concern (VOCs) have emerged[48] (Table 1). These VOCs can evade antibody responses by mutating portions of the virus, including many mutations in the RBD of S affecting epitopes of potent nAbs in class 1 and class 2 (overlapping ACE2 binding site, Figure 5B). The emergence of the omicron variant in November 2021 was especially problematic. This VOC contained more mutations than any previous VOC, including 30 substitutions, three deletions, and one insertion in S of the earliest isolated omicron lineage BA.1[48] (Table 1). Protection acquired from natural infection or through FDA-approved 2-dose mRNA vaccines Pfizer-BioNTech (BNT162b2) and Moderna (mRNA-1273) or 1-dose Johnson & Johnson-Jansen vaccine (Ad26.COV2.S) was greatly decreased against omicron.[49] Finding common features in S that are widely conserved across VOCs will help address these emerging variants and produce antibody immunity that is resistant to escape.

SARS-CoV-2 VOCs are not the only coronaviruses posing imminent risk to human health. Coronaviruses are part of the subgenera *Coronaviridae*. This subfamily is divided into four genera, *Alphacoronavirus, Betacoronavirus, Gammacoronavirus, and Deltacoronavirus*. *Betacoronaviruses* contain all three coronaviruses that have caused major outbreaks in recent history (SARS-CoV, MERS-CoV, and SARS-CoV-2) as well two human coronaviruses that typically cause mild respiratory infections (HCoV-OC43, and HKU1).[35] The *Betacoronavirus* genus can be further subdivided into five subclades or lineages, one of which is called lineage B or *sarbecovirus. Sarbecovirus* contains both SARS-CoV and SARS-CoV-2.[50] Studies on *sarbecoviruses* entry mechanisms using published S sequences suggest that many of them pose high potential for crossing over into humans from their animal hosts, although the majority of them do not use currently known coronavirus entry receptors.[51] Of particular note, with adequate cleavage of the S1/S2 subunits, at least thirteen *sarbecoviruses* S proteins can be used to infect human cells *in vitro* including two bat coronaviruses WIV1 and SHC014 that use ACE2 as an entry receptor.[42,51]

The genetic similarities between coronaviruses, specifically between S proteins of different *sarbecoviruses* and SARS-CoV-2 VOCs, has raised the question of cross-protective

immunity—whether natural or by design. In early 2020 at the beginning of the SARS-CoV-2 pandemic, studies were performed to understand if prior infection by other human coronaviruses would provide immunity against the newly emerging SARS-CoV-2. Disappointingly, prior infection with common cold betacoronaviruses OC43 or HKU1 did not demonstrate any protection against SARS-CoV-2 despite cross-binding of SARS-CoV-2 S by antibodies in SARS-CoV-2 naïve patient serum.[52] Similarly, a report of a potent SARS-CoV nAb CR3022 showed cross-binding of SARS-CoV-2 S and RBD but not cross-neutralization of SARS-CoV-2.[53,54] Still, the sequence similarity in the RBD of *sarbecovirus* S[50] and cross-binding properties of naturally derived non-SARS-CoV-2 antibodies like CR3022 raised the possibility that a cross-binding antibody raised against the right RBD epitope could produce cross-neutralization.

Sequence alignments of *sarbecovirus* RBDs show that the most divergent portion of the RBD is at the receptor binding site. This does not come as a surprise since there is no universal coronavirus entry receptor for infection.[51] Interestingly, at the base of the RBD distal from the receptor binding site, patches of conserved residues are present including a highly conserved region termed the 'cryptic' epitope overlapping the class 4 epitope where CR3022 antibody binds.[53,54]

Chapter 5 of this thesis discusses a subset of anti-RBD antibodies within the class 4 group that can bind to this highly conserved, cryptic epitope on the *sarbecovirus* RBD. This patch near the base of the RBD and facing towards the central axis of the S is remarkably conserved among sarbecovirus and, indeed, these cross-reactive antibodies are able to bind and neutralize a range of *sarbecoviruses.*[55]

The combination of VOCs and other coronaviruses poised for entry into the human population has certainly raised the idea of developing a pan-coronavirus vaccine that could protect against future coronaviruses; moving forward, vaccines will need to be designed that have robust activity against both new VOCs and emerging coronaviruses. Sequence differences amongst all clades of coronaviruses suggest that a pan-coronavirus vaccine at this point is unlikely. Despite this, cross-reactive epitopes certainly raise the possibility that

a well-designed immunogen could potentially be used to make a pan-*sarbecovirus* vaccine. Other groups have also reported various antibodies of a similar binding mode to the two that we reported[53,54,56–61] suggesting that their development within humans in an immune response is not a rare event and could be induced with the correct immunogen.

4.1: Structural Biology and its uses

A difficulty in studying proteins and other biological molecules is their small size. Numerous techniques have been repurposed or developed specifically to study these challenging samples. Within this thesis, I present works with structures solved by X-ray crystallography and single particle cryo-electron microscopy (sp cryo-EM). Like all scientific techniques, both methods have their strengths and weaknesses, but fundamentally each has played a massive role along in understanding how biological molecules look and function.

Historically, X-ray crystallography had a long tenure as arguably the most effective technique for determining structures of biological molecules to atomic resolution. This technique relies on ordering of very pure sample into delicate crystals which are shot with coherent waves of high energy X-rays. The structure is then deduced from the resulting diffraction pattern.[62] Several big hurdles exist in determining structures through X-ray crystallography, most of which boil down to challenges in obtaining a highly ordered, pure crystal lattice of protein that can be frozen and shot with X-rays. Every step from sample preparation through solving of the structures must work to obtain an electron density map that can successfully yield a model at high resolution. When all goes well, beautiful, insightful structures can be determined. Unfortunately, many structures have been unable to be tackled due to difficulties in sample preparation, flexibility, crystallization, and challenges in the diffraction data.

In some important ways, cryo-EM does not suffer the same limitations as X-ray crystallography. Cryo-EM uses an electron beam shot at a sample frozen in a native or native-like environment in non-crystalline ice to produce high resolution images. Sp cryo-EM uses purified molecules in solution whose images can be used to determine density maps of

molecules to build structural models. Of note, sp cryo-EM requires much less sample and can tolerate more flexibility and heterogeneity than X-ray crystallography. The use of electron microscopy to solve unstained structures of biological molecules to near atomic resolution dates back to 1975 when Unwin and Henderson solved a bacteriorhodopsin structure to 7Å.[63] While major advances in cryo-EM continued through the 1980s and 1990s including breakthroughs in sample freezing methods, it was the development of digital cameras and direct detectors for electron microscopes that began the cryo-EM revolution in the world of structural biology.[62] Since then, many structures of increasingly higher resolution have been determined, published, and deposited into the world wide Protein Data Bank (http://www.wwpdb.org/). Exciting developments in data processing software have now further pushed the field of structural biology to enter into the territory of understanding 3D structures of proteins not as static snapshots from crystal structures, but rather as small, moving biological machines.[64,65]

4.2: Creating the best samples for Env and S

Type I fusion proteins including the HIV-1 Env and the SARS-CoV-2 S are large, flexible, trimeric, transmembrane proteins—all qualities that make them difficult for structural determination. A critical advance in the HIV-1 field was the engineering of a stable, soluble, well-behaved trimeric form of Env[66] that could successfully mimic full-length, membrane-bound Env.[67,68] Prior to this many experiments (including structural ones) were performed using fragments of the gp41 helices or gp120 cores, which have all of their flexible variable loops removed.[69,70] Use of these components was important for understanding direct interactions with gp41 or gp120. In fact, numerous valuable structures exist of small molecules, peptides, antibodies, and other molecules bound to gp120 cores (including many structures of gp120 with CD4m), but these complexes are unable to give direct evidence about specific interactions in a fully trimeric Env. Cryoelectron tomography work had been done on native Env and these gave insights into the 3-D organization and conformations of Env, however the maps produced at the time were of modest resolution and could not yield high-resolution information such as conformations of sidechains or specifics of

interactions.[67] Further modifications to the original SOSIP produced what is now known as the Env SOSIP.664. The modern Env SOSIP.664 is a stable soluble protein truncated to remove the transmembrane domain at residue 664, containing stabilizing disulfides between the gp120 and gp41 subunits, and stabilizing Isoleucine to Proline mutations at I559P.[71,72] It is worth mentioning that SOSIPs were not the first example using proline mutations to stabilize large, Type I fusion proteins and had been successfully used in other viruses including influenza virus's fusion protein Hemagglutinin.[73,74] Many structures have now been published of Env SOSIPs in complex with various drugs and antibody Fab fragments. In combination with improved techniques for B cell sorting and cloning of antibody genes, it has been possible to understand how antibody responses are shaped during natural infections or during vaccine trials.

Similarly to the Env SOSIP, a stabilized structure was engineered for the SARS-CoV S and MERS-CoV S.[75] The engineered '2p' S contained two helix-breaking proline mutations that stabilized the pre-fusion S as well as truncated transmembrane domains. Sequence homology between existing engineered S and SARS-CoV-2 S allowed scientists to produce an equivalent engineered SARS-CoV-2 S that contained similar mutations.[44] This was further stabilized by the introduction of four additional Pro mutations to create the '6p' engineered S.[76]

As the main component for receptor binding, the receptor binding domain (RBD) of the S has also been truncated to produce various soluble RBD constructs. These have especially useful for higher resolution Fab-RBD structures as well as biochemical experiments that probe direct interactions to the RBD without the added complexities of having three RBDs present on a single S molecule. Much like the Env SOSIP and gp120 cores, the '2p' S, '6p' S, and RBD truncations have proven to be excellent substitutes for native membrane-bound forms of the protein and opened up many avenues of study.

4.3: The future of human tropic viruses

The world of scientific research was in a unique position when SARS-CoV-2 emerged. First and foremost, previous studies on SARS-CoV which is very similar in sequence to SARS-

CoV-2 had already established various important reagents. One of these was the engineered soluble prefusion '2p' S protein of MERS-CoV[75] that allowed scientists to very quickly design an equivalent engineered protein that was immediately used for experiments including multiple cryo-EM structures within mere weeks of the sequence being published.[43,44] Another major established technology was an mRNA vaccine against MERS-CoV (containing the stabilized '2p' S) which could be adapted quickly to SARS-CoV-2.[77] Both of these advances very much shortened the timeline that was needed to create effective monoclonal therapies and vaccines to treat and prevent SARS-CoV-2 infection and COVID-19 disease.

Secondly, another important aspect to the quick response to SARS-CoV-2 was a robust infrastructure for research on other human viruses especially in the field of HIV-1 which translated superbly to SARS-CoV-2. For the Bjorkman Lab and our collaborators, this was especially applicable to established techniques for cloning antibodies from convalescent COVID-19 donors, expressing viral proteins and human-derived antibodies, and being able to characterize them biochemically and biophysically.

The immediate and devastating impact of SARS-CoV-2 has highlighted the danger of zoonotic viruses with imminent spillover potential. From the perspectives listed above, we were extremely lucky with SARS-CoV-2 to be in a position to immediately produce effective scientific and clinical responses to an outbreak. There are numerous viruses that pose a danger of spillover into humans including coronaviruses outside of the Betacoronaviruses or in other viral genera that that are not as well studied to enable a quick response in the event of an outbreak. In particular, the huge viral loads and known viruses that bats carry makes them of particular concern for future viral outbreaks.[36] Moving forward, I hope that the worldwide experience with SARS-CoV-2 will serve as a lesson to us on the importance of viral research and the value of science, technology, and global health to prepare us for future outbreaks.

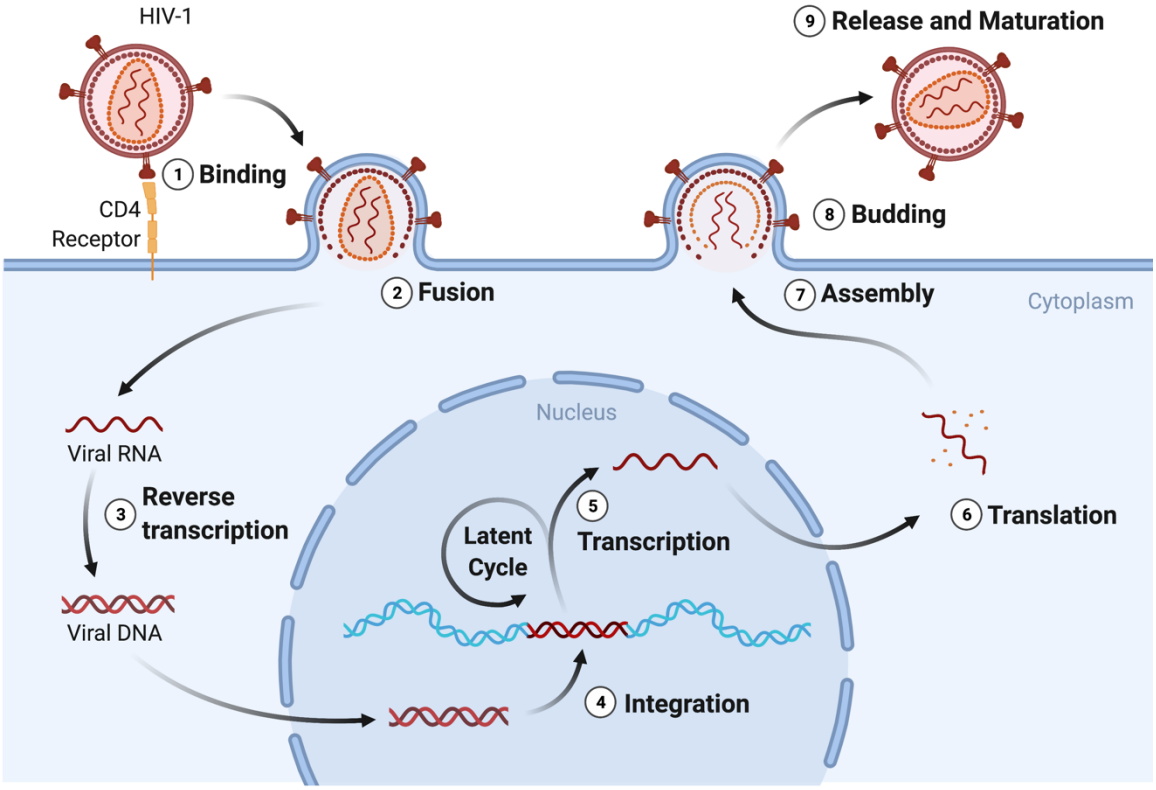

Figure 1: HIV-1 Lifecycle
Simplified cartoon depiction of the HIV-1 lifecycle. Adapted from "Retrovirus Replication Cycle," by BioRender.com (2022). Retrieved from https://app.biorender.com/biorender-templates.

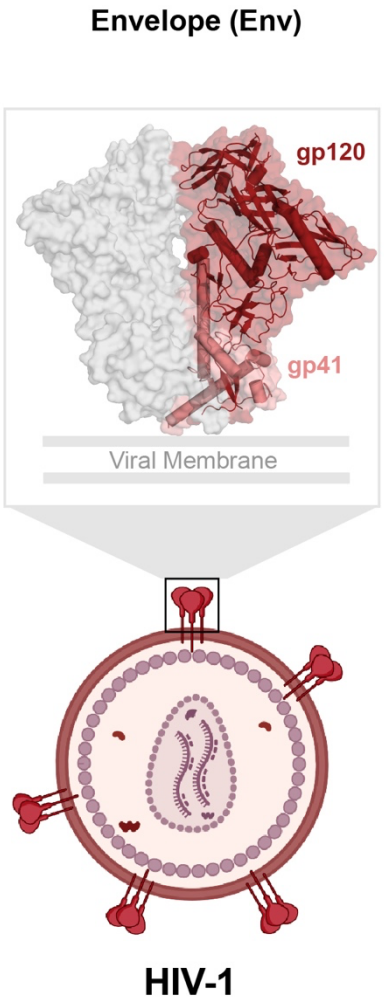

Figure 2: HIV-1 virus and Env protein structure
Schematic of HIV-1 with the Env protein boxed in grey. Surface and cartoon structure of HIV-1 Env shown with gp120 (dark red) and gp41 (salmon) highlighted. Adapted from Abernathy et al. *Viruses* 2021. Portions of this figure were produced using biorender.com.

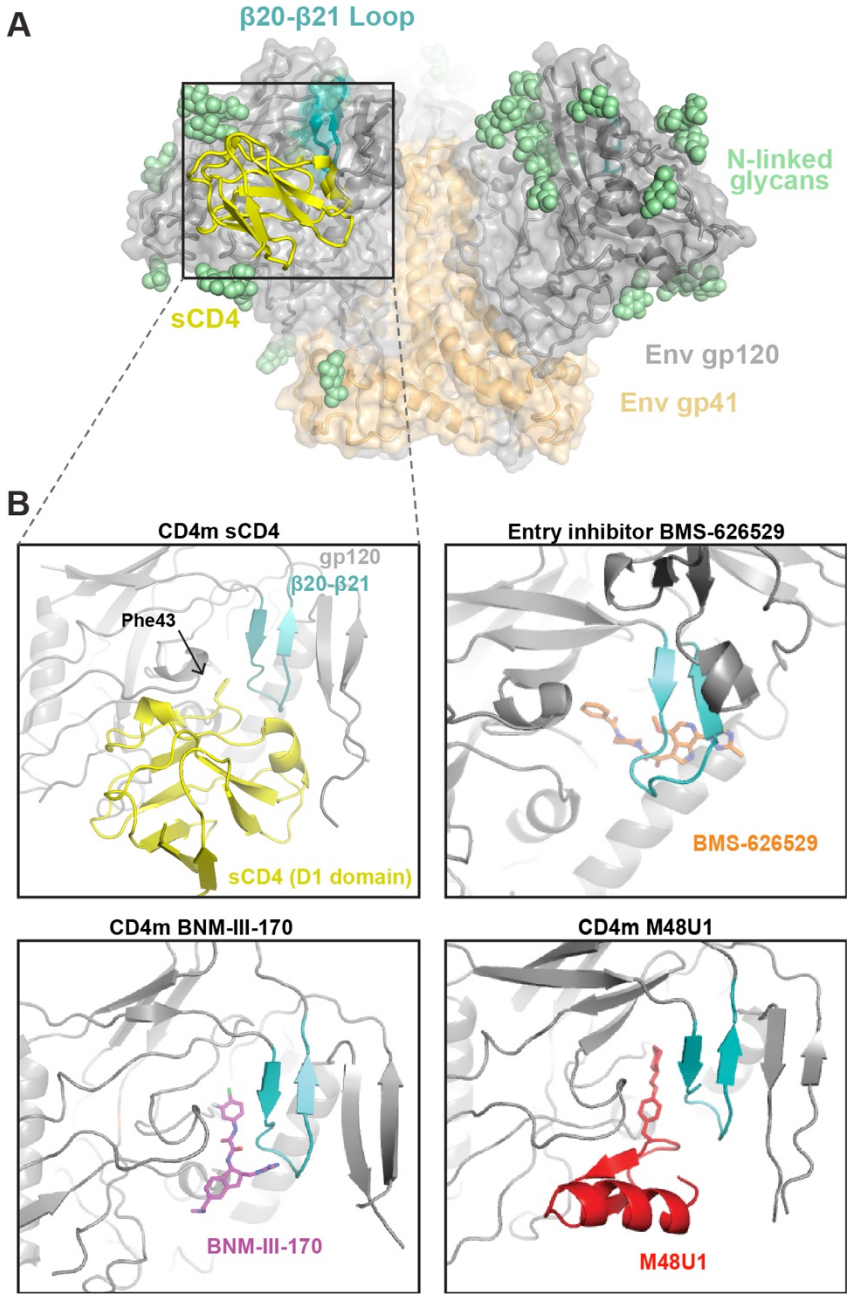

Figure 3: Drugs targeting the CD4 binding site.
(A) HIV-1 Env in an open, CD4-bound conformation (PDB: 6U0L). sCD4 D1 shown in yellow, gp120 in grey, gp41 in light orange, N-linked glycans as light green spheres, and the β20-β21 loop in deep teal.
(B) Individual panels showing various CD4m or entry inhibitors including sCD4 (yellow, PDB: 6U0L), BMS-626529 (orange, PDB:5U7O), BNM-III-170 (magenta, PDB: 7LO6), and M48U1 (PDB: 7LOK).

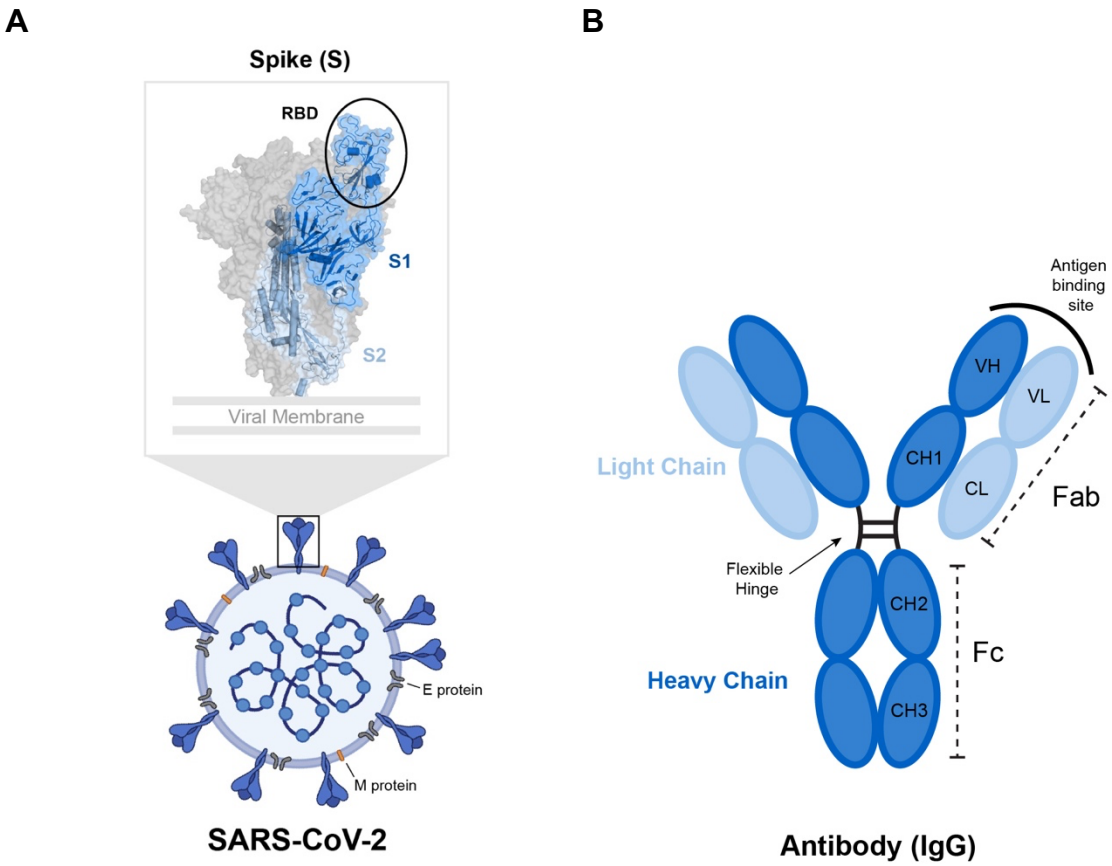

Figure 4: SARS-CoV-2 virus and antibody structures
(A) Schematic diagram of a SARS-CoV-2 virus with the S protein boxed in grey. Surface and cartoon structure of SARS-COV-2 S shown with S1 (dark blue) and S2 (light blue) highlighted. A single 'up' RBD is circled in black. Adapted from Abernathy et al. *Viruses* 2021. Portions of this figure were produced using biorender.com.
(B) Schematic diagram of an IgG antibody.

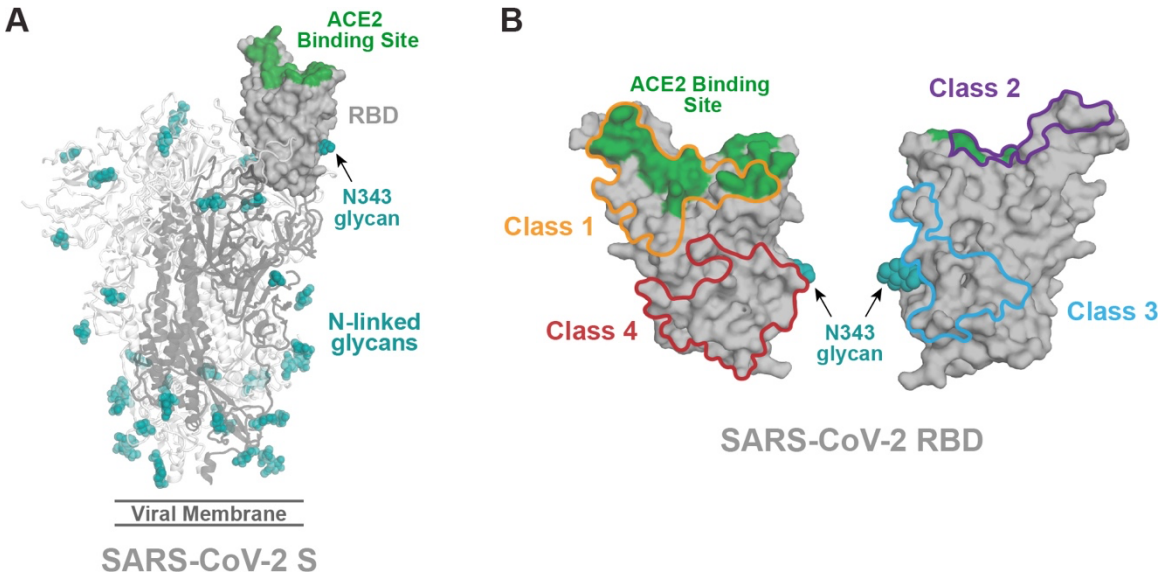

Figure 5: RBD-binding antibody classes
(A) Cartoon representation of SARS-CoV-2 S protein with one 'up' RBD shown as a surface representation. ACE2 binding site is highlighted in green. N-linked glycans shown in teal spheres. (B) Surface representation of RBD showing outlines of representative epitopes for antibodies from class 1 (C102 Ab), class 2 (C144), class 3 (S309), and class 4 (CR3022). The ACE2 binding site is highlighted in green and the N343 glycan is shown as teal spheres. (PDBs: S, 7M6E; RBD 7BZ5)

Table 1: SARS-CoV-2 Variants of concern (VOCs)		
Variant	**Pango nomenclature**	**Spike Mutations (RBD mutations in bold)**
Alpha	B.1.1.7	69-70 del, Y144 del, **N501Y**, A570D, D614G, P681H, T716I, S982A, D1118H
Beta	B.1.351	D80A, D215G, 242-244 del, **K417N, E484K, N501Y,** D614G, A701V
Gamma	P.1	L18F, T20N, P26S, D138Y, R190S, **K417T, E484K, N501Y,** D614G, H655Y, T1027I, V1176F
Delta	B.1.617.2	T19R, G142D, E156-F157 del, R158G, **L452R, T478K**, D614G, P681R, D950N
Omicron	B.1.1.529 (BA.1 sub-lineage mutations shown)	A67V, del69-70, T95I, del142-144, Y145D, del211, L212I, ins214EPE, **G339D, S371L, S373P, S375F, K417N, N440K, G446S, S477N, T478K, E484A, Q493R, G496S, Q498R, N501Y, Y505H,** T547K, D614G, H655Y, N679K, P681H, N764K, D796Y, N856K, Q954H, N969K, L981F

SARS-CoV-2 Variants of concern as listed by the World Health Organization (WHO)
Listed substitutions were accessed at the WHO website (https://www.who.int/docs/default-source/coronaviruse/spike-omicron-ba-1-ba-2.pdf?sfvrsn=d33f5c42_15) and are for amino acid changes present in ≥ 85% of the analyzed sequences when compared to the wild-type virus (GISAID EPI_ISL_402124).[48]

References

1. Centers for Disease Control (CDC). Kaposi's sarcoma and Pneumocystis pneumonia among homosexual men--New York City and California. *MMWR Morb Mortal Wkly Rep* **30**, 305–308 (1981).
2. *Global HIV & AIDS statistics — Fact sheet*. https://www.unaids.org/en/resources/fact-sheet. Accessed March 22, 2022.
3. Stevenson, M. HIV-1 pathogenesis. *Nat Med* **9**, 853–860 (2003).
4. Thomas, J., Ruggiero, A., Paxton, W. A. & Pollakis, G. Measuring the Success of HIV-1 Cure Strategies. *Front. Cell. Infect. Microbiol.* **10**, 134 (2020).
5. Klein, J. S. & Bjorkman, P. J. Few and Far Between: How HIV May Be Evading Antibody Avidity. *PLoS Pathog* **6**, e1000908 (2010).
6. Ward, A. B. & Wilson, I. A. The HIV-1 envelope glycoprotein structure: nailing down a moving target. *Immunol Rev* **275**, 21–32 (2017).
7. Kwong, P. D. *et al.* Structure of an HIV gp120 envelope glycoprotein in complex with the CD4 receptor and a neutralizing human antibody. *Nature* **393**, 648–659 (1998).
8. Ozorowski, G. *et al.* Open and closed structures reveal allostery and pliability in the HIV-1 envelope spike. *Nature* **547**, 360–363 (2017).
9. Wang, H. *et al.* Cryo-EM structure of a CD4-bound open HIV-1 envelope trimer reveals structural rearrangements of the gp120 V1V2 loop. *Proc Natl Acad Sci U S A* **113**, E7151–E7158 (2016).
10. Wang, H., Barnes, C. O., Yang, Z., Nussenzweig, M. C. & Bjorkman, P. J. Partially Open HIV-1 Envelope Structures Exhibit Conformational Changes Relevant for Coreceptor Binding and Fusion. *Cell Host Microbe* **24**, 579-592.e4 (2018).
11. Yang, Z., Wang, H., Liu, A. Z., Gristick, H. B. & Bjorkman, P. J. Asymmetric opening of HIV-1 Env bound to CD4 and a coreceptor-mimicking antibody. *Nat Struct Mol Biol* **26**, 1167–1175 (2019).
12. Punt, J., Stranford, S. A., Jones, P. P. & Owen, J. A. *Kuby immunology*. (Macmillan Learning, 2019).
13. Rambaut, A., Posada, D., Crandall, K. A. & Holmes, E. C. The causes and consequences of HIV evolution. *Nat Rev Genet* **5**, 52–61 (2004).
14. Wagh, K., Hahn, B. H. & Korber, B. Hitting the sweet spot: exploiting HIV-1 glycan shield for induction of broadly neutralizing antibodies. *Current Opinion in HIV and AIDS* **15**, 267–274 (2020).
15. Chaudhuri, S., Symons, J. A. & Deval, J. Innovation and trends in the development and approval of antiviral medicines: 1987–2017 and beyond. *Antiviral Research* **155**, 76–88 (2018).
16. Larder, B. A., Darby, G. & Richman, D. D. HIV with Reduced Sensitivity to Zidovudine (AZT) Isolated During Prolonged Therapy. *Science* **243**, 1731–1734 (1989).
17. Eggleton, J. S. & Nagalli, S. Highly Active Antiretroviral Therapy (HAART). in *StatPearls* (StatPearls Publishing, 2022).

18. Shafer, R. W. & Vuitton, D. A. Highly active antiretroviral therapy (Haart) for the treatment of infection with human immunodeficiency virus type 1. *Biomedicine & Pharmacotherapy* **53**, 73–86 (1999).

19. Marcus, J. L. *et al.* Comparison of Overall and Comorbidity-Free Life Expectancy Between Insured Adults With and Without HIV Infection, 2000-2016. *JAMA Network Open* **3**, e207954 (2020).

20. *FDA-Approved HIV Medicines | NIH*. https://hivinfo.nih.gov/understanding-hiv/fact-sheets/fda-approved-hiv-medicines. Accessed March 22, 2022.

21. Henrich, T. J. & Kuritzkes, D. R. HIV-1 entry inhibitors: recent development and clinical use. *Curr Opin Virol* **3**, 51–57 (2013).

22. Iacob, S. A. & Iacob, D. G. Ibalizumab Targeting CD4 Receptors, An Emerging Molecule in HIV Therapy. *Front Microbiol* **8**, 2323 (2017).

23. Nowicka-Sans, B. *et al.* In Vitro Antiviral Characteristics of HIV-1 Attachment Inhibitor BMS-626529, the Active Component of the Prodrug BMS-663068. *Antimicrobial Agents and Chemotherapy* **56**, 3498–3507 (2012).

24. Pancera, M. *et al.* Crystal structures of trimeric HIV envelope with entry inhibitors BMS-378806 and BMS-626529. *Nat Chem Biol* **13**, 1115–1122 (2017).

25. Laumaea, A., Smith, A. B., Sodroski, J. & Finzi, A. Opening the HIV envelope: potential of CD4 mimics as multifunctional HIV entry inhibitors. *Current Opinion in HIV and AIDS* **15**, 300–308 (2020).

26. Madani, N. *et al.* A CD4-mimetic compound enhances vaccine efficacy against stringent immunodeficiency virus challenge. *Nat Commun* **9**, 2363 (2018).

27. Bouchemal, K. *et al.* Thermosensitive and Mucoadhesive Pluronic-Hydroxypropylmethylcellulose Hydrogel Containing the Mini-CD4 M48U1 Is a Promising Efficient Barrier against HIV Diffusion through Macaque Cervicovaginal Mucus. *Antimicrob Agents Chemother* **59**, 2215–2222 (2015).

28. Madani, N. *et al.* Activation and Inactivation of Primary Human Immunodeficiency Virus Envelope Glycoprotein Trimers by CD4-Mimetic Compounds. *J Virol* **91**, e01880-16 (2017).

29. Zhao, Q. *et al.* Identification of N-phenyl-N′-(2,2,6,6-tetramethyl-piperidin-4-yl)-oxalamides as a new class of HIV-1 entry inhibitors that prevent gp120 binding to CD4. *Virology* **339**, 213–225 (2005).

30. Courter, J. R. *et al.* Structure-based design, synthesis and validation of CD4-mimetic small molecule inhibitors of HIV-1 entry: conversion of a viral entry agonist to an antagonist. *Acc Chem Res* **47**, 1228–1237 (2014).

31. Melillo, B. *et al.* Small-Molecule CD4-Mimics: Structure-Based Optimization of HIV-1 Entry Inhibition. *ACS Med. Chem. Lett.* **7**, 330–334 (2016).

32. Vita, C. *et al.* Rational engineering of a miniprotein that reproduces the core of the CD4 site interacting with HIV-1 envelope glycoprotein. *Proc Natl Acad Sci U S A* **96**, 13091–13096 (1999).

33. Acharya, P. *et al.* Structural basis for highly effective HIV-1 neutralization by CD4-mimetic miniproteins revealed by 1.5 Å cocrystal structure of gp120 and M48U1. *Structure* **21**, 1018–1029 (2013).

34. Madani, N. *et al.* CD4-Mimetic Small Molecules Sensitize Human Immunodeficiency Virus to Vaccine-Elicited Antibodies. *J Virol* **88**, 6542–6555 (2014).

35. Cui, J., Li, F. & Shi, Z.-L. Origin and evolution of pathogenic coronaviruses. *Nat Rev Microbiol* **17**, 181–192 (2019).

36. Letko, M., Seifert, S. N., Olival, K. J., Plowright, R. K. & Munster, V. J. Bat-borne virus diversity, spillover and emergence. *Nat Rev Microbiol* **18**, 461–471 (2020).

37. Zhou, P. *et al.* A pneumonia outbreak associated with a new coronavirus of probable bat origin. *Nature* **579**, 270–273 (2020).

38. Salzberger, B. *et al.* Epidemiology of SARS-CoV-2. *Infection* **49**, 233–239 (2021).

39. Michelen, M. *et al.* Characterising long COVID: a living systematic review. *BMJ Glob Health* **6**, e005427 (2021).

40. Almeida, J. D. & Tyrrell, D. A. J. The Morphology of Three Previously Uncharacterized Human Respiratory Viruses that Grow in Organ Culture. *Journal of General Virology* **1**, 175–178 (1967).

41. bioMerieux Connection Editors. June Almeida & The Discovery of the First Human Coronavirus. *bioMérieux Connection* https://www.biomerieuxconnection.com/2020/08/27/june-almeida-the-discovery-of-the-first-human-coronavirus/ (2020). Accessed March 22, 2022.

42. V'kovski, P., Kratzel, A., Steiner, S., Stalder, H. & Thiel, V. Coronavirus biology and replication: implications for SARS-CoV-2. *Nat Rev Microbiol* **19**, 155–170 (2021).

43. Walls, A. C. *et al.* Structure, Function, and Antigenicity of the SARS-CoV-2 Spike Glycoprotein. *Cell* **181**, 281-292.e6 (2020).

44. Wrapp, D. *et al.* Cryo-EM structure of the 2019-nCoV spike in the prefusion conformation. *Science* **367**, 1260–1263 (2020).

45. Samavati, L. & Uhal, B. D. ACE2, Much More Than Just a Receptor for SARS-COV-2. *Front Cell Infect Microbiol* **10**, 317 (2020).

46. Fung, T. S. & Liu, D. X. Human Coronavirus: Host-Pathogen Interaction. *Annu. Rev. Microbiol.* **73**, 529–557 (2019).

47. Barnes, C. O. *et al.* SARS-CoV-2 neutralizing antibody structures inform therapeutic strategies. *Nature* **588**, 682–687 (2020).

48. Tracking SARS-CoV-2 variants. https://www.who.int/health-topics/typhoid/tracking-SARS-CoV-2-variants. Accessed March 22, 2022.

49. Schmidt, F. *et al.* Plasma Neutralization of the SARS-CoV-2 Omicron Variant. *N Engl J Med* **386**, 599–601 (2022).

50. Cohen, A. A. *et al.* Mosaic nanoparticles elicit cross-reactive immune responses to zoonotic coronaviruses in mice. *Science* **371**, 735–741 (2021).

51. Letko, M., Marzi, A. & Munster, V. Functional assessment of cell entry and receptor usage for SARS-CoV-2 and other lineage B betacoronaviruses. *Nat Microbiol* **5**, 562–569 (2020).

52. Anderson, E. M. *et al.* Seasonal human coronavirus antibodies are boosted upon SARS-CoV-2 infection but not associated with protection. *Cell* **184**, 1858-1864.e10 (2021).

53. Huo, J. *et al.* Neutralization of SARS-CoV-2 by Destruction of the Prefusion Spike. *Cell Host Microbe* **28**, 445-454.e6 (2020).

54. Yuan, M. *et al.* A highly conserved cryptic epitope in the receptor binding domains of SARS-CoV-2 and SARS-CoV. *Science* **368**, 630–633 (2020).

55. Jette, C. A. *et al.* Broad cross-reactivity across sarbecoviruses exhibited by a subset of COVID-19 donor-derived neutralizing antibodies. *Cell Rep* **36**, 109760 (2021).

56. Liu, H. *et al.* Cross-Neutralization of a SARS-CoV-2 Antibody to a Functionally Conserved Site Is Mediated by Avidity. *Immunity* **53**, 1272-1280.e5 (2020).

57. Piccoli, L. *et al.* Mapping Neutralizing and Immunodominant Sites on the SARS-CoV-2 Spike Receptor-Binding Domain by Structure-Guided High-Resolution Serology. *Cell* **183**, 1024-1042.e21 (2020).

58. Pinto, D. *et al.* Broad betacoronavirus neutralization by a stem helix-specific human antibody. *Science* eabj3321 (2021) doi:10.1126/science.abj3321.

59. Starr, T. N. *et al.* SARS-CoV-2 RBD antibodies that maximize breadth and resistance to escape. *Nature* **597**, 97–102 (2021).

60. Tortorici, M. A. *et al.* Broad sarbecovirus neutralization by a human monoclonal antibody. *Nature* **597**, 103–108 (2021).

61. Zhou, D. *et al.* Structural basis for the neutralization of SARS-CoV-2 by an antibody from a convalescent patient. *Nat Struct Mol Biol* **27**, 950–958 (2020).

62. Callaway, E. The revolution will not be crystallized: a new method sweeps through structural biology. *Nature* **525**, 172–174 (2015).

63. Unwin, P. N. T. & Henderson, R. Molecular structure determination by electron microscopy of unstained crystalline specimens. *Journal of Molecular Biology* **94**, 425–440 (1975).

64. Punjani, A. & Fleet, D. J. 3D variability analysis: Resolving continuous flexibility and discrete heterogeneity from single particle cryo-EM. *Journal of Structural Biology* **213**, 107702 (2021).

65. Zhong, E. D., Bepler, T., Berger, B. & Davis, J. H. CryoDRGN: reconstruction of heterogeneous cryo-EM structures using neural networks. *Nat Methods* **18**, 176–185 (2021).

66. Sanders, R. W. *et al.* Stabilization of the soluble, cleaved, trimeric form of the envelope glycoprotein complex of human immunodeficiency virus type 1. *J Virol* **76**, 8875–8889 (2002).

67. Liu, J., Bartesaghi, A., Borgnia, M. J., Sapiro, G. & Subramaniam, S. Molecular architecture of native HIV-1 gp120 trimers. *Nature* **455**, 109–113 (2008).

68. Stadtmueller, B. M. *et al.* DEER Spectroscopy Measurements Reveal Multiple Conformations of HIV-1 SOSIP Envelopes that Show Similarities with Envelopes on Native Virions. *Immunity* **49**, 235-246.e4 (2018).

69. Chan, D. C., Fass, D., Berger, J. M. & Kim, P. S. Core structure of gp41 from the HIV envelope glycoprotein. *Cell* **89**, 263–273 (1997).

70. Kwon, Y. D. *et al.* Unliganded HIV-1 gp120 core structures assume the CD4-bound conformation with regulation by quaternary interactions and variable loops. *Proc Natl Acad Sci U S A* **109**, 5663–5668 (2012).

71. Klasse, P. J. *et al.* Influences on trimerization and aggregation of soluble, cleaved HIV-1 SOSIP envelope glycoprotein. *J Virol* **87**, 9873–9885 (2013).

72. Sanders, R. W. *et al.* A next-generation cleaved, soluble HIV-1 Env trimer, BG505 SOSIP.664 gp140, expresses multiple epitopes for broadly neutralizing but not non-neutralizing antibodies. *PLoS Pathog* **9**, e1003618 (2013).

73. Qiao, H. *et al.* Specific Single or Double Proline Substitutions in the "Spring-loaded" Coiled-Coil Region of the Influenza Hemagglutinin Impair or Abolish Membrane Fusion Activity. *Journal of Cell Biology* **141**, 1335–1347 (1998).

74. Rey, F. A. & Lok, S.-M. Common Features of Enveloped Viruses and Implications for Immunogen Design for Next-Generation Vaccines. *Cell* **172**, 1319–1334 (2018).

75. Pallesen, J. *et al.* Immunogenicity and structures of a rationally designed prefusion MERS-CoV spike antigen. *Proc Natl Acad Sci USA* **114**, E7348–E7357 (2017).

76. Hsieh, C.-L. *et al.* Structure-based design of prefusion-stabilized SARS-CoV-2 spikes. *Science* **369**, 1501–1505 (2020).

77. Corbett, K. S. *et al.* SARS-CoV-2 mRNA vaccine design enabled by prototype pathogen preparedness. *Nature* **586**, 567–571 (2020).

Chapter 2

HOW ANTIBODIES RECOGNIZE PATHOGENIC VIRUSES: STRUCTURAL CORRELATES OF ANTIBODY NEUTRALIZATION OF HIV-1, SARS-COV-2, AND ZIKA

Abernathy, M.E.*, Dam, K.-M.A.*, Esswein, S.R.*, **Jette, C.A.***, Bjorkman, P.J. How Antibodies Recognize Pathogenic Viruses: Structural Correlates of Antibody Neutralization of HIV-1, SARS-CoV-2, and Zika. *Viruses* **13**, 2106 (2021). doi:10.3390/v13102106

* Equal Contribution

Summary

The H1N1 pandemic of 2009-2010, MERS epidemic of 2012, Ebola epidemics of 2013-2016 and 2018-2020, Zika epidemic of 2015-2016, and COVID-19 pandemic of 2019-2021, are recent examples in the long history of epidemics that demonstrate the enormous global impact of viral infection. The rapid development of safe and effective vaccines and therapeutics has proven vital to reducing morbidity and mortality from newly emerging viruses. Structural biology methods can be used to determine how antibodies elicited during infection or vaccination target viral proteins and identify viral epitopes that correlate with potent neutralization. Here we review how structural and molecular biology approaches have contributed to our understanding of antibody recognition of pathogenic viruses, specifically HIV-1, SARS-CoV-2, and Zika. Determining structural correlates of neutralization of viruses has guided the design of vaccines, monoclonal antibodies, and small molecule inhibitors in response to the global threat of viral epidemics.

Introduction

Advances in structural biology in recent decades have played a key role in the determination of disease-relevant protein complexes and guided the design of new therapeutics and vaccines. An early pioneer in structural biology was the X-ray crystallographer Rosalind Franklin. While she is best known for her role in collecting the X-ray fiber diffraction patterns that revealed the 3D structure of DNA, her contributions in biologically-related fields also included insights into the structures of protein encapsulated viruses such as tobacco mosaic

virus (TMV), poliovirus, and turnip yellow mosaic virus. During Franklin's studies of viruses in the 1950s, a central question was how viruses managed to build a protein shell to shield their genetic material given that only a limited number of viral capsid proteins could be encoded within a viral genome based on capsid size constraints. Franklin's X-ray analysis revealed the arrangement of the protein subunits in TMV, allowing her to create the first three-dimensional model of a virus [1–4]. Following this work, she used X-ray data to determine the position and orientation of RNA packaged inside of the rod-shaped TMV [5]. Unlike prior speculation that placed the RNA at the center of the rod, her work revealed the virus was hollow, which led to the discovery that the RNA spiraled with the helical protein capsid. This work was fundamental in understanding principles of virus structure. Franklin's contributions to the field of virology are summarized on her tombstone, which reads, "Her research and discoveries on viruses remain of lasting benefit to mankind." Together, her remarkable contributions to structural studies in three separate areas, DNA, coal, and viruses, before her death at the age of 37 make her an inspiration to future generations of structural biologists, particularly women. We are proud to follow in her footsteps to use structural biology to gain insight into viruses with the goal of providing benefits to human health.

The severe acute respiratory syndrome coronavirus (SARS-CoV) epidemic of 2002, Middle East Respiratory Syndrome (MERS) epidemic of 2012, acquired immune deficiency syndrome (AIDS) pandemic starting in 1981, the Zika virus (ZIKV) epidemic of 2015-2016, and the ongoing SARS-CoV-2/COVID-19 pandemic are examples of the enormous global burden of viruses and the urgent need for vaccine and therapeutic development. Building on the prior contributions of early pioneers such as Rosalind Franklin, structural biologists continue to advance techniques in X-ray crystallography and cryo-electron microscopy (cryo-EM) to investigate viruses and viral proteins. We are interested in investigating antibody (Ab) recognition of viruses, which we do by solving 3D structures of viral proteins bound to Abs elicited by infection or vaccination. Understanding the structural correlates of Ab recognition of viruses is key for the development of effective monoclonal Ab therapies and vaccines (Figure 1).

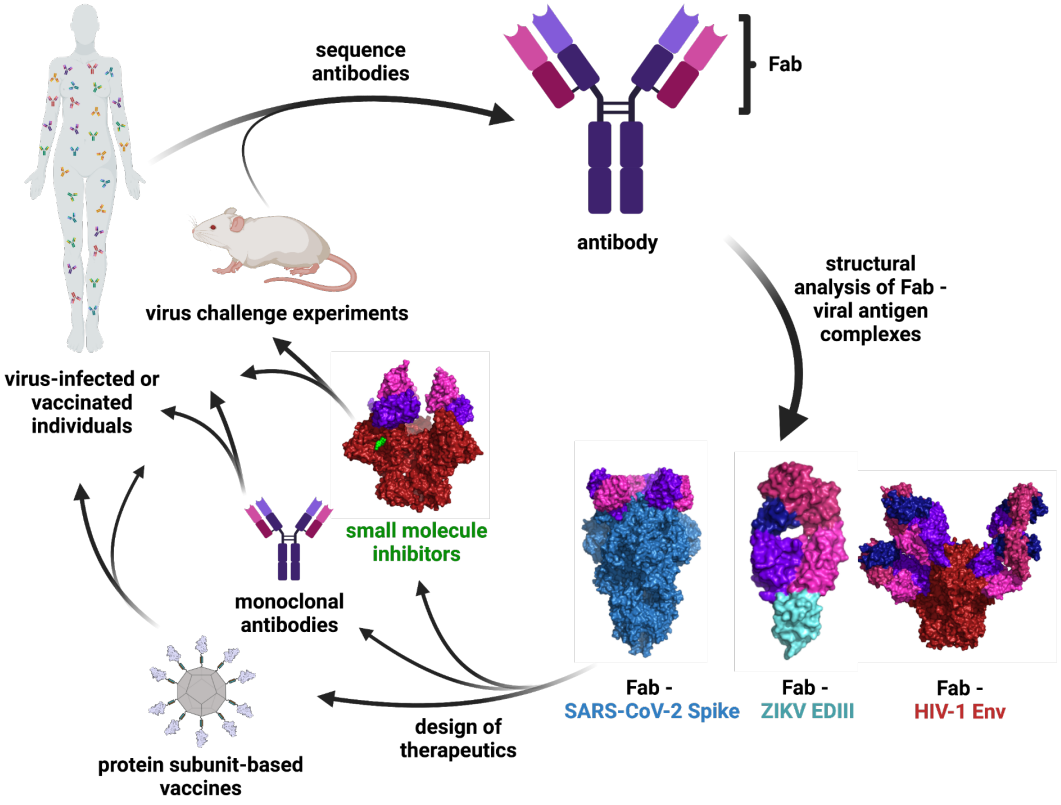

Figure 1: Schematic of Ab characterization and therapeutic development.
The binding epitopes of Abs isolated from infected or vaccinated individuals or animal studies are determined through structural analysis of Fab - viral antigen complexes. These structures inform the design of vaccines, monoclonal Abs, and small molecule therapeutics that can be tested in clinical trials and animal models. Surface representations are shown for the following structures: Fab - SARS-CoV-2 S (PDB 7K90), Fab - ZIKV EDIII (PDB 5VIG), Fab - HIV-1 Env (PDB 5T3Z), and small molecule inhibitor - HIV-1 Env (PDB 7LO6).

Human immunodeficiency virus 1 (HIV-1) is responsible for the AIDS pandemic and 36 million deaths to date [6] and has long posed a challenge for vaccine development due its remarkable ability to evade the host immune response and establish latent reservoirs. HIV-1 contains a single viral protein on its surface that facilitates infection of immune cells. This protein, named Envelope or Env, is a trimer of gp120/gp41 heterodimers (Figure 2A). The gp120 portion of Env interacts with host CD4 receptors, which stimulates conformational changes that allow binding to the co-receptor, usually a host chemokine receptor called CCR5 [7]. These events trigger rearrangements in gp41 that allow fusion of the viral and host cell membranes, which is required for entry of the HIV-1 genome into the host cell [7].

In addition to small molecule anti-retroviral drug treatments to treat infected individuals, current strategies to prevent HIV-1 infection include vaccine design. Vaccine efforts seek to stimulate the evolution of broadly neutralizing Abs (bNAbs) that have been isolated in rare cases of human HIV-1 infection and are capable of broad and potent protection [8–10]. Advances in X-ray crystallography and cryo-EM have given us the invaluable opportunity to structurally characterize bNAb interactions with Env and Env conformational changes which have informed vaccine design efforts.

SARS-CoV-2, the virus responsible for the COVID-19 pandemic, has caused 4.5 million deaths and an estimated 225 million infections as of September 2021 [11]. The spike (S) proteins on the surface of SARS-CoV-2 allow it to infect host cells by binding the host cellular angiotensin-converting enzyme 2 (ACE2) receptor [12,13]. Each of the three protomers on an S protein includes two subunits, S1 and S2. The receptor binding domain (RBD) on S1 is the component that recognizes ACE2 during cell entry (Figure 2B) [13–16]. While the RBD can adopt both 'up' and 'down' conformations, it can only bind ACE2 when it is an 'up' conformation [14–20]. Due to the critical role of the RBD in facilitating infection, neutralizing Abs that target the RBD are an important component of the immune response against SARS-CoV-2 [21–31]. Structural biology has been instrumental in the rapid characterization and evaluation of the S protein and Abs produced in natural infection [15,21,21–33]. This work has contributed to the development of COVID-19 vaccines and monoclonal Ab (mAb) therapeutics, which have saved countless lives.

ZIKV is a mosquito-borne virus that can cause microcephaly and neurodevelopmental abnormalities in the newborns of infected mothers [34–37]. As part of the *flavivirus* genus, ZIKV shares similar features as other widespread flaviviruses such as dengue (DENV), West Nile virus (WNV), and yellow fever virus (YFV) [38–41]. Mature ZIKV has seven non-structural proteins (NS1, NS2A, NS2B, NS3, NS4A, NS4B and NS5) and three structural proteins: envelope (E), membrane (M), and capsid (C) [42–44]. The surface of ZIKV is coated by 180 copies of the E protein arranged as 90 dimers, and each E protein includes three ectodomains, EDI, EDII, and EDIII (Figure 2C) [38,42,43]. The flexible regions

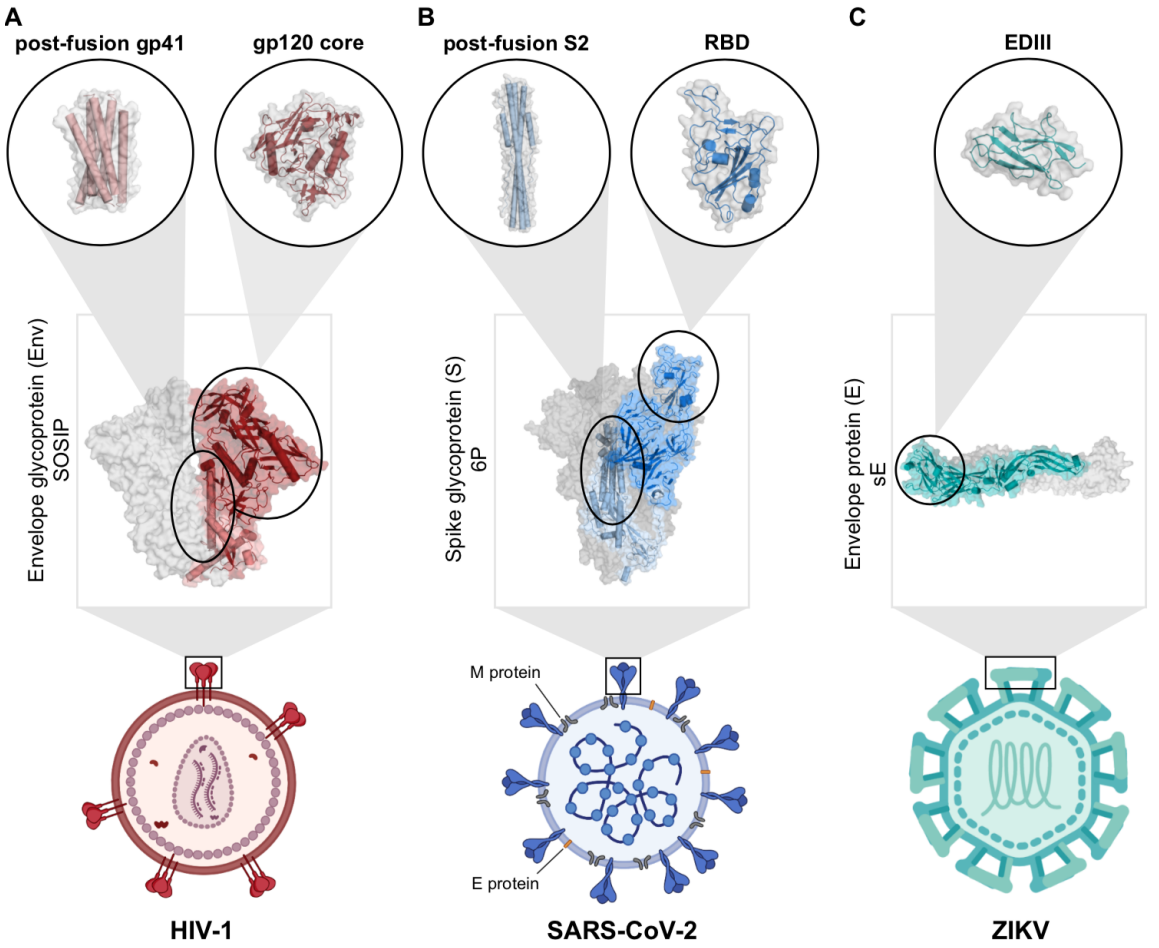

Figure 2: Structural targets of HIV-1, SARS-CoV-2, and ZIKV.
(A) Cartoon HIV-1 virion with a closed, pre-fusion Env protein structure highlighted (PDB: 6UDJ). Circles show crystal structures of the postfusion gp41 bundle (left, PDB: 1AIK) and gp120 core (right, PDB: 5F4P).
(B) Cartoon SARS-CoV-2 virion with S protein (blue), M protein (grey), and E protein (orange). The closed, pre-fusion S protein structure with one 'up' RBD (blue subunit) and two 'down' RBDs (grey subunits) is shown in the box (PDB: 7K8V). Circles show postfusion S2 helices (left, PDB: 6LXT) and RBD (right, PDB: 7K8M) structures.
(C) Cartoon ZIKV virion with E protein (teal). The soluble E (sE) protein dimer structure is shown in the box with one E protein highlighted (PDB: 5JHM).The EDIII structure is shown in the circle (PDB: 6UTA).

between the domains allows dynamic conformational changes to occur during viral entry and fusion [38,45–48]. EDII contains a conserved fusion loop (FL) peptide that becomes exposed after viral entry into cells and initiates endosomal fusion [42,43,49,50]. EDIII is thought to be important for receptor binding during infection, and consequently, is an important target

for neutralizing Abs [51–56]. There is not yet a safe and effective vaccine against ZIKV that is universally available.

Here we review how approaches in structural and molecular biology have increased our understanding of Ab recognition of HIV-1, SARS-CoV-2, and ZIKV. We discuss how the design of stable and soluble viral antigens amenable for structural approaches has enabled our ability to analyze complexes of viral antigens bound by the antigen binding fragment (Fab) of Abs. Use of both cryo-EM and X-ray crystallography has increased our understanding of key viral epitopes targeted by Abs and conformational changes of viral proteins necessary for infection. These structural insights, combined with analyses of the levels of somatic hypermutation found in potently neutralizing Abs, provide valuable information for the development of effective vaccines and monoclonal Ab therapies to reduce global morbidity and mortality from epidemic/pandemic-causing viruses.

Main Body

Engineering viral surface proteins for structural studies

Structural biology techniques such as X-ray crystallography and single particle cryo-EM require samples that are stable enough to be isolated and manipulated in the laboratory. For some viruses, especially those that are symmetric, it is feasible to structurally characterize intact viruses using cryo-EM. For example, cryo-EM structures of intact, whole ZIKV have been solved with and without Fabs of Abs bound [42,43,57–62]. Viruses with pleomorphic structures (e.g., most enveloped viruses) can also be investigated structurally using cryo-electron tomography [63–65]. In order to prepare surface viral proteins of enveloped viruses for structural studies and therapeutic development, it has been necessary to produce soluble, native-like versions that are stabilized in a pre-fusion conformation that is targeted by neutralizing Abs.

Classically, the simplest way to solubilize a surface viral protein is to remove the transmembrane and cytoplasmic domains by truncation [66,67]. Truncation has also been used to produce smaller components such as single domains. Examples of truncated domains include gp120 cores of HIV-1 Env, which have the β4 and β26 strands and all flexible loops removed [68,69], coronavirus RBDs truncated at the base where the flexible hinge connects them to the rest of the S1 subunit [70,71], and the individual EDIII truncated from the rest of the ZIKV E protein [52–54,72,73]. Truncation of individual domains has been especially powerful for X-ray crystallography as crystallization is hindered by flexible regions such as loops or inter-domain linkers and hinges. Single domains are useful for solving high resolution structures of Fab-domain complexes that provide detail about the Ab interactions that may not be possible using single particle cryo-EM due to flexibility or heterogeneity of larger protein complex structures [32,52–54,72–74].

While truncated proteins have been useful in the field of structural biology, they do not necessarily reflect all aspects of the whole antigen and cannot always recapitulate the properties of a native viral protein. An extra layer of complexity exists since many viral proteins adopt distinct conformations depending on the step in the viral life cycle, requiring engineering and stabilization of the desired conformation for larger, multi-subunit complexes [43,46,47,57]. Fusion proteins such as Env and S include folded helical bundles that must extend for fusion of the viral and host cell membrane bilayers. These proteins are metastable in their pre-fusion conformation, which is usually the target of neutralizing Abs [75]. The introduction of stabilizing mutations can be helpful for preparing soluble constructs of larger, multi-subunit complexes. For example, helix-breaking proline mutations have been introduced into the central helices of fusion proteins, preventing the extension of helices required for membrane fusion [76]. In combination with an inter-subunit disulfide bond and truncation after residue 664, these mutations were introduced into HIV-1 Env to produce the pre-fusion stabilized SOSIP.664 trimers [77]. The proline helix-breaking stabilizing mutations have been successfully adapted to other viral fusion proteins including those on coronaviruses, RSV, Ebola virus, human metapneumovirus, and Lassa virus [75]. For SARS-CoV-2 S, additional prolines were introduced that further stabilize the trimer in the 6P, or

'HexaPro' version [67]. For studies of the ZIKV E protein soluble constructs of both monomeric E protein [56,78–80] and engineered disulfide-linked E protein dimers [55,81] have been designed.

Most regions of proteins have a purpose that is important to their function, particularly transmembrane regions and cytoplasmic tails [82]. Consequently, truncated and stabilized proteins used as substitutes for full-length equivalents are only useful to the extent that they are able to approximate the native state of the protein. It is essential for the engineered forms used for structural studies to be characterized with non-structural methods to confirm that they behave in a similar fashion to the native form in the context they are being studied.

Dominant Ab Epitopes on Viral Fusion Proteins

Structural analysis has facilitated identification of neutralizing epitopes on HIV-1, SARS-CoV-2 and ZIKV. Both X-ray crystallography and cryo-EM analyses of viral antigens in complex with neutralizing Ab Fabs have provided insights into mechanisms of neutralization by Abs and identified new therapeutic targets [7,32]. Neutralizing epitopes tend to be in structurally functional regions, and in many cases facilitate or hinder a structural change. In addition to neutralizing Abs, an immune response to a pathogen or vaccine can produce weakly neutralizing or non-neutralizing antibodies. which can be protective through various mechanisms such as antibody dependent cell cytotoxicity (ADCC) [83–86]. For viral fusion, there is typically a dramatic conformational change that occurs in the fusion protein to expose receptor binding sites for attachment and to insert the fusion machinery into the target membrane to undergo fusion [87]. Requiring a large conformational change is a strategy that allows viruses to hide vulnerable regions that are necessary for interactions important for viral function, such as target receptor binding. Many Abs bind in ways that can hinder or trigger fusion-necessitated conformational changes, resulting in various neutralization mechanisms [7].

HIV-1 Env Epitopes

HIV-1 Env is present on the surfaces of virions in a closed pre-fusion conformation that includes centrally located gp120 subunits and the V1/V2 and V3 variable loops interacting about the apex of the trimer, hiding the co-receptor binding site on V3 [88]. Upon binding to the host cell receptor CD4 at the CD4 binding site (CD4bs) in the gp120 subunit, the Env protein rearranges to an open state in which the gp120s are rotated outwards, the V1/V2 loop is displaced to the sides of the Env trimer, and the V3 loop is exposed, allowing access to the co-receptor binding site on V3 [89–93] (**Figure 3A**). In the CD4-bound open conformation, a 4-stranded antiparallel bridging sheet is formed by the gp120 β-strands β20, β21, β2, and β3, the gp120 subunits swing away from the central axis and rotate slightly counter-clockwise, and the gp41 HR1 helices become more ordered and extended [90–92]. In this conformation, the V3 loop is exposed and can then bind to the co-receptor, which is required for entry [93]. HIV-1 Env epitopes target some of these intermediate fusion conformations, in addition to the closed, pre-fusion structure.

The epitopes of bNAbs often include conserved functional regions that are conformationally masked in the closed, pre-fusion structure or sterically restricted by N-linked glycans [7]. In fact, in many cases, N-glycans that occlude the protein surface of Env actually become part of the Ab epitope. HIV-1 epitope targets of bNAbs can be divided into the following categories: (1) bNAbs that bind at the apex of the trimer, specifically to the V1/V2 loops that undergo a dramatic rearrangement during host receptor engagement [94–96], (2) bNAbs against the V3-glycan patch, which includes the highly conserved GDIR motif and several N-linked glycans on and around the V3 loop [97,98], (3) CD4bs bNAbs that target the host receptor binding domain [7,74,99], (4) bNAbs that only bind to Envs in a CD4-induced open state [68,89,91], (5) “silent face” bNAbs that target a glycan-rich patch on the opposite face from the CD4bs on gp120 [98,100,101], (6) bNAbs that target the gp120/gp41 interface, including those that interact with the fusion peptide [102,103], and (7) bNAbs that bind to the membrane proximal external region (MPER) on gp41 [104] (**Figure 4A**).

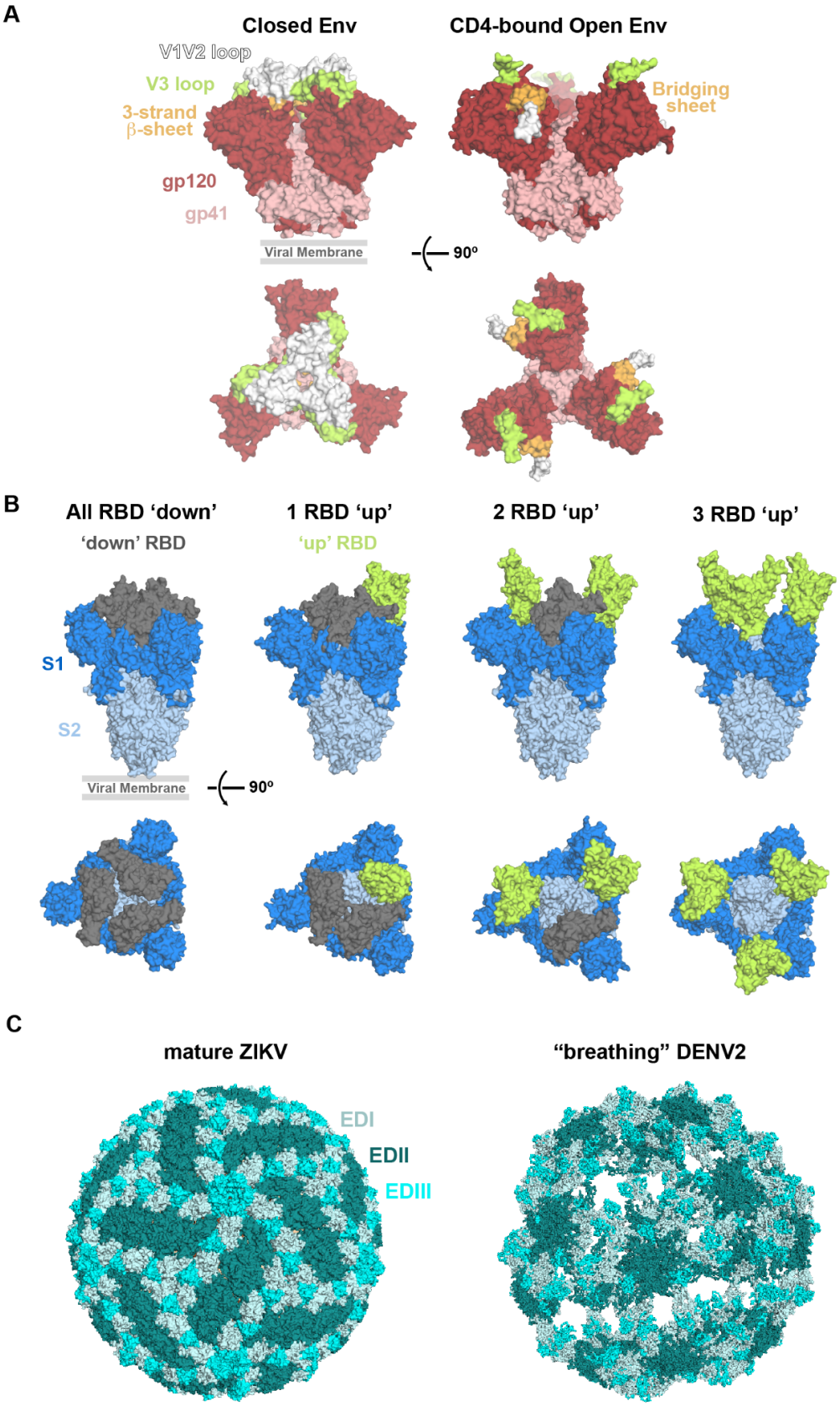
A
Closed Env
CD4-bound Open Env
V1V2 loop
V3 loop
3-strand β-sheet
gp120
gp41
Viral Membrane
Bridging sheet
90°
B
All RBD 'down'
1 RBD 'up'
2 RBD 'up'
3 RBD 'up'
'down' RBD
'up' RBD
S1
S2
Viral Membrane
90°
C
mature ZIKV
"breathing" DENV2
EDI
EDII
EDIII

Figure 3: Conformational changes of HIV-1 Env, SARS-CoV-2 S, and ZIKV E.
(A) Surface depictions of top down and side views of (left) closed, pre-fusion Env (PDB: 6UDJ) and (right) CD4-bound open conformation Env (PDB: 5VN3) highlighting the V1V2 loop (white), V3 loop (green), and 3-strand beta sheet (bright orange). Gp120 = dark red, gp41 = salmon.
(B) Surface depictions of side and top down views of closed, pre-fusion S with three 'down' RBDs (grey, PDB: 7K90), 1 'up' RBD (green, PDB: 7K8V), 2 'up' RBDs (7K8Y), and 3 'up' RBDs (6XCN). The location of the viral membrane is indicated in side views of viral proteins.
(C) Surface depictions comparing the smooth mature ZIKV (PDB: 6CO8) and spiky "breathing" DENV2 (PDB: 3ZKO) structures. In the "breathing" DENV2 structure, EDI and EDIII of the E protein are protruding, giving the virus a "spiky" appearance, and holes are found in the surface.

Each epitope presents a distinct landscape for bNAb binding and poses different challenges for Abs to overcome. For most epitopes, N-linked glycans on the heavily-glycosylated Env trimer sterically restrict access to conserved protein regions, and therefore bNAbs tend to include conserved N-linked glycans in the epitope and/or develop long complementary determining region (CDR) loops to penetrate through the glycan shield [7]. This is the case for V1/V2, V3, and silent face epitopes. For example, the V3-glycan patch epitope is defined by the V3 loop that is essential for co-receptor binding and several N-linked glycans. bNAbs that target this region, including 10-1074, PGT121, and BG18, have long, 20+ amino acid CDRH3 loops that reach through the glycan patch to bind a conserved V3 motif from gp120 residues 324-327 with the sequence GDIR [97]. These bNAbs also make important contacts with conserved glycans $Asn156_{gp120}$ and $Asn332_{gp120}$. In contrast, some bNAbs against the CD4bs require short CDR loops to accommodate an N-linked glycan in that region. CD4bs bNAb 3BNC117 has a 5-residue deletion in CDRL1 that is necessary to prevent steric clashes with the $Asn276_{gp120}$ glycan and a short, 5-amino acid CDRL3 that is essential to avoid clashes with gp120 [105]. The gp120-gp41 interface epitope is composed of protein and glycan residues in both subunits. This category includes bNAbs that target the fusion peptide (FP), which are the highly conserved N terminal residues of gp41 responsible for burying into the host cell membrane during the fusion process of viral entry. FP bNAb VRC34.01 binds primarily to the N-terminal 8 residues of gp41 with the remainder of interactions made with $Asn88_{gp120}$ [102]. Together, these examples demonstrate the diverse epitope landscape of the HIV-1 Env trimer and how Abs develop particular features to overcome challenges posed by the dense glycan shield.

The mode of binding for bNAbs at all epitopes has been greatly illuminated by structural biology. In particular, X-ray crystallographic and cryo-EM structures of Ab:Env complexes have been essential tools to characterize which epitope newly isolated bNAbs bind, the mode of binding implemented, and to understand the context of atypical features in the sequence such as CDR lengths. The wealth of structural data has enabled structure-based design of gp120 and SOSIP-based immunogens that seek to elicit responses to particular epitopes and design small molecule drugs.

SARS-CoV-2 S Epitopes

The SARS-CoV-2 fusion machinery is the surface protein S, which is composed of three identical subunits each containing an RBD that sits at the apex of S and is attached to the rest of the subunits with a flexible hinge [14]. The RBDs are able to sample a 'down' conformation that hides the ACE2 binding site by packing it against a neighboring RBD, or an 'up' conformation, which exposes the ACE2 binding site at the tip of the RBD and is required for host receptor binding [15,32,106] (**Figure 3B**).

Abs that recognize the RBD of the SARS-CoV-2 S protein are a vital part of the neutralizing Ab response to infection and vaccination because the RBD contains the binding site for ACE2. Effective neutralization by many anti-RBD Abs is due to their ability to block the RBD from binding the host ACE2 receptor. The epitopes targeted by Abs against the RBD can be organized into four simplified classes [32]. Class 1, *VH3-53/VH3-63*-derived Abs, target epitopes overlapping with the ACE2 binding site and only bind 'up' conformation RBDs. Class 2 Abs target epitopes overlapping with the ACE2 binding site and can bind both 'up' and 'down' RBDs. Class 3 Abs target epitopes that do not overlap with the ACE2 binding site and bind both 'up' and 'down' RBDs. Finally, class 4 Abs target a cryptic surface facing the S trimer interior and only bind 'up' RBDs [32] (**Figure 4B**).

While the anti-SARS-CoV-2 Ab landscape has primarily focused on the RBD, a growing number of neutralizing Abs that target other regions of the S protein are being found.

Neutralizing Abs that bind to the N terminal domain (NTD) [107–109] and the S2 domain [107,110–113] have been reported, indicating that the RBD is not the only site of neutralization. In addition, some of these Abs are also broadly cross-reactive to other betacoronaviruses as they target highly conserved regions of S such as the class 4 cryptic epitope on the RBD [24,114–116] or the stem helix of S2 [111–113].

ZIKV Epitopes

The E protein of ZIKV and other flaviviruses is key for facilitating cellular entry and fusion [48]. The mature structure of ZIKV displays smooth virus particles with 180 copies of the E protein arranged as 90 dimers with icosahedral symmetry, and EDIII is thought to be responsible for binding cellular receptors [43,48,117–120]. After cellular entry through receptor-mediated endocytosis, the acidic pH triggers a conformational change by which the E proteins form trimers and expose the FL on EDII for membrane fusion [121–123].

Given its role in fusion, the E protein is an important target of neutralizing Abs that effectively clear ZIKV, inhibit ZIKV infection in vitro, decrease vertical transmission, and are protective in ZIKV challenge in animal models [53–56,72,79,124,125] (**Figure 2C)**. Structural characterization of Abs that bind the ZIKV E protein have revealed multiple epitopes on the three domains: (1) the conserved FL found on EDII [56,126], (2) EDIII [52–54,72,73,127], (3) multiple domains of single E protein [79,80], (4) multiple domains spanning an E protein dimer [55,60,79,125,128,129], and (5) multiple domains spanning neighboring E dimer pairs [61,62,79,129]. Abs against the FL in EDII compose a large portion of the response to infection, and because the FL is conserved among flaviviruses, these Abs can cross-react with different flaviviruses [56,79,124–126,130]. However, many potently-neutralizing Abs target EDIII and these Abs tend to be more specific for ZIKV than other flaviviruses [51–56,61,72,124,125,131–137] (**Figure 2C)**.

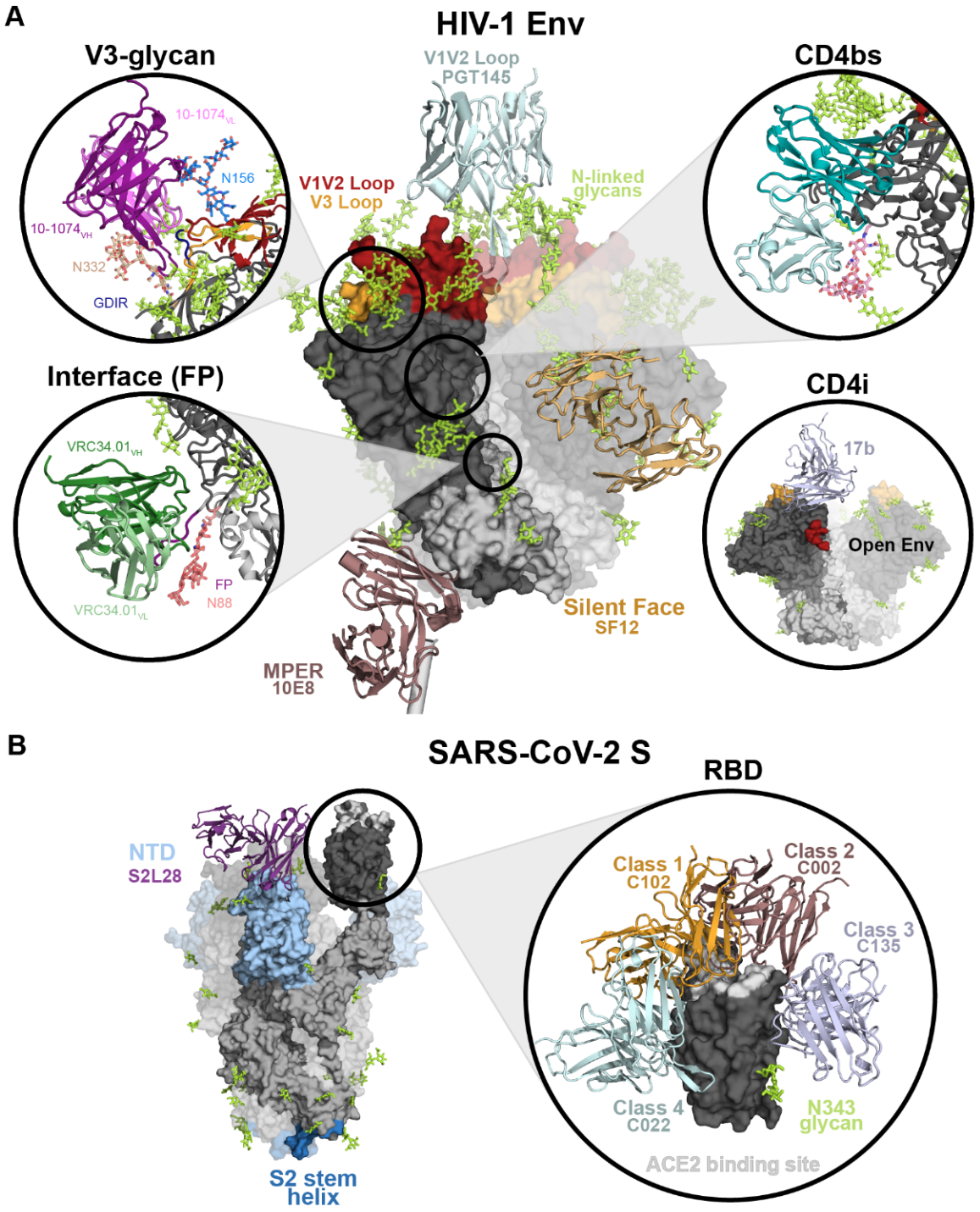
A
HIV-1 Env
V3-glycan
10-1074VL
N156
10-1074VH
N332
GDIR
V1V2 Loop
PGT145
V1V2 Loop
V3 Loop
N-linked
glycans
CD4bs
Interface (FP)
VRC34.01VH
FP
N88
VRC34.01VL
CD4i
17b
Open Env
Silent Face
SF12
MPER
10E8
B
SARS-CoV-2 S
RBD
NTD
S2L28
Class 1
C102
Class 2
C002
Class 3
C135
Class 4
C022
N343
glycan
ACE2 binding site
S2 stem
helix

Figure 4: Neutralizing epitopes on HIV-1 Env and SARS-CoV-2 S.
(A) HIV-1 Env structure (left) highlighting epitopes of representative bNAbs for each bNAb class. Env (PDB: 5T3Z) is shown as a surface with green N-linked glycans shown as sticks. Gp41 is light grey and gp120 is dark grey except for the V1V2 loop (dark red) and V3 loop (light orange). V_HV_L domains of Abs binding the epitopes MPER (mauve, 10E8, PDB: 6VPX), V1V2 loop (pale cyan, PGT145, PDB: 5V8L) or Silent Face (sand, SF12, PDB: 6OKP) are shown as cartoons. Circles show details for Ab binding to the V3-glycan (10-1074, PDB: 5T3Z), interface (VRC34.01, PDB: 5I8H), CD4bs (3BNC117, PDB: 5V8L), and CD4i (17b, PDB: 7LO6).
(B) SARS-CoV-2 S protein structure (left) highlighting the RBD (dark grey), S2 (blue), and NTD (light blue) Ab binding regions. V_HV_L domains of Ab binding to an NTD (S2L28, PDB: 7LXX) epitope is shown as a cartoon representation. The circle (right) shows an enlarged view of the RBD surface with V_HV_L domains for RBD-binding Abs shown as cartoons: Class 1 (light orange, C102, PDB: 7K8M), Class 2 (mauve, C002, PDB: 7K8S), Class 3 (pale purple, C135, PDB: 7K8Z), and Class 4 (pale cyan, C022, PDB: 7RKU). The ACE2 binding site is highlighted on the RBD in white.

Notably, some Ab epitopes characterized by crystallography are not accessible on the known cryo-EM structures of mature ZIKV [43,54,56,126] (**Figure 3C)**. While cryo-EM structures show a static envelope, evidence suggests the E proteins are dynamic and sample different conformations. The phenomenon of flavivirus "breathing" may result from conformational changes of the E protein during the viral life cycle, such as during fusion. The flavivirus DENV serotype 2 (DENV2) structure showed E protein rearrangements when heated to 37°C, providing further evidence for flavivirus breathing [47,138] (**Figure 3C)**. However, ZIKV maintains a smooth structure at 40°C and its breathing conformation has not yet been determined [42].

Somatic Hypermutation of Neutralizing Abs

Abs evolve to neutralize antigen targets through the process of affinity maturation. This process begins when germline-encoded B cell receptors interact with an antigen and receive signals from T cells. This activation stimulates iterative rounds of somatic hypermutation (SHM), whereby a cellular mechanism orchestrates single base pair mutations, insertions, and deletions (indels) primarily in the CDRs of Abs [139]. These mutations are random, although favorable mutations that enhance recognition of antigen are selected for in further rounds of SHM [139]. Affinity maturation can rapidly diversify the Ab repertoire, allowing for the recognition of innumerable antigens that can mutate to evade Ab recognition [140].

This arms race between distinct Abs and antigens has been monitored through structural biology, which can illuminate how SHM impacts the antigen:Ab interface. For different viral antigens, SHM plays different roles in overcoming infection.

In HIV-1 infection, SHM plays a major role in the creation of bNAbs. Human Abs that have undergone affinity maturation on average carry 15-20 nucleotide mutations in the variable heavy (V_H) gene; however, HIV-1 bNAbs include 40-100 V_H gene mutations [141]. High levels of bNAb SHM are necessary to combat a rapidly evolving antigen target in which Env mutations are selected to evade bNAb recognition. In fact, these mutations have been deemed critical for recognition and neutralization of native viral envelopes, as unmutated germline precursors of bNAbs do not usually interact with viral Envs [142]. X-ray crystallography and cryo-EM have allowed for the characterization of bNAb SHM to understand how mutated residues interact with HIV-1 Env and confer broadly neutralizing activity and potency [7,143,144]. Structures of Env:bNAb complexes have identified individual SHMs that are critical for neutralization activity at different epitopes and have set forth criteria for predicting the capability of newly isolated bNAbs.

Furthermore, structural biology has given context to unusual bNAb characteristics brought on by SHM; namely, framework region (FWR) mutations and indels. The FWRs of an Ab variable domain are the relatively constant sequences that provide a scaffold for the more diverse CDR loops. SHMs in FWRs are often poorly tolerated as they impair the structural integrity of the Ab [145–147]. However, HIV-1 bNAbs FWR SHM has been found to be critical for breadth and potency [145]. Analysis of crystal structures of bNAbs bound to gp120s revealed that regions of FWR SHM can directly interact with the antigen to increase the binding affinity or contribute to the structural rigidity and flexibility of a Fab for optimal binding [99,145]. HIV-1 bNAbs also contain unusually high levels of SHM indels [76, 73]. Prior studies reporting sequences of Ab genes from memory B cells found between 1-3% of Ab genes contained indels [148]. For HIV-1 bNAbs, approximately 40% of bNAbs include indel mutations that range from 3-33 nucleotides in length [76, 73]. Analysis of crystal structures of bNAb:gp120 complexes found that these indels are preferentially found within

10Å of the Ab:antigen interface [149]. Indels are therefore important to optimize interactions with Env, specifically to penetrate the dense glycan shield. Thus, structural biology has aided in elucidating how unusual SHM features in HIV-1 bNAbs contribute to breadth and potency.

Unlike HIV-1 bNAbs, Abs against SARS-CoV-2 S and ZIKV E protein have much lower levels of SHM and, in fact, affinity maturation via SHM is not always required to interact with their viral antigen targets [23,54,150]. Longitudinal studies tracking Ab evolution after SARS-CoV-2 infection found 1.3 months post-infection averages of 4.2 V_H and 2.8 V_L nucleotide mutations [151]. However, after 12 months past infection, SHM increased to approximately 15 V_H and 8 V_L nucleotide mutations [152]. Low levels of SHM have also been reported in longitudinal studies tracking ZIKV infection and comparisons of mature and germline versions of anti-ZIKV Abs [52,54,56,150,153,154]. Inferred germline Abs have been shown to be able to bind and even weakly neutralize ZIKV [52,54,153,155]. Structural analysis of Ab:antigen complexes for SARS-CoV-2 and ZIKV suggests most SHMs are found in CDR loops and contribute to the complex interface to create optimal contacts for antigen recognition [25,32,52,54]. For both of these viruses, the relatively low levels of SHM indicate near-germline and germline Abs are readily capable of recognizing viral antigens and maturing into potently neutralizing Abs.

Structure-guided design of vaccines, small molecules inhibitors, and Ab therapeutics

Structural biology has played a pivotal role in characterizing the optimal human Ab response which vaccines and therapeutics can be designed to mimic (**Figure 1**). For many viruses, the ability to produce a cross reactive response either to many strains of the same virus or to different viruses in the same group is necessary for complete protection from disease, presenting a challenge for vaccine design [156].Therefore, the structure-guided development of small molecules, peptides, and protein decoys as therapeutics is a complementary strategy for treating viral infection [157].

Structural biology has allowed for the advancement of structure-based vaccine design, which is considered to be one of the current avenues most likely to eventually lead to an HIV-1 vaccine after the failure of subunit vaccines [158]. bNAbs are only elicited by a small subset of the population infected with HIV-1; even so these 'elite controllers' still never clear the virus [159]. In fact, arguably the biggest hurdle in creating an HIV-1 vaccine is eliciting an immune response that is far better than what is observed in infected people. The vast number of HIV-1 strains means a vaccine must protect against initial infection of countless distinct viral species rather than a single, or only a few, strains. Due to the inherent difficulty of eliciting bNAbs against HIV-1, some current structure-based efforts for HIV-1 vaccine design rely on structurally characterizing bNAbs in an effort to reverse engineer an immunogen that can elicit them, rather than the commonly-observed strain-specific, autologous neutralizing responses [158]. Structures of antigen:Ab complexes have allowed for the classification of Abs by their epitopes, which is necessary for the design of effective therapeutic monoclonal Ab cocktails [7]. In many cases, the dosing of single monoclonals is often suboptimal due to the ability of viruses to rapidly mutate. For example, in the case of HIV-1, the viral swarm inside a patient can evolve resistance mutations that make a therapy either less or not effective within days to weeks [160]. Therapeutics have also been designed to mimic an existing interaction by binding directly, such as CD4 mimetic drugs that bind into the CD4 pocket on gp120 [161,162]. As an alternative therapeutic approach, binding targets separate from canonical interaction sites can be used to inhibit function by preventing conformational changes, such as inhibitors directed at the HIV-1 Env fusion peptide [163].

In the case of SARS-CoV-2, which mutates at a lower frequency than HIV-1 but whose variants of concern are posing current problems, future efforts will need to focus on producing vaccines that are effective in the face of new variants [164,165]. Key regions of the S protein are highly conserved across the subgenus of sarbecovirus coronaviruses, of which at least three others can infect human cells: SARS-CoV, SHC014, and RaTG13 [166]. Neutralizing Abs that target the S of SARS-CoV-2 and also bind and neutralize other sarbecoviruses including SARS-CoV-2 variants of concern have been identified by several groups and have been structurally characterized [24,112–116,167,168], suggesting that an

immunogen could be designed to produce a pan-sarbecovirus vaccine. Additionally, therapeutic mAb cocktails have successfully been developed for the treatment of SARS-CoV-2 [169]. Therapeutics have also been designed to mimic an existing interaction by binding directly, such as ACE2-S small protein decoys [170].

For ZIKV, design of a safe vaccine is complicated due to the similarities in structures between ZIKV and other flaviviruses. Since the structure of ZIKV is similar to that of DENV, WENV and YFV [38–41], there is concern that Abs elicited during infection with one flavivirus may cross-react with, but not neutralize, other flaviviruses during a later infection. This cross-reactive Ab recognition may worsen symptoms due to a phenomenon termed Ab-dependent enhancement (ADE), by which Ab-bound viruses can infect cells through interactions of the Fc regions of the bound Abs with the host Fcγ receptor, resulting in infection of cells after endocytosis of the Ab-virus complex [38,130,154,171–178]. This is of particular concern for the mosquito-borne virus DENV, since it has been shown that prior DENV or ZIKV infection that results in low or intermediate Ab titers increases the risk of worsened disease severity from a subsequent DENV infection with a different serotype [38,179–187]. However, potent neutralizing Abs against ZIKV EDIII have been identified that appear to be more specific for ZIKV than other flaviviruses, suggesting ZIKV EDIII is a potential candidate for the design of a safe vaccine [51–56,61,72,124,125,131–136]. No vaccine is yet universally available for ZIKV, although both the full E protein and individual EDIII have been investigated as potential immunogens [78,135,188–194].

Conclusions

Structural biology has allowed for a deeper understanding of the immune responses to many viruses, including HIV-1, SARS-CoV-2, and ZIKV discussed here. Mutations have been engineered that stabilize surface proteins in their pre-fusion conformations for use as starting immunogens for structure-based vaccine design and as laboratory reagents that can be used to study other aspects of the elicited humoral immune response. Structures of Abs bound to these stabilized proteins have allowed for the elucidation of neutralizing epitopes on the viral

surface proteins. Additionally, such structures have increased our understanding of the role of features that Abs develop in response to antigens, such as somatic hypermutation, insertions, and deletions. For targets where whole inactivated or subunit vaccines have failed, structures of viral antigens bound to elicited Abs have facilitated alternative routes for structure-based design of vaccines, small molecules therapeutics, and Ab cocktails. It is through structural biology, inspired by advancements by Rosalind Franklin, that we are able to make progress toward vaccines and Ab treatments for the viruses we study, including HIV-1, SARS-CoV-2, and ZIKV.

Methods

Biorender.com was used to produce portions of Figure 1 and Figure 2. All structure renderings were made using PyMOL ver. 2.5.0. or 1.7.6.4.

Figure 4 was produced in PyMOL by aligning the HIV-1 Env or SARS-CoV-2 S proteins of each Fab-bound structure with the structure of the viral protein depicted in the figure (Env PDB: 5T3Z, S PDB: 7K8V). Only V_HV_L domains are shown for each Ab.

Acknowledgements

Structural biology studies in our laboratory were supported by the National Institute of Allergy and Infectious Diseases (NIAID) Grant HIVRAD P01 AI100148, the Bill and Melinda Gates Foundation Collaboration for AIDS Vaccine Discovery (CAVD) grant INV-002143, a George Mason University Fast Grant GMU.SARSCOV2, an NSF GRFP (to M.E.A.), a NIH National Research Service Award Fellowship F30AI147579 (S.R.E.), NIH National Institute of General Medical Sciences Training Grant T32-GM008042 (to S.R.E.) through the University of California, Los Angeles–California Institute of Technology Medical Scientist Training Program, and the National Institutes of Health (NIH) Grant AI138938. We would also like to thank members of the Bjorkman laboratory for helpful discussions, the Caltech Merkin Institute for Translational Research for resources that enable our work, the Caltech Beckman Institute Resource Center for Transmission Electron Microscopy for support in cryo-EM projects, the Gordon and Betty Moore and Beckman

Foundations for gifts to support the Molecular Observatory at Caltech that provides aid for protein crystallization, and the Stanford Synchrotron Radiation Lightsource (SSRL) that provides data collection capabilities for X-ray crystallography.

Finally, we are grateful for Rosalind Franklin's contributions to structural biology and for her brazen career as a female scientist that continues to embolden researchers, especially women.

Author Contributions

M.E.A., K.A.D., S.R.E., and C.A.J. wrote and edited this review article with critical reading and editing by P.J.B.

Conflicts of Interest

The authors declare no conflict of interest for this work.

References

1. Creager, A.N.H.; Morgan, G.J. After the Double Helix: Rosalind Franklin's Research on Tobacco Mosaic Virus. *Isis* **2008**, *99*, 239–272, doi:https://doi.org/10.1086/588626.
2. Franklin, R.E.; Klug, A. The Nature of the Helical Groove on the Tobacco Mosaic Virus Particle X-Ray Diffraction Studies. *Biochim. Biophys. Acta* **1956**, *19*, 403–416, doi:https://doi.org/10.1016/0006-3002(56)90463-2.
3. Franklin, R.E.; Holmes, K.C. The Helical Arrangement of the Protein Sub-Units in Tobacco Mosaic Virus. *Biochim. Biophys. Acta* **1956**, *21*, 405–406, doi:https://doi.org/10.1016/0006-3002(56)90043-9.
4. Franklin, R.E. X-Ray Diffraction Studies of Cucumber Virus 4 and Three Strains of Tobacco Mosaic Virus. *Biochim. Biophys. Acta* **1956**, *19*, 203–211, doi:10.1016/0006-3002(56)90421-8.
5. FRANKLIN, R.E. Structure of Tobacco Mosaic Virus: Location of the Ribonucleic Acid in the Tobacco Mosaic Virus Particle. *Nature* **1956**, *177*, 928–930, doi:10.1038/177928b0.
6. *Global HIV & AIDS Statistics Available Online: Https://Www.Unaids.Org/En/Resources/Fact-Sheet (Accessed on 13 September 2021).*;
7. West Jr, A.P.; Scharf, L.; Scheid, J.F.; Klein, F.; Bjorkman, P.J.; Nussenzweig, M.C. Structural Insights on the Role of Antibodies in HIV-1 Vaccine and Therapy. *Cell* **2014**, *156*, 633–648, doi:10.1016/j.cell.2014.01.052.
8. Gray, E.S.; Madiga, M.C.; Hermanus, T.; Moore, P.L.; Wibmer, C.K.; Tumba, N.L.;

Werner, L.; Mlisana, K.; Sibeko, S.; Williamson, C.; et al. The Neutralization Breadth of HIV-1 Develops Incrementally over Four Years and Is Associated with CD4+ T Cell Decline and High Viral Load during Acute Infection. *J. Virol.* **2011**, *85*, 4828–4840, doi:10.1128/JVI.00198-11.

9. Sather, D.N.; Armann, J.; Ching, L.K.; Mavrantoni, A.; Sellhorn, G.; Caldwell, Z.; Yu, X.; Wood, B.; Self, S.; Kalams, S.; et al. Factors Associated with the Development of Cross-Reactive Neutralizing Antibodies during Human Immunodeficiency Virus Type 1 Infection. *J. Virol.* **2009**, *83*, 757–769, doi:10.1128/JVI.02036-08.
10. Doria-Rose, N.A.; Klein, R.M.; Manion, M.M.; O'Dell, S.; Phogat, A.; Chakrabarti, B.; Hallahan, C.W.; Migueles, S.A.; Wrammert, J.; Ahmed, R.; et al. Frequency and Phenotype of Human Immunodeficiency Virus Envelope-Specific B Cells from Patients with Broadly Cross-Neutralizing Antibodies. *J. Virol.* **2009**, *83*, 188–199, doi:10.1128/JVI.01583-08.
11. COVID-19 Map Available online: https://coronavirus.jhu.edu/map.html (13 September 2021).
12. Hoffmann, M.; Kleine-Weber, H.; Schroeder, S.; Krüger, N.; Herrler, T.; Erichsen, S.; Schiergens, T.S.; Herrler, G.; Wu, N.-H.; Nitsche, A.; et al. SARS-CoV-2 Cell Entry Depends on ACE2 and TMPRSS2 and Is Blocked by a Clinically Proven Protease Inhibitor. *Cell* **2020**, *181*, 271-280.e8, doi:10.1016/j.cell.2020.02.052.
13. Lan, J.; Ge, J.; Yu, J.; Shan, S.; Zhou, H.; Fan, S.; Zhang, Q.; Shi, X.; Wang, Q.; Zhang, L.; et al. Structure of the SARS-CoV-2 Spike Receptor-Binding Domain Bound to the ACE2 Receptor. *Nature* **2020**, *581*, 215–220, doi:10.1038/s41586-020-2180-5.
14. Wrapp, D.; Wang, N.; Corbett, K.S.; Goldsmith, J.A.; Hsieh, C.-L.; Abiona, O.; Graham, B.S.; McLellan, J.S. Cryo-EM Structure of the 2019-NCoV Spike in the Prefusion Conformation. *Science* **2020**, *367*, 1260–1263, doi:10.1126/science.abb2507.
15. Walls, A.C.; Park, Y.-J.; Tortorici, M.A.; Wall, A.; McGuire, A.T.; Veesler, D. Structure, Function, and Antigenicity of the SARS-CoV-2 Spike Glycoprotein. *Cell* **2020**, *181*, 281-292.e6, doi:10.1016/j.cell.2020.02.058.
16. Kirchdoerfer, R.N.; Cottrell, C.A.; Wang, N.; Pallesen, J.; Yassine, H.M.; Turner, H.L.; Corbett, K.S.; Graham, B.S.; McLellan, J.S.; Ward, A.B. Pre-Fusion Structure of a Human Coronavirus Spike Protein. *Nature* **2016**, *531*, 118–121, doi:10.1038/nature17200.
17. Yuan, Y.; Cao, D.; Zhang, Y.; Ma, J.; Qi, J.; Wang, Q.; Lu, G.; Wu, Y.; Yan, J.; Shi, Y.; et al. Cryo-EM Structures of MERS-CoV and SARS-CoV Spike Glycoproteins Reveal the Dynamic Receptor Binding Domains. *Nat. Commun.* **2017**, *8*, 15092, doi:10.1038/ncomms15092.
18. Li, Z.; Tomlinson, A.C.; Wong, A.H.; Zhou, D.; Desforges, M.; Talbot, P.J.; Benlekbir, S.; Rubinstein, J.L.; Rini, J.M. The Human Coronavirus HCoV-229E S-Protein Structure and Receptor Binding. *eLife* **2019**, *8*, e51230, doi:10.7554/eLife.51230.
19. Walls, A.C.; Tortorici, M.A.; Bosch, B.-J.; Frenz, B.; Rottier, P.J.M.; DiMaio, F.; Rey, F.A.; Veesler, D. Cryo-Electron Microscopy Structure of a Coronavirus Spike Glycoprotein Trimer. *Nature* **2016**, *531*, 114–117, doi:10.1038/nature16988.
20. Roy, S.; Jaiswar, A.; Sarkar, R. Dynamic Asymmetry Exposes 2019-NCoV Prefusion Spike. *J. Phys. Chem. Lett.* **2020**, *11*, 7021–7027, doi:10.1021/acs.jpclett.0c01431.
21. Brouwer, P.J.M.; Caniels, T.G.; Straten, K. van der; Snitselaar, J.L.; Aldon, Y.; Bangaru,

S.; Torres, J.L.; Okba, N.M.A.; Claireaux, M.; Kerster, G.; et al. Potent Neutralizing Antibodies from COVID-19 Patients Define Multiple Targets of Vulnerability. *Science* **2020**, *369*, 643–650, doi:10.1126/science.abc5902.

22. Cao, Y.; Su, B.; Guo, X.; Sun, W.; Deng, Y.; Bao, L.; Zhu, Q.; Zhang, X.; Zheng, Y.; Geng, C.; et al. Potent Neutralizing Antibodies against SARS-CoV-2 Identified by High-Throughput Single-Cell Sequencing of Convalescent Patients' B Cells. *Cell* **2020**, *182*, 73-84.e16, doi:10.1016/j.cell.2020.05.025.
23. Kreer, C.; Zehner, M.; Weber, T.; Ercanoglu, M.S.; Gieselmann, L.; Rohde, C.; Halwe, S.; Korenkov, M.; Schommers, P.; Vanshylla, K.; et al. Longitudinal Isolation of Potent Near-Germline SARS-CoV-2-Neutralizing Antibodies from COVID-19 Patients. *Cell* **2020**, *182*, 843-854.e12, doi:10.1016/j.cell.2020.06.044.
24. Liu, H.; Wu, N.C.; Yuan, M.; Bangaru, S.; Torres, J.L.; Caniels, T.G.; van Schooten, J.; Zhu, X.; Lee, C.-C.D.; Brouwer, P.J.M.; et al. Cross-Neutralization of a SARS-CoV-2 Antibody to a Functionally Conserved Site Is Mediated by Avidity. *Immunity* **2020**, *53*, 1272-1280.e5, doi:10.1016/j.immuni.2020.10.023.
25. Robbiani, D.F.; Gaebler, C.; Muecksch, F.; Lorenzi, J.C.C.; Wang, Z.; Cho, A.; Agudelo, M.; Barnes, C.O.; Gazumyan, A.; Finkin, S.; et al. Convergent Antibody Responses to SARS-CoV-2 in Convalescent Individuals. *Nature* **2020**, *584*, 437–442, doi:10.1038/s41586-020-2456-9.
26. Rogers, T.F.; Zhao, F.; Huang, D.; Beutler, N.; Burns, A.; He, W.; Limbo, O.; Smith, C.; Song, G.; Woehl, J.; et al. Isolation of Potent SARS-CoV-2 Neutralizing Antibodies and Protection from Disease in a Small Animal Model. *Science* **2020**, *369*, 956–963, doi:10.1126/science.abc7520.
27. Seydoux, E.; Homad, L.J.; MacCamy, A.J.; Parks, K.R.; Hurlburt, N.K.; Jennewein, M.F.; Akins, N.R.; Stuart, A.B.; Wan, Y.-H.; Feng, J.; et al. Analysis of a SARS-CoV-2-Infected Individual Reveals Development of Potent Neutralizing Antibodies with Limited Somatic Mutation. *Immunity* **2020**, *53*, 98-105.e5, doi:10.1016/j.immuni.2020.06.001.
28. Shi, R.; Shan, C.; Duan, X.; Chen, Z.; Liu, P.; Song, J.; Song, T.; Bi, X.; Han, C.; Wu, L.; et al. A Human Neutralizing Antibody Targets the Receptor-Binding Site of SARS-CoV-2. *Nature* **2020**, *584*, 120–124, doi:10.1038/s41586-020-2381-y.
29. Zost, S.J.; Gilchuk, P.; Case, J.B.; Binshtein, E.; Chen, R.E.; Nkolola, J.P.; Schäfer, A.; Reidy, J.X.; Trivette, A.; Nargi, R.S.; et al. Potently Neutralizing and Protective Human Antibodies against SARS-CoV-2. *Nature* **2020**, *584*, 443–449, doi:10.1038/s41586-020-2548-6.
30. Zost, S.J.; Gilchuk, P.; Chen, R.E.; Case, J.B.; Reidy, J.X.; Trivette, A.; Nargi, R.S.; Sutton, R.E.; Suryadevara, N.; Chen, E.C.; et al. Rapid Isolation and Profiling of a Diverse Panel of Human Monoclonal Antibodies Targeting the SARS-CoV-2 Spike Protein. *Nat. Med.* **2020**, *26*, 1422–1427, doi:10.1038/s41591-020-0998-x.
31. Pinto, D.; Park, Y.-J.; Beltramello, M.; Walls, A.C.; Tortorici, M.A.; Bianchi, S.; Jaconi, S.; Culap, K.; Zatta, F.; De Marco, A.; et al. Cross-Neutralization of SARS-CoV-2 by a Human Monoclonal SARS-CoV Antibody. *Nature* **2020**, *583*, 290–295, doi:10.1038/s41586-020-2349-y.
32. Barnes, C.O.; Jette, C.A.; Abernathy, M.E.; Dam, K.-M.A.; Esswein, S.R.; Gristick, H.B.; Malyutin, A.G.; Sharaf, N.G.; Huey-Tubman, K.E.; Lee, Y.E.; et al. SARS-CoV-

2 Neutralizing Antibody Structures Inform Therapeutic Strategies. *Nature* **2020**, *588*, 682–687, doi:10.1038/s41586-020-2852-1.

33. Barnes, C.O.; West, A.P.; Huey-Tubman, K.E.; Hoffmann, M.A.G.; Sharaf, N.G.; Hoffman, P.R.; Koranda, N.; Gristick, H.B.; Gaebler, C.; Muecksch, F.; et al. Structures of Human Antibodies Bound to SARS-CoV-2 Spike Reveal Common Epitopes and Recurrent Features of Antibodies. *Cell* **2020**, *182*, 828-842.e16, doi:10.1016/j.cell.2020.06.025.
34. Suy, A.; Sulleiro, E.; Rodo, C.; Vazquez, E.; Bocanegra, C.; Molina, I.; Esperalba, J.; Sanchez-Seco, M.P.; Boix, H.; Pumarola, T.; et al. Prolonged Zika Virus Viremia during Pregnancy. *N Engl J Med* **2016**, *375*, 2611–2613, doi:10.1056/NEJMc1607580.
35. Brasil, P.; Pereira, J.P.; Moreira, M.E.; Ribeiro Nogueira, R.M.; Damasceno, L.; Wakimoto, M.; Rabello, R.S.; Valderramos, S.G.; Halai, U.A.; Salles, T.S.; et al. Zika Virus Infection in Pregnant Women in Rio de Janeiro. *N Engl J Med* **2016**, *375*, 2321–2334, doi:10.1056/NEJMoa1602412.
36. Coyne, C.B.; Lazear, H.M. Zika Virus - Reigniting the TORCH. *Nat Rev Microbiol* **2016**, *14*, 707–715, doi:10.1038/nrmicro.2016.125.
37. Mlakar, J.; Korva, M.; Tul, N.; Popović, M.; Poljšak-Prijatelj, M.; Mraz, J.; Kolenc, M.; Resman Rus, K.; Vesnaver Vipotnik, T.; Fabjan Vodušek, V.; et al. Zika Virus Associated with Microcephaly Available online: https://www.nejm.org/doi/10.1056/NEJMoa1600651 (accessed on 18 June 2021).
38. Heinz, F.X.; Stiasny, K. The Antigenic Structure of Zika Virus and Its Relation to Other Flaviviruses: Implications for Infection and Immunoprophylaxis. *Microbiol Mol Biol Rev* **2017**, *81*, doi:10.1128/MMBR.00055-16.
39. Chang, H.-H.; Huber, R.G.; Bond, P.J.; Grad, Y.H.; Camerini, D.; Maurer-Stroh, S.; Lipsitch, M. Systematic Analysis of Protein Identity between Zika Virus and Other Arthropod-Borne Viruses. *Bull. World Health Organ.* **2017**, *95*, 517-525I, doi:10.2471/BLT.16.182105.
40. da Fonseca, N.J.; Lima Afonso, M.Q.; Pedersolli, N.G.; de Oliveira, L.C.; Andrade, D.S.; Bleicher, L. Sequence, Structure and Function Relationships in Flaviviruses as Assessed by Evolutive Aspects of Its Conserved Non-Structural Protein Domains. *Biochem. Biophys. Res. Commun.* **2017**, *492*, 565–571, doi:10.1016/j.bbrc.2017.01.041.
41. Ye, Q.; Liu, Z.-Y.; Han, J.-F.; Jiang, T.; Li, X.-F.; Qin, C.-F. Genomic Characterization and Phylogenetic Analysis of Zika Virus Circulating in the Americas. *Infect. Genet. Evol.* **2016**, *43*, 43–49, doi:10.1016/j.meegid.2016.05.004.
42. Kostyuchenko, V.A.; Lim, E.X.; Zhang, S.; Fibriansah, G.; Ng, T.S.; Ooi, J.S.; Shi, J.; Lok, S.M. Structure of the Thermally Stable Zika Virus. *Nature* **2016**, *533*, 425–8, doi:10.1038/nature17994.
43. Sirohi, D.; Chen, Z.; Sun, L.; Klose, T.; Pierson, T.C.; Rossmann, M.G.; Kuhn, R.J. The 3.8 A Resolution Cryo-EM Structure of Zika Virus. *Science* **2016**, *352*, 467–70, doi:10.1126/science.aaf5316.
44. Pierson, T.C.; Diamond, M.S. The Emergence of Zika Virus and Its New Clinical Syndromes. *Nature* **2018**, *560*, 573–581, doi:10.1038/s41586-018-0446-y.
45. Kuhn, R.J.; Dowd, K.A.; Beth Post, C.; Pierson, T.C. Shake, Rattle, and Roll: Impact of the Dynamics of Flavivirus Particles on Their Interactions with the Host. *Virology* **2015**, *479–480*, 508–17, doi:10.1016/j.virol.2015.03.025.

46. Dowd, K.A.; DeMaso, C.R.; Pierson, T.C. Genotypic Differences in Dengue Virus Neutralization Are Explained by a Single Amino Acid Mutation That Modulates Virus Breathing. *MBio* **2015**, *6*, e01559-15, doi:10.1128/mBio.01559-15.
47. Fibriansah, G.; Ng, T.-S.; Kostyuchenko, V.A.; Lee, J.; Lee, S.; Wang, J.; Lok, S.-M. Structural Changes in Dengue Virus When Exposed to a Temperature of 37°C. *J. Virol.* **2013**, *87*, 7585–7592, doi:10.1128/JVI.00757-13.
48. Mukhopadhyay, S.; Kuhn, R.J.; Rossmann, M.G. A Structural Perspective of the Flavivirus Life Cycle. *Nat. Rev. Microbiol.* **2005**, *3*, 13–22, doi:10.1038/nrmicro1067.
49. Yu, I.M.; Zhang, W.; Holdaway, H.A.; Li, L.; Kostyuchenko, V.A.; Chipman, P.R.; Kuhn, R.J.; Rossmann, M.G.; Chen, J. Structure of the Immature Dengue Virus at Low PH Primes Proteolytic Maturation. *Science* **2008**, *319*, 1834–7, doi:10.1126/science.1153264.
50. Kuhn, R.J.; Zhang, W.; Rossmann, M.G.; Pletnev, S.V.; Corver, J.; Lenches, E.; Jones, C.T.; Mukhopadhyay, S.; Chipman, P.R.; Strauss, E.G.; et al. Structure of Dengue Virus: Implications for Flavivirus Organization, Maturation, and Fusion. *Cell* **2002**, *108*, 717–725, doi:10.1016/S0092-8674(02)00660-8.
51. Pierson, T.C.; Fremont, D.H.; Kuhn, R.J.; Diamond, M.S. Structural Insights into the Mechanisms of Antibody-Mediated Neutralization of Flavivirus Infection: Implications for Vaccine Development. *Cell Host Microbe* **2008**, *4*, 229–38, doi:10.1016/j.chom.2008.08.004.
52. Esswein, S.R.; Gristick, H.B.; Jurado, A.; Peace, A.; Keeffe, J.R.; Lee, Y.E.; Voll, A.V.; Saeed, M.; Nussenzweig, M.C.; Rice, C.M.; et al. Structural Basis for Zika Envelope Domain III Recognition by a Germline Version of a Recurrent Neutralizing Antibody. *Proc. Natl. Acad. Sci.* **2020**, doi:10.1073/pnas.1919269117.
53. Keeffe, J.R.; Van Rompay, K.K.A.; Olsen, P.C.; Wang, Q.; Gazumyan, A.; Azzopardi, S.A.; Schaefer-Babajew, D.; Lee, Y.E.; Stuart, J.B.; Singapuri, A.; et al. A Combination of Two Human Monoclonal Antibodies Prevents Zika Virus Escape Mutations in Non-Human Primates. *Cell Rep.* **2018**, *25*, 1385-1394.e7, doi:10.1016/j.celrep.2018.10.031.
54. Robbiani, D.F.; Bozzacco, L.; Keeffe, J.R.; Khouri, R.; Olsen, P.C.; Gazumyan, A.; Schaefer-Babajew, D.; Avila-Rios, S.; Nogueira, L.; Patel, R.; et al. Recurrent Potent Human Neutralizing Antibodies to Zika Virus in Brazil and Mexico. *Cell* **2017**, *169*, 597-609.e11, doi:10.1016/j.cell.2017.04.024.
55. Barba-Spaeth, G.; Dejnirattisai, W.; Rouvinski, A.; Vaney, M.C.; Medits, I.; Sharma, A.; Simon-Loriere, E.; Sakuntabhai, A.; Cao-Lormeau, V.M.; Haouz, A.; et al. Structural Basis of Potent Zika-Dengue Virus Antibody Cross-Neutralization. *Nature* **2016**, *536*, 48–53, doi:10.1038/nature18938.
56. Dai, L.; Song, J.; Lu, X.; Deng, Y.Q.; Musyoki, A.M.; Cheng, H.; Zhang, Y.; Yuan, Y.; Song, H.; Haywood, J.; et al. Structures of the Zika Virus Envelope Protein and Its Complex with a Flavivirus Broadly Protective Antibody. *Cell Host Microbe* **2016**, *19*, 696–704, doi:10.1016/j.chom.2016.04.013.
57. Prasad, V.M.; Miller, A.S.; Klose, T.; Sirohi, D.; Buda, G.; Jiang, W.; Kuhn, R.J.; Rossmann, M.G. Structure of the Immature Zika Virus at 9 A Resolution. *Nat Struct Mol Biol* **2017**, *24*, 184–186, doi:10.1038/nsmb.3352.
58. Sevvana, M.; Long, F.; Miller, A.S.; Klose, T.; Buda, G.; Sun, L.; Kuhn, R.J.; Rossmann, M.G. Refinement and Analysis of the Mature Zika Virus Cryo-EM Structure at 3.1 Å

Resolution. *Structure* **2018**, *26*, 1169-1177.e3, doi:10.1016/j.str.2018.05.006.
59. Morrone, S.R.; Chew, V.S.Y.; Lim, X.-N.; Ng, T.-S.; Kostyuchenko, V.A.; Zhang, S.; Wirawan, M.; Chew, P.-L.; Lee, J.; Tan, J.L.; et al. High Flavivirus Structural Plasticity Demonstrated by a Non-Spherical Morphological Variant. *Nat. Commun.* **2020**, *11*, 3112, doi:10.1038/s41467-020-16925-y.
60. Tyagi, A.; Ahmed, T.; Shi, J.; Bhushan, S. A Complex between the Zika Virion and the Fab of a Broadly Cross-Reactive Neutralizing Monoclonal Antibody Revealed by Cryo-EM and Single Particle Analysis at 4.1 Å Resolution. *J. Struct. Biol. X* **2020**, 100028, doi:10.1016/j.yjsbx.2020.100028.
61. Zhang, S.; Loy, T.; Ng, T.-S.; Lim, X.-N.; Chew, S.-Y.V.; Tan, T.Y.; Xu, M.; Kostyuchenko, V.A.; Tukijan, F.; Shi, J.; et al. A Human Antibody Neutralizes Different Flaviviruses by Using Different Mechanisms. *Cell Rep.* **2020**, *31*, 107584, doi:10.1016/j.celrep.2020.107584.
62. Long, F.; Doyle, M.; Fernandez, E.; Miller, A.S.; Klose, T.; Sevvana, M.; Bryan, A.; Davidson, E.; Doranz, B.J.; Kuhn, R.J.; et al. Structural Basis of a Potent Human Monoclonal Antibody against Zika Virus Targeting a Quaternary Epitope. *Proc. Natl. Acad. Sci.* **2019**, *116*, 1591–1596, doi:10.1073/pnas.1815432116.
63. Jiang, W.; Tang, L. Atomic Cryo-EM Structures of Viruses. *Curr. Opin. Struct. Biol.* **2017**, *46*, 122–129, doi:10.1016/j.sbi.2017.07.002.
64. Luque, D.; Castón, J.R. Cryo-Electron Microscopy for the Study of Virus Assembly. *Nat. Chem. Biol.* **2020**, *16*, 231–239, doi:10.1038/s41589-020-0477-1.
65. Grünewald, K.; Cyrklaff, M. Structure of Complex Viruses and Virus-Infected Cells by Electron Cryo Tomography. *Curr. Opin. Microbiol.* **2006**, *9*, 437–442, doi:10.1016/j.mib.2006.06.016.
66. Klasse, P.J.; Depetris, R.S.; Pejchal, R.; Julien, J.-P.; Khayat, R.; Lee, J.H.; Marozsan, A.J.; Cupo, A.; Cocco, N.; Korzun, J.; et al. Influences on Trimerization and Aggregation of Soluble, Cleaved HIV-1 SOSIP Envelope Glycoprotein. *J. Virol.* **2013**, *87*, 9873–9885, doi:10.1128/JVI.01226-13.
67. Hsieh, C.-L.; Goldsmith, J.A.; Schaub, J.M.; DiVenere, A.M.; Kuo, H.-C.; Javanmardi, K.; Le, K.C.; Wrapp, D.; Lee, A.G.; Liu, Y.; et al. Structure-Based Design of Prefusion-Stabilized SARS-CoV-2 Spikes. *Science* **2020**, *369*, 1501–1505, doi:10.1126/science.abd0826.
68. Kwong, P.D.; Wyatt, R.; Robinson, J.; Sweet, R.W.; Sodroski, J.; Hendrickson, W.A. Structure of an HIV Gp120 Envelope Glycoprotein in Complex with the CD4 Receptor and a Neutralizing Human Antibody. *Nature* **1998**, *393*, 648–659, doi:10.1038/31405.
69. Diskin, R.; Marcovecchio, P.M.; Bjorkman, P.J. Structure of a Clade C HIV-1 Gp120 Bound to CD4 and CD4-Induced Antibody Reveals Anti-CD4 Polyreactivity. *Nat. Publ. Group* **2010**, *17*, 608–613, doi:10.1038/nsmb.1796.
70. Li, F. Structure of SARS Coronavirus Spike Receptor-Binding Domain Complexed with Receptor. *Science* **2005**, *309*, 1864–1868, doi:10.1126/science.1116480.
71. Du, L.; Kou, Z.; Ma, C.; Tao, X.; Wang, L.; Zhao, G.; Chen, Y.; Yu, F.; Tseng, C.-T.K.; Zhou, Y.; et al. A Truncated Receptor-Binding Domain of MERS-CoV Spike Protein Potently Inhibits MERS-CoV Infection and Induces Strong Neutralizing Antibody Responses: Implication for Developing Therapeutics and Vaccines. *PLoS ONE* **2013**, *8*, e81587, doi:10.1371/journal.pone.0081587.

72. Zhao, H.; Fernandez, E.; Dowd, K.A.; Speer, S.D.; Platt, D.J.; Gorman, M.J.; Govero, J.; Nelson, C.A.; Pierson, T.C.; Diamond, M.S.; et al. Structural Basis of Zika Virus-Specific Antibody Protection. *Cell* **2016**, *166*, 1016–27, doi:10.1016/j.cell.2016.07.020.
73. Zhao, H.; Xu, L.; Bombardi, R.; Nargi, R.; Deng, Z.; Errico, J.M.; Nelson, C.A.; Dowd, K.A.; Pierson, T.C.; Crowe, J.E.; et al. Mechanism of Differential Zika and Dengue Virus Neutralization by a Public Antibody Lineage Targeting the DIII Lateral Ridge. *J. Exp. Med.* **2020**, *217*, doi:10.1084/jem.20191792.
74. Zhou, T.; Zhu, J.; Wu, X.; Moquin, S.; Zhang, B.; Acharya, P.; Georgiev, I.S.; Altae-Tran, H.R.; Chuang, G.-Y.; Joyce, M.G.; et al. Multidonor Analysis Reveals Structural Elements, Genetic Determinants, and Maturation Pathway for HIV-1 Neutralization by VRC01-Class Antibodies. *Immunity* **2013**, *39*, 245–258, doi:10.1016/j.immuni.2013.04.012.
75. Sanders, R.W.; Moore, J.P. Virus Vaccines: Proteins Prefer Prolines. *Cell Host Microbe* **2021**, *29*, 327–333, doi:10.1016/j.chom.2021.02.002.
76. Qiao, H.; Pelletier, S.L.; Hoffman, L.; Hacker, J.; Armstrong, R.T.; White, J.M. Specific Single or Double Proline Substitutions in the "Spring-Loaded" Coiled-Coil Region of the Influenza Hemagglutinin Impair or Abolish Membrane Fusion Activity. *J. Cell Biol.* **1998**, *141*, 1335–1347, doi:10.1083/jcb.141.6.1335.
77. Sanders, R.W.; Vesanen, M.; Schuelke, N.; Master, A.; Schiffner, L.; Kalyanaraman, R.; Paluch, M.; Berkhout, B.; Maddon, P.J.; Olson, W.C.; et al. Stabilization of the Soluble, Cleaved, Trimeric Form of the Envelope Glycoprotein Complex of Human Immunodeficiency Virus Type 1. *J VIROL* **2002**, *76*, 15.
78. Qu, P.; Zhang, W.; Li, D.; Zhang, C.; Liu, Q.; Zhang, X.; Wang, X.; Dai, W.; Xu, Y.; Leng, Q.; et al. Insect Cell-Produced Recombinant Protein Subunit Vaccines Protect against Zika Virus Infection. *Antiviral Res.* **2018**, *154*, 97–103, doi:10.1016/j.antiviral.2018.04.010.
79. Wang, Q.; Yang, H.; Liu, X.; Dai, L.; Ma, T.; Qi, J.; Wong, G.; Peng, R.; Liu, S.; Li, J.; et al. Molecular Determinants of Human Neutralizing Antibodies Isolated from a Patient Infected with Zika Virus. *Sci Transl Med* **2016**, *8*, 369ra179, doi:10.1126/scitranslmed.aai8336.
80. Dussupt, V.; Sankhala, R.S.; Gromowski, G.D.; Donofrio, G.; De La Barrera, R.A.; Larocca, R.A.; Zaky, W.; Mendez-Rivera, L.; Choe, M.; Davidson, E.; et al. Potent Zika and Dengue Cross-Neutralizing Antibodies Induced by Zika Vaccination in a Dengue-Experienced Donor. *Nat. Med.* **2020**, *26*, 228–235, doi:10.1038/s41591-019-0746-2.
81. Slon Campos, J.L.; Marchese, S.; Rana, J.; Mossenta, M.; Poggianella, M.; Bestagno, M.; Burrone, O.R. Temperature-Dependent Folding Allows Stable Dimerization of Secretory and Virus-Associated E Proteins of Dengue and Zika Viruses in Mammalian Cells. *Sci. Rep.* **2017**, *7*, 966, doi:10.1038/s41598-017-01097-5.
82. Harrison, S.C. Viral Membrane Fusion. *Virology* **2015**, *479–480*, 498–507, doi:10.1016/j.virol.2015.03.043.
83. Ackerman, M.E.; Mikhailova, A.; Brown, E.P.; Dowell, K.G.; Walker, B.D.; Bailey-Kellogg, C.; Suscovich, T.J.; Alter, G. Polyfunctional HIV-Specific Antibody Responses Are Associated with Spontaneous HIV Control. *PLOS Pathog.* **2016**, *12*, e1005315, doi:10.1371/journal.ppat.1005315.
84. Gunn, B.M.; Yu, W.-H.; Karim, M.M.; Brannan, J.M.; Herbert, A.S.; Wec, A.Z.;

Halfmann, P.J.; Fusco, M.L.; Schendel, S.L.; Gangavarapu, K.; et al. A Role for Fc Function in Therapeutic Monoclonal Antibody-Mediated Protection against Ebola Virus. *Cell Host Microbe* **2018**, *24*, 221-233.e5, doi:10.1016/j.chom.2018.07.009.

85. Lu, L.L.; Suscovich, T.J.; Fortune, S.M.; Alter, G. Beyond Binding: Antibody Effector Functions in Infectious Diseases. *Nat. Rev. Immunol.* **2018**, *18*, 46–61, doi:10.1038/nri.2017.106.
86. Saphire, E.O.; Schendel, S.L.; Gunn, B.M.; Milligan, J.C.; Alter, G. Antibody-Mediated Protection against Ebola Virus. *Nat. Immunol.* **2018**, *19*, 1169–1178, doi:10.1038/s41590-018-0233-9.
87. White, J.M.; Delos, S.E.; Brecher, M.; Schornberg, K. Structures and Mechanisms of Viral Membrane Fusion Proteins: Multiple Variations on a Common Theme. *Crit. Rev. Biochem. Mol. Biol.* **2008**, *43*, 189–219, doi:10.1080/10409230802058320.
88. Ward, A.B.; Wilson, I.A. The HIV-1 Envelope Glycoprotein Structure: Nailing down a Moving Target. *Immunol. Rev.* **2017**, *275*, 21–32, doi:10.1111/imr.12507.
89. Ozorowski, G.; Pallesen, J.; de Val, N.; Lyumkis, D.; Cottrell, C.A.; Torres, J.L.; Copps, J.; Stanfield, R.L.; Cupo, A.; Pugach, P.; et al. Open and Closed Structures Reveal Allostery and Pliability in the HIV-1 Envelope Spike. *Nature* **2017**, *547*, 360–363, doi:10.1038/nature23010.
90. Wang, H.; Barnes, C.O.; Yang, Z.; Nussenzweig, M.C.; Bjorkman, P.J. Partially Open HIV-1 Envelope Structures Exhibit Conformational Changes Relevant for Coreceptor Binding and Fusion. *Cell Host Microbe* **2018**, *24*, 579-592.e4, doi:10.1016/j.chom.2018.09.003.
91. Yang, Z.; Wang, H.; Liu, A.Z.; Gristick, H.B.; Bjorkman, P.J. Asymmetric Opening of HIV-1 Env Bound to CD4 and a Coreceptor-Mimicking Antibody. *Nat. Struct. Mol. Biol.* **2019**, *26*, 1167–1175, doi:10.1038/s41594-019-0344-5.
92. Wang, H.; Cohen, A.A.; Galimidi, R.P.; Gristick, H.B.; Jensen, G.J.; Bjorkman, P.J. Cryo-EM Structure of a CD4-Bound Open HIV-1 Envelope Trimer Reveals Structural Rearrangements of the Gp120 V1V2 Loop. *Proc. Natl. Acad. Sci. U. S. A.* **2016**, *113*, E7151–E7158, doi:10.1073/pnas.1615939113.
93. Alkhatib, G. The Biology of CCR5 and CXCR4: *Curr. Opin. HIV AIDS* **2009**, *4*, 96–103, doi:10.1097/COH.0b013e328324bbec.
94. Lee, J.H.; Andrabi, R.; Su, C.-Y.; Yasmeen, A.; Julien, J.-P.; Kong, L.; Wu, N.C.; McBride, R.; Sok, D.; Pauthner, M.; et al. A Broadly Neutralizing Antibody Targets the Dynamic HIV Envelope Trimer Apex via a Long, Rigidified, and Anionic β-Hairpin Structure. *Immunity* **2017**, *46*, 690–702, doi:10.1016/j.immuni.2017.03.017.
95. Gorman, J.; Soto, C.; Yang, M.M.; Davenport, T.M.; Guttman, M.; Bailer, R.T.; Chambers, M.; Chuang, G.-Y.; DeKosky, B.J.; Doria-Rose, N.A.; et al. Structures of HIV-1 Env V1V2 with Broadly Neutralizing Antibodies Reveal Commonalities That Enable Vaccine Design. *Nat. Struct. Mol. Biol.* **2016**, *23*, 81–90, doi:10.1038/nsmb.3144.
96. Walker, L.M.; Phogat, S.K.; Chan-Hui, P.-Y.; Wagner, D.; Phung, P.; Goss, J.L.; Wrin, T.; Simek, M.D.; Fling, S.; Mitcham, J.L.; et al. Broad and Potent Neutralizing Antibodies from an African Donor Reveal a New HIV-1 Vaccine Target. *Science* **2009**, *326*, 285–289, doi:10.1126/science.1178746.
97. Fera, D.; Lee, M.S.; Wiehe, K.; Meyerhoff, R.R.; Piai, A.; Bonsignori, M.; Aussedat, B.;

Walkowicz, W.E.; Ton, T.; Zhou, J.O.; et al. HIV Envelope V3 Region Mimic Embodies Key Features of a Broadly Neutralizing Antibody Lineage Epitope. *Nat. Commun.* **2018**, *9*, 1111, doi:10.1038/s41467-018-03565-6.

98. Barnes, C.O.; Gristick, H.B.; Freund, N.T.; Escolano, A.; Lyubimov, A.Y.; Hartweger, H.; West, A.P.; Cohen, A.E.; Nussenzweig, M.C.; Bjorkman, P.J. Structural Characterization of a Highly-Potent V3-Glycan Broadly Neutralizing Antibody Bound to Natively-Glycosylated HIV-1 Envelope. *Nat. Commun.* **2018**, *9*, 1251, doi:10.1038/s41467-018-03632-y.
99. Scheid, J.F.; Mouquet, H.; Ueberheide, B.; Diskin, R.; Klein, F.; Oliveira, T.Y.K.; Pietzsch, J.; Fenyo, D.; Abadir, A.; Velinzon, K.; et al. Sequence and Structural Convergence of Broad and Potent HIV Antibodies That Mimic CD4 Binding. *Science* **2011**, *333*, 1633–1637, doi:10.1126/science.1207227.
100. Schoofs, T.; Barnes, C.O.; Suh-Toma, N.; Golijanin, J.; Schommers, P.; Gruell, H.; West, A.P.; Bach, F.; Lee, Y.E.; Nogueira, L.; et al. Broad and Potent Neutralizing Antibodies Recognize the Silent Face of the HIV Envelope. *Immunity* **2019**, *50*, 1513-1529.e9, doi:10.1016/j.immuni.2019.04.014.
101. Zhou, T.; Zheng, A.; Baxa, U.; Chuang, G.-Y.; Georgiev, I.S.; Kong, R.; O'Dell, S.; Shahzad-ul-Hussan, S.; Shen, C.-H.; Tsybovsky, Y.; et al. A Neutralizing Antibody Recognizing Primarily N-Linked Glycan Targets the Silent Face of the HIV Envelope. *Immunity* **2018**, *48*, 500-513.e6, doi:10.1016/j.immuni.2018.02.013.
102. Xu, K.; Acharya, P.; Kong, R.; Cheng, C.; Chuang, G.-Y.; Liu, K.; Louder, M.K.; O'Dell, S.; Rawi, R.; Sastry, M.; et al. Epitope-Based Vaccine Design Yields Fusion Peptide-Directed Antibodies That Neutralize Diverse Strains of HIV-1. *Nat. Med.* **2018**, *24*, 857–867, doi:10.1038/s41591-018-0042-6.
103. Scharf, L.; Wang, H.; Gao, H.; Chen, S.; McDowall, A.W.; Bjorkman, P.J. Broadly Neutralizing Antibody 8ANC195 Recognizes Closed and Open States of HIV-1 Env. *Cell* **2018**, 1–13, doi:10.1016/j.cell.2015.08.035.
104. Caillat, C.; Guilligay, D.; Sulbaran, G.; Weissenhorn, W. Neutralizing Antibodies Targeting HIV-1 Gp41. *Viruses* **2020**, *12*, 1210, doi:10.3390/v12111210.
105. West Jr, A.P. Structural Basis for Germ-Line Gene Usage of a Potent Class of Antibodies Targeting the CD4-Binding Site of HIV-1 Gp120. **2012**, 1–8, doi:10.1073/pnas.1208984109/-/DCSupplemental.
106. Zhou, P.; Yang, X.-L.; Wang, X.-G.; Hu, B.; Zhang, L.; Zhang, W.; Si, H.-R.; Zhu, Y.; Li, B.; Huang, C.-L.; et al. A Pneumonia Outbreak Associated with a New Coronavirus of Probable Bat Origin. *Nature* **2020**, *579*, 270–273, doi:10.1038/s41586-020-2012-7.
107. Shiakolas, A.R.; Kramer, K.J.; Wrapp, D.; Richardson, S.I.; Schäfer, A.; Wall, S.; Wang, N.; Janowska, K.; Pilewski, K.A.; Venkat, R.; et al. Cross-Reactive Coronavirus Antibodies with Diverse Epitope Specificities and Fc Effector Functions. *Cell Rep. Med.* **2021**, *2*, 100313, doi:10.1016/j.xcrm.2021.100313.
108. Chi, X.; Yan, R.; Zhang, J.; Zhang, G.; Zhang, Y.; Hao, M.; Zhang, Z.; Fan, P.; Dong, Y.; Yang, Y.; et al. A Neutralizing Human Antibody Binds to the N-Terminal Domain of the Spike Protein of SARS-CoV-2. *Science* **2020**, *369*, 650–655, doi:10.1126/science.abc6952.
109. McCallum, M.; De Marco, A.; Lempp, F.A.; Tortorici, M.A.; Pinto, D.; Walls, A.C.; Beltramello, M.; Chen, A.; Liu, Z.; Zatta, F.; et al. N-Terminal Domain Antigenic

Mapping Reveals a Site of Vulnerability for SARS-CoV-2. *Cell* **2021**, *184*, 2332-2347.e16, doi:10.1016/j.cell.2021.03.028.

110. Song, G.; He, W.; Callaghan, S.; Anzanello, F.; Huang, D.; Ricketts, J.; Torres, J.L.; Beutler, N.; Peng, L.; Vargas, S.; et al. Cross-Reactive Serum and Memory B-Cell Responses to Spike Protein in SARS-CoV-2 and Endemic Coronavirus Infection. *Nat. Commun.* **2021**, *12*, 2938, doi:10.1038/s41467-021-23074-3.
111. Wang, C.; van Haperen, R.; Gutiérrez-Álvarez, J.; Li, W.; Okba, N.M.A.; Albulescu, I.; Widjaja, I.; van Dieren, B.; Fernandez-Delgado, R.; Sola, I.; et al. A Conserved Immunogenic and Vulnerable Site on the Coronavirus Spike Protein Delineated by Cross-Reactive Monoclonal Antibodies. *Nat. Commun.* **2021**, *12*, 1715, doi:10.1038/s41467-021-21968-w.
112. Pinto, D.; Sauer, M.M.; Czudnochowski, N.; Low, J.S.; Tortorici, M.A.; Housley, M.P.; Noack, J.; Walls, A.C.; Bowen, J.E.; Guarino, B.; et al. Broad Betacoronavirus Neutralization by a Stem Helix-Specific Human Antibody. *Science* **2021**, eabj3321, doi:10.1126/science.abj3321.
113. Sauer, M.M.; Tortorici, M.A.; Park, Y.-J.; Walls, A.C.; Homad, L.; Acton, O.J.; Bowen, J.E.; Wang, C.; Xiong, X.; de van der Schueren, W.; et al. Structural Basis for Broad Coronavirus Neutralization. *Nat. Struct. Mol. Biol.* **2021**, *28*, 478–486, doi:10.1038/s41594-021-00596-4.
114. Lv, Z.; Deng, Y.-Q.; Ye, Q.; Cao, L.; Sun, C.-Y.; Fan, C.; Huang, W.; Sun, S.; Sun, Y.; Zhu, L.; et al. Structural Basis for Neutralization of SARS-CoV-2 and SARS-CoV by a Potent Therapeutic Antibody. *Science* **2020**, *369*, 1505–1509, doi:10.1126/science.abc5881.
115. Starr, T.N.; Czudnochowski, N.; Liu, Z.; Zatta, F.; Park, Y.-J.; Addetia, A.; Pinto, D.; Beltramello, M.; Hernandez, P.; Greaney, A.J.; et al. SARS-CoV-2 RBD Antibodies That Maximize Breadth and Resistance to Escape. *Nature* **2021**, *597*, 97–102, doi:10.1038/s41586-021-03807-6.
116. Tortorici, M.A.; Czudnochowski, N.; Starr, T.N.; Marzi, R.; Walls, A.C.; Zatta, F.; Bowen, J.E.; Jaconi, S.; Di Iulio, J.; Wang, Z.; et al. Broad Sarbecovirus Neutralization by a Human Monoclonal Antibody. *Nature* **2021**, *597*, 103–108, doi:10.1038/s41586-021-03817-4.
117. Lee, E.; Lobigs, M. Substitutions at the Putative Receptor-Binding Site of an Encephalitic Flavivirus Alter Virulence and Host Cell Tropism and Reveal a Role for Glycosaminoglycans in Entry. *J. Virol.* **2000**, *74*, 8867–8875, doi:10.1128/JVI.74.19.8867-8875.2000.
118. Watterson, D.; Kobe, B.; Young, P.R.Y. 2012 Residues in Domain III of the Dengue Virus Envelope Glycoprotein Involved in Cell-Surface Glycosaminoglycan Binding. *J. Gen. Virol. 93*, 72–82, doi:10.1099/vir.0.037317-0.
119. Chu, J.J.H.; Rajamanonmani, R.; Li, J.; Bhuvanakantham, R.; Lescar, J.; Ng, M.-L.Y. 2005 Inhibition of West Nile Virus Entry by Using a Recombinant Domain III from the Envelope Glycoprotein. *J. Gen. Virol. 86*, 405–412, doi:10.1099/vir.0.80411-0.
120. Bhardwaj, S.; Holbrook, M.; Shope, R.E.; Barrett, A.D.T.; Watowich, S.J. Biophysical Characterization and Vector-Specific Antagonist Activity of Domain III of the Tick-Borne Flavivirus Envelope Protein. *J. Virol.* **2001**, *75*, 4002–4007, doi:10.1128/JVI.75.8.4002-4007.2001.

121. Modis, Y.; Ogata, S.; Clements, D.; Harrison, S.C. Structure of the Dengue Virus Envelope Protein after Membrane Fusion. *Nature* **2004**, *427*, 313–9, doi:10.1038/nature02165.
122. Stiasny, K.; Allison, S.L.; Marchler-Bauer, A.; Kunz, C.; Heinz, F.X. Structural Requirements for Low-PH-Induced Rearrangements in the Envelope Glycoprotein of Tick-Borne Encephalitis Virus. *J. Virol.* **1996**, *70*, 8142–8147, doi:10.1128/JVI.70.11.8142-8147.1996.
123. Stiasny, K.; Bressanelli, S.; Lepault, J.; Rey, F.A.; Heinz, F.X. Characterization of a Membrane-Associated Trimeric Low-PH-Induced Form of the Class II Viral Fusion Protein E from Tick-Borne Encephalitis Virus and Its Crystallization. *J. Virol.* **2004**, *78*, 3178–3183, doi:10.1128/JVI.78.6.3178-3183.2004.
124. Stettler, K.; Beltramello, M.; Espinosa, D.A.; Graham, V.; Cassotta, A.; Bianchi, S.; Vanzetta, F.; Minola, A.; Jaconi, S.; Mele, F.; et al. Specificity, Cross-Reactivity, and Function of Antibodies Elicited by Zika Virus Infection. *Science* **2016**, *353*, 823–6, doi:10.1126/science.aaf8505.
125. Sapparapu, G.; Fernandez, E.; Kose, N.; Bin, C.; Fox, J.M.; Bombardi, R.G.; Zhao, H.; Nelson, C.A.; Bryan, A.L.; Barnes, T.; et al. Neutralizing Human Antibodies Prevent Zika Virus Replication and Fetal Disease in Mice. *Nature* **2016**, *540*, 443–447, doi:10.1038/nature20564.
126. Deng, Y.-Q.; Dai, J.-X.; Ji, G.-H.; Jiang, T.; Wang, H.-J.; Yang, H.; Tan, W.-L.; Liu, R.; Yu, M.; Ge, B.-X.; et al. A Broadly Flavivirus Cross-Neutralizing Monoclonal Antibody That Recognizes a Novel Epitope within the Fusion Loop of E Protein. *PLOS ONE* **2011**, *6*, e16059, doi:10.1371/journal.pone.0016059.
127. Wang, J.; Bardelli, M.; Espinosa, D.A.; Pedotti, M.; Ng, T.-S.; Bianchi, S.; Simonelli, L.; Lim, E.X.Y.; Foglierini, M.; Zatta, F.; et al. A Human Bi-Specific Antibody against Zika Virus with High Therapeutic Potential. *Cell* **2017**, *171*, 229-241.e15, doi:10.1016/j.cell.2017.09.002.
128. Rouvinski, A.; Guardado-Calvo, P.; Barba-Spaeth, G.; Duquerroy, S.; Vaney, M.-C.; Kikuti, C.M.; Navarro Sanchez, M.E.; Dejnirattisai, W.; Wongwiwat, W.; Haouz, A.; et al. Recognition Determinants of Broadly Neutralizing Human Antibodies against Dengue Viruses. *Nature* **2015**, *520*, 109–113, doi:10.1038/nature14130.
129. Zhang, S.; Kostyuchenko, V.A.; Ng, T.S.; Lim, X.N.; Ooi, J.S.; Lambert, S.; Tan, T.Y.; Widman, D.G.; Shi, J.; Baric, R.S.; et al. Neutralization Mechanism of a Highly Potent Antibody against Zika Virus. *Nat Commun* **2016**, *7*, 13679, doi:10.1038/ncomms13679.
130. Dejnirattisai, W.; Jumnainsong, A.; Onsirisakul, N.; Fitton, P.; Vasanawathana, S.; Limpitikul, W.; Puttikhunt, C.; Edwards, C.; Duangchinda, T.; Supasa, S.; et al. Cross-Reacting Antibodies Enhance Dengue Virus Infection in Humans. *Science* **2010**, *328*, 745–748, doi:10.1126/science.1185181.
131. Oliphant, T.; Engle, M.; Nybakken, G.E.; Doane, C.; Johnson, S.; Huang, L.; Gorlatov, S.; Mehlhop, E.; Marri, A.; Chung, K.M.; et al. Development of a Humanized Monoclonal Antibody with Therapeutic Potential against West Nile Virus. *Nat. Med.* **2005**, *11*, 522–530, doi:10.1038/nm1240.
132. Wang, L.; Wang, R.; Wang, L.; Ben, H.; Yu, L.; Gao, F.; Shi, X.; Yin, C.; Zhang, F.; Xiang, Y.; et al. Structural Basis for Neutralization and Protection by a Zika Virus-Specific Human Antibody. *Cell Rep.* **2019**, *26*, 3360-3368.e5,

doi:10.1016/j.celrep.2019.02.062.
133. Yu, L.; Wang, R.; Gao, F.; Li, M.; Liu, J.; Wang, J.; Hong, W.; Zhao, L.; Wen, Y.; Yin, C.; et al. Delineating Antibody Recognition against Zika Virus during Natural Infection. *JCI Insight* **2017**, *2*, doi:10.1172/jci.insight.93042.
134. Wahala, W.M.P.B.; Kraus, A.A.; Haymore, L.B.; Accavitti-Loper, M.A.; de Silva, A.M. Dengue Virus Neutralization by Human Immune Sera: Role of Envelope Protein Domain III-Reactive Antibody. *Virology* **2009**, *392*, 103–113, doi:10.1016/j.virol.2009.06.037.
135. Slon-Campos, J.L.; Dejnirattisai, W.; Jagger, B.W.; López-Camacho, C.; Wongwiwat, W.; Durnell, L.A.; Winkler, E.S.; Chen, R.E.; Reyes-Sandoval, A.; Rey, F.A.; et al. A Protective Zika Virus E-Dimer-Based Subunit Vaccine Engineered to Abrogate Antibody-Dependent Enhancement of Dengue Infection. *Nat. Immunol.* **2019**, *20*, 1291–1298, doi:10.1038/s41590-019-0477-z.
136. Watanabe, S.; Chan, K.W.K.; Wang, J.; Rivino, L.; Lok, S.-M.; Vasudevan, S.G. Dengue Virus Infection with Highly Neutralizing Levels of Cross-Reactive Antibodies Causes Acute Lethal Small Intestinal Pathology without a High Level of Viremia in Mice. *J. Virol.* **2015**, *89*, 5847–5861, doi:10.1128/JVI.00216-15.
137. Heinz, F.X.; Stiasny, K. Flaviviruses and Flavivirus Vaccines. *Vaccine* **2012**, *30*, 4301–4306, doi:10.1016/j.vaccine.2011.09.114.
138. Zhang, X.; Sheng, J.; Plevka, P.; Kuhn, R.J.; Diamond, M.S.; Rossmann, M.G. Dengue Structure Differs at the Temperatures of Its Human and Mosquito Hosts. *Proc. Natl. Acad. Sci.* **2013**, *110*, 6795–6799, doi:10.1073/pnas.1304300110.
139. Victora, G.D.; Nussenzweig, M.C. Germinal Centers. *Annu. Rev. Immunol.* **2012**, *30*, 429–457, doi:10.1146/annurev-immunol-020711-075032.
140. Milstein, C.; Neuberger, M.S. Maturation of the Immune Response. In *Advances in Protein Chemistry*; Richards, F.M., Eisenberg, D.E., Kim, P.S., Eds.; Academic Press, 1996; Vol. 49, pp. 451–485 ISBN 0065-3233.
141. Tiller, T.; Tsuiji, M.; Yurasov, S.; Velinzon, K.; Nussenzweig, M.C.; Wardemann, H. Autoreactivity in Human IgG+ Memory B Cells. 9.
142. Davenport, T.M.; Gorman, J.; Joyce, M.G.; Zhou, T.; Soto, C.; Guttman, M.; Moquin, S.; Yang, Y.; Zhang, B.; Doria-Rose, N.A.; et al. Somatic Hypermutation-Induced Changes in the Structure and Dynamics of HIV-1 Broadly Neutralizing Antibodies. *Structure* **2016**, *24*, 1346–1357, doi:10.1016/j.str.2016.06.012.
143. Klein, F.; Mouquet, H.; Dosenovic, P.; Scheid, J.F.; Scharf, L.; Nussenzweig, M.C. Antibodies in HIV-1 Vaccine Development and Therapy. *Science* **2013**, *341*, 1199–1204, doi:10.1126/science.1241144.
144. Kwong, P.D.; Mascola, J.R. HIV-1 Vaccines Based on Antibody Identification, B Cell Ontogeny, and Epitope Structure. *Immunity* **2018**, *48*, 855–871, doi:10.1016/j.immuni.2018.04.029.
145. Klein, F.; Diskin, R.; Scheid, J.F.; Gaebler, C.; Mouquet, H.; Georgiev, I.S.; Pancera, M.; Zhou, T.; Incesu, R.-B.; Fu, B.Z.; et al. Somatic Mutations of the Immunoglobulin Framework Are Generally Required for Broad and Potent HIV-1 Neutralization. *Cell* **2013**, *153*, 126–138, doi:10.1016/j.cell.2013.03.018.
146. Wagner, S.D.; Milstein, C.; Neuberger, M.S. Codon Bias Targets Mutation. *Nature* **1995**, *376*, 732–732, doi:10.1038/376732a0.

147. Reynaud, C.-A.; Garcia, C.; Hein, W.R.; Weill, J.-C. Hypermutation Generating the Sheep Immunoglobulin Repertoire Is an Antigen-Independent Process. *Cell* **1995**, *80*, 115–125, doi:10.1016/0092-8674(95)90456-5.
148. Briney, B.S.; Willis, J.R.; Crowe, J.E. Location and Length Distribution of Somatic Hypermutation-Associated DNA Insertions and Deletions Reveals Regions of Antibody Structural Plasticity. *Genes Immun.* **2012**, *13*, 523–529, doi:10.1038/gene.2012.28.
149. Kepler, T.B.; Liao, H.-X.; Alam, S.M.; Bhaskarabhatla, R.; Zhang, R.; Yandava, C.; Stewart, S.; Anasti, K.; Kelsoe, G.; Parks, R.; et al. Immunoglobulin Gene Insertions and Deletions in the Affinity Maturation of HIV-1 Broadly Reactive Neutralizing Antibodies. *Cell Host Microbe* **2014**, *16*, 304–313, doi:10.1016/j.chom.2014.08.006.
150. Niu, X.; Yan, Q.; Yao, Z.; Zhang, F.; Qu, L.; Wang, C.; Wang, C.; Lei, H.; Chen, C.; Liang, R.; et al. Longitudinal Analysis of the Antibody Repertoire of a Zika Virus-Infected Patient Revealed Dynamic Changes in Antibody Response. *Emerg. Microbes Infect.* **2020**, *9*, 111–123, doi:10.1080/22221751.2019.1701953.
151. Gaebler, C.; Wang, Z.; Lorenzi, J.C.C.; Muecksch, F.; Finkin, S.; Tokuyama, M.; Cho, A.; Jankovic, M.; Schaefer-Babajew, D.; Oliveira, T.Y.; et al. Evolution of Antibody Immunity to SARS-CoV-2. *Nature* **2021**, *591*, 639–644, doi:10.1038/s41586-021-03207-w.
152. Wang, Z.; Muecksch, F.; Schaefer-Babajew, D.; Finkin, S.; Viant, C.; Gaebler, C.; Hoffmann, H.-H.; Barnes, C.O.; Cipolla, M.; Ramos, V.; et al. Naturally Enhanced Neutralizing Breadth against SARS-CoV-2 One Year after Infection. *Nature* **2021**, *595*, 426–431, doi:10.1038/s41586-021-03696-9.
153. Magnani, D.M.; Silveira, C.G.T.; Rosen, B.C.; Ricciardi, M.J.; Pedreno-Lopez, N.; Gutman, M.J.; Bailey, V.K.; Maxwell, H.S.; Domingues, A.; Gonzalez-Nieto, L.; et al. A Human Inferred Germline Antibody Binds to an Immunodominant Epitope and Neutralizes Zika Virus. *PLoS Negl Trop Dis* **2017**, *11*, e0005655, doi:10.1371/journal.pntd.0005655.
154. Rogers, T.F.; Goodwin, E.C.; Briney, B.; Sok, D.; Beutler, N.; Strubel, A.; Nedellec, R.; Le, K.; Brown, M.E.; Burton, D.R.; et al. Zika Virus Activates de Novo and Cross-Reactive Memory B Cell Responses in Dengue-Experienced Donors. *Sci Immunol* **2017**, *2*, doi:10.1126/sciimmunol.aan6809.
155. Gao, F.; Lin, X.; He, L.; Wang, R.; Wang, H.; Shi, X.; Zhang, F.; Yin, C.; Zhang, L.; Zhu, J.; et al. Development of a Potent and Protective Germline-like Antibody Lineage against Zika Virus in a Convalescent Human. *bioRxiv* **2019**, 661918, doi:10.1101/661918.
156. Kennedy, R.B. Current Challenges in Vaccinology. *Front. Immunol.* **2020**, *11*, 18.
157. Narkhede, Y.B.; Gonzalez, K.J.; Strauch, E.-M. Targeting Viral Surface Proteins through Structure-Based Design. *Viruses* **2021**, *13*, 1320, doi:10.3390/v13071320.
158. Burton, D.R. What Are the Most Powerful Immunogen Design Vaccine Strategies?: Reverse Vaccinology 2.0 Shows Great Promise. *Cold Spring Harb. Perspect. Biol.* **2017**, *9*, a030262, doi:10.1101/cshperspect.a030262.
159. Gebara, N.Y.; Kamari, V.E.; Rizk, N. HIV-1 Elite Controllers: An Immunovirological Review and Clinical Perspectives. 4.
160. Caskey, M.; Schoofs, T.; Gruell, H.; Settler, A.; Karagounis, T.; Kreider, E.F.; Murrell, B.; Pfeifer, N.; Nogueira, L.; Oliveira, T.Y.; et al. Antibody 10-1074 Suppresses Viremia

in HIV-1-Infected Individuals. *Nat Med* **2017**, *23*, 185–191, doi:10.1038/nm.4268.

161. Courter, J.R.; Madani, N.; Sodroski, J.; Schön, A.; Freire, E.; Kwong, P.D.; Hendrickson, W.A.; Chaiken, I.M.; LaLonde, J.M.; Smith, A.B. Structure-Based Design, Synthesis and Validation of CD4-Mimetic Small Molecule Inhibitors of HIV-1 Entry: Conversion of a Viral Entry Agonist to an Antagonist. *Acc. Chem. Res.* **2014**, *47*, 1228–1237, doi:10.1021/ar4002735.
162. Vita, C.; Drakopoulou, E.; Vizzavona, J.; Rochette, S.; Martin, L.; Ménez, A.; Roumestand, C.; Yang, Y.-S.; Ylisastigui, L.; Benjouad, A.; et al. Rational Engineering of a Miniprotein That Reproduces the Core of the CD4 Site Interacting with HIV-1 Envelope Glycoprotein. *Proc. Natl. Acad. Sci. U. S. A.* **1999**, *96*, 13091–13096.
163. Ozorowski, G.; Torres, J.L.; Santos-Martins, D.; Forli, S.; Ward, A.B. A Strain-Specific Inhibitor of Receptor-Bound HIV-1 Targets a Pocket near the Fusion Peptide. *Cell Rep.* **2020**, *33*, 108428, doi:10.1016/j.celrep.2020.108428.
164. Fischer, W.; Giorgi, E.E.; Chakraborty, S.; Nguyen, K.; Bhattacharya, T.; Theiler, J.; Goloboff, P.A.; Yoon, H.; Abfalterer, W.; Foley, B.T.; et al. HIV-1 and SARS-CoV-2: Patterns in the Evolution of Two Pandemic Pathogens. *Cell Host Microbe* **2021**, *29*, 1093–1110, doi:10.1016/j.chom.2021.05.012.
165. Hastie, K.M.; Li, H.; Bedinger, D.; Schendel, S.L.; Dennison, S.M.; Li, K.; Rayaprolu, V.; Yu, X.; Mann, C.; Zandonatti, M.; et al. Defining Variant-Resistant Epitopes Targeted by SARS-CoV-2 Antibodies: A Global Consortium Study. *Science* **2021**, doi:10.1126/science.abh2315.
166. Letko, M.; Marzi, A.; Munster, V. Functional Assessment of Cell Entry and Receptor Usage for SARS-CoV-2 and Other Lineage B Betacoronaviruses. *Nat. Microbiol.* **2020**, *5*, 562–569, doi:10.1038/s41564-020-0688-y.
167. Jette, C.A.; Cohen, A.A.; Gnanapragasam, P.N.P.; Muecksch, F.; Lee, Y.E.; Huey-Tubman, K.E.; Schmidt, F.; Hatziioannou, T.; Bieniasz, P.D.; Nussenzweig, M.C.; et al. Broad Cross-Reactivity across Sarbecoviruses Exhibited by a Subset of COVID-19 Donor-Derived Neutralizing Antibodies. *Cell Rep.* **2021**, 109760, doi:10.1016/j.celrep.2021.109760.
168. Wec, A.Z.; Wrapp, D.; Herbert, A.S.; Maurer, D.P.; Haslwanter, D.; Sakharkar, M.; Jangra, R.K.; Dieterle, M.E.; Lilov, A.; Huang, D.; et al. Broad Neutralization of SARS-Related Viruses by Human Monoclonal Antibodies. *Science* **2020**, *369*, 731–736, doi:10.1126/science.abc7424.
169. Taylor, P.C.; Adams, A.C.; Hufford, M.M.; de la Torre, I.; Winthrop, K.; Gottlieb, R.L. Neutralizing Monoclonal Antibodies for Treatment of COVID-19. *Nat. Rev. Immunol.* **2021**, *21*, 382–393, doi:10.1038/s41577-021-00542-x.
170. Linsky, T.W.; Vergara, R.; Codina, N.; Nelson, J.W.; Walker, M.J.; Su, W.; Barnes, C.O.; Hsiang, T.-Y.; Esser-Nobis, K.; Yu, K.; et al. De Novo Design of Potent and Resilient HACE2 Decoys to Neutralize SARS-CoV-2. *Science* **2020**, *370*, 1208–1214, doi:10.1126/science.abe0075.
171. Bardina, S.V.; Bunduc, P.; Tripathi, S.; Duehr, J.; Frere, J.J.; Brown, J.A.; Nachbagauer, R.; Foster, G.A.; Krysztof, D.; Tortorella, D.; et al. Enhancement of Zika Virus Pathogenesis by Preexisting Antiflavivirus Immunity. *Science* **2017**, *356*, 175–180, doi:10.1126/science.aal4365.
172. Harrison, S.C. Immunogenic Cross-Talk between Dengue and Zika Viruses. *Nat*

Immunol **2016**, *17*, 1010–2, doi:10.1038/ni.3539.
173. Priyamvada, L.; Quicke, K.M.; Hudson, W.H.; Onlamoon, N.; Sewatanon, J.; Edupuganti, S.; Pattanapanyasat, K.; Chokephaibulkit, K.; Mulligan, M.J.; Wilson, P.C.; et al. Human Antibody Responses after Dengue Virus Infection Are Highly Cross-Reactive to Zika Virus. *Proc Natl Acad Sci U A* **2016**, *113*, 7852–7, doi:10.1073/pnas.1607931113.
174. Vaughn, D.W.; Green, S.; Kalayanarooj, S.; Innis, B.L.; Nimmannitya, S.; Suntayakorn, S.; Endy, T.P.; Raengsakulrach, B.; Rothman, A.L.; Ennis, F.A.; et al. Dengue Viremia Titer, Antibody Response Pattern, and Virus Serotype Correlate with Disease Severity. *J. Infect. Dis.* **2000**, *181*, 2–9, doi:10.1086/315215.
175. Halstead, S.B. Neutralization and Antibody-Dependent Enhancement of Dengue Viruses. *Adv Virus Res* **2003**, *60*, 421–67.
176. Dejnirattisai, W.; Supasa, P.; Wongwiwat, W.; Rouvinski, A.; Barba-Spaeth, G.; Duangchinda, T.; Sakuntabhai, A.; Cao-Lormeau, V.M.; Malasit, P.; Rey, F.A.; et al. Dengue Virus Sero-Cross-Reactivity Drives Antibody-Dependent Enhancement of Infection with Zika Virus. *Nat Immunol* **2016**, *17*, 1102–8, doi:10.1038/ni.3515.
177. Wahala, W.M.; Silva, A.M. The Human Antibody Response to Dengue Virus Infection. *Viruses* **2011**, *3*, 2374–95, doi:10.3390/v3122374.
178. Alwis, R. de; Williams, K.L.; Schmid, M.A.; Lai, C.-Y.; Patel, B.; Smith, S.A.; Crowe, J.E.; Wang, W.-K.; Harris, E.; Silva, A.M. de Dengue Viruses Are Enhanced by Distinct Populations of Serotype Cross-Reactive Antibodies in Human Immune Sera. *PLOS Pathog.* **2014**, *10*, e1004386, doi:10.1371/journal.ppat.1004386.
179. Nisalak, A.; Clapham, H.E.; Kalayanarooj, S.; Klungthong, C.; Thaisomboonsuk, B.; Fernandez, S.; Reiser, J.; Srikiatkhachorn, A.; Macareo, L.R.; Lessler, J.T.; et al. Forty Years of Dengue Surveillance at a Tertiary Pediatric Hospital in Bangkok, Thailand, 1973–2012. *Am. J. Trop. Med. Hyg.* **2016**, *94*, 1342–1347, doi:10.4269/ajtmh.15-0337.
180. Sangkawibha, N.; Rojanasuphot, S.; Ahandrik, S.; Viryapongse, S.; Jaatnasen, S.; Salitul, V.; Phanthumachinda, B.; Halstead, S.B. Risk Facttors in Dengue Shock Syndrom: A Prospective Epidemiologic Study in Rayong, Thailand: I. The 1980 Outbreak. *Am. J. Epidemiol.* **1984**, *120*, 653–669, doi:10.1093/oxfordjournals.aje.a113932.
181. Katzelnick, L.C.; Narvaez, C.; Arguello, S.; Mercado, B.L.; Collado, D.; Ampie, O.; Elizondo, D.; Miranda, T.; Carillo, F.B.; Mercado, J.C.; et al. Zika Virus Infection Enhances Future Risk of Severe Dengue Disease. *Science* **2020**, *369*, 1123–1128, doi:10.1126/science.abb6143.
182. Halstead, S.B. In Vivo Enhancement of Dengue Virus Infection in Rhesus Monkeys by Passively Transferred Antibody. *J. Infect. Dis.* **1979**, *140*, 527–533, doi:10.1093/infdis/140.4.527.
183. Waggoner, J.J.; Katzelnick, L.C.; Burger-Calderon, R.; Gallini, J.; Moore, R.H.; Kuan, G.; Balmaseda, A.; Pinsky, B.A.; Harris, E. Antibody-Dependent Enhancement of Severe Disease Is Mediated by Serum Viral Load in Pediatric Dengue Virus Infections. *J. Infect. Dis.* **2020**, *221*, 1846–1854, doi:10.1093/infdis/jiz618.
184. Katzelnick, L.C.; Gresh, L.; Halloran, M.E.; Mercado, J.C.; Kuan, G.; Gordon, A.; Balmaseda, A.; Harris, E. Antibody-Dependent Enhancement of Severe Dengue Disease in Humans. *Science* **2017**, *358*, 929–932, doi:10.1126/science.aan6836.

185. Salje, H.; Cummings, D.A.T.; Rodriguez-Barraquer, I.; Katzelnick, L.C.; Lessler, J.; Klungthong, C.; Thaisomboonsuk, B.; Nisalak, A.; Weg, A.; Ellison, D.; et al. Reconstruction of Antibody Dynamics and Infection Histories to Evaluate Dengue Risk. *Nature* **2018**, *557*, 719–723, doi:10.1038/s41586-018-0157-4.
186. Cattarino, L.; Rodriguez-Barraquer, I.; Imai, N.; Cummings, D.A.T.; Ferguson, N.M. Mapping Global Variation in Dengue Transmission Intensity. *Sci. Transl. Med.* **2020**, *12*, doi:10.1126/scitranslmed.aax4144.
187. Faria, N.R.; Quick, J.; Claro, I.M.; Thézé, J.; de Jesus, J.G.; Giovanetti, M.; Kraemer, M.U.G.; Hill, S.C.; Black, A.; da Costa, A.C.; et al. Establishment and Cryptic Transmission of Zika Virus in Brazil and the Americas. *Nature* **2017**, *546*, 406–410, doi:10.1038/nature22401.
188. Yang, C.; Zeng, F.; Gao, X.; Zhao, S.; Li, X.; Liu, S.; Li, N.; Deng, C.; Zhang, B.; Gong, R. Characterization of Two Engineered Dimeric Zika Virus Envelope Proteins as Immunogens for Neutralizing Antibody Selection and Vaccine Design. *J. Biol. Chem.* **2019**, *294*, 10638–10648, doi:10.1074/jbc.RA119.007443.
189. Cimica, V.; Williams, S.; Adams-Fish, D.; McMahon, C.; Narayanan, A.; Rashid, S.; Stedman, T.T. Zika Virus-Like Particle (VLP) Vaccine Displaying Envelope (E) Protein CD Loop Antigen Elicits Protective and Specific Immune Response in a Murine Model. *Biochem. Biophys. Res. Commun.* **2020**, *529*, 805–811, doi:10.1016/j.bbrc.2020.05.161.
190. Tai, W.; Chen, J.; Zhao, G.; Geng, Q.; He, L.; Chen, Y.; Zhou, Y.; Li, F.; Du, L. Rational Design of Zika Virus Subunit Vaccine with Enhanced Efficacy. *J. Virol.* **2019**, *93*, e02187-18, doi:10.1128/JVI.02187-18.
191. Shanmugam, R.K.; Ramasamy, V.; Shukla, R.; Arora, U.; Swaminathan, S.; Khanna, N. Pichia Pastoris-Expressed Zika Virus Envelope Domain III on a Virus-like Particle Platform: Design, Production and Immunological Evaluation. *Pathog. Dis.* **2019**, *77*, doi:10.1093/femspd/ftz026.
192. Yang, M.; Lai, H.; Sun, H.; Chen, Q. Virus-like Particles That Display Zika Virus Envelope Protein Domain III Induce Potent Neutralizing Immune Responses in Mice. *Sci. Rep.* **2017**, *7*, 7679, doi:10.1038/s41598-017-08247-9.
193. Espinosa, D.; Mendy, J.; Manayani, D.; Vang, L.; Wang, C.; Richard, T.; Guenther, B.; Aruri, J.; Avanzini, J.; Garduno, F.; et al. Passive Transfer of Immune Sera Induced by a Zika Virus-Like Particle Vaccine Protects AG129 Mice Against Lethal Zika Virus Challenge. *EBioMedicine* **2018**, *27*, 61–70, doi:10.1016/j.ebiom.2017.12.010.
194. Cabral-Miranda, G.; Lim, S.M.; Mohsen, M.O.; Pobelov, I.V.; Roesti, E.S.; Heath, M.D.; Skinner, M.A.; Kramer, M.F.; Martina, B.E.E.; Bachmann, M.F. Correction: Zika Virus-Derived E-DIII Protein Displayed on Immunologically Optimized VLPs Induces Neutralizing Antibodies without Causing Enhancement of Dengue Virus Infection. Vaccines 2019, 7, 72. *Vaccines* **2020**, *8*, 94, doi:10.3390/vaccines8010094.

Chapter 3

CRYO-EM STRUCTURES OF HIV-1 TRIMER BOUND TO CD4-MIMETICS BNM-III-170 AND M48U1 ADOPT A CD4-BOUND OPEN CONFORMATION

Jette, C.A., Barnes, C.O., Kirk, S.M., Melillo, B., Smith, A.B., Bjorkman, P.J. Cryo-EM structures of HIV-1 trimer bound to CD4-mimetics BNM-III-170 and M48U1 adopt a CD4-bound open conformation. *Nat Commun* **12,** 1950 (2021).
doi: 10.1038/s41467-021-21816-x

Summary

Human Immunodeficiency Virus-1 (HIV-1), the causative agent of AIDS, impacts millions of people. Entry into target cells is mediated by the HIV-1 envelope (Env) glycoprotein interacting with host receptor CD4, which triggers conformational changes allowing binding to a coreceptor and subsequent membrane fusion. Small molecule or peptide CD4-mimetic drugs mimic CD4's Phe43 interaction with Env by inserting into the conserved Phe43 pocket on Env subunit gp120. Here, we present single-particle cryo-EM structures of CD4-mimetics BNM-III-170 and M48U1 bound to a BG505 native-like Env trimer plus the CD4-induced antibody 17b at 3.7Å and 3.9Å resolution, respectively. CD4-mimetic-bound BG505 exhibits canonical CD4-induced conformational changes including trimer opening, formation of the 4-stranded gp120 bridging sheet, displacement of the V1V2 loop, and formation of a compact and elongated gp41 HR1C helical bundle. We conclude that CD4-induced structural changes on both gp120 and gp41 Env subunits are induced by binding to the gp120 Phe43 pocket.

Introduction

Human Immunodeficiency Virus 1 (HIV-1) is the causative agent of Acquired Immunodeficiency Syndrome (AIDS) and currently infects over 37.5 million people[1]. Entry of HIV-1 into host target cells is initiated by binding of the host receptor CD4 to the only

viral protein on the surface of HIV-1, the envelope (Env) glycoprotein, a trimer of gp120-gp41 heterodimers[2]. Env binding to CD4 induces a well-characterized set of conformational changes[3-6] that expose an occluded binding site in the gp120 V3 region for a co-receptor, either CCR5 or CXCR4[7]. Upon co-receptor binding, Env undergoes further conformational changes resulting in insertion of the gp41 fusion peptide into the target cell membrane, allowing fusion of the viral and host membranes and entry of the HIV-1 genetic material into the target cell[2].

X-ray and cryo-EM structures of native-like soluble HIV-1 Env trimers (SOSIPs[8]) have defined a closed, prefusion state in which the V1V2 loops at the trimer apex shield the co-receptor binding site on the V3 region[9], and a CD4-bound open state in which the gp120 subunits rotate outwards from the trimer axis, the V1V2 loops are displaced to the sides of the trimer, and the V3 loops are exposed[3-6]. A key interaction for exposure of the co-receptor binding site upon CD4 binding is the insertion of CD4 residue $Phe43_{CD4}$ into a conserved, 150Å^2 hydrophobic cavity at the junction between the gp120 inner domain, outer domain, and bridging sheet[10]. This interaction was first observed in crystal structures of monomeric gp120 cores complexed with CD4[10], which adopt a hallmark feature of CD4-bound Env trimers in the presence or absence of CD4: a 4-stranded anti-parallel β-sheet comprising β-strands β20, β21, β2, and β3[11]. By contrast, SOSIP Env trimers in the closed, prefusion state contain a mixed parallel/anti-parallel 3-stranded β-sheet comprising strands β20, β21, and β3[12]. Upon CD4 binding to an Env trimer, the loop between strands β20 and β21 is displaced, triggering changes that are propagated through the inner domain of gp120 and resulting in trimer opening, V1V2 displacement, and 4-stranded bridging sheet formation[3-6]. Identification of the importance of the gp120 Phe43 cavity for CD4 binding led to development of cavity-interacting small molecule and peptide compounds called CD4 mimetic (CD4m) inhibitors[13-20].

Small molecule HIV-1 entry inhibitors that prevent HIV-1 trimer opening include BMS-378806 and a related family of compounds including BMS-626529, which bind orthogonally to the Phe43 opening beneath the Env β20-21 loop and extend into the base of the Phe43

cavity. Upon inhibitor binding, the Env trimer is kept closed by allosterically preventing CD4 binding by separating the bridging sheet and the inner domain of gp120[20,21].

CD4m compounds that open trimers by binding directly into the Phe43 pocket were initially identified with the discovery of NBD-556 and NBD-557, two small molecules that inhibit HIV-1 entry into cells expressing CD4 and a co-receptor, but enhance entry into cells that express a co-receptor in the absence of CD4[13]. Subsequent studies showed that premature allosteric activation of trimer opening by these small molecules could inhibit viral entry after an initial period of increased activation[22], leading to modification of these compounds and the development of CD4m small molecule inhibitors such as BNM-III-170 that bind to the Phe43 pocket but prevent infection of cells lacking CD4[13,14]. Members of this class were also shown to induce an intermediate Env conformation that can be stabilized by gp120 inner-domain-targeting Abs, permitting Antibody-Dependent Cellular Cytotoxicity[23].

Concurrent with the development of small molecule CD4m inhibitors, peptide CD4m inhibitors were developed using scorpion toxin scyllatoxin scaffolds in which the CDR2-like loop of CD4 containing Phe43 had been grafted[24-26]. Unlike small molecule CD4m compounds, which primarily insert directly into the Phe43 cavity with few external interactions, CD4m peptides contain a more extensive gp120 binding interface involving not only a synthetic Phe43-equivalent residue, but also an equivalent to $Arg59_{CD4}$, which forms a salt bridge with the highly-conserved $Asp368_{gp120}$[10] and an exposed C-terminal β-strand that forms hydrogen bonds with the β15 strand of gp120 immediately adjacent to the Phe43 cavity opening[15]. These peptides directly compete with CD4 binding and inhibit HIV-1 infection of cells[24,25].

Recent reports of structures of CD4-bound partially-open[5] and fully-open but asymmetric Env trimers[6] demonstrated that there are different conformations of open HIV-1 Env trimers. In addition, the structure of an Env trimer bound to the CD4-binding site antibody b12 exhibited yet another open Env conformation[4]. Here we investigated the open conformation(s) of HIV-1 Env induced by two CD4m compounds: BNM-III-170, a small

molecule, and M48U1, a peptide, both of which have been structurally characterized when bound to gp120 monomeric cores[14,15].We report single-particle cryo-EM structures of complexes of these trimer-opening CD4m compounds with the BG505 SOSIP.664 trimer[8] (hereafter BG505), which provide information about potential V1V2 displacement, V3 rearrangement, and gp41 changes that cannot be assessed in structures involving gp120 monomeric cores. These structures revealed interactions of CD4m compounds with the Phe43 cavity in complexes with three CD4m and three 17b Fabs per BG505 trimer. Inter-protomer dimensions of M48U1 and BNM-III-170-bound Env closely matched those of an open, sCD4-bound Env. In addition, the CD4m-Env structures exhibited canonical features of CD4-bound open trimer for all three protomers, including a 4-stranded bridging sheet, a displaced V1V2 loop, an exposed and displaced V3 loop, and a compact arrangement of extended gp41 HR1C helices. We conclude that BNM-III-170 and M48U1 induce Env trimers to open in a similar manner as the native CD4 ligand despite fewer contacts with gp120.

Results

M48U1-BG505 and BNM-III-170-BG505 complexes bind 17b IgG

17b, a CD4-induced (CD4i) antibody that binds Env only when the gp120 V3 loop is exposed after V1V2 loop displacement characteristic of CD4-induced Env opening, has been used as a measure of trimer opening[3-6,27,28]. We first recapitulated and extended studies showing that binding of BNM-III-170 and M48U1 CD4m compounds open Env trimers[29,30] as assessed by a 17b binding assay[31]. D7324-tagged BG505 trimers[8] were immobilized on ELISA plates by binding to the JR-52 antibody as described[8] and then incubated with either buffer, BNM-III-170, M48U1, BMS-626529, or soluble CD4 (sCD4), and the binding of CD4-induced antibodies 17b and 21c, V1V2 bNAbs BG1 and PG16, and V3 bNAb 10-1074 was measured.

BG1, PG16, and 10-1074 IgGs bound to BG505 under both closed and open conditions (Supplementary Fig. 1a). As expected, BG505 did not bind 17b or 21c IgGs in the absence of sCD4 or BNM-III-170 and M48U1 inhibitors, indicating the Env trimers were well-

folded. When incubated with BNM-III-170, M48U1, or sCD4, BG505 bound to 17b IgG, confirming previous results[29,30] and demonstrating accessibility of the V3 loop in an open state (Supplementary Fig. 1b-d). Of note, binding of 17b was lower for BG505 incubated with BNM-III-170 (Supplementary Fig. 1c), suggesting that some of the BG505 Envs were in a conformation not accessible for binding to 17b. 21c IgG bound to BG505 plus sCD4, but did not bind to BG505 incubated with BNM-III-170 or M48U1 (Supplementary Fig. 1b-d), consistent with the requirement of the epitope of this antibody spanning CD4 and gp120[32]. BG505 incubated with BMS-626529 showed little or no binding to 17b IgG, consistent with a BG505–BMS-626529 crystal structure in the closed, prefusion state[20] (Supplementary Fig. 1a).

These results demonstrated that binding of M48U1 and BNM-III-170 caused BG505 Env trimer to adopt a conformation in which the 17b binding site on V3 was exposed.

Cryo-EM structures of BNM-III-170-BG505-17b and BG505-M48U1-17b complexes show densities for CD4m compounds

Although the BNM-III-170 and M48U1 CD4m compounds demonstrated 17b binding consistent with trimer opening, it was not known if other CD4-induced conformational changes in Env took place since the CD4 binding site on gp120 encompasses more than the CD4 Phe43 sidechain interacting with the gp120 Phe43 pocket (Fig. 2c). For example, other conserved interactions with gp120 include CD4 residues 29, 33, 34, 44, and 59[10].

We used single-particle cryo-EM to determine the structural effects of binding BNM-III-170 and M48U1 to an HIV-1 Env trimer. For structure determinations, BG505 was incubated with a CD4m and 17b Fab and then purified by size exclusion chromatography (SEC) to obtain CD4m-BG505-17b complexes. Samples were frozen on grids in vitrified ice and micrographs were collected on a Titan Krios microscope. 3D reconstructions were produced by iterative 2D classification, 3D classification, and 3D refinement followed by polishing[33,34]. Final reconstructions were produced for each complex at 3.7Å for BNM-III-170-BG505-17b and 3.9Å for M48U1-BG505-17b, as determined by the gold-standard

FSC[35] (Fig. 1a,b; Supplementary Fig. 2,3). Both structures were solved by fitting three copies of the gp120 and gp41 coordinates for open conformation A from a single-particle cryo-EM structure of sCD4-E51-BG505[6] and three copies of 17b Fab variable domain coordinates[36]. Initial models were refined without placement of CD4m compounds. Following refinement, density that could not be accounted for by Env or 17b Fab was present within the Phe43 pockets in all gp120 protomers of both maps. Overlaying of the BNM-III-170-gp120 and M48U1-gp120 crystal structures[14,15] allowed placement of the CD4m compounds into these densities within the Phe43 pocket.

CD4m-bound BG505 trimers displayed conformational heterogeneity

During processing of both CD4m-BG505 data sets, it became clear that one protomer in each structure had consistently worse density for the gp120 and 17b regions (Supplementary Fig. 4a). To determine if the lower resolution of this region in the BNM-III-170-BG505-17b complex resulted from sub-stoichiometric binding of 17b Fab, we performed iterative rounds of 3D classification. Rather than yielding classes with different 17b binding stoichiometries, the analysis produced nearly identical classes with 17b Fab densities for all protomers and similar numbers of particles in each class regardless of the number of subclasses (k=4, or 8) defined. Overlaying and alignment of the reconstructions showed that the 17b Fab with the weakest density was rotated at varying degrees away from the central axis of the Env in each subclass, but the resulting 3D classes were of poorer resolution (~6-8Å) and precluded detailed analysis to identify differences in conformation of the trimers in each subclass (Supplementary Fig. 2d). To improve the resolutions of the subclasses, we collected a second data set for the BNM-III-170-BG505-17b complex and repeated the analysis with more particles. Classification and analysis of the merged data produced similar 3D classes as in the first data set, but at a higher resolution (~6–7.4Å) with close overlays of two protomers (defined as protomers 1 and 2) and different positions for protomer 3 (Supplementary Fig. 2d, 4c-d). Re-fitting gp120 and gp41 coordinates into the gp120 densities revealed that the position of the gp120 core changed between classes and hinged as a rigid body about the gp120 β4 and β26 strands (Supplementary Fig. 4c). Since protomers in all 3D classes showed

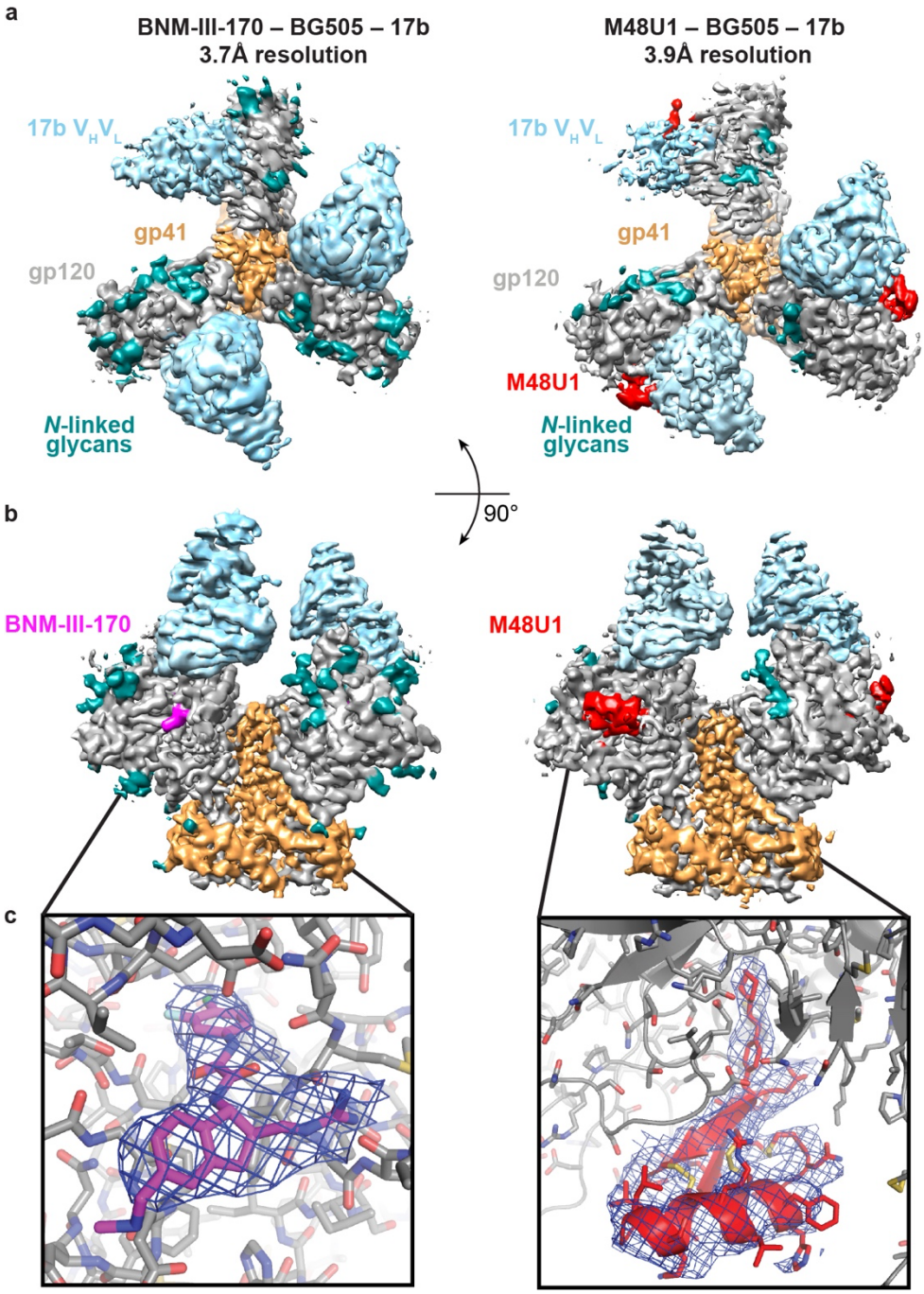

Figure 1: Cryo-EM structures of BNM-III-170-BG505-17b and M48U1-BG505-17b. a, Top-down view of density maps for BNM-III-170-BG505-17b and M48U1-BG505-17b complexes. **b**, Side view of density maps for BNM-III-170-BG505-17b and M48U1-BG505-17b complexes. Boxed region indicates binding site for one CD4m molecule on each structure. **c**, Close-up views of densities (blue) in CD4m binding sites. Densities shown at 7σ. Structure colors: 17b variable domain = light blue, gp120 = gray, gp41 = light orange, N-linked glycans = teal, BNM-III-170 = magenta, M48U1 = red, carbon atoms = gray, magenta, or red, oxygen atoms = red, nitrogen atoms = blue, sulfur atoms = yellow, chlorine atoms = green, fluorine atoms = pale blue.

similar conformations and the overall resolution was better for the combined reconstruction, we performed analyses on the models built and refined into the maps containing all particles without discarding classes in final 3D classification (Fig. 1). This resulted in a 3.7Å map of the BNM-III-170-BG505-17b complex with two well-defined gp120-gp41-17b protomers and one protomer with weaker density for 17b and gp120. As classification results for M48U1-BG505-17b were similar (Supplementary Fig. 3, 5), we also retained all particles without 3D classification for the final reconstruction at 3.9Å resolution.

BNM-III-170 and M48U1 bind in Phe43 pockets of BG505 Env trimer

While the overall resolution of the BNM-III-170-BG505-17b complex was 3.7Å, the local resolution for the gp120 Phe43 pocket was ~3.5Å (Supplementary Fig. 4a), and with the exception of $Glu478_{gp120}$, there was density for sidechains of gp120 residues lining the Phe43 pocket in protomers 1 and 2 (Supplementary Fig. 6a). Alignment of the gp120s from the BNM-III-170-BG505-17b complex with the monomeric core gp120 from the BNM-III-170-gp120 crystal structure[14] demonstrated structural similarity (root mean square deviation, RMSD, = 1.2-1.3 Å for 320 Cα atoms), and the BNM-III-170 from the gp120 core complex structure[14] aligned with the unaccounted density in the cryo-EM reconstruction (Supplementary Fig. 7a). In this position, BNM-III-170 fit into the gp120 Phe43 pocket beside the gp120 β20-β21 loop. In sCD4-bound gp120 structures, there is an 8Å gap between the tip of the phenyl ring of the $Phe43_{CD4}$ residue and the base of the Phe43 hydrophobic cavity in gp120, leading to the development of CD4m such as BNM-III-170 that reach further into the pocket[13]. As also found for the BNM-III-170 compound in the BNM-III-170-gp120 core structure[14], the BNM-III-170 molecule bound to each protomer in the BNM-III-170-BG505-17b structure extended to the base of the Phe43 cavity (Fig. 2a).

Interactions between BNM-III-170 and gp120 in the gp120 core structure[14] occur near the entrance of the Phe43 cavity and involve H-bonds between the guanidinium of BNM-III-170 and backbone carbonyls of $Arg429_{gp120}$ and $Met426_{gp120}$ and the methyl amine of BNM-III-170 with the carbonyl of $Gly473_{gp120.}$ In addition, a fourth hydrogen bond is formed halfway

into the Phe43 cavity between the backbone carbonyl of Asn425$_{gp120}$ and a hydrogen on the more buried nitrogen of the oxalamide linker of BNM-III-170[14]. Positioning of BNM-III-170 in the highest resolution protomer (protomer 1) of the BNM-III-170-BG505-17 structure placed its oxalamide linker within hydrogen bonding distance of Asn425$_{gp120}$ and Gly473$_{gp120}$ (Fig. 2b), consistent with previously-reported interactions[14]. Poor density for the

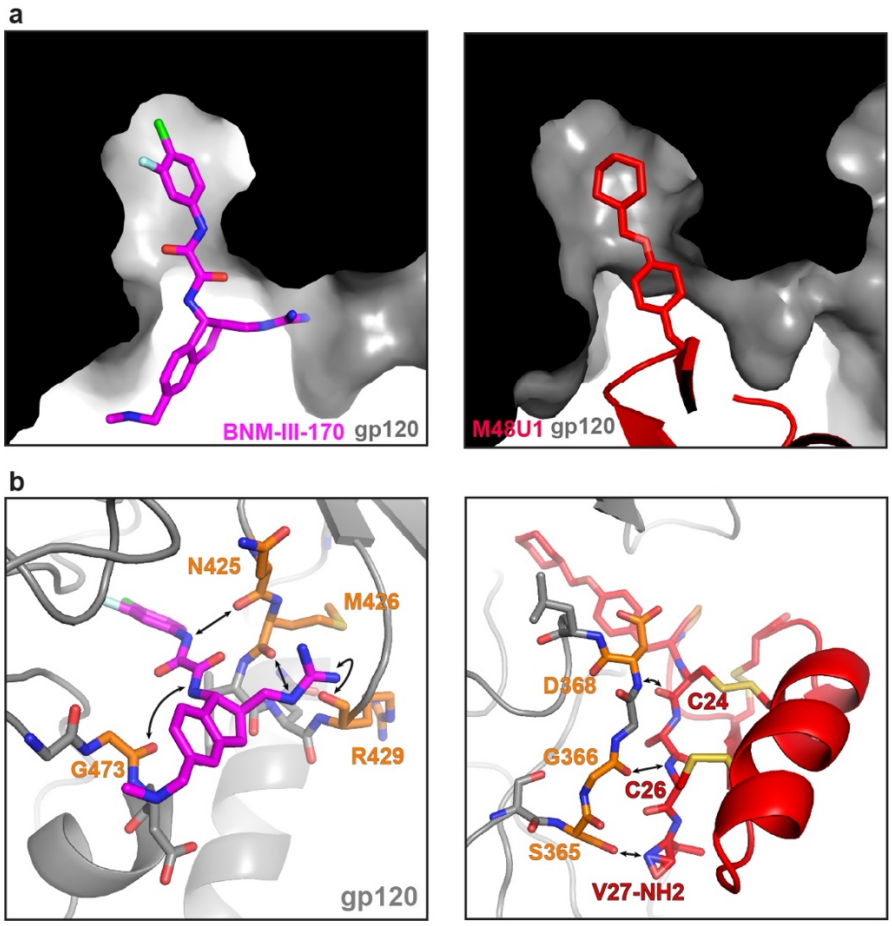

Figure 2: BNM-III-170 and M48U1 binding to the gp120 Phe43 pocket. Atom colors: carbon = magenta (BNM-III-170), red (M48U1), or orange (gp120), nitrogen = blue, oxygen = red, sulfur = yellow, chlorine = green; fluorine = cyan**. a,** Cut-away side view of gp120 showing BNM-III-170 or M48U1 inserting into Phe43 pocket cavity of gp120 (black/gray). **b,** Left: Stick model of BNM-III-170 within gp120 Phe43 pocket. Potential interactions between BNM-III-170 and backbone atoms of gp120 residues indicated by an arrow pointing to colored atoms of gp120 residues (sidechains omitted for clarity). Right: Stick and cartoon model of M48U1 within gp120 Phe43 pocket. **c,** Surface rendering of gp120 showing interacting residues for sCD4 (PDB: 6U0L, left, yellow), BNM-III-170 (middle, magenta), or M48U1 (right, red). Highlighted residues are 4Å or less from bound molecule. gp120 = gray, * = Phe43 cavity entrance.

guanidinium of BNM-III-170 made modeling of its orientation with respect to the β-turn of the gp120 β20-β21 hairpin loop difficult. However, the density supported its placement in close proximity to backbone carbonyls of both $Met426_{gp120}$ and $Asn429_{gp120}$ (Fig. 2b), suggesting that these interactions also occur in the BNM-III-170-BG505-17b complex.

The density for M48U1 in the M48U1-BG505-17b complex was well ordered, allowing placement of its α-helix and two-stranded β-sheet into density along with the coordinates for gp120, gp41, and 17b (Fig. 1b, c). As also found for the BNM-III-170-BG505-17b complex, one protomer of the BG505 trimer showed weaker density for 17b, gp120, and M48U1 (Supplementary Fig. 7b).

The cyclohexylmethoxy phenylalanine side chain at M48U1 position 23 occupies a structurally-equivalent position with respect to $Phe43_{CD4}$. Whereas $Phe43_{CD4}$ inserts only 8Å into the gp120 cavity, the hydrophobic cyclohexylmethoxy phenylalanine inserts and extends ~11.5Å from its Cα, reaching to the base of the gp120 Phe43 cavity (Fig. 2a). Unlike BNM-III-170, all polar contacts between M48U1 and gp120 occur outside of the Phe43 cavity. The β-strand spanning residues $Cys24_{M48U1}$ to $Cys26_{M48U1}$ (equivalent to $Leu44_{CD4}$ to $Lys46_{CD4}$) forms hydrogen bonds with backbone atoms of residues $Asp368_{gp120}$, $Gly367_{gp120}$, and $Gly366_{gp120}$ (Fig. 2b). In previous crystal structures, $Asp368_{gp120}$ was identified as an important binding residue both for $Arg59_{CD4}$ and for the M48U1-equivalent residue $Arg9_{M48U1}$[10,15]. However, reduced sidechain density for the M48U1 helix in the M48U1-BG505 structure limited accurate placement of sidechains.

BNM-III-170 and M48U1 open BG505 trimer to a similar degree as CD4

To evaluate conformations of HIV-1 Env, we previously used distance measurements between equivalent residues within gp120 subunits of an Env trimer, from which we could compare the degree of gp120 opening between trimers in closed, b12-bound, and sCD4-bound states[5,6,37]. Here we used this method to assess the effects of BNM-III-170 and M48U1 binding on the BG505 conformation (Fig. 3). Measurements for the CD4m-BG505 complexes were complicated by the lack of three-fold Env trimer symmetry due to the

heterogeneity of one of the protomers (designated as protomer 3 in each complex) (Supplementary Fig. 4-5). Thus the measurements between equivalent residues in protomers 1 and 2 are more accurate than measurements between protomers 2 and 3 and between protomers 1 and 3. For distance measurement comparisons with sCD4-bound Env trimers, we averaged distances from conformations A and B of an asymmetric sCD4-BG505-E51 Fab complex[6] and a symmetric sCD4-B41-17b complex[4] (Fig. 3c). We also averaged measured distances between protomers for each CD4m-BG505 complex. We report a single distance for three-fold symmetric Env structures and an average distance with a standard deviation for asymmetric structures in order to more clearly address whether the CD4m-Env structures adopt what can be described as a sCD4-bound open Env trimer structure (Fig. 3c).

As previously described, the V3 regions of closed Env and b12-bound open Env are occluded by the V1V2 loop[5] (Fig. 4a,b). Opening of b12- or sCD4-bound Env involves rotation of the gp120 as a rigid body away from the central gp41 helices, hinging on the loops connecting the β26 and β4 strands to the gp120 core.[5,38] A hallmark of sCD4, but not b12, binding to Env trimers is displacement of V1V2 to expose the coreceptor binding site on V3 and the resulting disorder of most of the V1V2 and V3 loops[3,5,6]. These conformational changes have corresponding changes in positioning of residues in the V1V2 loop, the V3 loop, and the CD4 binding site (CD4bs) that can be evaluated by measuring between the three copies of $Pro124_{gp120}$ at the V1V2 base, the three copies of $His330_{gp120}$ at the V3 base, and the three copies of $Asp368_{gp120}$ at the CD4bs. A typical closed Env structure[39] displayed V1V2 distances of 14Å and V3 distances of 69Å (Fig. 3c). Similarly, an Env trimer that was kept in a closed conformation by the Phe43 cavity-binding small molecule BMS-626529[20] showed V1V2 and V3 inter-protomer distances of 14Å and 55Å, respectively. In sCD4-liganded open Env, the displacement of V1V2 from the trimer apex to the sides of Env trimer resulted in inter-protomer V1V2 distances of 77Å ± 5.9Å and V3 distances of 74Å ± 4Å.

The BNM-III-170-BG505-17b and M48U1-BG505-17b structures both showed similar inter-protomer measurements as sCD4-bound Envs for V1V2 displacement (74Å ± 3.5Å and 75Å ± 2.8Å, for the BNM-III-170 and M48U1 complexes, respectively) and V3 positioning

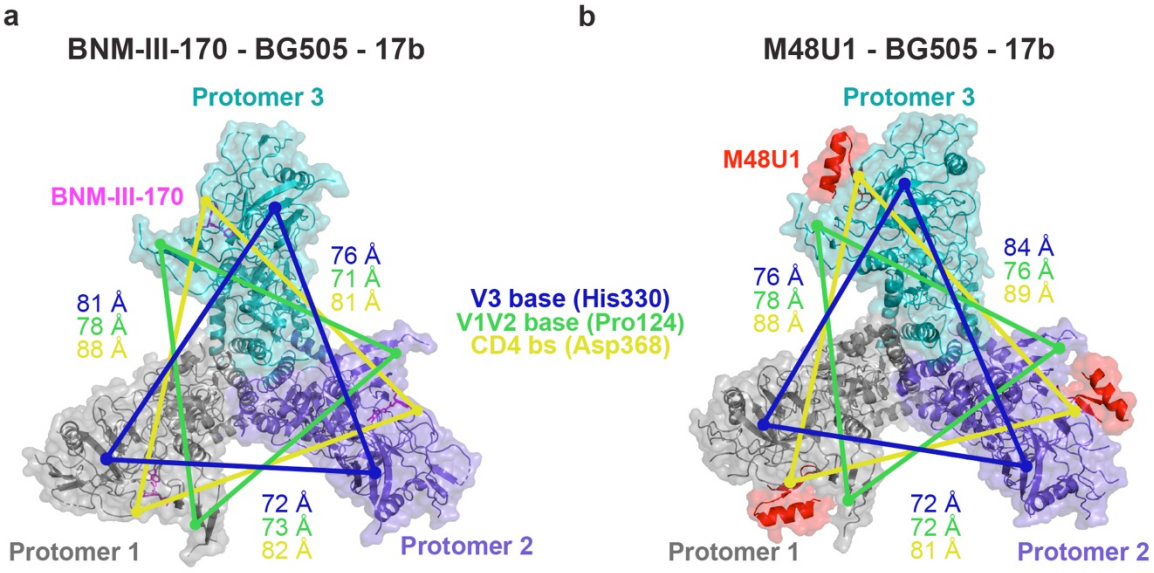

c

			Average inter-protomer distance (Å ± s.d.)		
Structure	PBD Code	State	V3 Base ($His330_{gp120}$)	V1/V2 Base ($Pro124_{gp120}$)	CD4bs ($Asp368_{gp120}$)
BG505 - IOMA - 10-1074	5T3Z	closed	69	14	54
BMS-626529 - BG505 - PGT122 - 35O22	5U70	closed	69	14	55
b12 - B41	5VN8	open	75 ± 0.3 (n=3)	69 ± 0.2 (n=3)	85 ± 0.0 (n=3)
sCD4 - Env- 17b	5VN3 6U0L 6U0N	open	74 ± 4.0 (n=9)	77 ± 5.9 (n=9)	80 ± 5.0 (n=9)
BNM-III-170 - BG505 - 17b	this study	open	76 ± 4.6 (n=3)	74 ± 3.7 (n=3)	84 ± 3.4 (n=3)
M48U1 - BG505 - 17b	this study	open	77 ± 5.9 (n=3)	75 ± 2.8 (n=3)	86 ± 4.2 (n=3)

Figure 3: BNM-III-170- and M48U1-bound Env inter-protomer dimensions match those of open CD4-bound Env. Structure colors: Protomer 1 = gray, protomer 2 = purple, protomer 3 = teal, BNM-III-170 = magenta, M48U1 = red. Top-down view of surface and cartoon rendering of **a,** BNM-III-170-bound and **b,** M48U1-bound Env trimer structures showing inter-protomer distance measurements between reference residues for the base of the V3 loop ($His330_{gp120}$, blue), the base of the V1/V2 loop ($Pro124_{gp120}$, green), and the CD4 binding site (CD4bs, $Asp368_{gp120}$, yellow). 17b Fabs have been removed for clarity. **c**, Table of average inter-protomer distances for CD4-bound open Env structures, closed BMS-626529-bound Env structure, and BNM-III-170 and M48U1-bound open Env. All measurements were made between the Cα of the indicated residues.

(76Å ± 4.6Å and 77Å ± 5.9Å, respectively). In addition, as found in CD4-bound open structures[3-6], most of the V1V2 and V3 loops were disordered in the CD4m-bound Env structures.

Opening of both b12- and CD4-bound trimers leads to hinging about the loops connecting the β26 and β4 strands to the main portion of the gp120 subunit and rotation of the gp120 as a rigid body away from the central gp41 helices[5,38]. This is reflected in changes of the average inter-protomer distances between $Asp368_{gp120}$ residues in the CD4 binding site: from 54Å and 55Å in closed Env structures to 80Å ± 5.0Å in CD4-bound open Env and 85Å ± 0Å for b12-bound open Env. The analogous measurements for the CD4m-BG505 complexes (84Å ± 3.4Å and 86Å ± 4.2Å) suggested that CD4m binding induced equivalent gp120 rotation and displacement indicative of trimer opening.

Taken together, the inter-protomer distances for V1V2, V3, and the CD4 binding site provide quantitative verification that BNM-III-170 and M48U1 induce an open BG505 structure similar to the sCD4-bound open conformation.

BNM-III-170 and M48U1 induce additional structural changes similar to those induced by sCD4 binding

In addition to gp120 rotation and displacement to create an open Env trimer, sCD4-bound Env structures exhibit structural changes within the gp120 and gp41 subunits compared with closed Env structures. In order to determine if the CD4m-bound Env structures demonstrated similar conformational changes as sCD4-bound open Envs, we compared specific regions of closed and open Env structures. For comparisons with sCD4-bound Env trimer, we choose conformation A from a structure of sCD4-BG505-E51 Fab[6] that differs from a slightly different conformation (conformation B) also observed for the asymmetric sCD4-BG505-E51 complex[6] and for a symmetric sCD4-B41-17b complex[4]. We chose conformation A for comparisons because, like our CD4m-bound open Env structures, the fusion peptide was ordered in conformation A (Fig. 4e), but was disordered in conformation B.

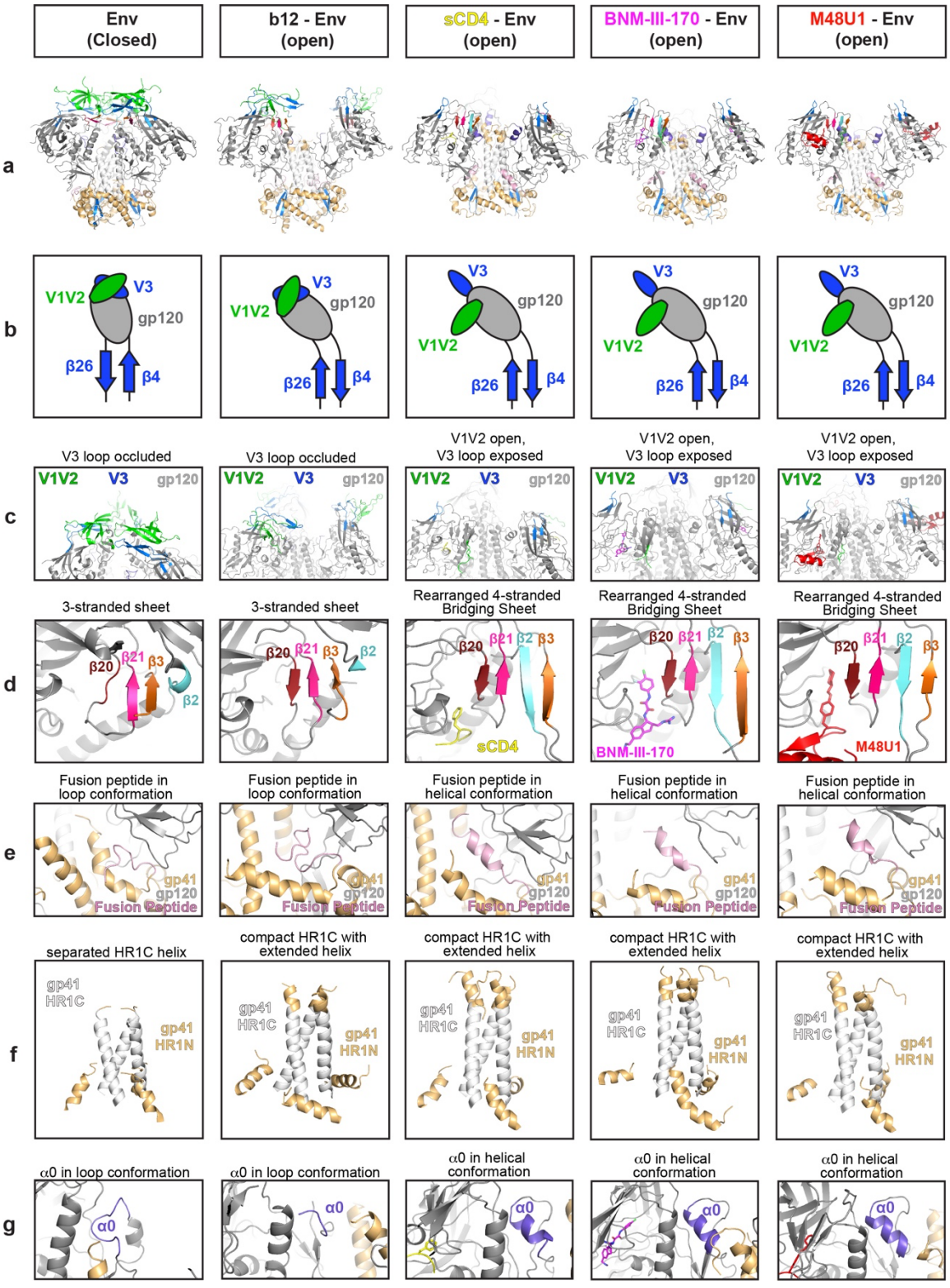
Env (Closed)
b12 - Env (open)
sCD4 - Env (open)
BNM-III-170 - Env (open)
M48U1 - Env (open)
a
b
V1V2
V3
gp120
β26
β4
c
V3 loop occluded
V1V2 open, V3 loop exposed
d
3-stranded sheet
Rearranged 4-stranded Bridging Sheet
β20
β21
β3
β2
sCD4
BNM-III-170
M48U1
e
Fusion peptide in loop conformation
Fusion peptide in helical conformation
gp41
Fusion Peptide
f
separated HR1C helix
compact HR1C with extended helix
gp41 HR1C
gp41 HR1N
g
α0 in loop conformation
α0 in helical conformation
α0

Figure 4: Conformational features of gp120 and gp41 in structures of closed and open Envs. Cartoon and schematic models showing features of the HIV-1 Env trimers in the closed conformation (PDB 5T3Z), b12-bound open conformation (PDB 5VN8), sCD4-bound open conformation (PDB 6U0L, Conformation A), the BNM-III-170-bound open conformation, and the M48U1-bound open conformation. Structure colors: gp120 = gray, gp41 = light orange, CD4 Phe43 loop = yellow, BNM-III-170 = magenta, M48U1 = red, V1V2 loop = green, V3 loop = blue, β20 strand = dark red, β21 strand = hot pink, β3 strand = orange, β2 strand = cyan, HR1C helix = white, fusion peptide = light pink, α0 loop = purple. **a**, Cartoon depiction of BG505 Env with regions of interest colored. **b**, Schematic of gp120 angle with relation to the β26/β4 β-strands and V1V2 and V3 loop positioning. **c,** V1V2 and V3 loop positions. **d**, 3-stranded β-sheet (β20-β21, β3 β-strands) versus 4-stranded bridging sheet (β20-β21, β2, β3 β-strands). **e, F**usion peptide conformation. **f,** gp41 HR1C helix conformation (gp120 N-terminal portion of gp41 removed for clarity). **g,** α0 loop versus α0 helix conformation.

A large conformational change that occurs upon sCD4 binding to Env trimer is displacement of V1V2 to expose the coreceptor binding site on V3[3,5,6]. As previously described, the V3 regions of closed Env and b12-bound open Env are occluded by the V1V2 loop[5] (Fig. 4a-c). The CD4m-bound open Env complexes showed displacement of the V1V2 loop and exposure of the V3 loop in a similar manner as in sCD4-bound open Env (Fig. 4b-c).

Accompanying the opening of the V1V2 loop, the 3-stranded β-sheet formed by the β20, β21, and β3 strands in closed Env structures[12] undergoes a rearrangement upon binding of CD4 in which β2 becomes an ordered β-strand and swaps positions with the β3 strand, forming a 4-stranded β-sheet[5,6,38] called the bridging sheet[10] (Fig. 4d). Although the b12-bound Env structure can be classified as open with respect to its gp120 positions[38], it retains the 3-stranded β-sheet found in closed Env structures (Fig. 4d), likely because the V1V2 and V3 regions move as a rigid body with gp120 rather than V1V2 being displaced to the sides of Env[5]. In common with sCD4-bound open Env structures, CD4m-bound Envs included 4-stranded bridging sheets (Fig. 4d).

The fusion peptide also exists in several conformations: an unstructured loop in closed and b12-bound open structures versus a helical conformation in sCD4-bound and CD4m-bound open conformations (Fig. 4e). In addition, the rotation and repositioning of the gp120 subunits upon trimer opening permits the rearrangement of the gp41 helices to form a

compact HR1C helical bundle, as also found in b12-bound and sCD4-bound open Env trimers (Fig. 4f). The CD4m-BG505 complexes adopted the same gp120 positioning and gp41 rearrangements as found in sCD4- and b12-bound Envs (Fig. 4f). While the HR1C helix became more compact upon rearrangement in the CD4m-bound structures, it also extended and formed several additional ordered helical turns at the tip of the gp41 bundle that make up part of HR1N (Fig. 4f), as also found in the b12- and sCD4-bound open structures, therefore its occurrence in CD4m-bound open Env structures suggests this is a conformational change that typically occurs upon trimer opening.

In closed or b12-bound Envs, the gp120 α0 region nestled against the top of the gp41 helices is in an unstructured loop (Fig. 4g). When sCD4 is bound, the α0 adopts a helical structure and is located at the top of the HR1 helix of the adjacent protomer (Fig. 4g). Likewise, the CD4m-BG505 open structures showed analogous placement and helical α0 conformations to the sCD4-bound structure for the three protomers in each Env trimer (Fig. 4g).

We conclude that the CD4m-bound Envs exhibit structural changes within the gp120 and gp41 subunits characteristic of sCD4-bound open Env structures.

Discussion

Viral fusion protein flexibility is required for their functions in fusing the viral and host cell membranes[2]. Indeed, HIV-1 Env trimers exhibit different degrees of opening in response to external signals[9]. Here, we investigated how the activating CD4m molecules BNM-III-170 and M48U1 alter the conformation of Env trimers. Since the CD4m-gp120 interface is smaller than the sCD4-gp120 interface, it was possible that, rather than adopting a fully open conformation normally induced by host receptor binding, activating CD4m molecules could induce a partially-open conformation (e.g., similar to sCD4 plus 8ANC195-bound Env trimers[5]) or an open conformation without V1V2 displacement as in the b12-bound Env trimer[4]. Alternatively, since CD4m molecules have little to no bulk that could interact outside the gp120 Phe43 pocket, they could also allow the trimer to adopt a previously-unseen open conformation due to limiting steric clashes that would occur in the presence of bound CD4.

Using single-particle cryo-EM, we found that two CD4m compounds, BNM-III-170 and M48U1, bound to the native-like BG505 Env trimer resulted in open trimer structures similar to sCD4-bound structures, both in terms of inter-subunit gp120 rotation and displacement and in terms of intra-subunit conformational changes. These results demonstrate that interactions of small molecule compounds at the gp120 Phe43 pocket are sufficient to cause Env trimer opening and structural rearrangements similar to those induced by the CD4 host receptor. These results can be used to inform design of CD4m compounds as possible therapeutics.

Methods

Protein Expression and Purification

A construct encoding the BG505 SOSIP.664 native-like envelope gp140 trimer including stabilizing mutations ($A501C_{gp120}$, $T605C_{gp120}$, $I559P_{gp41}$), an introduced glycosylation site ($T332N_{gp120}$), an improved furin protease cleavage site (REKR to RRRRRR), and truncation after residue 664 in gp41[8] was subcloned into the pTT5 expression vector (National Research Council of Canada) and transiently expressed in HEK293F cells. BG505 trimer was purified from supernatant by 2G12 Fab immunoaffinity chromatography followed by SEC using a Superdex 200 Increase 10/300 GL column (GE Life Sciences) running in TBS (20mM Tris pH 8, 150mM NaCl) plus 0.02% NaN_3 as described[37]. BG505 trimer that was C-terminally tagged with the D7324 sequence[31] was prepared in the same way. For some experiments, BG505 SOSIP.664 was expressed and purified from supernatants of a stable CHO cell line (kind gift of John Moore, Weill Cornell Medical College) as described[40].

Expression plasmids encoding JR-52 IgG were the kind gift of James Robinson (Tulane University) and John Moore (Weill Cornell Medical College). Expression plasmids encoding the heavy and light chains of 17b, BG1, 21c, PG16, 10-1074, JR-52 IgGs were transiently co-transfected into Expi293F cells (Gibco) using Expofectamine (Invitrogen). IgGs were purified from supernatants by protein A chromatography (GE Life Sciences) followed by

SEC using a Superdex 200 Increase 10/300 GL column (GE Life Sciences). IgGs were stored in TBS. 6x-His tagged version of 17b Fab and sCD4 (domains 1 and 2 of CD4; amino acids 1-186) were expressed as described[5].

CD4 mimetic compounds

The (+)(*R*,*R*)BNM-III-170 small molecule (referred to as BNM-III-170 throughout the manuscript) was synthesized as described[14,41] and stored at -20ºC in DMSO until use. Lyophilized M48U1 peptide (sequence reported in ref.[15]) was purchased from Presto Pepscan Inc. (Lelystad, The Netherlands) and resuspended in DMSO before use.

ELISA

96-well plates (Corning, #9018) were coated with JR-52 IgG at 5µg/mL in 0.1M $NaHCO_3$ pH 8.6 at 4ºC overnight. sCD4-BG505, BNM-III-170-BG505, M48U1-BG505, and BMS-626529 complexes were prepared by incubating CD4m with D7324-tagged BG505 trimer[31] at a 15:1 small molecule to trimer ratio or a 6:1 sCD4 to trimer overnight at room temperature in TBS. Plates were blocked on the following day for 1hr with TBS-TMS (20mM Tris pH 8, 150mM NaCl, 0.05% Tween 20, 1% non-fat dry milk, 1% goat serum (Gibco 16210-072)). Complexes diluted to a final concentration of 10µg/mL in TBS-TMS were incubated on coated plates for 1 hour at room temperature and three 10-minute washes were performed using TBS-T (20mM Tris pH 8, 150mM NaCl, 0.05% Tween 20). IgG versions of 17b, 21c, BG1, PG16, and 10-1074 were diluted from 20µg/µL to 1ng/µL in 2-fold increments. Plates with trimer complexes were incubated with IgGs for 2 hours at room temperature, followed by 3 washes of TBS-T, and then incubation for 30 mins at room temperature with anti-human IgG HRP at 1:4000 (Southern Biotech #2040-05). 5 washes of TBST were done followed by development using 1-Step Ultra TMB-ELISA Substrate Solution (ThermoFisher Scientific, 43028) and quenching with 1N HCl. Quantification of results was performed using a plate reader detecting absorbance at 450nm. All samples were evaluated in duplicate (n=2). After averaging duplicates, individual data points were graphed and figures were made using Graphpad Prism v8.

Cryo-EM Sample Preparation

BNM-III-170-BG505-17b and M48U1-BG505-17b complexes were assembled by incubating CD4m compounds BNM-III-170 or M48U1 with BG505 overnight at room temperature at a molar ratio of 10:1 (CD4m:trimer). 17b Fab was added the next day at a 9:1 ratio (Fab:trimer) and incubated at room temperature for 2-4 hours. Complexes were purified by SEC on a Superdex 200 Increase GL 50/150 or a Superdex 200 Increase 10/300 GL column (GE Healthcare) and fractions containing CD4m-BG505-17b complexes were concentrated to 1.4-1.5mg/mL. Cryo-EM grids were frozen using a Mark IV Vitrobot (ThermoFisher) at 22°C and 100% humidity. 3.1µL of sample was applied to Quantifoil R2/2 300 mesh grids, blotted for 3 or 3.5 seconds, and plunge frozen into liquid ethane. Grids were then transferred to grid boxes in liquid nitrogen and stored until data collection.

Cryo-EM Data Collection and Processing

Cryopreserved grids were loaded into a Titan Krios electron microscope (ThermoFisher) equipped with a GIF Quantum energy filter (slit width 20eV) operating at 300kV and a nominal 80,000 magnification. Images were recorded using a K3 direct electron detector (Gatan) in counting mode with a pixel size of 1.104Å/pixel and defocus range of 1-3.5µm using SerialEM acquisition software (ver. 3.8 Beta). Images were exposed for a total dose of 40 or 60e^-/pixel fractionated into 40 subframes. Micrographs were manually curated after motion correction with MotionCor2[42] and the contrast transfer function was fit with Gctf ver. 1.06[43] to remove cracked or icy micrographs. Initial particles from 100 randomly selected micrographs were picked using the RELION autopicker[33,34], and reference-free two-dimensional (2D) classes were generated in RELION ver. 3.0. Particles from good initial classes were used to generate *Ab initio* models in CryoSPARC ver. 2.15.0[44]. RELION autopicker was then used to pick particles from all micrographs and subjected to 2D reference-free classification in RELION. Good 2D classes were selected and subjected to two rounds of 2D classification. 3D classification was performed on 2D averages using RELION[33,34]. Rounds of 3D classification were attempted with different numbers of subclasses (k=4, 8) for data sets. The final 3D classification used for analysis included 4 subclasses (k=4) and 1 round of classification for M48U1-BG505-17b and 4 subclasses (k=4)

and 2 iterative rounds for merged data sets of BNM-III-170-BG505-17b. The 3D classes were used for analysis; however, no 3D classes were discarded for at the final round of 3D classification before proceeding to 3D refinement and polishing because higher resolution maps for the areas of interest (Env and CD4m compounds) were obtained when using all particles. 3D reconstructions were produced in RELION 3D auto-refine using *ab initio* models as starting models[33,34]. CTF correction and polishing were performed in RELION, and final maps were generated after a final round of 3D auto-refining. Sphericity was calculated using the 3DFSC server[45].

Model building

Coordinates of gp120 (PDB 6U0L, Conformation B), gp41 (PDB 6U0L, Conformation B), and 17b Fab V_H-V_L domains (PDB 2NXY) were fitted into map density using UCSF Chimera ver. 1.14[46]. Coordinates were initially refined using phenix.real_space_refine[47] from the Phenix package ver. 1.18.1[48] and manually refined using Coot v0.8.9.1[49]. Initial refinement rounds were performed without placing CD4m compounds. Placement of BNM-III-170 or M48U1 was done in UCSF Chimera by overlaying the refined gp120 portions of our cryo-EM structures with corresponding X-ray crystal structures of M48U1-gp120 (PDB 4JZZ) or BNM-III-170-gp120 (PDB 5F4P), which placed CD4m compounds into unambiguous, unaccounted-for density within the Phe43 pocket region of gp120. CD4m were then rigid body fit in Chimera to better fit the density. Further rounds of manual and automated refinement of models containing CD4m were performed. As resolution was not sufficient to determine conformations of M48U1 BNM-III-170 in the third protomer, the conformations from the crystal structures were modeled into the density using rigid body fitting and were not further refined. In addition, we trimmed side chains to C α of M48U1-BG505-17b protomer 3 gp120,17b V_H-V_L and M48U1 (except for the cyclohexylmethoxy phenylalanine at position 23) due to poor resolution. Coordinates from final models were rigid body fit into 3D subclasses using phenix.real_space_refine[48] followed by rigid body fitting for the β4/β26 strands in Coot[49].

Structural analysis

Structure figures were made using UCSF Chimera[46] or PyMOL[50]. Unless otherwise noted, figures showing a single gp120-gp41 protomer were made using one of the two protomers (protomers 1 and 2) in each complex showing the best density. Potential hydrogen bonds were assigned as interactions that were <4.0Å and with A-D-H angle >90°. Potential van der Waals interactions between atoms were assigned as interactions that were <4.0Å. Due to low resolution, hydrogen-bond and van der Waals interaction assignments should be considered tentative. Interacting residues for Fig. 2c were determined as residues within 4Å of bound CD4m or sCD4 using PyMOL[50]. Inter-protomer Cα distances were measured between Cα atoms using the Measurement Wizard tool in PyMOL version 2.3.2. Average interprotomer distances in Fig. 3c were calculated as the mean between distances of each protomer ± the standard deviation. Distances for three-fold symmetric structures are listed without a standard deviation. Distances for sCD4-bound open Env structures were derived from two asymmetric structures of sCD4-BG505-E51 (PDBs 6U0L and 6U0N) and one structure of a more symmetric sCD4-B41-17b (PDB 5VN3).

Pairwise Cα alignments between CD4-bound gp120-core structures and CD4m-bound Env gp120 core structures in Supplementary Fig. 8 were done using the alignment function PyMOL v2.3.2 without excluding outliers. Atoms belonging to regions that were not present in both gp120 and gp120 core structures were excluded.

Data Availability

The structural coordinates were deposited into the Worldwide Protein Data Bank (wwPDB) with accession code 7LO6 (BNM-III-170-BG505-17b) and 7LOK (M48U1-BG505-17b). EM density maps were deposited into EMDB with accession numbers EMD-23462 (BNM-III-170-BG505-17b) and EMD-23465 (M48U1-BG505-17b). Other data are available upon reasonable request.

Acknowledgements

Cryo-EM was performed in the Beckman Institute Resource Center for Transmission Electron Microscopy at Caltech with assistance from directors A. Malyutin and S. Chen. We thank J. Vielmetter and the Beckman Institute Protein Expression Center at Caltech for protein production, J.E. Robinson (Tulane University) for the JR-52 antibody, John Moore (Weill Cornell Medical College) for the BG505 stable cell line. This work was supported by the Bill and Melinda Gates Foundation Collaboration for AIDS Vaccine Discovery (CAVD) grant INV-002143 and the National Institute of Allergy and Infectious Diseases (NIAID) Grant numbers 2 P50 AI150464 and HIVRAD P01 AI100148 (P.J.B.) and AI50471 and GM56550 (A.B.S.). A portion of this research was supported by NIH grant U24GM129547 and performed at the PNCC at OHSU and accessed through EMSL (grid.436923.9), a DOE Office of Science User Facility sponsored by the Office of Biological and Environmental Research.

Author Contributions

C.A.J. designed experiments, purified proteins, assembled protein and cryo-EM samples, collected cryo-EM data, processed cryo-EM data, performed model building and refinement, analyzed data, performed ELISA experiments, and wrote the manuscript. C.O.B. designed experiments, purified proteins, collected cryo-EM data, assisted in data processing, assisted in model building and refinement, and assisted in ELISA experiments. S.M.K. and B.M. developed and synthesized BNM-III-170. A.B.S. supervised and guided BNM-III-170 development. P.J.B. supervised and guided the project and wrote the manuscript.

Competing Interests

The authors declare no competing interests.

References

1. Johnson, L. F. et al. Global variations in mortality in adults after initiating antiretroviral treatment: an updated analysis of the International epidemiology Databases to Evaluate AIDS cohort collaboration. AIDS 33, S283–S294 (2019).

2. Harrison, S. C. Viral membrane fusion. Virology 479–480, 498–507 (2015).

3. Wang, H. et al. Cryo-EM structure of a CD4-bound open HIV-1 envelope trimer reveals structural rearrangements of the gp120 V1V2 loop. *Proc Natl Acad Sci* USA 113, E7151–E7158 (2016).

4. Ozorowski, G. et al. Open and closed structures reveal allostery and pliability in the HIV-1 envelope spike. *Nature* 547, 360–363 (2017).

5. Wang, H., Barnes, C. O., Yang, Z., Nussenzweig, M. C. & Bjorkman, P. J. Partially open HIV-1 envelope structures exhibit conformational changes relevant for coreceptor binding and fusion. *Cell Host Microbe* 24, 579–592 e4 (2018).

6. Yang, Z., Wang, H., Liu, A. Z., Gristick, H. B. & Bjorkman, P. J. Asymmetric opening of HIV-1 Env bound to CD4 and a coreceptor-mimicking antibody. *Nat Struct Mol Biol* 26, 1167–1175 (2019).

7. Alkhatib, G. The biology of CCR5 and CXCR4. *Curr Opin HIV AIDS* 4,96–103 (2009).

8. Sanders, R. W. et al. A next-generation cleaved, soluble HIV-1 Env Trimer,BG505 SOSIP.664 gp140, expresses multiple epitopes for broadly neutralizing but not non-neutralizing antibodies. *PLoS Pathog* 9, e1003618 (2013).

9. Ward, A. B. & Wilson, I. A. The HIV-1 envelope glycoprotein structure: nailing down a moving target. *Immunol Rev* 275,21–32 (2017).

10. Kwong, P. D. et al. Structure of an HIV gp120 envelope glycoprotein in complex with the CD4 receptor and a neutralizing human antibody. *Nature* 393, 648–659 (1998).

11. Kwon, Y. D. et al. Unliganded HIV-1 gp120 core structures assume the CD4-bound conformation with regulation by quaternary interactions and variable loops. *Proc Natl Acad Sci* USA 109, 5663–5668 (2012).

12. Lyumkis, D. et al. Cryo-EM structure of a fully glycosylated soluble cleaved HIV-1 envelope trimer. *Science* 342, 1484–1490 (2013).

13. Courter, J. R. et al. Structure-based design, synthesis and validation of CD4-mimetic small molecule inhibitors of HIV-1 entry: conversion of a viral entry agonist to an antagonist. *Acc Chem Res* 47, 1228–1237 (2014).

14. Melillo, B. et al. Small-molecule CD4-mimics: structure-based optimization of HIV-1 entry inhibition. *ACS Med Chem Lett* 7, 330–334 (2016).

15. Acharya, P. et al. Structural basis for highly effective HIV-1 neutralization by CD4-mimetic miniproteins revealed by 1.5 A cocrystal structure of gp120 and M48U1. *Structure* 21, 1018–1029 (2013).

16. Acharya, P., Lusvarghi, S., Bewley, C. A. & Kwong, P. D. HIV-1 gp120 as a therapeutic target: navigating a moving labyrinth. *Expert Opin Ther Targets* 19, 765–783 (2015).

17. Lalonde, J. M. et al. Design, synthesis and biological evaluation of small molecule inhibitors of CD4-gp120 binding based on virtual screening. *Bioorg Med Chem* 19, 91–101 (2011).

18. Guo, Q. et al. Biochemical and genetic characterizations of a novel human immunodeficiency virus type 1 inhibitor that blocks gp120-CD4 interactions. *J Virol* 77, 10528–10536 (2003).

19. Wang, T. et al. Discovery of 4-benzoyl-1-[(4-methoxy-1H-pyrrolo[2,3-b]pyridin-3-yl)oxoacetyl]-2- (R)-methylpiperazine (BMS-378806): a novel HIV-1 attachment inhibitor that interferes with CD4-gp120 interactions. *J Med Chem* 46, 4236–4239 (2003).

20. Pancera, M. et al. Crystal structures of trimeric HIV envelope with entry inhibitors BMS-378806 and BMS-626529. *Nat Chem Biol* 13, 1115–1122 (2017).

21. Lai, Y. T. et al. Lattice engineering enables definition of molecular features allowing for potent small-molecule inhibition of HIV-1 entry. *Nat Commun* 10, 47 (2019).

22. Haim, H. et al. Soluble CD4 and CD4-mimetic compounds inhibit HIV-1 infection by induction of a short-lived activated state. *PLoS Pathog* 5, e1000360 (2009).

23. Alsahafi, N. et al. An asymmetric opening of HIV-1 envelope mediates antibody-dependent cellular cytotoxicity. *Cell Host Microbe* 25, 578–587 e5 (2019).

24. Vita, C. et al. Rational engineering of a miniprotein that reproduces the core ofthe CD4 site interacting with HIV-1 envelope glycoprotein. *Proc Natl Acad Sci* USA 96, 13091–13096 (1999).

25. Huang, C. C. et al. Scorpion-toxin mimics of CD4 in complex with human immunodeficiency virus gp120 crystal structures, molecular mimicry, and neutralization breadth. *Structure* 13, 755–768 (2005).

26. Stricher, F. et al. Combinatorial optimization of a CD4-mimetic miniprotein and cocrystal structures with HIV-1 gp120 envelope glycoprotein. *J Mol Biol* 382, 510–524 (2008).

27. Thali, M. et al. Characterization of conserved human immunodeficiency virus type 1 gp120 neutralization epitopes exposed upon gp120-CD4 binding.J.Virol.67, 3978–3988 (1993).

28. Huang, C. C. et al. Structural basis of tyrosine sulfation and VH-gene usage in antibodies that recognize the HIV type 1 coreceptor-binding site on gp120. *Proc Natl Acad Sci* USA 101, 2706–11 (2004).

29. Prevost, J. et al. The HIV-1 Env gp120 Inner Domain Shapes the Phe43 Cavity and the CD4 Binding Site. *mBio* 11, e00280-20 (2020).

30. Tolbert, W. D. et al. Targeting the late stage of HIV-1 entry for antibody-dependent cellular cytotoxicity: structural basis for env epitopes in the C11 region. *Structure* 25, 1719–1731 e4 (2017).

31. Derking, R. et al. Comprehensive antigenic map of a cleaved soluble HIV-1envelope trimer. *PLoS Pathog* 11, e1004767 (2015).

32. Diskin, R., Marcovecchio, P. M. & Bjorkman, P. J. Structure of a clade C HIV-1 gp120 bound to CD4 and CD4-induced antibody reveals anti-CD4 polyreactivity. *Nat Struct Mol Biol* 17, 608–613 (2010).

33. Scheres, S. H. RELION: implementation of a Bayesian approach to cryo-EM structure determination. *J Struct Biol* 180, 519–530 (2012).

34. Zivanov, J. et al. New tools for automated high-resolution cryo-EM structure determination in RELION-3. *Elife* 7, e42166 (2018).

35. Scheres, S. H. & Chen, S. Prevention of overfitting in cryo-EM structure determination. *Nat Methods* 9, 853–854 (2012).

36. Zhou, T. et al. Structural definition of a conserved neutralization epitope on HIV-1 gp120. *Nature* 445, 732–737 (2007).

37. Scharf, L. et al. Broadly neutralizing antibody 8ANC195 recognizes closed and open states of HIV-1 Env. *Cell* 162, 1379–1390 (2015).

38. Ozorowski, G. et al. Effects of adjuvants on HIV-1 envelope glycoprotein SOSIP trimers in vitro. *J Virol* https://doi.org/10.1128/JVI.00381-18. (2018).

39. Gristick, H. B. et al. Natively glycosylated HIV-1 Env structure reveals new mode for antibody recognition of the CD4-binding site. *Nat Struct Mol Biol* 23, 906–915 (2016).

40. Dey, A. K. et al. cGMP production and analysis of BG505 SOSIP.664, an extensively glycosylated, trimeric HIV-1 envelope glycoprotein vaccine candidate. *Biotechnol Bioeng* https://doi.org/10.1002/bit.26498. (2017).

41. Chen, J. et al. Development of an effective scalable enantioselective synthesis of the HIV-1 entry inhibitor BNM-III-170 as the Bis-trifluoroacetate Salt. *Org Process Res Dev* 23, 2464–2469 (2019).

42. Zheng, S. Q. et al. MotionCor2: anisotropic correction of beam-induced motion for improved cryo-electron microscopy. *Nat Methods* 14, 331–332 (2017).

43. Zhang, K. Gctf: Real-time CTF determination and correction. *J Struct Biol* 193, 1–12 (2016).

44. Punjani, A., Rubinstein, J. L., Fleet, D. J. & Brubaker, M. A. cryoSPARC: algorithms for rapid unsupervised cryo-EM structure determination. *Nat Methods* 14, 290–296 (2017).

45. Tan, Y. Z. et al. Addressing preferred specimen orientation in single-particle cryo-EM through tilting. *Nat Methods* 14, 793–796 (2017).

46. Goddard, T. D., Huang, C. C. & Ferrin, T. E. Visualizing density maps with UCSF Chimera. *J Struct Biol* 157, 281–287 (2007).

47. Afonine, P. V. et al. Real-space refinement in PHENIX for cryo-EM and crystallography. *Acta Crystallogr D Struct Biol* 74, 531–544 (2018).

48. Liebschner, D. et al. Macromolecular structure determination using X-rays, neutrons and electrons: recent developments in Phenix. *Acta Crystallogr D Struct Biol* 75, 861–877 (2019).

49. Emsley, P., Lohkamp, B., Scott, W. G. & Cowtan, K. Features and development of Coot. *Acta Crystallogr D Biol Crystallogr* 66, 486–501 (2010).

50. Schrödinger, L. The PyMOL Molecular Graphics System. 1.2r3pre edn. (ThePyMOL Molecular Graphics System, 2011).

Supplemental Material

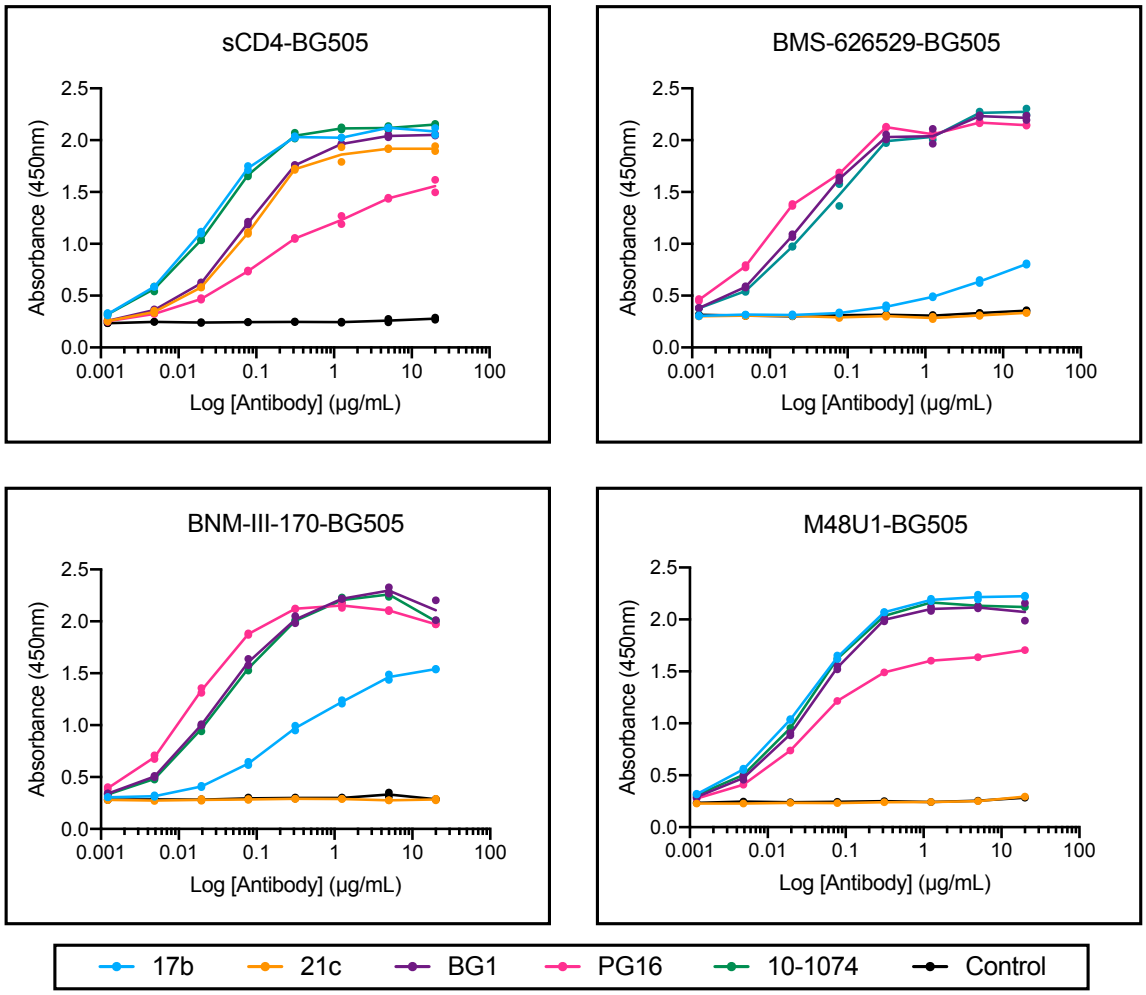

Supplementary Figure 1. Binding of HIV-1 antibodies to sCD4-Env or CD4m-Env complexes. ELISAs evaluating binding of IgG versions of anti-Env antibodies 17b, 21c, BG1, PG16, and 10-1074 or control (no antibody added) to **a**, sCD4-BG505 Env, **b**, BMS-626529-BG505, **c**, BNM-III-170-BG505 Env, and **d**, M48U1-BG505 Env. Values are shown as mean of two individual replicates. Colors: 17b = light blue, 21c = light orange, BG1 = purple, PG16 = hot pink, 10-1074 = green, control = black. Results shown for n=2 individual replicates. Connecting line is for mean of individual replicates.

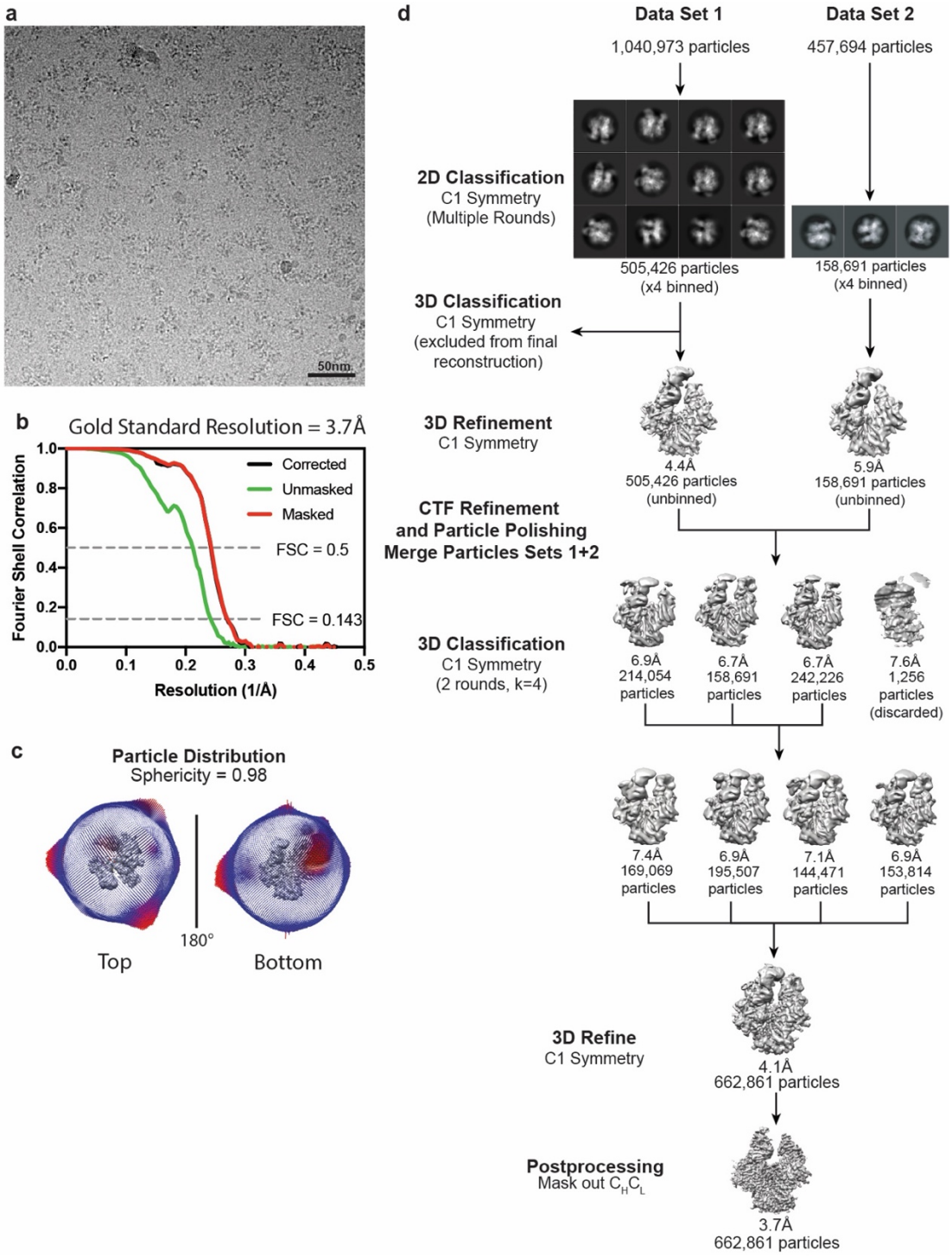

Supplementary Figure 2. Data Processing for BNM-III-170-BG505-17b complex.
a, Representative EM micrograph of data set. 2739 and 2048 micrographs were collected for data set 1 and 2, respectively. Scale bar is 50nm. **b,** Gold Standard 3D FSC chart for final reconstruction map using combined data sets. **c,** Particle orientation distribution and sphericity for final reconstruction of combined data sets. **d,** Schematic of processing pipeline.

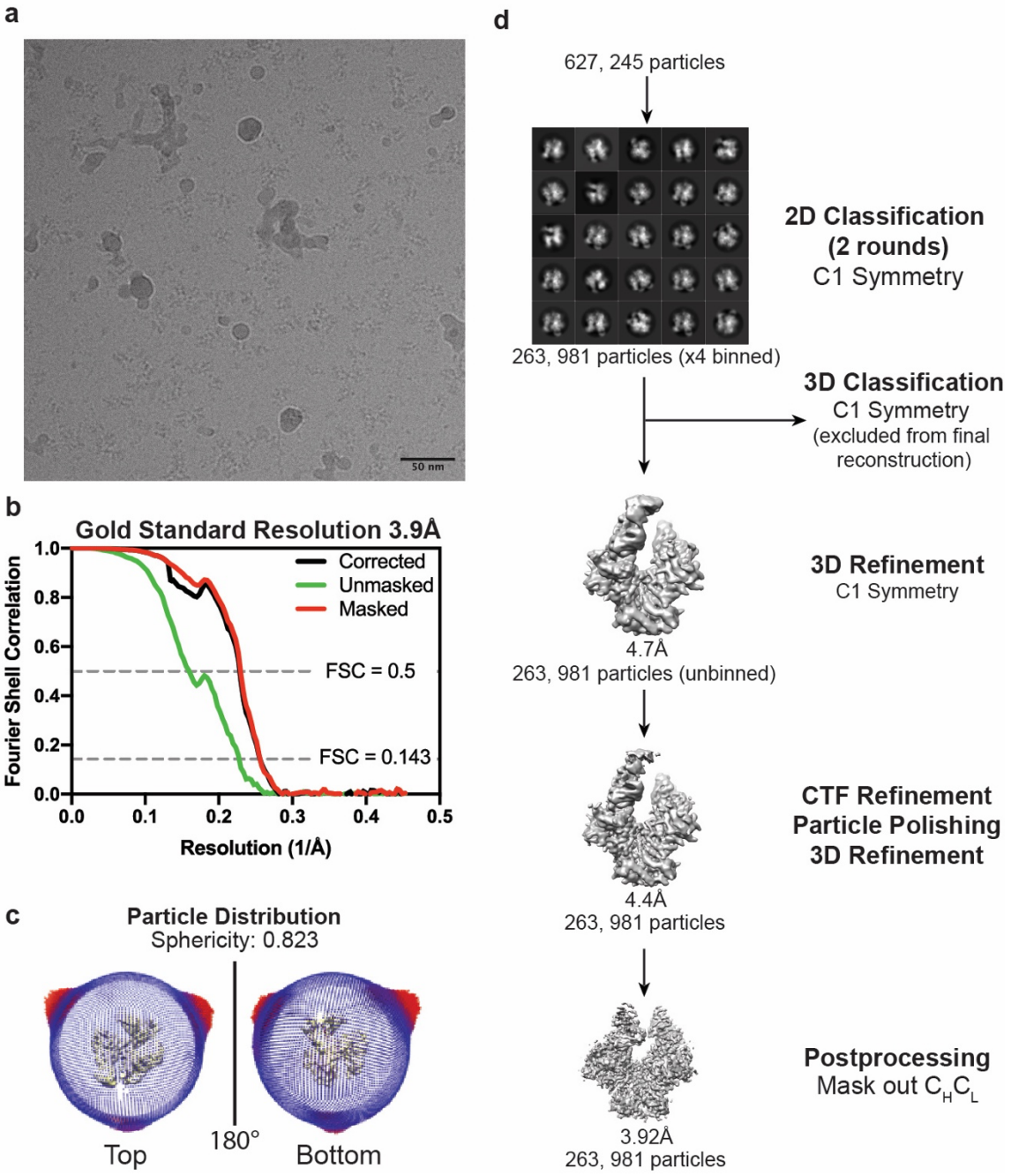

Supplementary Figure 3. Data Processing for the M48U1-BG505-17b complex.
a, Representative EM micrograph of data set. 2688 total micrographs were collected. Scale bar is 50nm. **b,** Gold Standard 3D FSC chart for final reconstruction map using combined data sets. **c,** Particle orientation distribution and sphericity for final reconstruction of combined data sets. **d,** Schematic of Processing pipeline.

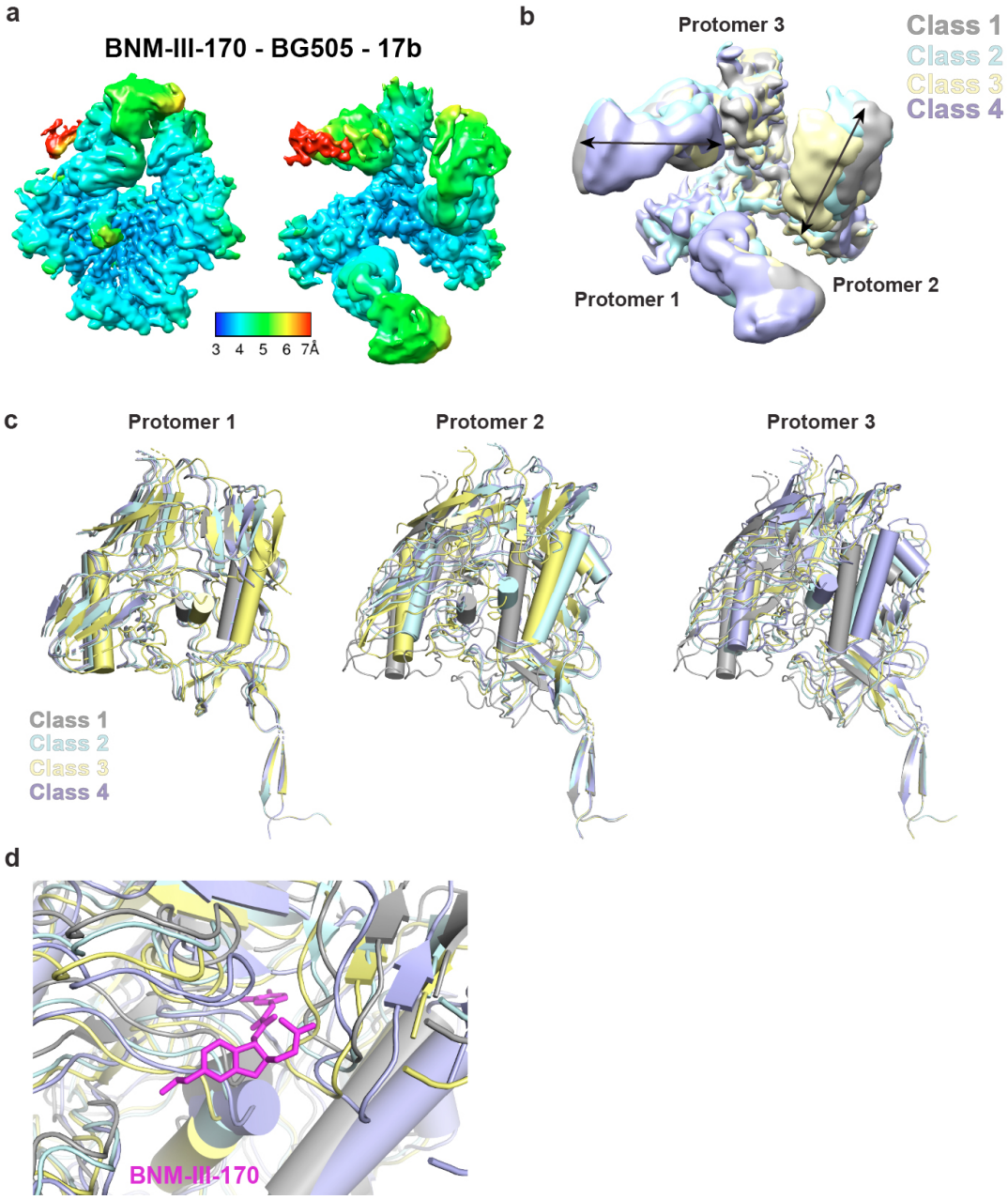

Supplementary Figure 4. 3D classification of BNM-III-170-BG505-17b shows differences in positioning of gp120 and 17b.

a, Local resolution map of BNM-III-170-BG505-17b reconstruction. **b,** Overlay of 3D classes of BNM-III-170-BG505-17b produced in final classification round after merging and polishing particles for classes (gray, pale cyan, pale yellow, light purple for Class 1-4, respectively). Double-headed arrow on Protomer 3 shows direction of displacement of 17b and gp120 between 3D classes. **c,** Cartoon models of gp120 subunits rigid body fit into BNM-III-170-BG505-17b 3D classification maps. The β4/β26 strands were fit separately from the rest of the gp120 and alignments were done using Cα of β4/β26 strands. **d,** Cartoon model overlay of Protomer 3 showing gp120 Phe43 pocket for each 3D class and BNM-III-170 (magenta) from final model.

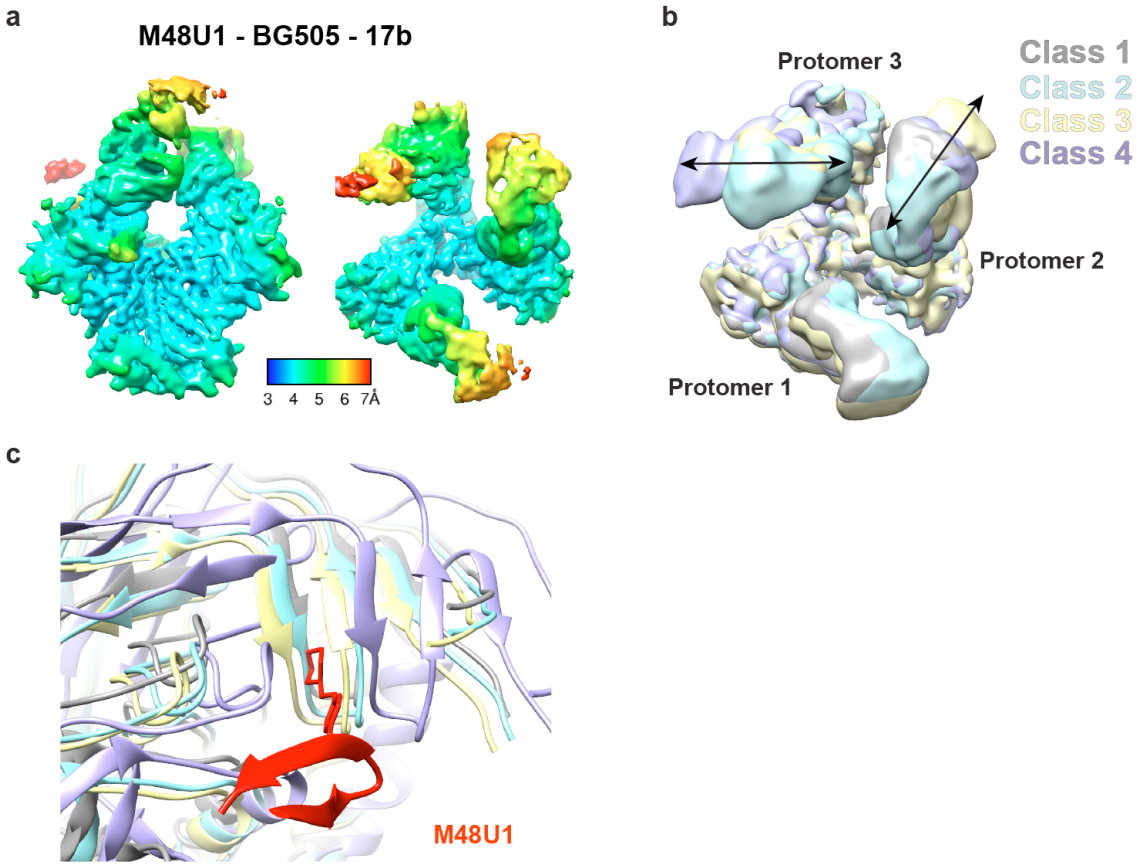

Supplementary Figure 5. 3D classification of M48U1-BG505-17b shows differences in positioning of gp120 and 17b.
a, Local resolution map of M48U1-17b reconstruction. **b,** Overlay of 3D classes of M48U1-BG505-17b (gray, pale cyan, pale yellow, light purple for Class 1-4, respectively). Double-headed arrow on Protomer 3 shows direction of displacement of 17b and gp120 between 3D classes. **c,** Cartoon model overlay of Protomer 3 gp120 Phe43 pocket for all 3D classes with M48U1 (red) from final model. M48U1 helix removed for clarity.

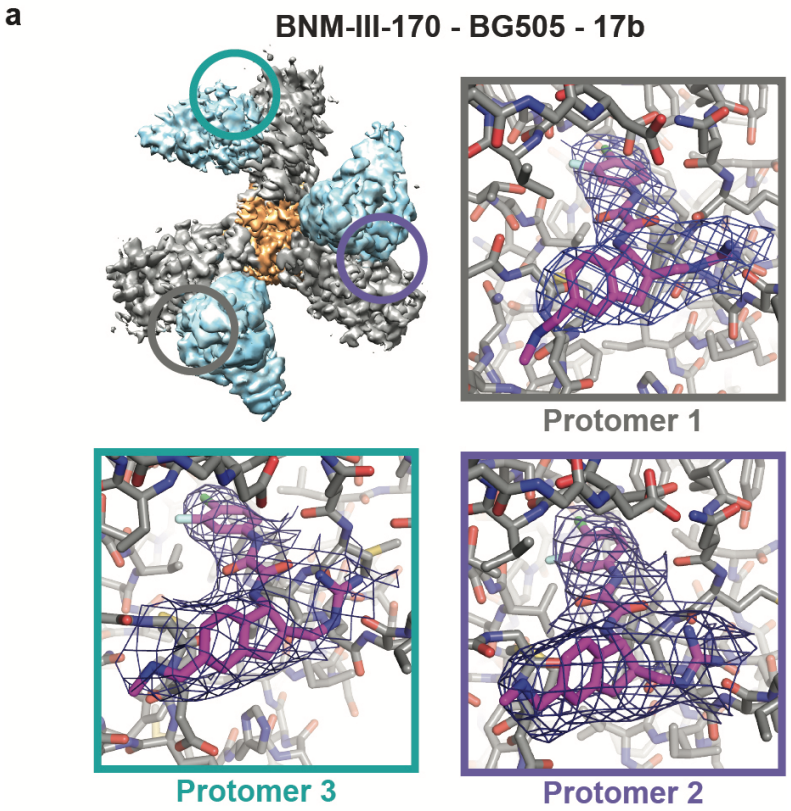
a
BNM-III-170 - BG505 - 17b
Protomer 1
Protomer 3
Protomer 2
b
M48U1 - BG505 - 17b
Protomer 1

Supplementary Figure 6. CD4m density is present within gp120 Phe43 cavity.
a, Top-down view of BNM-III-170-BG505-17b density (top left, 17b = light blue, gp120 = gray, gp41 = light orange) with regions containing BNM-III-170 circled. Surrounding panels show zoomed-in views of densities (blue) for the BNM-III-170 molecule and a cartoon/stick representation of the coordinates (BNM-III-170 = magenta, gp120 = gray) in Protomer 1 (gray), Protomer 2 (purple) and Protomer 3 (teal). Densities for protomers 1 and 2 are shown at 7σ and for protomer 3 at 5σ. **b**, Top-down view of M48U1-BG505-17b density (top left, 17b = light blue, gp120 = gray, gp41 = light orange) with regions containing M48U1 (red) circled in Protomer 1 (gray), Protomer 2 (purple) and Protomer 3 (teal). Surrounding panels show zoomed-in views of densities (blue) for the M48U1 molecule and a cartoon/stick representation of the coordinates (M48U1 = red, gp120 = gray) in each protomer. Density for protomer 1 is shown at 7σ and for protomers 2 and 3 at 5σ.

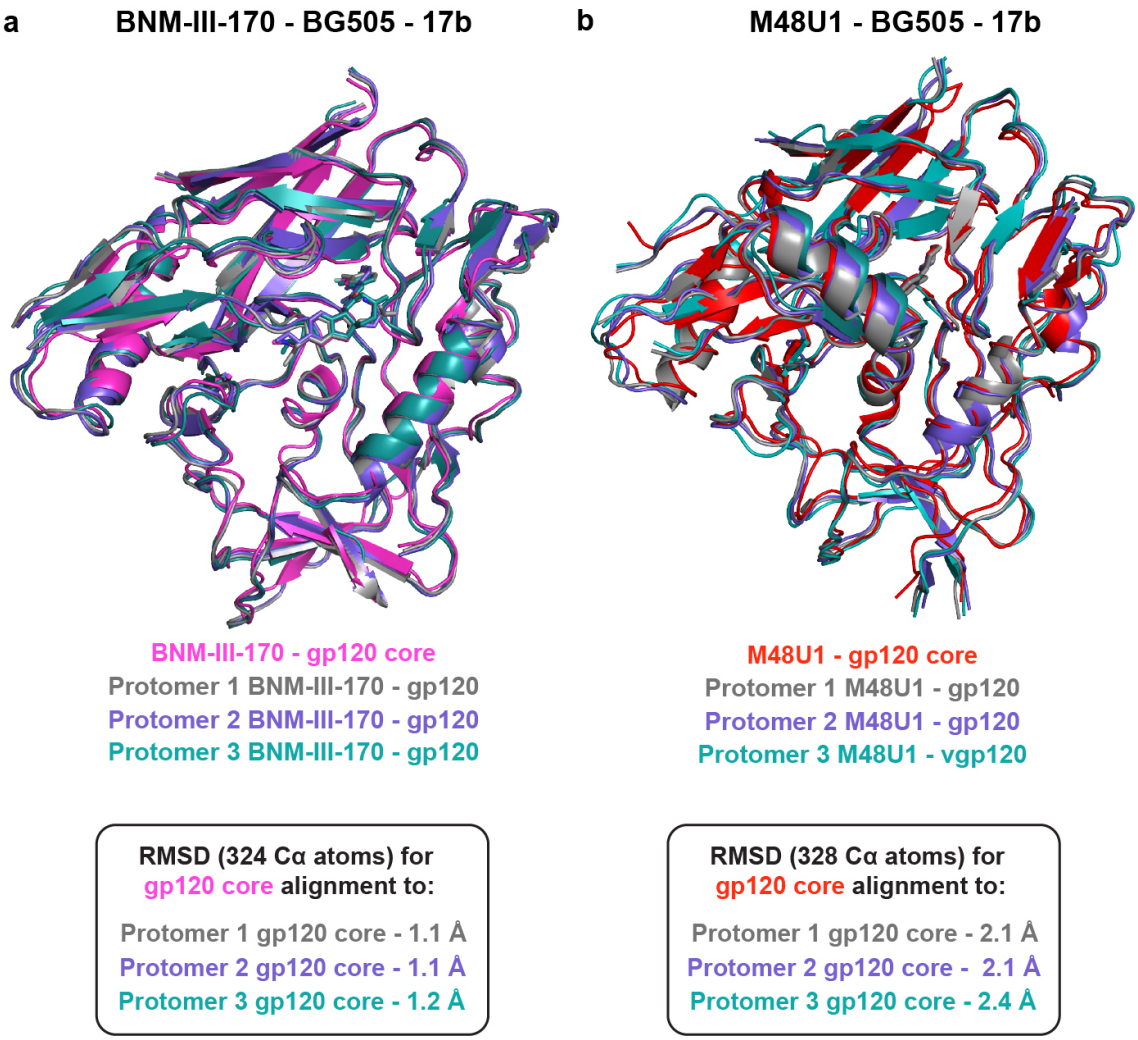

Supplementary Figure 7. Overlays of CD4m-gp120 core crystal structures with gp120 core portions of structures of CD4m-BG505 Env trimer complexes.
a, Alignment of BNM-III-170-gp120 core crystal structure (PDB 5F4P, magenta) and gp120 core regions from protomers 1 (gray), 2 (purple), and 3 (teal) of the BNM-III-170-BG505-17b complex**.** **b,** Alignment of M48U1-gp120 core crystal structure (PDB 4JZ, red) and gp120 core regions from protomers 1 (gray), 2 (purple), and 3 (teal) of M48U1-BG505-17b complex**.**

Supplementary Table 1: Cryo-EM data collection, refinement and validation statistics

	BNM-III-170-BG505 SOSIP.664-17b (Data Set 1)	BNM-III-170-BG505 SOSIP.664-17b (Data Set 2)	BNM-III-170-BG505 SOSIP.664-17b Combined Data (EMD-23462) (PDB 7LO6)	M48U1-BG505 SOSIP.664-17b (EMD-23465) (PDB 7LOK)
Data collection and processing				
Magnification	81, 000x	81, 000x	81, 000x	81, 000x
Voltage (kV)	300	300	300	300
Electron exposure (e–/Å^2)	40	40	40	60
Defocus range (μm)	-1.5 to -3.5	-1.5 to -3.5	-1.5 to -3.5	-1.5 to -3.5
Pixel size (Å)	1.104	1.104	1.104	1.104
Symmetry imposed	C1	C1	C1	C1
Initial particle images (no.)	1040973	457694	n/a	627245
Final particle images (no.)	505426	158691	662861	263981
Map resolution (Å)	4.0	4.6	3.7	3.9
FSC threshold	0.143	0.143	0.143	0.143
Map resolution range (Å)	n/a	n/a	3.7 – 4.1	3.9 – 4.4
Refinement				
Initial model used (PDB code)	n/a	n/a	6U0L, 5F4P, 2NXY	6U0L, 4JZZ, 2NXY
Model resolution (Å)	n/a	n/a	3.7	3.9
FSC threshold			0.143	0.143
Model resolution range (Å)	n/a	n/a	3.67 – 3.8	3.8 – 4.0
Map sharpening *B* factor (Å^2)	n/a	n/a	-124	-150
Model composition				
Non-hydrogen atoms	n/a	n/a	18015	14498
Protein residues	n/a	n/a	2198	1999
Ligands	n/a	n/a	MAN: 9 BMA: 3 NAG: 47 5VG: 3	MPT: 3 BMA : 3 NAG: 14 NH2: 3 MAN: 6 DPR: 3
B factors (Å^2)				
Protein	n/a	n/a	144.19	219.21
Ligand	n/a	n/a	142.22	118.36
R.m.s. deviations				
Bond lengths (Å)	n/a	n/a	0.011	0.007
Bond angles (°)	n/a	n/a	0.944	1.132
Validation				
MolProbity score	n/a	n/a	2.40	2.27
Clashscore	n/a	n/a	19.03	14.44
Poor rotamers (%)	n/a	n/a	0.69	0.39
Ramachandran plot				
Favored (%)	n/a	n/a	87.08	87.99
Allowed (%)	n/a	n/a	12.87	11.85
Disallowed (%)	n/a	n/a	0.05	0.16

Chapter 4

SARS-COV-2 NEUTRALIZING ANTIBODY STRUCTURES INFORM THERAPEUTIC STRATEGIES

Barnes, C.O., **Jette, C.A.**, Abernathy, M.E., Dam, K.-M.A., Esswein, S.R., Gristick, H.B., Malyutin, A.G., Sharaf, N.G., Huey-Tubman, K.E., Lee, Y.E., Robbiani, D.F., Nussenzweig, M.C., West, A.P., Bjorkman, P.J. SARS-CoV-2 neutralizing antibody structures inform therapeutic strategies. *Nature* **588,** 682–687 (2020).
doi:10.1038/s41586-020-2852-1

Summary
The coronavirus disease 2019 (COVID-19) pandemic presents an urgent health crisis. Human neutralizing antibodies that target the host ACE2 receptor-binding domain (RBD) of the severe acute respiratory syndrome coronavirus-2 (SARS-CoV-2) spike protein[1–5] show promise therapeutically and are being evaluated clinically[6–8]. Here, to identify the structural correlates of SARS-CoV-2 neutralization, we solved eight new structures of distinct COVID-19 human neutralizing antibodies[5] in complex with the SARS-CoV-2 spike trimer or RBD. Structural comparisons allowed us to classify the antibodies into categories: (1) neutralizing antibodies encoded by the *VH3-53* gene segment with short CDRH3 loops that block ACE2 and bind only to 'up' RBDs; (2) ACE2-blocking neutralizing antibodies that bind both up and 'down' RBDs and can contact adjacent RBDs; (3) neutralizing antibodies that bind outside the ACE2 site and recognize both up and down RBDs; and (4) previously described antibodies that do not block ACE2 and bind only to up RBDs[9]. Class 2 contained four neutralizing antibodies with epitopes that bridged RBDs, including a *VH3-53* antibody that used a long CDRH3 with a hydrophobic tip to bridge between adjacent down RBDs, thereby locking the spike into a closed conformation. Epitope and paratope mapping revealed few interactions with host-derived *N*-glycans and minor contributions of antibody somatic hypermutations to epitope contacts. Affinity measurements and mapping of naturally occurring and in vitro-selected spike mutants in 3D provided insight into the potential for SARS-CoV-2 to escape from antibodies elicited during infection or delivered therapeutically. These classifications and structural analyses provide rules for assigning current and future human RBD-targeting antibodies into classes, evaluating avidity effects and suggesting combinations for clinical use, and provide insight into immune responses against SARS-CoV-2.

Introduction

Neutralizing antibodies (NAbs) against SARS-CoV-2 protect against infection in animal models[1,3,4,10,11] and are being evaluated for prophylaxis and as therapeutic agents in humans[7,8]. These antibodies target the SARS-CoV-2 spike (S) trimer[3,5,10,12,13,14,15,16,17], a viral glycoprotein that mediates binding to the angiotensin-converting enzyme 2 (ACE2) receptor[18,19]. The S trimer comprises three copies of an S1 subunit that contains the RBD and three copies of S2, which includes the fusion peptide and transmembrane regions[20,21]. The RBDs of SARS-CoV-2 and other coronaviruses exhibit flexibility, such that they bind to ACE2 only when they are in an 'up' conformation, compared with the 'down' RBD conformation of the closed, prefusion S trimer[20,21,22,23,24,25].

Many human NAbs isolated from COVID-19-convalescent donors target the RBD, binding to distinct, sometimes non-overlapping, epitopes[3,4,5,10,12,13,14,17]. A subset of these antibodies blocks viral entry by binding to the ACE2-binding site on the RBD[6,11,13,15,26,27]. A family of recurrent ACE2-blocking human NAbs is composed of heavy chains encoded by the *VH3-53* or *VH3-66* gene segment[3,12,13,16,17,27,28,29], most of which are known or predicted[15,26,28,30,31] to exhibit a common RBD binding mode that results from the use of germline-encoded residues within the complementarity-determining regions 1 and 2 (CDRH1 and CDRH2) and a CDRH3 that is shorter than the average length (15 amino acids; IMGT[32] complementarity-determining region (CDR) definition) in human antibodies[33]. Other SARS-CoV-2 RBD-binding antibodies are encoded by *VH3-30*[5], and these have also been isolated from donors infected with SARS-CoV[34], and antibodies with a variety of the other V_H gene segments[3,5,10,12,13,14,15,16,17].

To classify commonalities and differences among RBD-binding human NAbs isolated from COVID-19-convalescent individuals[5], we solved complexes of NAbs with stabilized (2P and 6P versions)[35,36] soluble S trimer. Subsequently, we used high-resolution details of the binding orientations of NAbs encoded by the *VH1-2*, *VH1-46*, *VH3-30*, *VH3-53*, *VH4-34* and *VH5-51* gene segments to determine rules for binding by four distinct anti-RBD antibody classes (Supplementary Table 2). The NAbs chosen for structures are highly

potent, achieving 90% neutralization in pseudotype virus assays at concentrations ranging from 22 to 140 ng ml^{-1} (ref. [5]), and thus our structural analyses and classifications directly relate to understanding mechanisms of neutralization and potency differences between human NAbs.

Results

Class 1 *VH3-53* Nabs block ACE2 and bind to 'up' RBDs

We solved Fab and Fab–RBD crystal structures of C102 (Supplementary Table 1), which we compared to our previous[26] cryo-electron microscopy (cryo-EM) structure of S trimer complexed with the related human NAb C105 (Extended Data Figs. 1, 2). Both C102 and C105 are *VH3-53* NAbs with short (11 and 12 residues, respectively) CDRH3 loops (Extended Data Fig. 1g) that were isolated from the same donor[5]. They share structural similarities with each other and with other *VH3-53*-encoded short CDRH3 human NAb structures solved as complexes with RBDs[12,30,37,38] (Extended Data Fig. 2a). Notably, the C102–RBD structure resembled the analogous portion of the C105–S structure[26] (Extended Data Fig. 2a). These results establish that Fab–RBD structures can reproduce interactions with RBDs in the context of an S trimer; however, Fab–RBD structures do not reveal the state(s) of the antibody-bound RBD in the complex (up versus down) or the potential inter-protomer contacts by Fabs.

Because the C105 Fab bound to either two or three up RBDs on S with no observed interactions with down RBDs or with adjacent RBDs[26] (Extended Data Fig. 1f), we used the higher-resolution C102 Fab–RBD structure to deduce a more accurate epitope and paratope than was possible using the C105–S cryo-EM structure with flexible up RBDs (Extended Data Fig. 1a–e). Buried surface area calculations showed that the C102 CDRH3 region had a relatively minor role in the paratope: of 1,045 $Å^2$ of buried surface area on the antibody (786 $Å^2$ on the heavy chain; 259 $Å^2$ on the light chain), CDRH3 accounted for only 254 $Å^2$ (Extended Data Fig. 2b). This contrasts with most antibodies in which CDRH3 contributes equally or more to the interface with antigen than the sum of CDRH1 and

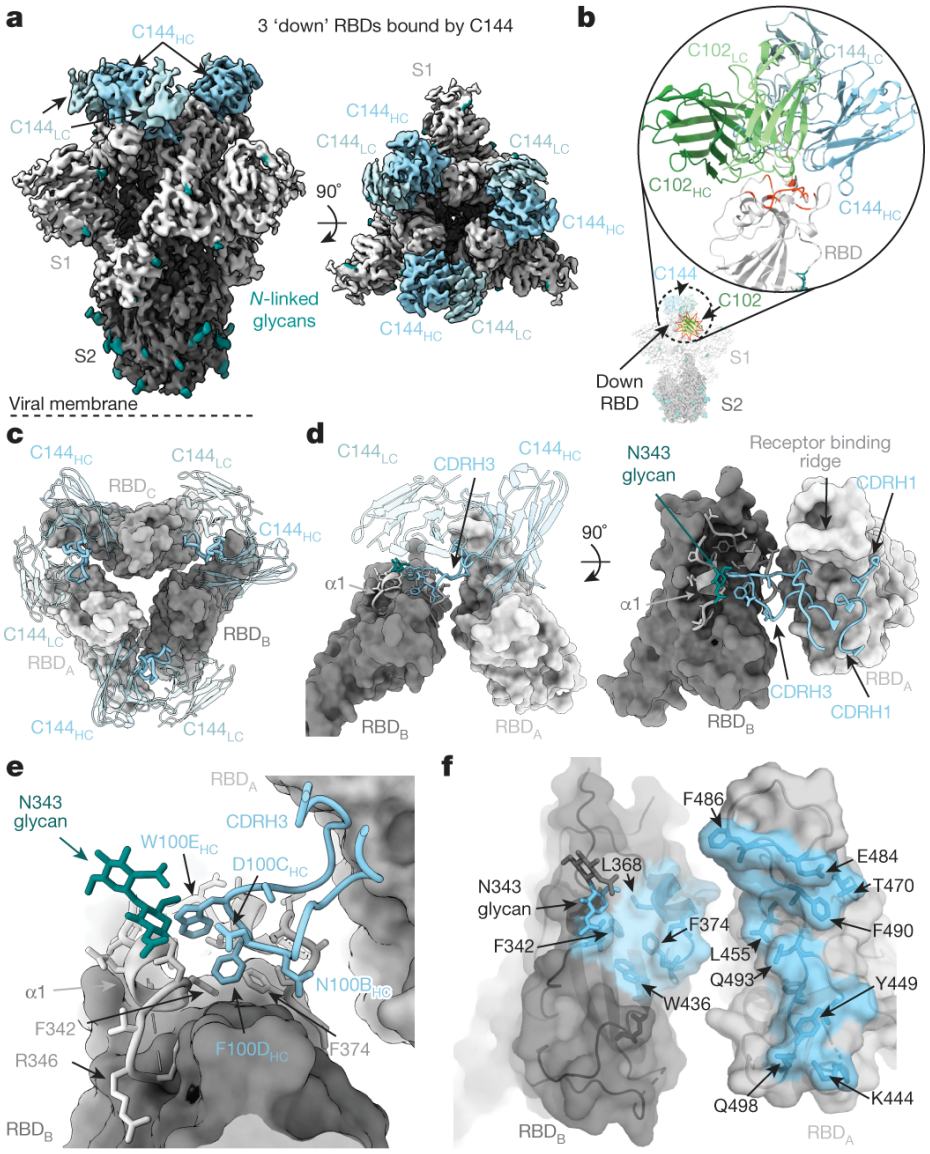

Fig. 1: Cryo-EM structure of the C144-S complex illustrates a distinct *VH3-53* Nab binding mode. a, 3.2 Å cryo-EM density for the C144–S trimer complex revealing C144 binding to a closed (three down RBDs) spike conformation. LC, light chain; HC, heavy chain. **b**, Overlay of C102 Fab (from C102–RBD crystal structure) (Extended Data Fig. 1) and C144 Fab (from C144–S structure) aligned on a RBD monomer. RBD residues corresponding to the ACE2 epitope (orange-red cartoon) are shown on the same RBD for reference. C144 adopts a distinct conformation relative to the C102-like *VH3-53*-encoded short CDRH3 NAb class, allowing binding to the down RBD conformation on trimeric spike, whereas C102-like NAbs can only bind to up RBDs. **c**, Quaternary epitope of C144 involving bridging between adjacent RBDs via the CDRH3 loop (illustrated as thicker ribbon). **d**, **e**, Close-up view of CDRH3-mediated contacts on adjacent protomer RBD (dark grey). C144 CDRH3 residues $F100_D$ and $W100_E$ are buried in a hydrophobic pocket comprising the RBD α1 helix, residue $F374_{RBD}$ and the $N343_{RBD}$ glycan. **f**, Surface representation of C144 epitope (light blue) across two adjacent RBDs. RBD epitope residues (defined as residues containing atom(s) within 4 Å of a Fab atom) are labelled in black.

CDRH2 contributions[39]. The epitopes on RBD for all available *VH3-53*-encoded short CDRH3 human NAbs span the ACE2-binding site[15,26,28,30,31] and show common RBD-binding interactions, represented by the C102 epitope (Extended Data Fig. 1b–e), which buried 1,017 Å^2 on RBD (Extended Data Fig. 2b). The ACE2-blocking epitope for these NAbs is sterically occluded in the RBD down conformation (Fig. 1b, Extended Data Fig. 1f); therefore, class 1 NAbs can only bind to up RBDs, as observed in the C105–S structure[26], and as previously discussed, IgGs in this class could crosslink adjacent RBDs within a single trimer to achieve tighter binding through avidity effects[26].

Class 2 Nabs recognize 'up' and 'down' RBDs

In addition to the recurrent *VH3-53*-encoded short CDRH3 NAb structures, a small subset of potently neutralizing *VH3-53*-encoded antibodies use longer CDRH3 regions[5, 12] (more than 15 residues, IMGT definition[32]) (Extended Data Fig. 1g). A recent structure of a RBD complexed with a *VH3-53*-encoded long CDRH3 human NAb (COVA2-39) revealed a different RBD binding mode[38], thus confirming predictions that binding with a C102-like interaction requires a short CDRH3[26,30]. To further determine molecular mechanisms for binding of *VH3-53*-encoded long CDRH3 human NAbs, we solved a 3.2 Å cryo-EM structure of C144 (encoded by the *VH3-53* and *VL2-14* gene segments; 25-residue CDRH3) bound to an S trimer[36] (Extended Data Fig. 3). Despite the ability of ligand-free stabilized S trimers to adopt up RBD conformations[36] and modelling suggesting the C144 binding site would be accessible on up RBDs (Fig. 1b), the C144–S structure revealed three C144 Fabs bound to a completely closed S with three down RBDs (Fig. 1a). The C144 binding mode differs from class 1 NAbs, the binding orientation of which is incompatible with down RBD conformations (Fig. 1b). In addition, the binding orientation observed for C144 differs from the binding described for COVA2-39, the RBD epitope of which is predicted to be accessible only on up RBDs[38] owing to steric hinderances imposed on the light chain by the $N343_{RBD}$-associated glycan on the adjacent RBD (Extended Data Fig. 1h). Despite differences in orientation, the RBD epitopes of C144, C102 and COVA2-39 overlap with the ACE2-binding site, which suggests a neutralization mechanism that involves direct competition with ACE2 (Fig. 1b).

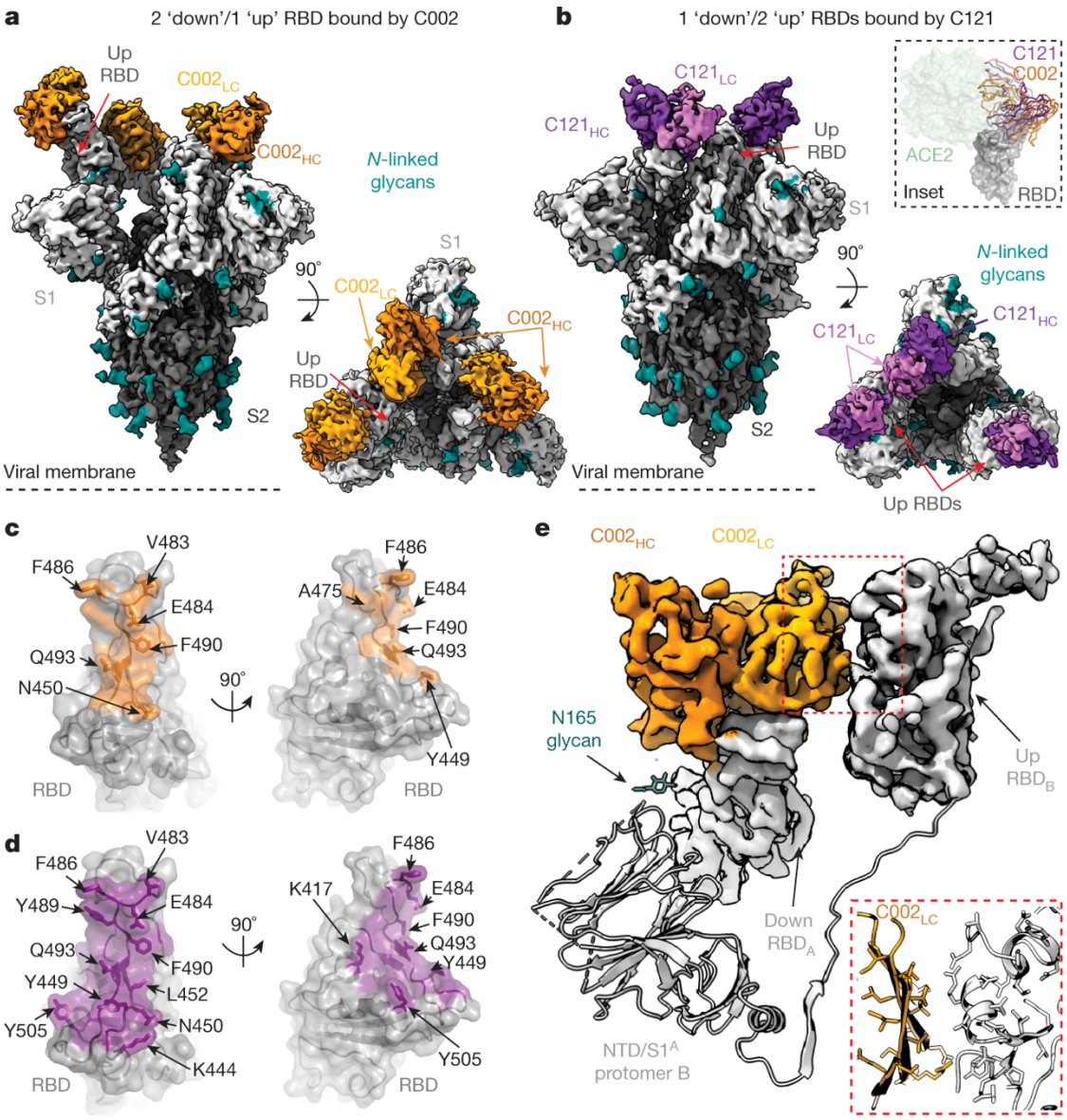

Fig. 2: Cryo-EM structures of class 2 C002 and C121 Nabs show binding to up and down RBDs. **a**, **b**, Cryo-EM densities for C002–S (**a**; 3.4 Å) and C121–S (**b**; 3.7 Å) complexes, revealing binding of C002 or C121 to both down and up RBDs. Inset, alignment of C002 and C121 Fabs on the same RBD. ACE2 is represented as a green surface for reference. **c**, **d**, Surface representations of C002 epitope (orange, **c**) and C121 epitope (purple, **d**) on the RBD surface (grey). RBD epitope residues (defined as residues containing atom(s) within 4 Å of a Fab atom) are labelled in black. **e**, C002 forms inter-protomer contacts via binding to an adjacent up RBD conformation on the surface of the trimer spike (also observed for class 2 C121–S, C119–S and C104–S structures) (Extended Data Fig. 5). Red box shows close-up of adjacent up RBD and C002 light-chain interface.

Despite overlapping with the ACE2-binding site on up RBDs, an interesting feature of C144 binding is that its long CDRH3 bridges between adjacent down RBDs to lock the spike glycoprotein into a closed, prefusion conformation, providing an additional neutralization mechanism in which S cannot open to engage ACE2 (Fig. 1c, d). The formation of the C144 quaternary epitope is driven by sandwiching CDRH3 residues $F100_D$ and $W100_E$ (in which subscripts denote numbering of the CDRH3 loop) into a hydrophobic RBD cavity at the base of an *N*-linked glycan attached to $N343_{RBD}$. The cavity comprises the RBD α1 helix (337–344), α2 helix (364–371), and hydrophobic residues ($F374_{RBD}$ and $W436_{RBD}$) at the edge of the RBD five-stranded β-sheet (Fig. 1e, f). In contrast to the CDRH3s of class 1 *VH3-53*-encoded short CDRH3 NAbs, the C144 CDRH3 contributed to most (approximately 60%) of the paratope and buried 330 $Å^2$ of surface area on the adjacent RBD (Extended Data Fig. 2b), rationalizing observed escape at $L455_{RBD}$ (Fig. 1f) in C144 selection experiments[40]. Despite adjacent CDRH3 hydrophobic residues ($F100_D$ and $W100_E$) likely to be solvent-exposed before antigen binding, C144 IgG showed no evidence of non-specific binding in a polyreactivity assay (Extended Data Fig. 1i).

Given the unusual binding characteristics of C144, we investigated whether antibodies that showed similar S binding orientations in low-resolution negative-stain electron microscopy reconstructions[5] use similar neutralization mechanisms. We characterized Fab–S cryo-EM structures (overall resolutions from 3.4 to 3.8 Å) of potent NAbs (C002, C104, C119 and C121) predicted to compete with ACE2 binding[5], which varied in their use of V gene segments and CDRH3 lengths (Fig. 2, Extended Data Figs. 3, 4, Extended Data Table 1). Fab–S cryo-EM structures of these class 2 NAbs showed bound RBDs in both up or down conformations, consistent with observations of similar human NAbs from negative-stain electron microscopy[5,12] and single-particle cryo-EM studies[10,34,41]. By contrast, the C144–S structure showed Fabs bound only to down RBDs (Fig. 1), which suggests that C144 binding requires recognition of the closed S trimer, or that C144 Fab(s) initially bound to up RBD(s) could trap the closed (three RBDs down) S conformation through CDRH3-mediated interactions between adjacent RBDs.

To understand commonalities of class 2 RBD epitopes better, we further analysed two additional potent human NAbs, C002 (encoded by *VH3-30* and *VK1-39* gene segments; 17-residue CDRH3, half-maximal inhibitory concentration (IC_{50}) = 8.0 ng ml^{-1})[5] and C121 (encoded by *VH1-2* and *VL2-23* gene segments; 23-residue CDRH3, IC_{50} = 6.7 ng ml^{-1})[5], for which cryo-EM Fab–S structures were solved to 3.4 Å and 3.6 Å, respectively (Fig. 2a, b), using crystal structures of unbound C002 and C121 Fabs for fitting (Supplementary Table 1). The C002 and C121 RBD epitopes are focused on the receptor-binding ridge, overlapping with polar and hydrophobic residues along the flat face of the RBD responsible for ACE2 interactions (Fig. 2c–e). Similar to C144, NAbs C002 and C121 buried most of their RBD epitopes against heavy-chain CDR loops, with light-chain CDR loops engaging the receptor-binding ridge (Fig. 3). Notably, Fab–S structures of C002, C121, C119 and C104 revealed a quaternary epitope involving an adjacent RBD (Extended Data Figs. 3, 4, 5a–c), albeit distinct from the quaternary binding of C144 (Fig. 1c–e). The C002/C121/C119/C104 type of secondary interaction was only observed when a Fab was bound to a down RBD and adjacent to an up RBD. The extent of secondary interactions varied depending on the antibody pose (Extended Data Fig. 5a–c). Bridging interactions between adjacent up and down RBDs would not allow the two Fabs of a single IgG to bind simultaneously to an S trimer. However, this class of antibodies could support bivalent interactions between two adjacent down RBDs (Extended Data Fig. 5h, Extended Data Table 1).

Characterization of the highest resolution interface (C002–S structure) showed C002 light-chain framework regions 1 and 2 (FWR1 and FWR2) interfaced with the RBD residues comprising the five-stranded β-sheet and α-helix that spans residues 440–444 (Fig. 2e), which is typically located near the three-fold axis of a closed S trimer. In addition to contacting neighbouring RBDs, inter-protomer engagement with the $N165_{NTD}$-associated glycan in the N-terminal domain (NTD) was observed for the class 2 NAb BD23[13]. If fully processed, the $N165_{NTD}$ glycan could adopt a conformation that would allow interactions with the heavy-chain FWR3 and CDRH1 (Fig. 2e). However, in the structures reported here, we did not observe $N165_{NTD}$ glycan density beyond the initial *N*-acetylglucosamine.

Given differences in class 2 human NAb V gene segments, CDRH3 lengths and antibody poses, we investigated sequence features that drive conserved interactions. Sequence differences between SARS-CoV-2 and SARS-CoV RBD, including at positions 486_{RBD} and 493_{RBD} (F and Q, respectively, in SARS-CoV-2), in the ACE2 receptor-binding motif allowed more favourable ACE2 binding to the SARS-CoV-2 RBD[42]. Analysis of interactions by C144, C002 and C121 revealed common interactions with these residues and also for

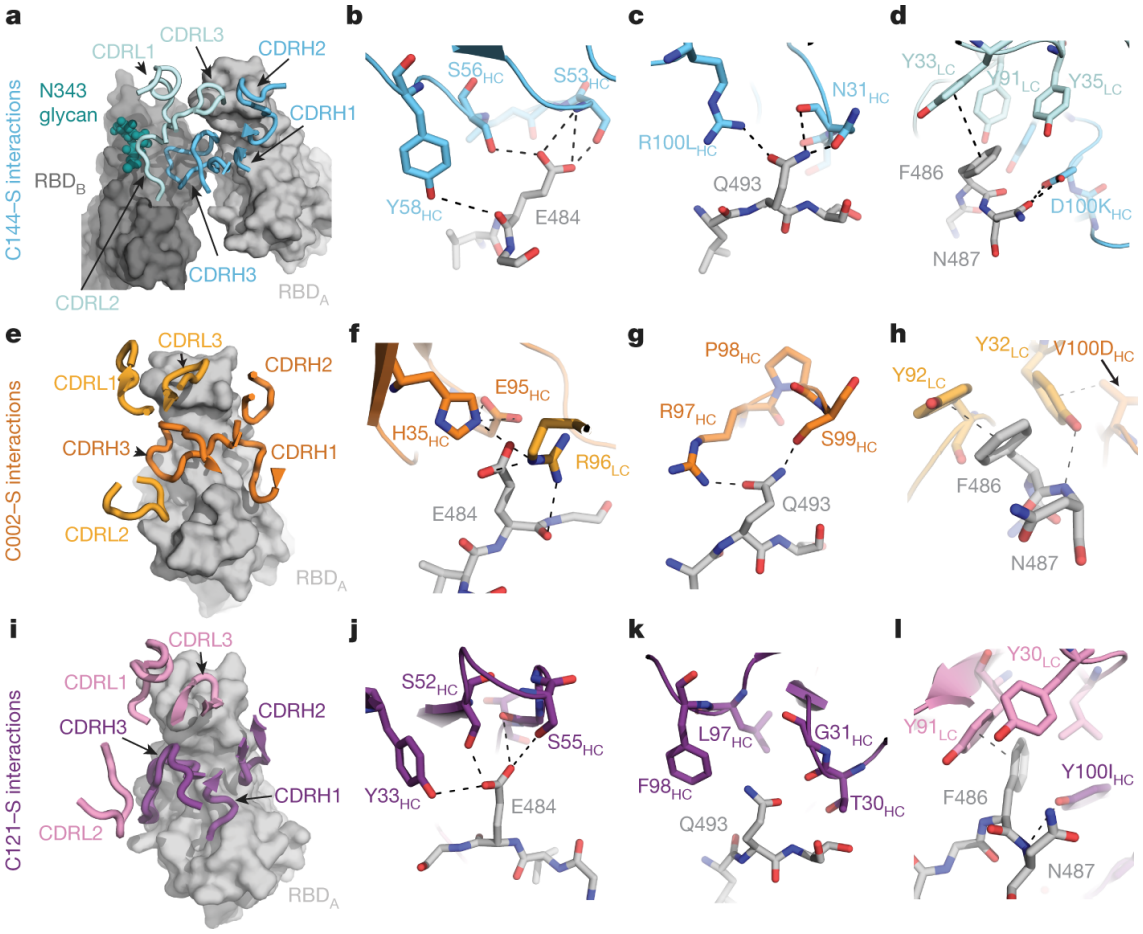

Fig. 3: Details of common RBD interactions among class 2 human Nabs.
a–**l**, Conserved interactions between the RBD and CDRs of class 2 NAbs as observed for C144 (HC, cyan; LC, sky blue) (**a**–**d**), C002 (HC, dark orange; LC, light orange) (**e**–**h**), and C121 (HC, purple; LC, pink) (**i**–**l**). Primary and secondary epitopes on adjacent down RBDs are shown for C144. Secondary epitopes for C002 and C121, which require adjacent up RBDs, are shown in Extended Data Fig. 5. RBDs are grey; potential hydrogen bonds and π–π stacking interactions (**d**, $Y33_{LC}$ and $F486_{RBD}$; **h**, $Y92_{LC}$ and $F486_{RBD}$; **l**, $Y91_{LC}$ and $F486_{RBD}$) are indicated by dashed lines.

$E484_{RBD}$ by both antibody heavy-chain and light-chain residues (Fig. 3). In particular, class 2 NAb interactions with $F486_{RBD}$ mimicked ACE2 interactions, in that $F486_{RBD}$ buries into a hydrophobic pocket typically involving CDRL1 or CDRL3 tyrosine residues[43] (Fig. 3d, h, l). Mimicking of the ACE2 F486 binding pocket by SARS-CoV-2 human NAbs was observed across different light-chain V gene segments (Extended Data Table 1), which suggests that there is no restriction in light-chain V gene segment usage for class 2 NAbs. Notably, a germline-encoded feature described for *VH3-53*-encoded short CDRH3 class 1 NAbs, the CDRH2 SXXS motif, is also found in other class 2 NAbs (for example, C121 and C119) despite different V_H gene segment usage. Similar to *VH3-53* NAbs C144 and COVA2-39, the C121 CDRH2 SXXS motif forms a potential hydrogen-bond network with $E484_{RBD}$ (Fig. 3b, j).

Overall, these results suggest a convergent mode of recognition by germline-encoded residues across diverse V_H/V_L gene segments for SARS-CoV-2, which may contribute to low levels of somatic hypermutation observed for these human NAbs (Extended Data Fig. 4i–n, Extended Data Table 1).

Class 3 Nabs bind outside the ACE2-binding site

C135 is a potent NAb that showed distinct binding properties from class 1, 2 and 4 NAbs, the latter of which bind a highly conserved buried epitope that is only accessible in up RBD conformations (Extended Data Table 1). To evaluate the mechanism of C135-mediated neutralization of SARS-CoV-2, we solved the cryo-EM structure of a C135–S complex to 3.5 Å (Fig. 4a, Extended Data Fig. 6), using an unbound C135 crystal structure for fitting (Supplementary Table 1). The structure revealed three C135 Fabs bound to an S trimer with two down and one up RBD, although the C135-bound up RBD conformation was weakly resolved and therefore not modelled. C135 recognizes a similar glycopeptidic epitope to the cross-reactive SARS-CoV NAb S309[34], focusing on a region of the RBD near the N343 glycan and non-overlapping with the ACE2-binding site (Fig. 4b, Extended Data Fig. 6c, d). Despite differences in binding orientations between C135 and S309, targeting of the RBD epitope was mainly V_H-mediated (the surface area buried by RBD on the C135 heavy chain

represented approximately 480 Å^2 of the 700 Å^2 total buried surface area) and included interactions with the core fucose moiety of the N343$_{RBD}$ glycan. The smaller C135 footprint relative to S309 (approximately 700 Å^2 versus 1,150Å^2 buried surface area, respectively) (Extended Data Fig. 6c, d) focused on interactions with R346$_{RBD}$ and N440$_{RBD}$, which are engaged by residues from heavy-chain and light-chain CDRs (Fig. 4c, d) and are not conserved between SARS-CoV-2 and SARS-CoV RBDs, rationalizing the lack of SARS-CoV cross-reactivity observed for C135[5].

The discovery of class 3 NAbs such as C135 and S309 that were raised during SARS-CoV-2 or SARS-CoV natural infections, respectively, and bind outside of the ACE2-binding site, provides the potential for additive neutralization effects when combined with NAbs that block ACE2, while also limiting viral escape[1,40]. A pair of antibodies in human clinical trials that includes REGN10987[8], a human NAb that binds distal to the ACE2-binding site, prevented SARS-CoV-2 viral escape in vitro, but did not show synergistic neutralization[6]. Comparison of C135 and REGN10987 interactions with S showed similarities in epitopes (interactions focused on R346$_{RBD}$ and N440$_{RBD}$) (Extended Data Fig. 7c, f). However, REGN10987 binding would sterically hinder ACE2 interactions, whereas C135 binding does not (Fig. 4b, Extended Data Fig. 6b). Notably, a structure of S complexed with C110 (encoded by the *VH5-51* and *VK1-5* gene segments), isolated from the same donor as the C102 and C105 (class 1) and C119 and C121 (class 2) NAbs[5], showed a binding pose that resembled that of REGN10987 (Extended Data Fig. 6b, e, f). The C110 epitope showed similarities with both class 3 and class 2 NAbs, binding distal to the ACE2-binding motif, but like REGN10987, could potentially sterically interfere with ACE2 (Extended Data Fig. 7). For each of these class 3 NAbs, the Fab binding pose suggests that inter-protomer crosslinking by a single IgG is not possible (Extended Data Table 1).

Class 3 human NAbs add to the anti-SARS-CoV-2 antibody repertoire and could probably be effectively used in therapeutic combinations with class 1 or 2 NAbs. However, when using structures to predict whether NAbs have overlapping epitopes, it is sometimes not

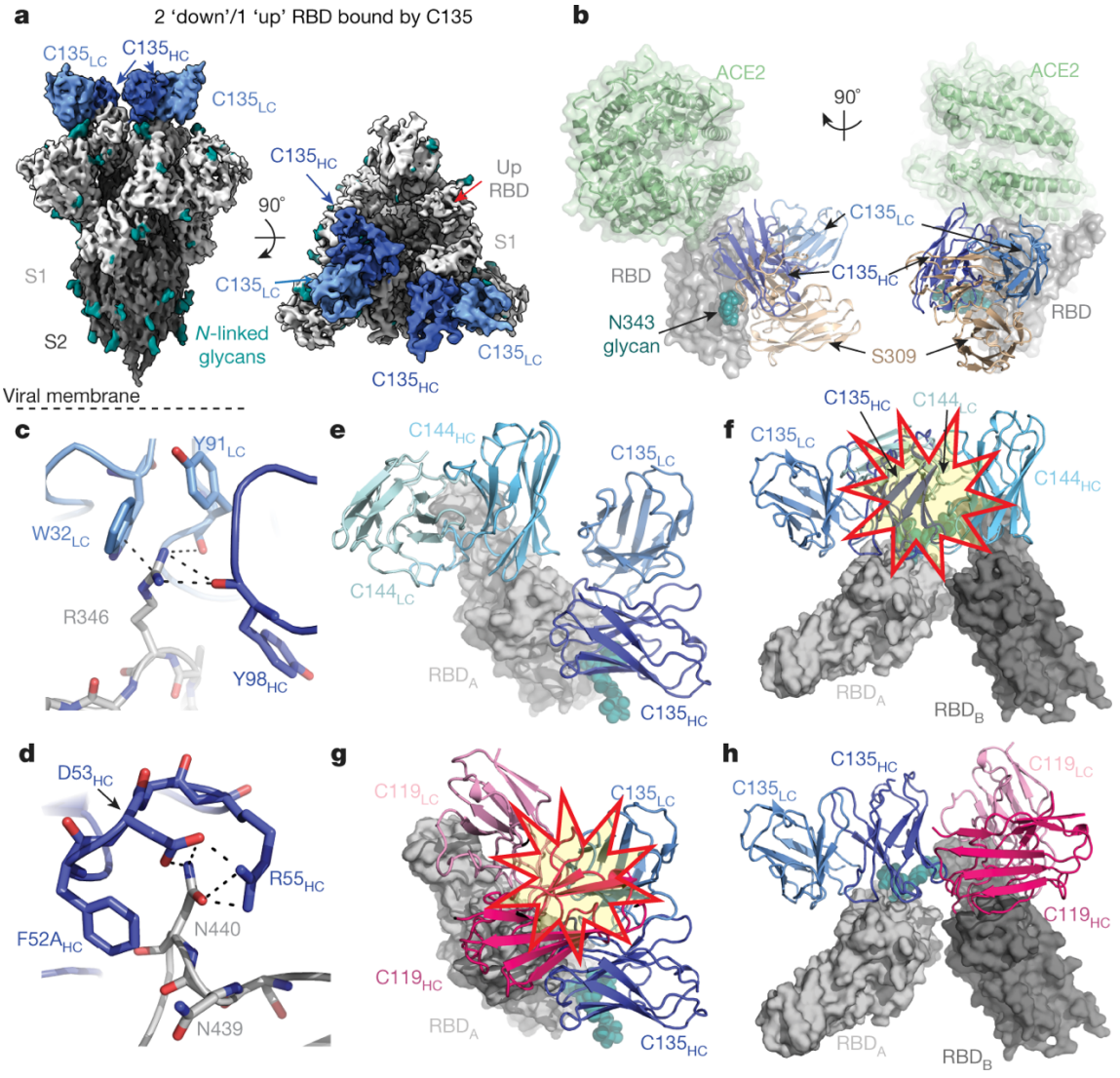

Fig. 4: Cryo-EM structure of S complexed with the class 3 (non-ACE2 blocking) human Nab C135.

a, 3.5 Å cryo-EM density of C135–S complex. **b**, Composite model of C135–RBD (blue and grey, respectively) overlaid with the SARS-CoV-2 NAb S309 (sand; PDB code 6WPS) and soluble ACE2 (green; PDB code 6M0J). The model was generated by aligning on 188 RBD Cα atoms. **c**, **d**, C135 CDRH (dark blue) and CDRL (light blue) interactions with $R346_{RBD}$ (**c**) and $N440_{RBD}$ (**d**). Potential π–π stacking interactions (**c**) and hydrogen bonds (**c**, **d**) are illustrated by dashed black lines. **e**, **f**, Model of RBD interactions of NAbs C135 (class 3) and C144 (class 2), demonstrating that both Fabs can bind simultaneously to a single monomeric RBD (**e**), but would clash if bound to adjacent down RDBs on S trimer (**f**). Steric clashes indicated by a red and yellow star in **f**. **g**, **h**, Model of RBD interaction of NAbs C135 (class 3) and C119 (class 2) demonstrating that both Fabs cannot bind simultaneously to a single monomeric RBD (**g**), but do not clash if bound to adjacent down RDBs on S trimer (**h**). Steric clashes indicated by a red and yellow star in **g**.

sufficient to only examine Fab–RBD structures or even static images of the S trimer because of the dynamic nature of the spike. Thus, what might appear to be non-overlapping epitopes on an isolated RBD could overlap in some (Fig. 4e, f), but not all (Extended Data Fig. 7), scenarios on a spike trimer, complicating interpretation of competition experiments using monomeric RBDs and S trimers. The opposite can also be true; that is, two Fabs predicted to be accommodated on a trimer could clash on an RBD monomer (Fig. 4g, h). Finally, adjacent monomers in different orientations could accommodate different antibodies that target overlapping sites (Extended Data Fig. 7).

RBD substitutions affect NAb binding

Vesicular stomatitis virus (VSV) reporter viruses pseudotyped with the SARS-CoV-2 S protein can escape by mutation(s) from the C121, C135 or C144 NAbs[40] that we used for structural studies. RBD mutations that were selected in response to antibody pressure correlated with the epitopes mapped from the structures of their Fabs complexed with the S trimer (Figs. 1, 2, 4).

To further assess the effects of these mutations and other RBD substitutions, we assayed NAbs for which we obtained structural information (eight from this study; C105–S complex previously described[26]) for binding to mutated RBD proteins. The RBD mutants included two that induced escape from the class 3 NAb C135 (R346S and N440K)[40] (Fig. 4c, d), one found in circulating isolates[44] that conferred partial resistance to C135 (N439K)[40] (Fig. 4d), a circulating variant (A475V) that conferred resistance to class 1 and 2 *VH3-53* NAbs[44], two that induced escape from C121 or C144 (E484K and Q493R)[40] (Fig. 3), and a circulating variant that conferred partial resistance to C121 (V483A)[40]. Kinetic and equilibrium constants for the original and mutant RBDs were derived from surface plasmon resonance (SPR) binding assays in which RBDs were injected over immobilized IgGs. Loss of binding affinity was consistent with RBD mutations that conferred escape (Extended Data Fig. 8). Comparing effects of point mutations between NAb classes showed that point mutations leading to a loss of binding for NAbs within one class did not affect NAbs in a different class, indicating that antibody pressure that leads

to escape from one NAb class would be unlikely to affect a different class. These results suggest a therapeutic strategy involving human NAbs of different classes for monoclonal NAb treatment of individuals infected with SARS-CoV-2.

Conclusions

Here we report structural, biophysical and bioinformatics analyses of SARS-CoV-2 NAbs (Extended Data Fig. 9), providing information for interpreting correlates of protection for clinical use. The structures reveal a wealth of unexpected interactions of NAbs with the spike protein, including five antibodies that reach between adjacent RBDs on the protomers of a single trimer. A notable example of bridging between spike protomers involved the human C144 NAb that uses a long CDRH3 with a hydrophobic tip to reach across to an adjacent RBD, resulting in all three RBDs on the spike trimer being locked into a closed conformation. This example, and four other NAbs that contact adjacent RBDs, demonstrates that crystal structures of Fab–monomeric RBD complexes, although informative for defining primary epitopes on one RBD, do not reveal how antibodies recognize the flexible up or down RBD conformations on the spike trimer that are targeted for neutralization on a virus. Indeed, our cryo-EM structures of Fab–spike trimer complexes showed all possible up and down combinations of recognized RBDs, with structures showing either three or two Fabs bound per trimer. By analysing approach angles of Fabs bound to RBDs on spike trimers, we predicted whether an IgG can bind to a single spike trimer to gain potency through avidity, which would also render the antibody more resistant to spike mutations. In addition, structural information allowed us to assess RBD mutants that arose in circulating viral isolates and/or were obtained by in vitro selection. Together, this study provides a blueprint for the design of antibody cocktails for therapeutic agents and potential spike-based immunogens for vaccines.

Methods

No statistical methods were used to predetermine sample size. The experiments were not randomized, and investigators were not blinded to allocation during experiments and outcome assessment.

Cell lines

Expi293F cells (GIBCO) for protein expression were maintained at 37 °C and 8% CO_2 in Expi293 Expression medium (GIBCO), transfected using Expi293 Expression System Kit (GIBCO) and maintained under shaking at 130 rpm. Cell lines were not specifically authenticated, but lines tested negative for contamination with mycoplasma.

Protein expression

Expression and purification of SARS-CoV-2 ectodomains were conducted as previously described[26]. In brief, constructs encoded the SARS-CoV-2 S ectodomain (residues 16–1206 of the early SARS-CoV-2 GenBank MN985325.1 sequence isolate with 2P[35] or 6P[36] stabilizing mutations, a mutated furin cleavage site between S1 and S2, a C-terminal TEV site, foldon trimerization motif, octa-His tag, and AviTag) were used to express soluble SARS-CoV-2 S ectodomains. Constructs encoding the SARS-CoV-2 RBD from GenBank MN985325.1 (residues 331–524 with C-terminal octa-His tag and AviTag) and mutant RBDs were made as described[26], SARS-CoV-2 2P S, 6P S, and RBD proteins were purified from the supernatants of transiently transfected Expi293F cells (Gibco) by nickel affinity and size-exclusion chromatography[26]. Peak fractions were identified by SDS–PAGE, and fractions corresponding to S trimers or monomeric RBDs were pooled and stored at 4 °C. Fabs and IgGs were expressed, purified, and stored as previously described[45,46].

X-ray crystallography

Crystallization trials were carried out at room temperature using the sitting drop vapour diffusion method by mixing equal volumes of a Fab or Fab–RBD complex and reservoir using a TTP LabTech Mosquito robot and commercially available screens (Hampton Research). Crystals were obtained in 0.2 M ammonium sulfate, 20% (w/v) PEG 3350 (C102 Fab), 0.2 M sodium citrate tribasic, 20% (w/v) PEG 3350 (C102–RBD), 0.2 M lithium sulfate monohydrate, 20% (w/v) PEG 3350 (C002 Fab), 0.04 M potassium phosphate, 16% (w/v) PEG 8000, 20% (v/v) glycerol (C135 Fab), 0.2 M ammonium citrate pH 5.1, 20% PEG 3350 (C121 Fab), or 0.2 M sodium tartrate dibasic dihydrate pH 7.3, 20% (w/v) PEG 3350 (C110 Fab). A C135 Fab crystal was directly looped and

cryopreserved in liquid nitrogen. Other crystals were quickly cryoprotected in a mixture of well solution with 20% glycerol and then cryopreserved in liquid nitrogen.

X-ray diffraction data were collected for Fabs and the Fab–RBD complex at the Stanford Synchrotron Radiation Lightsource (SSRL) beamline 12-1 on a Eiger X 16 M pixel detector (Dectris) at a wavelength of 1.0 Å. Data from single crystals of C121 Fab and C110 Fab were indexed and integrated in XDS[47] and merged using AIMLESS v.0.7.4 in *CCP4*[48] v.7.0.6 (Supplementary Table 1). Data from single crystals of C102 Fab, C135 Fab and C002 Fab were indexed and integrated using XDS[47] and merged in Phenix[49] (v.1.18). Data from a single crystal of C102 Fab–RBD complex were indexed and integrated using XIA2[50] v.0.3.8 implementing DIALS[51,52] v.2.2 and merged using AIMLESS in *CCP4*[48]. For C110 Fab and C121 Fabs, structures were determined by molecular replacement in PHASER[53] v.2.8.2 using the coordinates for B38 (PDB 7BZ5) or an inferred germline form of the HIV-1 NAb IOMA[54] inferred germline (unpublished), respectively, after removing CDR loops as a search model. For C002 Fab, C102 Fab, C102 Fab–RBD and C135 Fab, structures were determined by molecular replacement in PHASER[53] using B38 Fab coordinates (PDB 7BZ5) after trimming heavy and light chain variable domains using Sculptor[55] v.2.0 (and for the C102 Fab–RBD data, also RBD coordinates from PDB code 7BZ5) as search models. Coordinates were refined using Phenix[49] and cycles of manual building in Coot[56] (Supplementary Table 1).

Cryo-EM sample preparation

Purified Fabs were mixed with the SARS-CoV-2 S 2P trimer[35] or SARS-CoV-2 S 6P trimer[36] (1.1:1 molar ratio Fab per protomer) to a final Fab–S complex concentration of 2–3 mg ml^{-1} and incubated on ice for 30 min. Immediately before deposition of 3 µl of complex onto a 300 mesh, 1.2/1.3 UltrAuFoil grid (Electron Microscopy Sciences) that had been freshly glow-discharged for 1 min at 20 mA using a PELCO easiGLOW (Ted Pella), a 0.5% (w/v) octyl-maltoside, fluorinated solution (Anatrace) was added to each sample to a final concentration of 0.02%. Samples were vitrified in 100% liquid ethane

using a Mark IV Vitrobot (Thermo Fisher) after blotting at 22 °C and 100% humidity for 3 s with Whatman No. 1 filter paper.

Cryo-EM data collection and processing

Single-particle cryo-EM data were collected on a Titan Krios transmission electron microscope (Thermo Fisher) operating at 300 kV for all Fab–S complexes except for C144–S, which was collected on a Talos Arctica (Thermo Fisher) operating at 200 kV. Movies were collected using SerialEM v.3.7 automated data collection software[57] with beam-image shift over a 3-by-3 pattern of 1.2 μm holes with 1 exposure per hole. Movies were recorded in super-resolution mode on a K3 camera (Gatan) for the C144–S dataset on the Arctica (0.435Å per pixel) or on a K3 behind BioQuantum energy filter (Gatan) with a 20 eV slit on the Krios (0.418 Å per pixel) for all other datasets. Data collections parameters are summarized in Supplementary Table 2. In general, the data- processing workflow described below was performed for all datasets in cryoSPARC v.2.15[58].

Cryo-EM movies were patch motion corrected for beam-induced motion including dose weighting within cryoSPARC[58] after binning super-resolution movies. The non-dose-weighted images were used to estimate CTF parameters using CTFFIND4[59] v.4.1.14 or with cryoSPARC implementation of the Patch CTF job, and micrographs with power spectra that showed poor CTF fits or signs of crystalline ice were discarded. A subset of images was randomly selected and used for reference-free particle picking using Blob picker in cryoSPARC[58]. Particles were subjected to 2D classification and the best class averages that represented different views were used to generate 3 ab initio models. The particles from the best classes were used in another 2D classification job, and the best set of unique views was used as templates for particle picking on the full set of images. Initial particle stacks were extracted, downsampled twice, and used in heterogeneous refinement against the three ab initio volumes generated with the smaller dataset (ab initio volumes used were interpreted as a Fab–S complex, free Fab or dissociated S protomers, and junk/noise class). Particles assigned to the Fab–S volume were further cleaned via iterative rounds of 2D classification to select class averages that displayed unique views and

secondary structural elements. Resulting particle stacks were homogenously refined before being split into nine individual exposure groups based upon collection holes. Per particle CTF and aberration corrections were performed and the resulting particles further 3D refined. Additional processing details are summarized in Supplementary Table 2.

Given the known heterogeneity of spike trimers[20,21], homogenously refined particles were used for 3D classification in cryoSPARC[58] (ab initio job: $k = 4$ classes, class similarity = 0.3). This typically resulted in one or two majority Fab–S complexes, with the other minority populated classes representing junk or unbound S trimer. Particles from the good class(es) were further subjected to 3D classification (ab initio job: $k = 4$, class similarity = 0.7) to attempt to separate various Fab–S complex states. If several states were identified (as observed for the C002–S and C121–S complexes), particles were heterogeneously refined, followed by re-extraction without binning (0.836 Å per pixel) before homogeneous refinement of individual states. For all other datasets, most particles represented one state that was homogenously refined after re-extraction without binning.

Particle stacks for individual states were non-uniform refined with *C*1 symmetry and a dynamic mask. To improve resolution at the Fab–RBD interfaces, volumes were segmented in Chimera[60] and the regions corresponding to the NTD and RBD domains of the S1 subunit and the Fab V_H–V_L domains were extracted and used to generate a soft mask (5-pixel extension, 10-pixel soft cosine edge). Local refinements with the mask resulted in modest improvements of the Fab–RBD interface, which allowed for fitting and refinement of this region. The particles were then subjected to CTF refinement and aberration correction, followed by a focused, non-uniform refinement with polished particles imposing *C*1 symmetry (except for the C144–S complex, in which *C*3 symmetry was used). Final overall resolutions were according to the gold-standard FSC[61]. Details of overall resolution and locally refined resolutions according to the gold-standard FSC[61] can be found in Supplementary Table 2.

Cryo-EM structure modelling and refinement

Coordinates for initial complexes were generated by docking individual chains from reference structures into cryo-EM density using UCSF Chimera[62] v.1.13. The following coordinates were used: SARS-CoV-2 S trimers: PDB codes 6VXX, 6VYB and 6XKL, up RBD conformations: PDB codes 7BZ5 or 6W41, and unbound C102, C002, C110, C121, C135 Fab structures (this study) (Supplementary Table 1). Initial models were then refined into cryo-EM maps using one round of rigid body refinement followed by real space refinement. Sequence-updated models were built manually in Coot[56] v.0.8.9 and then refined using iterative rounds of refinement in Coot[56] and Phenix[49]. Glycans were modelled at potential *N*-linked glycosylation sites in Coot[56] using 'blurred' maps processed with a variety of B-factors[63]. Validation of model coordinates was performed using MolProbity[64] (Supplementary Table 2).

Structural analyses

CDR lengths were calculated based on IMGT definitions[32]. Structure figures were made with PyMOL (v.2.2 Schrodinger, LLC) or UCSF ChimeraX[60] v.1.0. Local resolution maps were calculated using cryoSPARC v.2.15[58]. Buried surface areas were calculated using PDBePISA v.1.48[65] and a 1.4 Å probe. Potential hydrogen bonds were assigned as interactions that were less than 4.0 Å and with an A-D-H angle above 90°. Potential van der Waals interactions between atoms were assigned as interactions that were less than 4.0 Å. Hydrogen bond and van der Waals interaction assignments are tentative due to resolution limitations. r.m.s.d. calculations following pairwise Cα alignments were done in PyMOL without rejecting outliers. Criteria for epitope assignments are described in figure legends.

To evaluate whether intra-spike crosslinking by an IgG binding to a single spike trimer was possible (Extended Data Table 1), we first measured the Cα distance between a pair of residues near the C termini of adjacent Fab C_H1 domains (residue 222 of the heavy chain on each Fab) (Extended Data Fig. 5h). We compared this distance to the analogous

distances in crystal structures of intact IgGs (42 Å, PDB code 1HZH; 48 Å, PDB code 1IGY; 52 Å, PDB code 1IGT). To account for potential influences of crystal packing in these measurements, as well as flexibility in the V_H–V_L/C_H1–C_L elbow bend angle and uncertainties in C_H1–C_L domain placement in Fab–S cryo-EM structures, we set a cut-off of ≤65 Å for this measured distance as possibly allowing for a single IgG to include both Fabs. Entries in the 'potential IgG intra-spike binding' column in Extended Data Table 1 are marked 'no' if all of the adjacent Fabs in cryo-EM classes of that structure are separated by more than 65 Å for this measured distance. Entries in the 'potential IgG intra-spike binding' column in Extended Data Table 1 are marked as 'yes' if at least one pair of the adjacent Fabs in cryo-EM classes of that structure are separated by ≤65 Å for this measured distance.

SPR binding experiments

SPR experiments were performed using a Biacore T200 instrument (GE Healthcare). IgGs were immobilized on a CM5 chip by primary amine chemistry (Biacore manual) to a final response level of approximately 3,000 resonance units. Concentration series of the original SARS-CoV-2 RBD and RBD mutants (six fourfold dilutions starting from a top concentration of 1,000 nM) were injected at a flow rate of 30 µl min over immobilized IgGs for a contact time of 60 s, followed by an injection of 0.01 M HEPES, pH 7.4, 0.15 M NaCl, 3 mM EDTA, 0.005% (v/v) surfactant P20 buffer for a dissociation time of 300 s. Binding reactions were allowed to reach equilibrium, and K_d values were calculated from the ratio of association and dissociation rates ($K_d = k_d/k_a$) derived from a 1:1 binding model (C002, C102, C105, C110 and C119 (except for C119 mutant E484K)), C121, C135 and C144), or from a two-state binding model ($K_d = k_d1/k_a1 \times k_d2/[k_d2 + k_a2]$) (C104 and C119 mutant E484K). Kinetic constants were calculated using Biacore T200 Evaluation Software v.3.2 using a global fit to all curves in each dataset. Flow cells were regenerated with 10 mM glycine, pH 2.0, at a flow rate of 90 µl min^{-1}.

Polyreactivity assays

IgGs were evaluated for off-target interactions by measuring binding to baculovirus extracts containing non-specific proteins and lipids as described[59]. The assays were automated on a Tecan Evo2 liquid handling robot fitted with a Tecan Infinite M1000 plate reader capable of reading luminescence. Maxisorb 384-well plates (Nunc) were adsorbed overnight with a 1% preparation of recombinant baculovirus particles generated in Sf9 insect cells[66]. The adsorbed plate was blocked with 0.5% bovine serum albumin (BSA) in PBS, then incubated with 20 μL of a 1.0 μg ml^{-1} solution of IgG in PBS for 3 h. Polyreactivity was quantified by detecting bound IgG using an HRP-conjugated anti-human IgG secondary antibody (SouthernBiotech) at a 1:5,000 dilution and SuperSignal ELISA Femto Maxiumum Sensitivity Substrate (Thermo Scientific). RLUs were measured at 475 nm in the integrated plate reader. Engineered human anti-HIV-1 IgGs previously demonstrated to exhibit high levels of polyreactivity (NIH45-46(G54W) and 45-46m2)[60,61] were used as positive controls. NIH45-46, which exhibited intermediate polyreactivity[62], was also evaluated for comparisons. Negative control IgGs with low polyreactivity included the human HIV-1 antibodies N6[63] and 3BNC117[62] and BSA. RLU values were plotted in GraphPad Prism v8.4.3 and presented as the mean and standard deviation of triplicate measurements ($n = 3$ biological replicates) with results for individual experiments shown as circles in Extended Data Fig. 1i.

Reporting Summary

Further information on research design is available in the Nature Research Reporting Summary linked to this paper.

Data availability

The atomic models generated from X-ray crystallographic studies of the C102–RBD complex, C102 Fab, C002 Fab, C110 Fab, C121 Fab and C135 Fab have been deposited at the Protein Data Bank (PDB) under accession codes 7K8M, 7K8N, 7K8O, 7K8P, 7K8Q

and 7K8R, respectively. The atomic models and cryo-EM maps generated from cryo-EM studies of the C002–S 2P (state 1), C002–S 2P (state 2), C104–S 2P, C110–S 2P, C119–S 2P, C121–S 2P (state 1), C121–S 2P (state 2), C135–S 2P and C144–S 6P complexes have been deposited at the PDB and the Electron Microscopy Data Bank (EMDB) under the following accession codes: PDB 7K8S, 7K8T, 7K8U, 7K8V, 7K8W, 7K8X, 7K8Y, 7K8Z and 7K90; EMD EMD-22729, EMD-22730, EMD-22731, EMD-22372, EMD-22733, EMD-22734, EMD-22735, EMD-22736 and EMD-22737.

Acknowledgements

We thank J. Vielmetter, P. Hoffman, and the Protein Expression Center in the Beckman Institute at Caltech for expression assistance, J. Vielmetter and J. Keeffe for setting up automated polyreactivity assays, J. Keeffe for construct design, and N. Koranda for help with cloning and protein purification. Electron microscopy was performed in the Caltech Beckman Institute Resource Center for Transmission Electron Microscopy with assistance from S. Chen. We thank the Gordon and Betty Moore and Beckman Foundations for gifts to Caltech to support the Molecular Observatory (J. Kaiser, director), and S. Russi, A. Cohen and C. Smith and the beamline staff at SSRL for data collection assistance. Use of the Stanford Synchrotron Radiation Lightsource, SLAC National Accelerator Laboratory, is supported by the US Department of Energy, Office of Science, Office of Basic Energy Sciences under contract no. DE-AC02-c76SF00515. The SSRL Structural Molecular Biology Program is supported by the DOE Office of Biological and Environmental Research, and by the National Institutes of Health, National Institute of General Medical Sciences (P41GM103393). The contents of this publication are solely the responsibility of the authors and do not necessarily represent the official views of NIGMS or NIH. This work was supported by NIH grant P01-AI138938-S1 (P.J.B. and M.C.N.), the Caltech Merkin Institute for Translational Research (P.J.B.), NIH grant P50 8 P50 AI150464-13 (P.J.B.), and a George Mason University Fast Grant (P.J.B.). C.O.B was supported by the Hanna Gray Fellowship Program from the Howard Hughes Medical Institute and the Postdoctoral Enrichment Program from the Burroughs Wellcome Fund. M.C.N. is a Howard Hughes Medical Institute Investigator.

Author contributions

C.O.B., M.C.N., A.P.W., and P.J.B. conceived the study and analyzed data; D.F.R. and M.C.N. provided monoclonal antibody sequences and plasmids derived from COVID-19 convalescent donors. C.O.B. and K.H.T. performed protein purifications and C.O.B. assembled complexes for cryo-EM and X-ray crystallography studies. C.O.B. performed cryo-EM and interpreted structures with assistance from M.A.E., K.A.D, S.R.E., A.G.M., and N.G.S. C.A.J. and C.O.B. performed and analyzed crystallographic structures, with refinement assistance from M.A.E and K.M.D. Y.E.L. performed polyreactivity assays. H.B.G. performed and analyzed SPR experiments. A.P.W. analyzed antibody sequences. C.O.B., M.C.N., A.P.W., and P.J.B. wrote the paper with contributions from other authors.

References

1. Baum, A. et al. REGN-COV2 antibody cocktail prevents and treats SARS-CoV-2 infection in rhesus macaques and hamsters. Science https://doi.org/10.1126/science.abe2402 (2020).

2. Baum, A. et al. Antibody cocktail to SARS-CoV-2 spike protein prevents rapid mutational escape seen with individual antibodies. Science **369**, 1014–1018 (2020).

3. Rogers, T. F. et al. Isolation of potent SARS-CoV-2 neutralizing antibodies and protection from disease in a small animal model. *Science* **369**, 956–963 (2020).

4. Zost, S. J. et al. Potently neutralizing and protective human antibodies against SARS-CoV-2. *Nature* **584**, 443–449 (2020).

5. Robbiani, D. F. et al. Convergent antibody responses to SARS-CoV-2 in convalescent individuals. *Nature* **584**, 437–442 (2020).

6. Hansen, J. et al. Studies in humanized mice and convalescent humans yield a SARS-CoV-2 antibody cocktail. *Science* **369**, 1010–1014 (2020).

7. US National Library of Medicine. A study of LY3819253 (LY-CoV555) in preventing SARS-CoV-2 infection and COVID-19 in nursing home residents and staff (BLAZE-2). ClinicalTrials.gov https://clinicaltrials.gov/ct2/show/NCT04497987 (2020).

8. NIH. Clinical trials of monoclonal antibodies to prevent COVID-19 now enrolling. https://www.nih.gov/news-events/news-releases/clinical-trials-monoclonal-antibodies-prevent-covid-19-now-enrolling (2020).

9. Yuan, M. et al. A highly conserved cryptic epitope in the receptor binding domains of SARS-CoV-2 and SARS-CoV. *Science* **368**, 630–633 (2020).

10. Liu, L. et al. Potent neutralizing antibodies against multiple epitopes on SARS-CoV-2 spike. *Nature* **584**, 450–456 (2020).

11. Kreye, J. et al. A SARS-CoV-2 neutralizing antibody protects from lung pathology in a COVID-19 hamster model. Preprint at https://doi.org/10.1101/2020.08.15.252320 (2020).

12. Brouwer, P. J. M. et al. Potent neutralizing antibodies from COVID-19 patients define multiple targets of vulnerability. *Science* **369**, 643–650 (2020).

13. Cao, Y. et al. Potent neutralizing antibodies against SARS-CoV-2 identified by high-throughput single-cell sequencing of convalescent patients' B cells. *Cell* **182**, 73–84 (2020).

14. Kreer, C. et al. Longitudinal isolation of potent near-germline SARS-CoV-2-neutralizing antibodies from COVID-19 patients. *Cell* **182**, 843–854 (2020).
15. Shi, R. et al. A human neutralizing antibody targets the receptor-binding site of SARS-CoV-2. *Nature* **584**, 120–124 (2020).

16. Zost, S. J. et al. Rapid isolation and profiling of a diverse panel of human monoclonal antibodies targeting the SARS-CoV-2 spike protein. *Nat. Med*. **26**, 1422–1427 (2020).

17. Seydoux, E. et al. Analysis of a SARS-CoV-2-infected individual reveals development of potent neutralizing antibodies with limited somatic mutation. *Immunity* **53**, 98–105 (2020).

18. Hoffmann, M. et al. SARS-CoV-2 cell entry depends on ACE2 and TMPRSS2 and is blocked by a clinically proven protease inhibitor. *Cell* **181**, 271–280 (2020).

19. Wang, Q. et al. Structural and functional basis of SARS-CoV-2 entry by using human ACE2. *Cell* **181**, 894–904 (2020).

20. Walls, A.C. et al. Structure, function, and antigenicity of the SARS-CoV-2 spike glycoprotein. *Cell* **181**, 281–292 (2020).

21. Wrapp, D. et al. Cryo-EM structure of the 2019-nCoV spike in the prefusion conformation. *Science* **367**, 1260–1263 (2020).

22. Walls, A. C. et al. Cryo-electron microscopy structure of a coronavirus spike glycoprotein trimer. *Nature* **531**, 114–117 (2016).

23. Yuan, Y. et al. Cryo-EM structures of MERS-CoV and SARS-CoV spike glycoproteins reveal the dynamic receptor binding domains. *Nat. Commun*. **8**, 15092 (2017).

24. Kirchdoerfer, R. N. et al. Pre-fusion structure of a human coronavirus spike protein. *Nature* **531**, 118–121 (2016).

25. Li, Z. et al. The human coronavirus HCoV-229E S-protein structure and receptor binding. *eLife* **8**, e51230 (2019).

26. Barnes, C.O. et al. Structures of human antibodies bound to SARS-CoV-2 spike reveal common epitopes and recurrent features of antibodies. *Cell* **182**, 828–842 (2020).

27. Ju, B. et al. Human neutralizing antibodies elicited by SARS-CoV-2 infection. *Nature* **584**, 115–119 (2020).

28. Wu, Y. et al. A noncompeting pair of human neutralizing antibodies block COVID-19 virus binding to its receptor ACE2. *Science* **368**, 1274–1278 (2020).

29. Chi, X. et al. A neutralizing human antibody binds to the N-terminal domain of the Spike protein of SARS-CoV-2. *Science* **369**, 650–655 (2020).

30. Yuan, M. et al. Structural basis of a shared antibody response to SARS-CoV-2. *Science* **369**, 1119–1123 (2020).

31. Hurlburt, N. K. et al. Structural basis for potent neutralization of SARS-CoV-2 and role of antibody affinity maturation. Preprint at https://doi.org/10.1101/2020.06.12.148692 (2020).

32. Lefranc, M. P. et al. IMGT®, the international ImMunoGeneTics information system® 25 years on. *Nucleic Acids Res*. **43**, D413–D422 (2015).

33. Briney, B., Inderbitzin, A., Joyce, C. & Burton, D. R. Commonality despite exceptional diversity in the baseline human antibody repertoire. *Nature* **566**, 393–397 (2019).

34. Pinto, D. et al. Cross-neutralization of SARS-CoV-2 by a human monoclonal SARS-CoV antibody. *Nature* **583**, 290–295 (2020).

35. Pallesen, J. et al. Immunogenicity and structures of a rationally designed prefusion MERS-CoV spike antigen. *Proc. Natl Acad. Sci. USA* **114**, E7348–E7357 (2017).

36. Hsieh, C. L. et al. Structure-based design of prefusion-stabilized SARS-CoV-2 spikes. *Science* **369**, 1501–155 (2020).

37. Wu, F. et al. Neutralizing antibody responses to SARS-CoV-2 in a COVID-19 recovered patient cohort and their implications. Preprint at https://doi.org/10.1101/2020.03.30.20047365 (2020).

38. Wu, N. C. et al. An alternative binding mode of IGHV3-53 antibodies to the SARS-CoV-2 receptor binding domain. *Cell Rep*. https://doi.org/10.1016/j.celrep.2020.108274 (2020).

39. Marillet, S., Lefranc, M. P., Boudinot, P. & Cazals, F. Novel structural parameters of Ig-Ag complexes yield a quantitative description of interaction specificity and binding affinity. *Front. Immunol*. **8**, 34 (2017).

40. Weisblum, Y. et al. Escape from neutralizing antibodies by SARS-CoV-2 spike protein variants. Preprint at https://doi.org/10.1101/2020.07.21.214759 (2020).

41. Wang, B. et al. Bivalent binding of a fully human IgG to the SARS-CoV-2 spike proteins reveals mechanisms of potent neutralization. Preprint at https://doi.org/10.1101/2020.07.14.203414 (2020).

42. Shang, J. et al. Structural basis of receptor recognition by SARS-CoV-2. *Nature* **581**, 221–224 (2020).

43. Yan, R. et al. Structural basis for the recognition of SARS-CoV-2 by full-length human ACE2. *Science* **367**, 1444–1448 (2020).

44. Li, Q. et al. The impact of mutations in SARS-CoV-2 spike on viral infectivity and antigenicity. *Cell* **182**, 1284–1294.e9 (2020).

45. Scharf, L. et al. Broadly neutralizing antibody 8ANC195 recognizes closed and open states of HIV-1 Env. *Cell* **162**, 1379–1390 (2015).

46. Schoofs, T. et al. Broad and potent neutralizing antibodies recognize the silent face of the HIV envelope. *Immunity* **50**, 1513–1529 (2019).

47. Kabsch, W. XDS. *Acta Crystallogr. D* **66**, 125–132 (2010).

48. Winn, M. D. et al. Overview of the CCP4 suite and current developments. *Acta Crystallogr. D* **67**, 235–242 (2011).

49. Adams, P. D. et al. PHENIX: a comprehensive Python-based system for macromolecular structure solution. *Acta Crystallogr. D* **66**, 213–221 (2010).

50. Winter, G. xia2: an expert system for macromolecular crystallography data reduction. *J. Appl. Crystallogr*. **43**, 186–190 (2010).

51. Beilsten-Edmands, J. et al. Scaling diffraction data in the DIALS software package: algorithms and new approaches for multi-crystal scaling. *Acta Crystallogr. D*. **76**, 385–399 (2020).

52. Winter, G. et al. DIALS: implementation and evaluation of a new integration package. *Acta Crystallogr. D* **74**, 85–97 (2018).

53. McCoy, A. J. et al. Phaser crystallographic software. *J. Appl. Crystallogr*. **40**, 658–674 (2007).

54. Gristick, H. B. et al. Natively glycosylated HIV-1 Env structure reveals new mode for antibody recognition of the CD4-binding site. *Nat. Struct. Mol. Biol*. **23**, 906–915 (2016).

55. Bunkóczi, G. & Read, R. J. Improvement of molecular-replacement models with Sculptor. *Acta Crystallogr. D* **67**, 303–312 (2011).

56. Emsley, P., Lohkamp, B., Scott, W. G. & Cowtan, K. Features and development of Coot. *Acta Crystallogr. D* **66**, 486–501 (2010).

57. Mastronarde, D. N. Automated electron microscope tomography using robust prediction of specimen movements. *J. Struct. Biol*. **152**, 36–51 (2005).

58. Punjani, A., Rubinstein, J. L., Fleet, D. J. & Brubaker, M. A. cryoSPARC: algorithms for rapid unsupervised cryo-EM structure determination. *Nat. Methods* **14**, 290–296 (2017).

59. Rohou, A. & Grigorieff, N. CTFFIND4: fast and accurate defocus estimation from electron micrographs. *J. Struct. Biol*. **192**, 216–221 (2015).

60. Goddard, T. D. et al. UCSF ChimeraX: meeting modern challenges in visualization and analysis. *Protein Sci*. **27**, 14–25 (2018).

61. Bell, J. M., Chen, M., Baldwin, P. R. & Ludtke, S. J. High resolution single particle refinement in EMAN2.1. *Methods* **100**, 25–34 (2016).

62. Goddard, T. D., Huang, C. C. & Ferrin, T. E. Visualizing density maps with UCSF Chimera. *J. Struct. Biol*. **157**, 281–287 (2007).

63. Terwilliger, T. C., Adams, P. D., Afonine, P. V. & Sobolev, O. V. A fully automatic method yielding initial models from high-resolution cryo-electron microscopy maps. *Nat. Methods* **15**, 905–908 (2018).

64. Chen, V. B. et al. MolProbity: all-atom structure validation for macromolecular crystallography. *Acta Crystallogr. D* **66**, 12–21 (2010).

65. Krissinel, E. & Henrick, K. Inference of macromolecular assemblies from crystalline state. *J. Mol. Biol*. **372**, 774–797 (2007).

66. Davis, M. I., Bennett, M. J., Thomas, L. M. & Bjorkman, P. J. Crystal structure of prostate-specific membrane antigen, a tumor marker and peptidase. *Proc. Natl Acad. Sci. USA* **102**, 5981–5986 (2005).

67. Liu, H. et al. Cross-neutralization of a SARS-CoV-2 antibody to a functionally conserved site is mediated by avidity. Preprint at https://doi.org/10.1101/2020.08.02.233536 (2020).

68. Zhou, D. et al. Structural basis for the neutralization of SARS-CoV-2 by an antibody from a convalescent patient. *Nat. Struct. Mol. Biol*. **27**, 950–958 (2020).

69. Piccoli, L. et al. Mapping neutralizing and immunodominant sites on the SARS-CoV-2 spike receptor-binding domain by structure-guided high-resolution serology. *Cell* **183**, 1024–1042 (2020).

70. Dunbar, J. et al. SAbDab: the structural antibody database. *Nucleic Acids Res*. **42**, D1140–D1146 (2014).

Extended Data Figures

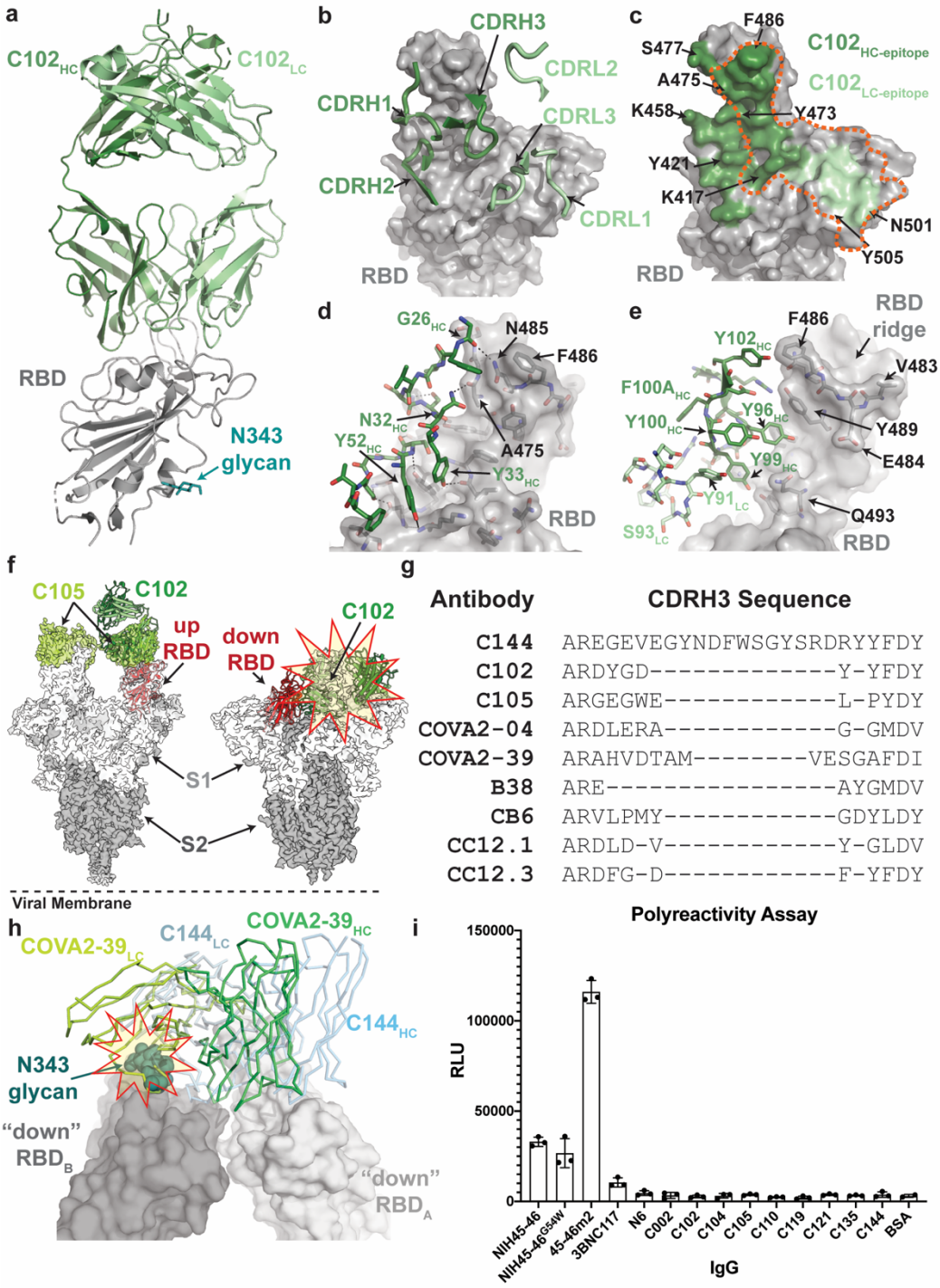

Extended Data Fig. 1: X-ray structure and epitope mapping of *VH3-53* NAb C102.
a, X-ray structure of the C102 Fab–$RBD_{331–518}$ complex. **b**, C102 CDR loops mapped on the RBD surface. **c**, Surface representation of C102 epitope coloured by C102 heavy chain (dark green) and light chain (light green) interactions. **d**, **e**, CDRH1, CDRH2 (**d**) and CDRH3 (**e**) interactions with RBD residues. Potential hydrogen-bond contacts are illustrated as dashed lines. **f**, Left, overlay of C102–RBD crystal structure (cartoon) with C105–S trimer cryo-EM density (PDB 6XCM, EMD-22127) illustrating conserved binding to RBD epitope in an up conformation. Right, the C102 epitope is sterically occluded when aligned to a down RBD conformation (red and yellow star). SARS-CoV-2 S domains are dark grey (S2 domain) and light grey (S1 domain); the C105 Fab is yellow-green. **g**, Alignment of selected CDRH3 sequences for *VH3-53*- or *VH3-66*-encoded SARS-CoV-2 neutralizing antibodies (IMGT definition[32]). **h**, Overlay of NAb COVA2-39 Fab[38] (lime green and lemon, from COVA2-39–RBD structure, PDB 7JMP) and C144 Fab (blue, from C144–S structure) aligned on a RBD_A of C144 epitope. COVA2-39 adopts a distinct conformation relative to the C102-like *VH3-53*-encoded short CDRH3 NAb class and to C144, recognizing its RBD epitope only in an up RBD conformations owing to steric clashes (red and yellow star) with the N343-associated glycan on the adjacent RBD. **i**, Polyreactivity assay. IgGs were evaluated for binding to baculovirus extracts to assess non-specific binding. Polyreactive positive control IgGs were NIH45-46, 45-46^{G54W} and 45-46m2. Negative controls were bovine serum albumin (BSA) and IgGs N6 and 3BNC117. Relative light unit (RLU) values are presented as the mean and s.d. of triplicate measurements (n = 3 biological replicates) with results for individual experiments shown as circles.

a

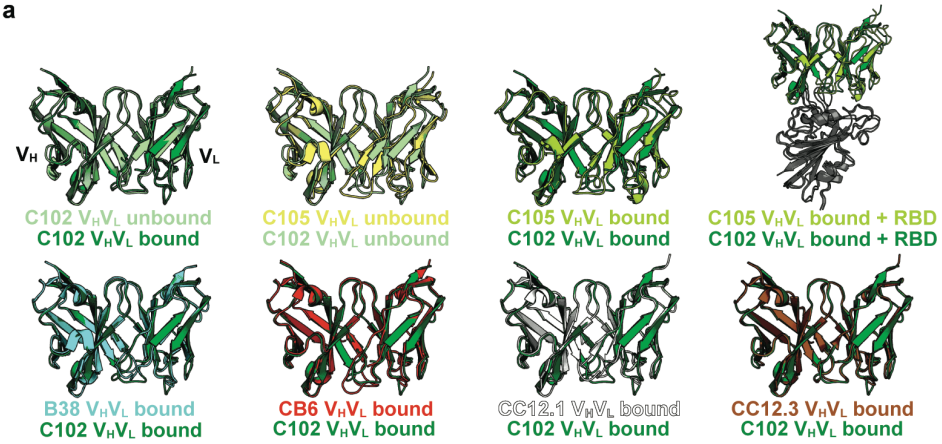

Alignments of V_HV_L Domains of *VH3-53*/short CDRH3 NAbs

Structure 1	Structure 2	# Ca atoms	RMSD (Å)	PDB Structure 1	PDB Structure 2
C102 unbound	C102 bound	225	0.9	This study	This study
C105 unbound	C102 unbound	220	2.0	6XCA	This study
C105 bound	C102 bound	220	3.0	6XCM	This study
C105 bound + RBD	C102 bound + RBD	403	2.4	6XCM	This study
B38 bound	C102 bound	222	1.1	7BZ5	This study
CB6 bound	C102 bound	223	1.2	7C01	This study
CC12.1 bound	C102 bound	224	1.1	6XC2	This study
CC12.3 bound	C102 bound	224	0.6	6XC4	This study

b

Interface Buried Surface Area (Å²)

Structure	C102 Fab/RBD	B38 Fab/RBD	CB6 Fab/RBD	CC12.1 Fab/RBD	CC12.3 Fab/RBD	C144 Fab/RBD	
PDB	this study	7BZ5	7C01	6XC2	6XC4	this study	
VH gene usage	*VH3-53*/short	*VH3-53*/short	*VH3-53*/short	*VH3-53*/short	*VH3-53*/short	*VH3-53*/long	
						RBD A	RBD B
Heavy Chain Paratope	796	735	732	786	721	707	367
FWRH1	29	22	17	23	25	6	0
CDRH1	275	267	211	223	217	161	0
FWRH2	0	0	0	0	0	0	0
CDRH2	199	203	210	215	204	127	0
FWRH3	34	40	43	82	42	95	0
CDRH3	259	203	251	243	233	318	367
FWRH4	0	0	0	0	0	0	0
Light Chain Paratope	257	485	355	559	164	87	20
FWRL1	0	15	0	18	1	0	0
CDRL1	217	239	127	262	111	51	0
FWRL2	0	0	0	0	0	0	0
CDRL2	0	0	0	0	0	0	0
FWRL3	0	35	1	48	0	0	20
CDRL3	40	196	227	231	52	36	0
FWRL4	0	0	0	0	0	0	0
Total Paratope	1052	1220	1087	1345	885	794	387
Heavy Chain Epitope	797	689	736	763	677	722	330
Light Chain Epitope	225	504	313	574	186	100	22
Total Epitope	1022	1193	1049	1337	863	822	351

c

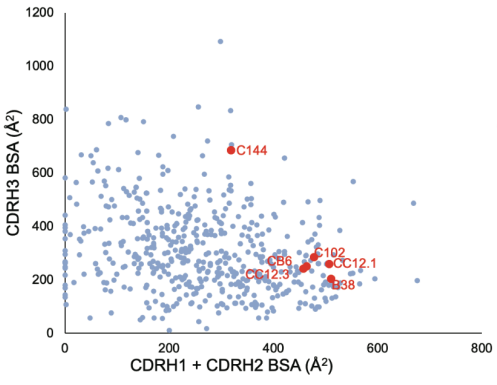

d

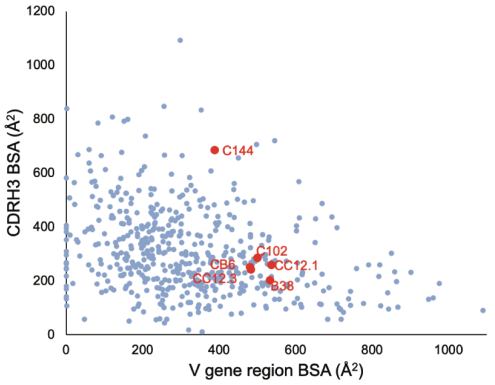

Extended Data Fig. 2: Overview of *VH3-53*/*VH3-66*-encoded human NAb structures.
a, Superimposition of V_H and V_L domains of C102 with other *VH3-53*- or *VH3-66*-encoded NAbs (top) and root mean square deviation (r.m.s.d.) calculations (bottom). **b**, Buried surface area comparisons for the indicated Fab–RBD structures. Buried surface areas were calculated using PDBePISA[65] and a 1.4 Å probe. **c**, **d**, Heavy-chain buried surface areas of anti-SARS-CoV-2 antibodies plotted as CDRH1 (IMGT residues 27–38) plus CDRH2 (residues 56–67*) versus CDRH3 (residues 105–117) (**c**), and V gene segment region (residues 1–105) versus CDRH3 (residues 106*–117) (**d**, asterisk indicates differences from IMGT definition). Blue data points represent 501 human antibodies complexed with protein antigens. IMGT-numbered structures (resolutions of 3.5 Å or better) were downloaded from the Structural Antibody Database (SAbDab)[70] and buried surface area were calculated using PISA[65]. Buried surface areas from antibody structures with identical or near-identical heavy chain sequences were averaged to give a single point on the graph.

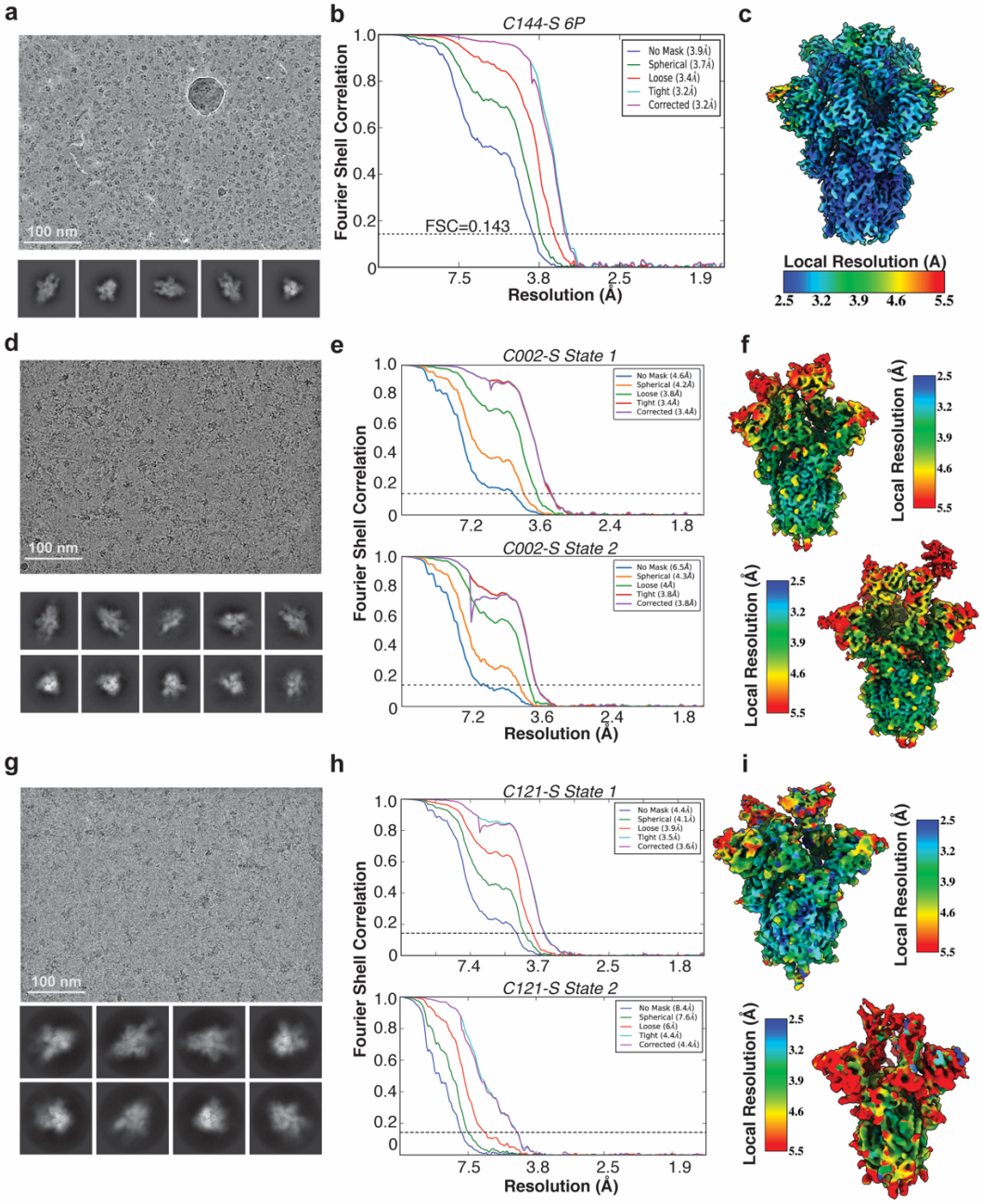

Extended Data Fig. 3: Cryo-EM data processing and validation for C144–S, C002–S and C121–S complexes.

a–**i**, Representative micrograph selected from total dataset (Supplementary Table 2), 2D class averages, gold-standard Fourier shell correlation (FSC) plots, and local resolution estimations for C144–S 6P (**a**–**c**), C002–S 2P (**d**–**f**) and C121–S 2P (**g**–**i**). Scale bars, 100 nm. For the C002–S dataset, two classes were resolved: state 1, C002 Fabs bound to three down RBDs, and state 2, C002 Fabs bound to two down and one up RBD. For the C121–S 2P dataset, two classes were resolved: state 1, C121 Fabs bound to two down and one up RBD and state 2, C121 Fabs bound to one down, two up RBDs.

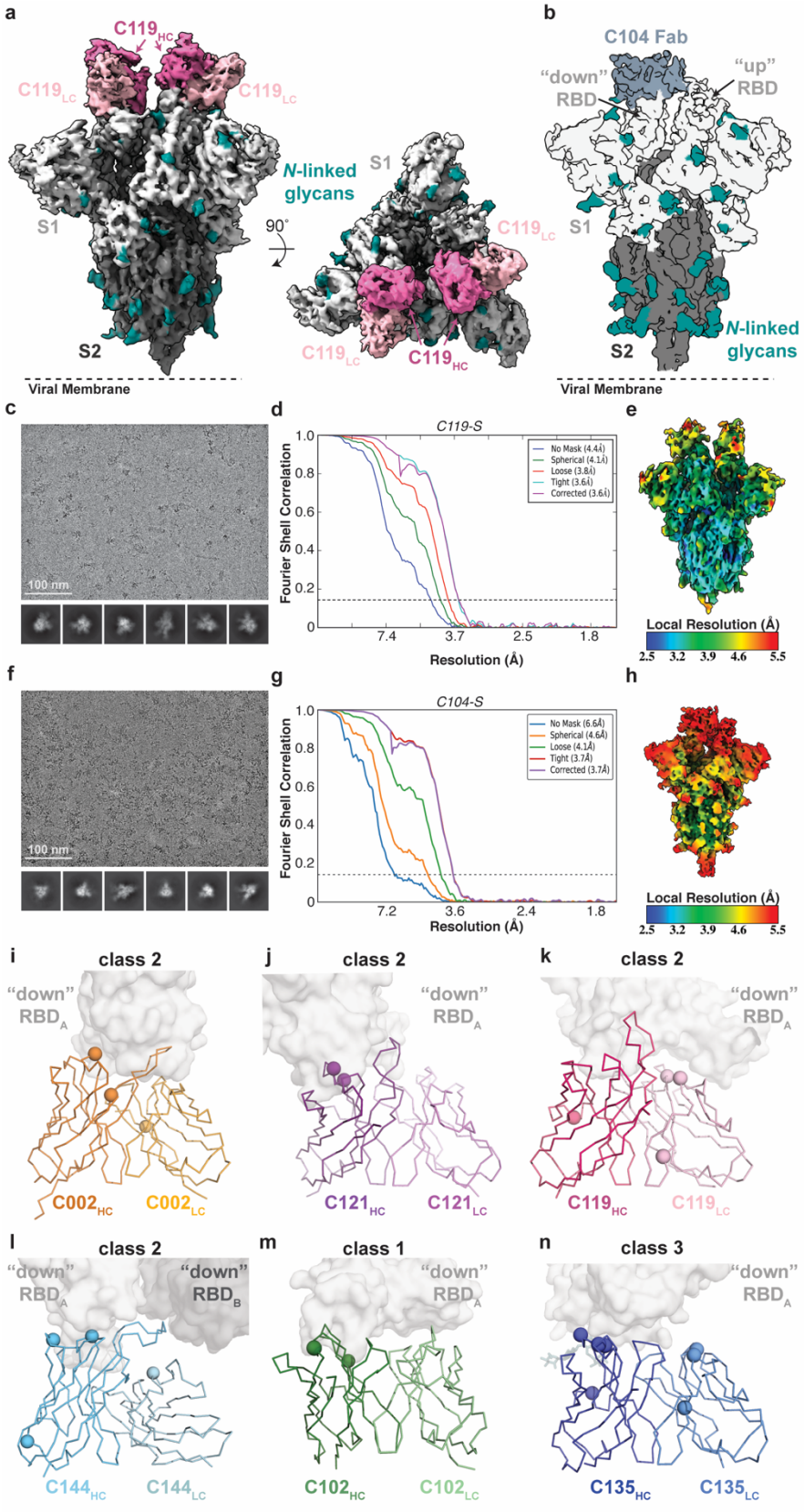
a
C119HC
C119LC
C119LC
S1
S2
N-linked glycans
90˚
S1
C119LC
C119LC
C119HC
Viral Membrane
b
C104 Fab
"down" RBD
"up" RBD
S1
S2
N-linked glycans
Viral Membrane
c
100 nm
d
C119-S
Fourier Shell Correlation
No Mask (4.4Å)
Spherical (4.1Å)
Loose (3.8Å)
Tight (3.6Å)
Corrected (3.6Å)
Resolution (Å)
e
Local Resolution (Å)
f
100 nm
g
C104-S
Fourier Shell Correlation
No Mask (6.6Å)
Spherical (4.6Å)
Loose (4.1Å)
Tight (3.7Å)
Corrected (3.7Å)
Resolution (Å)
h
Local Resolution (Å)
i
class 2
"down" RBDA
C002HC
C002LC
j
class 2
"down" RBDA
C121HC
C121LC
k
class 2
"down" RBDA
C119HC
C119LC
l
class 2
"down" RBDA
"down" RBDB
C144HC
C144LC
m
class 1
"down" RBDA
C102HC
C102LC
n
class 3
"down" RBDA
C135HC
C135LC

Extended Data Fig. 4 Cryo-EM processing, validation and reconstruction for C119–S and C104–S complexes.

a, 3.6 Å cryo-EM reconstruction for a C119–S trimer complex. **b**, 3.7 Å cryo-EM reconstruction for a C104–S trimer complex. Representative micrograph selected from the total dataset (Supplementary Table 2), 2D class averages, gold-standard FSC plot, and local resolution estimation for C119–S2P (**c**–**e**) and C104–S (**f**–**h**). Scale bars, 100 nm. Both complexes revealed binding of Fabs to both down and up RBD conformations. **i**–**n**, Somatic hypermutations in heavy- and light-chain V gene segments for C002 (**i**), C121 (**j**), C119 (**k**), C144 (**l**), C102 (**m**) and C135 (**n**) are shown as spheres on the antibody V_H and V_L domains (ribbon representations). The primary RBD epitope is shown as a light grey surface; secondary RBD epitope for C144 is in dark grey.

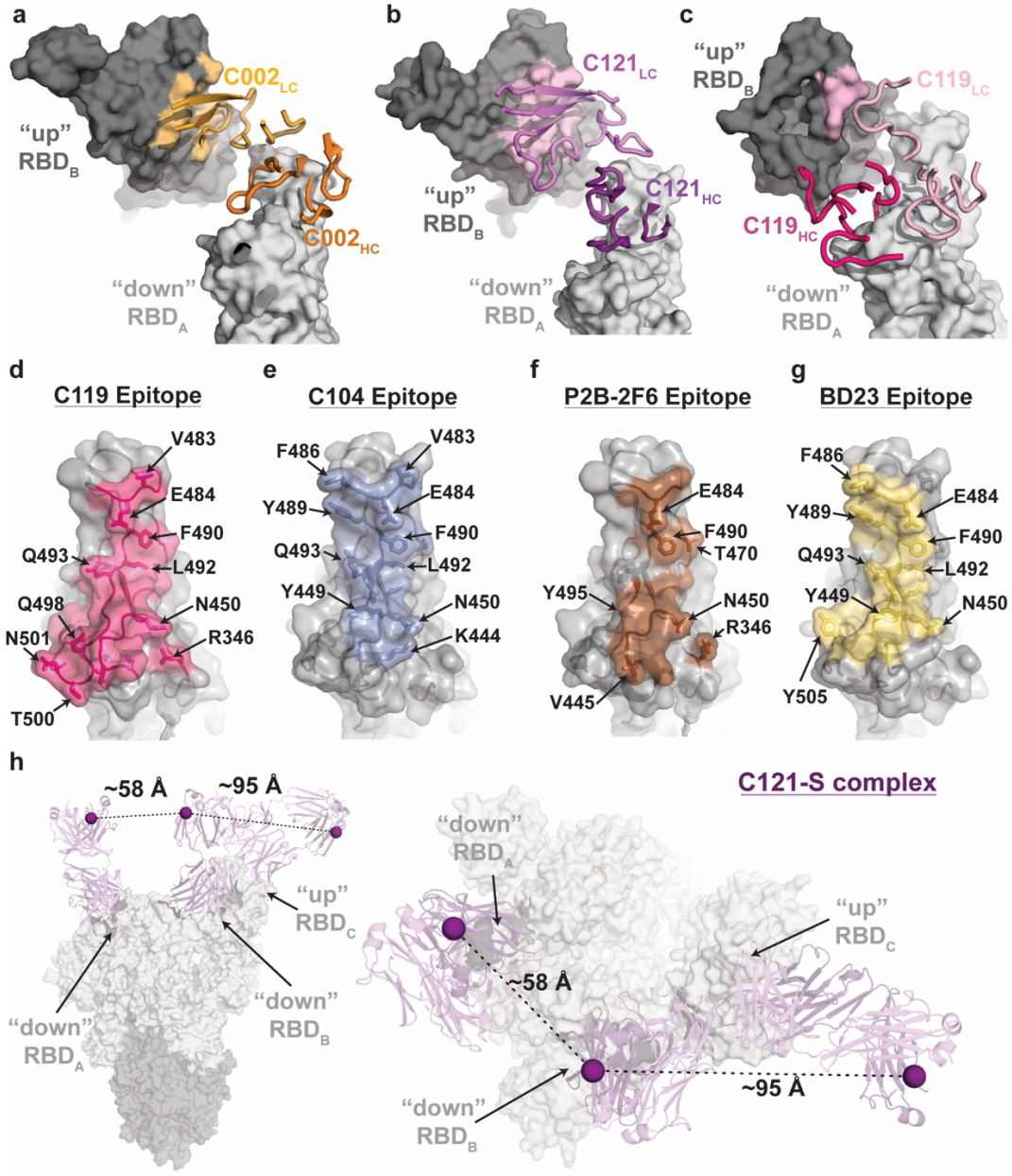

Extended Data Fig. 5: Primary and secondary epitopes of class 2 human NAbs.
a–**c**, Primary epitopes for C002 (**a**), C121 (**b**), and C119 (**c**) on down RBD. A secondary epitope is observed if a Fab is bound to an adjacent up RBD for these NAbs. Antibody paratopes are represented as cartoons. A similar interaction in the C104–S structure is not shown owing to low local resolution on the up RBD. **d**–**g**, Primary epitopes for C119 (**d**), C104 (**e**), P2B-2F6 (**f**; PDB 7BWJ), and BD23 (**g**; PDB 7BYR). The existence of secondary epitopes for P2B-2F6 and BD23 cannot be determined because the P2B-2F6 epitope was determined from a crystal structure with an RBD[27], and the BD23–S cryo-EM structure showed only one bound Fab[13]. **h**, Measurement of Cα distance between the C termini of adjacent C121 Ch1 domains (residue 222 of the heavy chain on each Fab). Measurements of this type were used to evaluate whether intra-spike crosslinking by an IgG binding to a single spike trimer was possible for human NAbs in Extended Data Table 1.

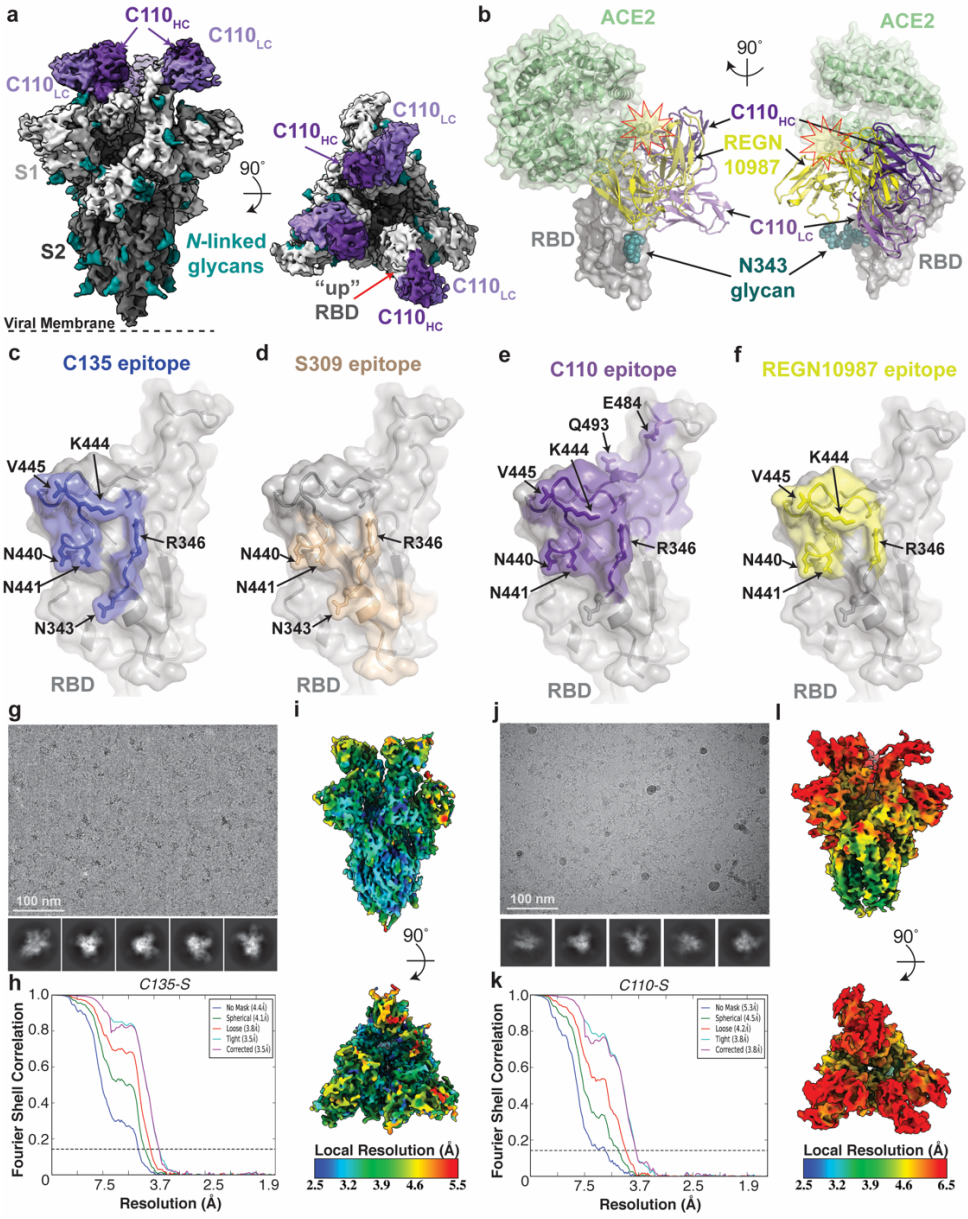

Extended Data Fig. 6: Cryo-EM structure of C110-S complex and epitope mapping.
a, 3.8 Å cryo-EM reconstruction of the C110–S trimer complex. **b**, Composite model of C110–RBD (purple and grey, respectively) overlaid with the SARS-CoV-2 NAb REGN-10987 (yellow, PDB 6XDG) and soluble ACE2 (green, PDB 6M0J). Model was generated by aligning structures on 188 RBD Cα atoms. **c**–**f**, Surface representation of RBD epitopes for C135 (blue) (**c**), S309 (brown, PDB 6WSP) (**d**), C110 (purple) (**e**) and REGN-10987 (yellow, PDB 6XDG) (**f**). Given the low resolution of the antibody–RBD interface, epitopes were assigned by selection of any RBD residue within 7 Å of any antibody Cα atom. Mutation sites found in sequence isolates[44] (green) and in laboratory selection assays[40] (red) are shown. Representative micrograph selected from total dataset (Supplementary Table 2), 2D class averages, gold-standard FSC plot, and local resolution estimation for C135–S 2P (**g**–**i**) and C110–S 2P (**j**–**l**). Scale bars, 100 nm. Both complexes revealed binding of Fabs to both two-down and one-up RBD conformations.

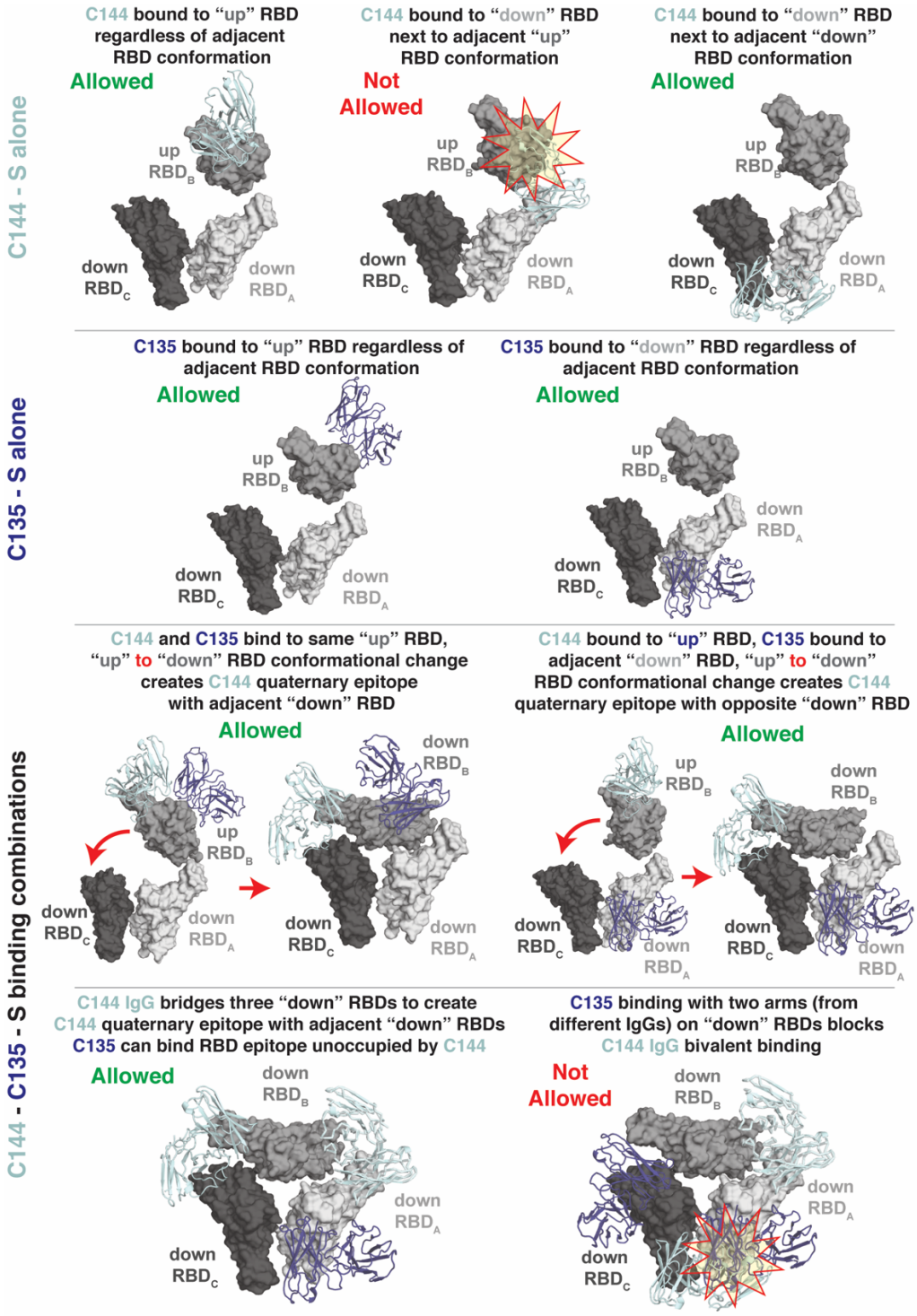

Extended Data Fig. 7: Possibilities for simultaneous engagement of C144 and C135 on spikes with different combinations of up and down RBDs.
Modelling of C144 (light blue) and C135 (dark blue) V_H–V_L domains on different RBD conformations. Steric clashes are shown as a red and yellow star.

a

C102
VH3-53/VK3-20 Class 1

RBD	k_a (10^5) ($M^{-1}s^{-1}$)	k_d (10^{-3}) (s^{-1})	K_D (nM)
wt	1.4	3.8	27
R346S	1.2	8.6	72
N439K	1.0	3.2	32
N440K	1.4	7.6	55
A475V	0.8	31.9	395
V483A	1.0	3.1	32
E484K	1.4	8.7	61
Q493R	2.2	17.5	81

C105
VH3-53/VL2-8 Class 1

RBD	k_a (10^5) ($M^{-1}s^{-1}$)	k_d (10^{-3}) (s^{-1})	K_D (nM)
wt	0.7	0.9	14
R346S	0.5	1.1	20
N439K	0.6	1.1	19
N440K	0.6	1.1	18
A475V	1.0	22	225
V483A	0.5	0.8	15
E484K	0.6	1.1	19
Q493R	0.7	0.4	6

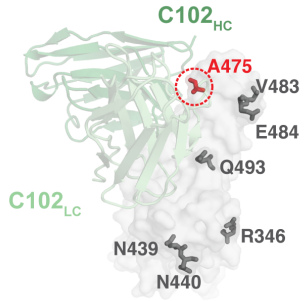

b

C144
VH3-53/VL2-14 Class 2

RBD	k_a (10^5) ($M^{-1}s^{-1}$)	k_d (10^{-3}) (s^{-1})	K_D (nM)
wt	2.3	4.1	18
R346S	1.1	5.6	52
N439K	1.2	3.6	29
N440K	1.4	5.8	40
A475V	2.3	53	228
V483A	1.3	4.1	32
E484K	n.b.	n.b.	n.b.
Q493R	n.b.	n.b.	n.b.

C002
VH3-30/VK1-39 Class 2

RBD	k_a (10^5) ($M^{-1}s^{-1}$)	k_d (10^{-3}) (s^{-1})	K_D (nM)
wt	8.3	9.0	11
R346S	3.2	8.6	27
N439K	6.0	9.7	16
N440K	3.3	8.1	24
A475V	2.1	6.3	31
V483A	2.7	2.9	11
E484K	n.b.	n.b.	n.b.
Q493R	1.8	106	596

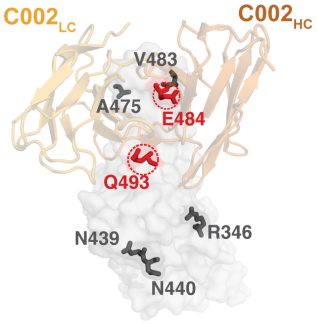

C121
VH1-2/VL2-23 Class 2

RBD	k_a (10^5) ($M^{-1}s^{-1}$)	k_d (10^{-3}) (s^{-1})	K_D (nM)
wt	5.2	2.5	0.5
R346S	6.3	5	0.8
N439K	5.0	3.8	0.8
N440K	6.9	4.1	0.6
A475V	6.4	4.7	0.7
V483A	2.0	1.5	0.8
E484K	n.b.	n.b.	n.b.
Q493R	10	115	111

C119
VH1-46/VL2-14 Class 2

RBD	k_a (10^5) ($M^{-1}s^{-1}$)	k_d (10^{-3}) (s^{-1})	K_D (nM)
wt	2.6	2.6	10
R346S	2.6	5.7	22
N439K	6.4	12.5	20
N440K	1.8	3.8	21
A475V	1.4	2.8	20
V483A	1.7	3.7	22
*E484K	1.1	.005	28	2.7	91
Q493R	5.3	11	20

***C104**
VH4-34/VK3-20 Class 2

RBD	k_a (10^5) ($M^{-1}s^{-1}$)		k_d (10^{-3}) (s^{-1})		K_D (nM)
wt	1.2	.008	17.6	1.3	19
R346S	1.4	.003	28.4	3.3	97
N439K	1.1	.008	28.4	0.9	24
N440K	1.5	.003	31.2	3.7	108
A475V	1.2	.004	25.0	5.2	124
V483A	0.9	.015	24.5	5.4	69
E484K	n.b.	n.b.	n.b.	n.b.	n.b.
Q493R	1.1	.022	36.1	1.2	17

c

C135
VH3-30/VK1-5 Class 3

RBD	k_a (10^5) ($M^{-1}s^{-1}$)	k_d (10^{-3}) (s^{-1})	K_D (nM)
wt	1.9	1.2	6
R346S	n.b.	n.b.	n.b.
N439K	1.3	4.9	37
N440K	n.b.	n.b.	n.b.
A475V	1.5	1.8	12
V483A	1.4	1.3	9
E484K	2.7	1.8	7
Q493R	1.3	1.7	13

C110
VH5-51/VK1-5 Class 3

RBD	k_a (10^5) ($M^{-1}s^{-1}$)	k_d (10^{-3}) (s^{-1})	K_D (nM)
wt	0.7	0.09	1.3
R346S	0.2	1.1	68
N439K	0.4	0.3	8
N440K	0.5	0.1	2
A475V	0.4	0.1	3
V483A	0.4	0.09	2
E484K	0.4	0.9	27
Q493R	0.3	0.3	12

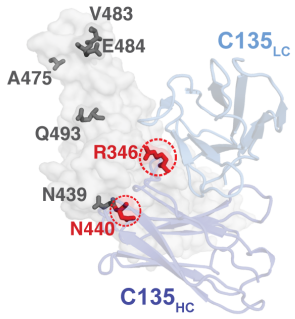

Extended Data Fig. 8: SPR binding data for NAbs.
a–**c**, Kinetic and equilibrium constants for binding to unaltered RBD (indicated as wild type, wt) and mutant RBDs are shown in tables beside structures of a representative NAb–RBD complex for each class. Residues that were mutated are highlighted as coloured side chains on a grey RBD surface. Antibody V_H–V_L domains are shown as cartoons. Kinetic and equilibrium constants for NAbs that contact adjacent RBDs on the S trimer (C144, C002, C119 and C121) do not account for contacts to a secondary RBD because binding was assayed by injected monomeric RBDs over immobilized IgGs. Asterisk indicates kinetic constants determined from a two-state binding model.

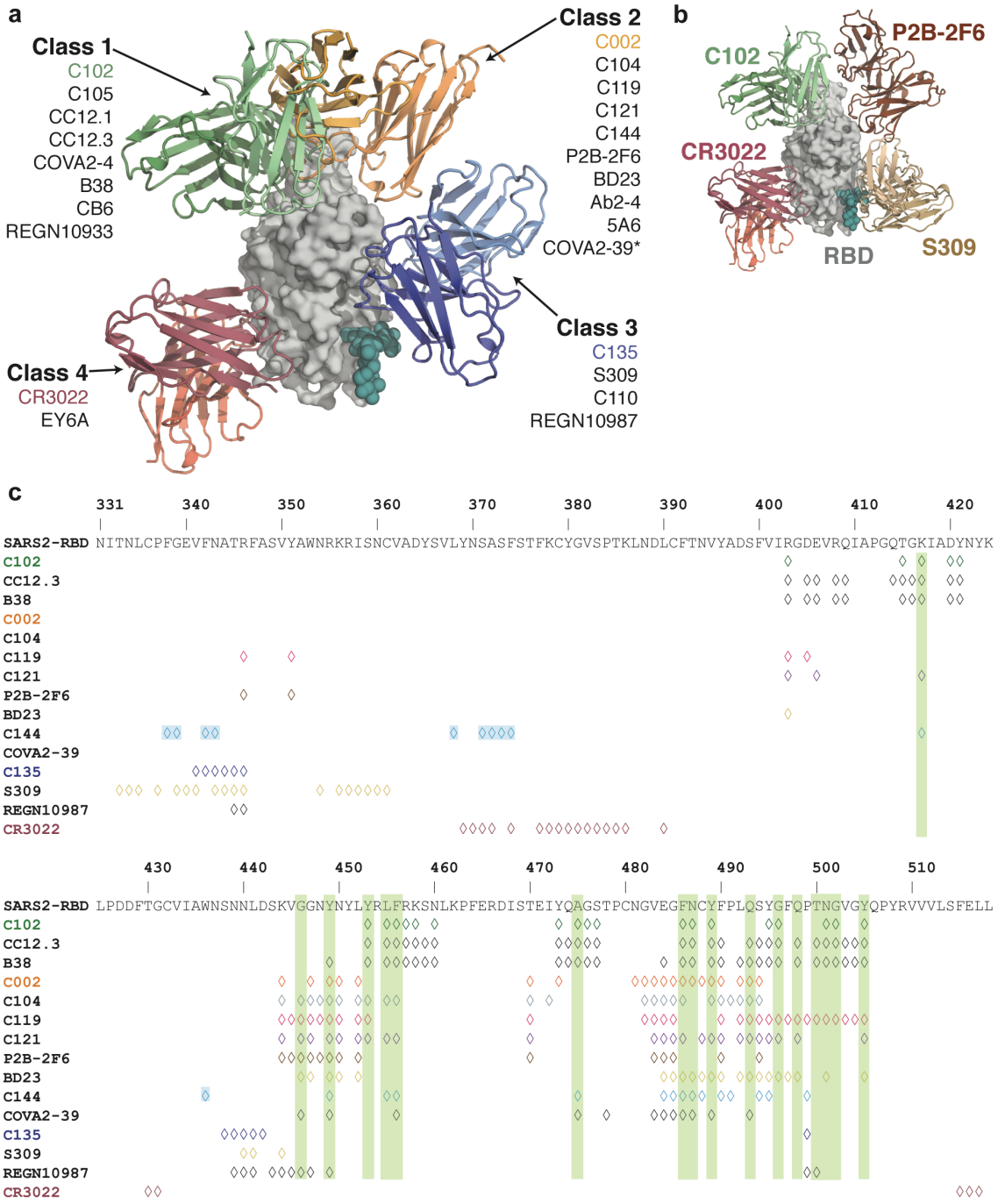

Extended Data Fig. 9: Summary of Nabs

a, Structural depiction of a representative NAb from each class binding its RBD epitope. **b**, Composite model illustrating non-overlapping epitopes of NAbs from each class bound to a RBD monomer. **c**, Epitopes for SARS-CoV-2 NAbs. RBD residues involved in ACE2 binding are boxed in green. Diamonds represent RBD residues contacted by the indicated antibody.

Extended Data Table 1: Classification and structural properties of SARS-CoV-2 RBD-specific antibodies

Antibody	Reference	IGHV (# of aa SHM)	CDRH3 length (aa)^	IGLV (# of aa SHM)	CDRL3 length (aa)^	IC_{50}/IC_{90} (ng/mL)†	Potential IgG intra-spike binding§	Contacts adjacent RBD	Structural Information
Class 1: Blocks ACE2, accessibility of RBD epitope only in "up" conformation									
C102	this study	*VH3-53* (2)	11	*VK3-20* (0)	9	34 / 143	???	???	3.0 Å Fab-RBD
C105	Barnes, et al.[26]	*VH3-53* (0)	12	*VL2-8* (1)	11	26.1 / 134	Yes	No	3.4 Å Fab-S. PDB 6XCM
B38	Wu, et al.[28]	*VH3-53* (1)	9	*VK1-9* (2)	10	117 / NA	???	???	1.8 Å Fab-RBD, PDB 7BZ5
CC12.3	Yuan, et al.[30]	*VH3-53* (3)	12	*VK3-20* (1)	9	20 / NA	???	???	2.9 Å. Fab-RBD, PDB 6XC7
Class 2: Blocks ACE2, accessibility of RBD epitope in "up"/"down" conformations									
C002	this study	*VH3-30* (1)	17	*VK1-39* (1)	9	8.9 / 37.6	Yes	Yes	3.4 Å Fab-S
C104	this study	*VH4-34* (6)	17	*VK3-20* (3)	9	23.3 / 140	Yes	Yes	3.7 Å Fab-S
C119	this study	*VH1-46* (1)	20	*VL2-14* (3)	11	9.1 / 97.8	Yes	Yes	3.5 Å Fab-S
C121	this study	*VH1-2* (2)	22	*VL2-23* (0)	10	6.7 / 22.3	Yes	Yes	3.6 Å Fab-S
C144	this study	*VH3-53* (3)	25	*VL2-14* (1)	10	6.9 / 29.7	Yes	Yes	3.3 Å Fab-S
COVA2-39	Wu, et al.[38]	*VH3-53* (3)	17	*VL2-23* (1)	10	36 / NA	???	???	1.7 Å Fab-RBD, PDB 7JMP
5A6	Wang, et al.[41]					75.5 / NA	Yes	Yes	2.4 Å Fab-S
P2B-2F6	Ju, et al.[27]	*VH4-38*02* (2)	20	*VL2-8* (0)	10	50 / NA	???	???	2.9 Å Fab-RBD, PDB 7BWJ
Ab2-4	Liu, et al.[10]	*VH1-2* (3)	15	*VL2-8* (0)	10	394 / NA	Yes	No	3.2 Å Fab-S, PDB 6XEY
BD23	Cao, et al.[13]	*VH7-4*02* (0)	19	*VK1-5*03* (0)	9	4800 / NA	No	No	3.8 Å Fab-S, PDB 7BYR
Class 3: Does not overlap with ACE2 binding site, accessibility of RBD epitope in "up"/"down" conformations									
C135	this study	*VH3-30* (4)	12	*VK1-5* (3)	9	16.6 / 48.9	No	No	3.5 Å Fab-S
S309	Pinto, et al.[34]	*VH1-18* (6)	20	*VK3-20* (3)	8	79* / NA	No	No	3.1 Å Fab-S, PDB 6WPS
C110	this study	*VH5-51* (2)	21	*VK1-5* (3)	9	18.4 / 77.3	No	No	3.8 Å Fab-S
REGN10987	Hansen, et al.[6]	*VH3-30* (4)	13	*VL2-14* (6)	10	6.1 / NA	???	???	3.9 Å Fab-RBD, PDB 6XDG
Class 4: Does not overlap with ACE2 binding site, accessibility of RBD epitope only in "up" conformation									
CR3022	Yuan, et al.[9]	*VH5-51* (8)	12	*VK4-1* (3)	9	>10,000 / NA	???	???	3.1 Å Fab-RBD, PDB 6W41
COV1-16	Liu, et al.[69]	*VH1-46* (1)	20	*VK1-33* (3)	10	130 / NA	???	???	2.9 Å Fab-RBD
EY6A	Zhou, et al.[70]	*VH3-30*18* (3)	14	*VK1-39* (0)	10	70-20,000**/ NA	No	Yes	3.7 Å Fab-S, PDB 6ZDH
S304	Pinto, et al.[34]	*VH3-13* (5)	14	*VK1-39* (6)	10	>5,000 / NA	No	Yes	4.3 Å Fab-S, PDB 7JW0
S2A4	Piccoli, et al.[71]	*VH3-7* (2)	?	*VL2-23* (0)	?	3,500 / NA	No	Yes	3.3 Å Fab-S, PDB 7JVC

Supplementary Table 1: X-ray Crystallography data collection and refinement statistics.

	C102 SARS-CoV-2 RBD	C102 Fab	C002 Fab	C110 Fab	C121 Fab	C135 Fab
PDB ID	**7K8M**	**7K8N**	**7K8O**	**7K8P**	**7K8Q**	**7K8R**
Data collection[a,b]						
Space group	$P2_12_12_1$	$P6_522$	$P3_121$	P2	$P6_122$	$P4_1$
Cell Dimensions						
a, b, c (Å)	54.6, 89.3, 175.1	88.8, 88.8, 218.93	92.3, 92.3, 130.9	48.5, 62.7, 78.4	71.3, 71.3, 404.8	102.3, 102.3, 53.3
α, β, γ (°)	90, 90, 90	90, 90, 90	90, 90, 120	90, 97.5, 90	90, 90, 120	90, 90, 90
Resolution (Å)	48.85-3.2 (3.31-3.2)	37.93-1.65 (1.71-1.65)	34.1-1.92 (1.99-1.92)	38.7 - 1.80 (1.86-1.80)	39.1-2.0 (2.05-2.0)	45.7-2.0 (2.07 - 2.0)
R_{merge} (%)	16.0 (49.2)	9.58 (148)	7.21 (203)	8.7 (107)	58.1 (136)	8.5 (213)
R_{pim} (%)	6.8 (23.2)	2.27 (33.4)	2.38 (71.4)	4.1 (81.9)	11.4 (81)	3.5 (88.9)
$CC_{1/2}$ (%)	98.7 (97.4)	99.8 (80.7)	99.9 (80.7)	99.6 (78.2)	99.5 (24.8)	99.8 (30.5)
$\langle I/\sigma I \rangle$	6 (0.86)	15.3 (1.6)	13.02 (0.88)	7.7 (2.0)	8.4 (0.6)	10.5 (0.76)
Completeness (%)	99.7 (99.5)	99.97 (99.95)	76.9 (8.41)	98.8 (99.2)	99.2 (97.7)	99.4 (98.4)
Redundancy	6.5 (6)	19.2 (19.3)	9.9 (8.7)	4.7 (2.0)	26.3 (26.8)	6.8 (6.6)
Wilson *B*-factor	28.5	28.5	32.1	23.8	44.3	52.6
Refinement and Validation						
Resolution (Å)	48.5 - 3.2	37.9 - 1.65	34.1-1.92	38.9 - 1.80	36.4 - 2.0	45.7 - 2.0
Unique Reflections	14,722 (1413)	62,121 (6095)	38260 (413)	42,891 (4,284)	42,233 (2,989)	37,324 (3071)
Number of atoms						
Protein	4,731	3,280	3,337	3,345	3,269	3,315
Ligand	14	58	53	n/a	14	18
Waters	0	78	63	172	12	30
R_{work}/R_{free} (%)	18.7/23.8	19.6/21.2	19.7/22.7	20.9/23.4	20.7/23.9	20.8/23.7
R.m.s. deviations						
Bond lengths (Å)	0.002	0.02	0.007	0.01	0.005	0.004
Bond angles (°)	0.5	1.7	0.9	1.1	0.7	1.02
Poor rotamers (%)	0.9	2.2	2.1	0	0.8	0.27
Ramachandran plot						
Favored (%)	94.7	97.4	97.5	97.9	97.5	97.2
Allowed (%)	5.1	2.6	2.3	2.1	2.5	2.5
Disallowed (%)	0.2	0	0.2	0	0	0
Average *B*-factor (Å)	80.2	42.6	43.2	32.8	53.5	59.8

[a]For each structure reported, data were derived from a single crystal.

[b]Numbers in parentheses correspond to the highest resolution shell

Supplementary Table 2: Cryo-EM data collection and refinement statistics.

	C002 SARS-CoV-2 S 2P (state 1)	C002 SARS-CoV-2 S 2P (state 2)	C104 SARS-CoV-2 S 2P (open state)	C110 SARS-CoV-2 S 2P (open state)	C119 SARS-CoV-2 S 2P (open state)	C121 SARS-CoV-2 S 2P (state 1)	C121 SARS-CoV-2 S 2P (state 2)	C135 SARS-CoV-2 S 2P (open state)	C144 SARS-CoV-2 S 6P (closed state)
PDB	**7K8S**	**7K8T**	**7K8U**	**7K8V**	**7K8W**	**7K8X**	**7K8Y**	**7K8Z**	**7K90**
EMD	**22729**	**22730**	**22731**	**22732**	**22733**	**22734**	**22735**	**22736**	**22737**
Data collection conditions									
Microscope	Titan Krios	Titan Krios	Titan Krios	Titan Krios	Titan Krios	Titan Krios	Titan Krios	Titan Krios	Talos Arctica
Camera	Gatan K3 Summit	Gatan K3 Summit	Gatan K3 Summit	Gatan K3 Summit	Gatan K3 Summit	Gatan K3 Summit	Gatan K3 Summit	Gatan K3 Summit	Gatan K3 Summit
Magnification	105,000x	105,000x	105,000x	105,000x	105,000x	105,000x	105,000x	105,000x	45,000x
Voltage (kV)	300	300	300	300	300	300	300	300	200
Recording mode	counting	counting	counting	counting	counting	counting	counting	counting	counting
Dose rate (e^-/pixel/s)	22.1	22.1	23.1	22.1	22.1	23.1	22.1	23.5	15.28
Electron dose ($e^-/Å^2$)	60	60	61	60	60	60	60	60	60
Defocus range (μm)	1.0 - 2.5	1.0 - 2.5	1.0 - 2.6	1.0 - 2.5	1.0 - 2.5	1.0 - 2.5	1.0 - 2.5	1.0 - 2.5	0.8 - 2.2
Pixel size (Å)	0.836	0.836	0.836	0.836	0.836	0.836	0.836	0.836	0.869
Micrographs collected	3,471	3,471	3,383	4,995	3,626	5,481	5,481	3,882	2,530
Micrographs used	3,105	3,105	2,668	2,923	3,069	3,671	3,671	3,184	2,184
Total extracted particles	1,691,930	1,691,930	1,181,957	840,293	1,381,582	892,954	892,954	634,621	376,586
Refined particles	51,915	49,238	40,469	43,981	140,378	40,489	14,999	101,114	212,876
Symmetry imposed	C1	C1	C1	C1	C1	C1	C1	C1	C3
Nominal Map Resolution (Å)									
FSC 0.143 (unmasked/masked)	4.4/3.4	4.6/3.4	6.6/3.7	5.3/3.8	4.4/3.6	4.4/3.6	8.4/4.4	7.4/3.5	3.9/3.2
FSC 0.143 local (unmasked/masked)	5.8/3.7	6.5/3.8	7.4/4.3	8.2/4.1	7.2/3.7	7.8/3.9	10.2/5.6	9.2/3.8	7.9/3.7
Refinement and Validation									
Initial model used	6VXX	6VYB	6VYB	6VYB	6VYB	6VYB	6VYB	6VYB	6XKL
Number of atoms									
Protein	28,865	28,871	23,852	25,365	25,662	27,399	25,098	23,436	28,466
Ligand	795	779	671	649	837	357	262	789	627
MapCC (global/local)	0.83/0.82	0.86/0.81	0.86/0.82	0.80/0.72	0.74/0.73	0.78/0.74	0.79/0.78	0.81/0.82	0.8/0.77
Map sharpening B-factor	88	79.1	135.1	98.4	80.7	58.1	42.4	71.4	66.9
R.m.s. deviations									
Bond lengths (Å)	0.01	0.01	0.01	0.01	0.01	0.003	0.002	0.006	0.003
Bond angles (°)	0.81	0.9	0.84	0.81	1	0.6	0.5	0.8	0.6
MolProbity score	2.56	2.14	2.27	2.33	2.46	2.06	2	2.3	2.37
Clashscore (all atom)	16.5	15.2	18.9	19.7	18.1	11.2	20.9	16.3	9.7
Poor rotamers (%)	0	0	0	2.1	2.4	2.4	0	0.2	1.3
Ramachandran plot									
Favored (%)	92.6	92.9	91.7	95.9	93.7	96.7	97.1	87.2	94
Allowed (%)	6.9	6.5	8.3	4.1	6.3	3.2	2.7	12.4	5.6
Disallowed (%)	0.5	0.6	0	0	0	0.1	0.2	0.4	0.4

Chapter 5

BROAD CROSS-REACTIVITY ACROSS SARBECOVIRUS EXHIBITED BY A SUBSET OF COVID-19 DONOR-DERIVED NEUTRALIZING ANTIBODIES

Jette, C.A.*, Cohen, A.A.*, Gnanapragasam, P.N.P., Muecksch, F., Lee, Y.E., Huey-Tubman, K.E., Schmidt, F., Hatziioannou, T., Bieniasz, P.D., Nussenzweig, M.C., West, A.P., Keeffe, J.R., Bjorkman, P.J. & Barnes, C.O. Broad cross-reactivity across sarbecoviruses exhibited by a subset of COVID-19 donor-derived neutralizing antibodies. *Cell Reports* **36,** 109760 (2021). doi:10.1016/j.celrep.2021.109760

* Equal Contributions

Summary

Many anti-SARS-CoV-2 neutralizing antibodies target the ACE2-binding site on viral spike receptor-binding domains (RBDs). Potent antibodies recognize exposed variable epitopes, often rendering them ineffective against other sarbecoviruses and SARS-CoV-2 variants. Class 4 anti-RBD antibodies against a less-exposed, but more-conserved, cryptic epitope could recognize newly-emergent zoonotic sarbecoviruses and variants, but usually show only weak neutralization potencies. Here, we characterize two class 4 anti-RBD antibodies derived from COVID-19 donors that exhibit breadth and potent neutralization of zoonotic coronaviruses and SARS-CoV-2 variants. C118-RBD and C022-RBD structures reveal orientations that extend from the cryptic epitope to occlude ACE2 binding, and CDRH3-RBD mainchain H-bond interactions that extend an RBD β-sheet, thus reducing sensitivity to RBD sidechain changes. A C118-spike trimer structure reveals rotated RBDs that allow access to the cryptic epitope and the potential for intra-spike crosslinking to increase avidity. These studies facilitate vaccine design and illustrate potential advantages of class 4 RBD-binding antibody therapeutics.

Introduction

The current SARS-CoV-2 pandemic is a crisis of immediate global concern, but two other zoonotic betacoronaviruses, SARS-CoV and MERS-CoV (Middle East Respiratory Syndrome), also resulted in epidemics within the last 20 years (de Wit et al., 2016). All three viruses likely originated in bats (Li et al., 2005; Zhou et al., 2021), with SARS-CoV and MERS-CoV having adapted to intermediary animal hosts, most likely palm civets (Song et

al., 2005) and dromedary camels (Haagmans et al., 2014), respectively, prior to infection of humans. Serological surveys of people living near caves where bats carry diverse coronaviruses suggests direct transmission of SARS-CoV-like viruses (Wang et al., 2018), raising the possibility of future outbreaks resulting from human infection with SARS-like betacoronaviruses (sarbecoviruses).

Coronaviruses encode a trimeric spike glycoprotein (S) that serves as the machinery for fusing the viral and host cell membranes (Fung and Liu, 2019). The first step in fusion is contact of S with a host receptor. The receptor-binding domains (RBDs) at the apex of the S trimers of SARS-CoV-2, SARS-CoV, HCoV-NL63, and some animal coronaviruses utilize angiotensin-converting enzyme 2 (ACE2) as their receptor (Hoffmann et al., 2020; Li et al., 2003; Zhou et al., 2020b). RBDs can adopt either 'down' or 'up' conformations, with ACE2 binding only possible to RBDs in an 'up' conformation (Kirchdoerfer et al., 2016; Li et al., 2019; Walls et al., 2020; Walls et al., 2016; Wrapp et al., 2020; Yuan et al., 2017). A phylogenetic tree of the relationship between coronavirus S protein RBDs shows that sarbecovirus RBDs form a separate branch (Figure 1A).

Consistent with their obligate role in viral entry, sarbecovirus S trimers are the primary targets of neutralizing antibodies (Brouwer et al., 2020; Cao et al., 2020; Fung and Liu, 2019; Kreer et al., 2020; Liu et al., 2020b; Robbiani et al., 2020; Rogers et al., 2020; Seydoux et al., 2020; Shi et al., 2020; Zost et al., 2020b), with many focusing on the RBD (Barnes et al., 2020a; Barnes et al., 2020b; Brouwer et al., 2020; Cao et al., 2020; Kreer et al., 2020; Liu et al., 2020b; Pinto et al., 2020; Robbiani et al., 2020; Rogers et al., 2020; Seydoux et al., 2020; Zost et al., 2020a). Structural analysis of the binding epitopes of anti-SARS-CoV-2 RBD antibodies enabled their classification into four initial categories: class 1, derived from *VH3-53*/*VH3-63* germlines and including a short heavy chain complementarity determining region 3 (CDRH3) that bind an epitope overlapping with the ACE2 binding site and only recognize 'up' RBDs; class 2, whose epitope also overlaps with the ACE2 binding site, but which can bind to both 'up' and 'down' RBD conformations; class 3, which bind to the opposite side of 'up' and 'down' RBDs adjacent to an N-glycan attached to residue N343; and class 4,

which are often weakly neutralizing antibodies that target a cryptic epitope facing the interior of the spike protein on ‘up’ RBDs (Barnes et al., 2020a) (Figure S1; Supplemental Movie 1).

Potent anti-SARS-CoV-2 neutralizing antibodies are typically class 1 or class 2 anti-RBD antibodies that block the ACE2 binding site (Barnes et al., 2020a; Dejnirattisai et al., 2021; Lee et al., 2021; Liu et al., 2020b; Piccoli et al., 2020b; Tortorici, 2020). Since class 1 and class 2 RBD epitopes are not well conserved (Figure 1B), antibodies in these classes are unlikely to strongly cross-react across sarbecovirus RBDs. However, an in vitro-selected variant of an ACE2 blocking antibody isolated from a SARS-infected survivor exhibited increased cross-reactive properties, showing neutralization of SARS-CoV-2 and other betacoronaviruses (Rappazzo et al., 2021). In general, however, as isolated from infected donors, class 3 and class 4 RBD-binding antibodies are better prospects for neutralizing across multiple strains and thereby potentially protecting against emergent sarbecoviruses. Indeed, S309, a class 3 anti-RBD antibody isolated from a SARS-CoV–infected donor, demonstrated cross-reactive neutralization of SARS-CoV-2 (Pinto et al., 2020). Furthermore, reports of class 4 human antibodies that exhibit cross-reactive binding and neutralization amongst sarbecoviruses (Liu et al., 2020a; Starr et al., 2021a; Tortorici et al., 2021) suggest that further investigation of antibodies from COVID-19 convalescent donors could lead to discoveries of potent and broadly cross-reactive class 4 antibodies that recognize the highly-conserved, ‘cryptic’ RBD epitope.

Here we investigated C118 and C022, two class 4 human antibodies isolated from COVID-19 donors (Robbiani et al., 2020) that show breadth of binding and neutralization across sarbecoviruses and SARS-CoV-2 variants of concern. We report crystal structures of C118 complexed with SARS RBD and C022 complexed with SARS-CoV-2 RBD, which revealed interactions with a conserved portion of the RBD in common with interactions of previously-described cross-reactive but more weakly-neutralizing class 4 antibodies; e.g., CR3022 (Huo et al., 2020; Yuan et al., 2020a; Yuan et al., 2020b), S304/S2A4 (Piccoli et al., 2020, Cell), and EY6A (Zhou et al., 2020a). Unlike these class 4 anti-RBD antibodies, C118 and C022

also occlude portions of the ACE2 binding site to facilitate more potent neutralization. A single-particle cryo-EM structure of a C118-S trimer complex demonstrated binding of C118 to an intact trimer, revealing an S configuration with increased separation between the RBDs than found in class 1-3 Fab-S or ACE2-S trimer structures, and revealed the potential for intra-spike crosslinking. These results define a cross-reactive class 4-like epitope on sarbecovirus RBDs that can be targeted in vaccine design and illustrate a mechanism by which the cryptic RBD epitope can be accessed on intact CoV S trimers.

Results

C022 and C118 IgGs recognize and neutralize diverse sarbecoviruses, including SARS-CoV-2 variants

From a survey to identify cross-reactive monoclonal antibodies isolated from SARS-CoV-2–infected donors from the New York area (Robbiani et al., 2020), we found antibodies isolated from different donors, C118 (*VH3-30/VL4-69*-encoded) and C022 (*VH4-39/VK1-5*-encoded), that recognized a diverse panel of 12 sarbecovirus RBDs spanning clades 1, 1/2, 2 and 3 (Figure 1). As evaluated by enzyme-linked immunosorbent assay (ELISA), C118 bound to RBDs from all sarbecoviruses tested, and C022 bound to all but two RBDs, similar to the class 4 anti-RBD antibody CR3022 (Figure 1C). By comparison, the cross-reactive class 3 anti-SARS RBD antibody S309 (Pinto et al., 2020) recognized half of the set of sarbecovirus RBDs, and C144, a more potent SARS-CoV-2 class 2 neutralizing antibody (Robbiani et al., 2020), bound to the SARS-CoV-2 RBD but not to RBDs from the other 11 sarbecovirus strains (Figure 1C).

To further define the C022 and C118 antibody epitopes, we evaluated binding of C118 and C022 to a panel of RBDs with mutations chosen from circulating variants that conferred resistance to one or more classes of anti-RBD antibodies (Li et al., 2020; Starr et al., 2021b; Weisblum et al., 2020). We also assessed binding to RBD substitutions identified in the B.1.1.7 and B.1.351 SARS-CoV-2 variants of concern (Rambaut et al., 2020; Tegally et al., 2020), and to mutations in the MA10 mouse-adapted SARS-CoV-2 virus (Leist et al., 2020).

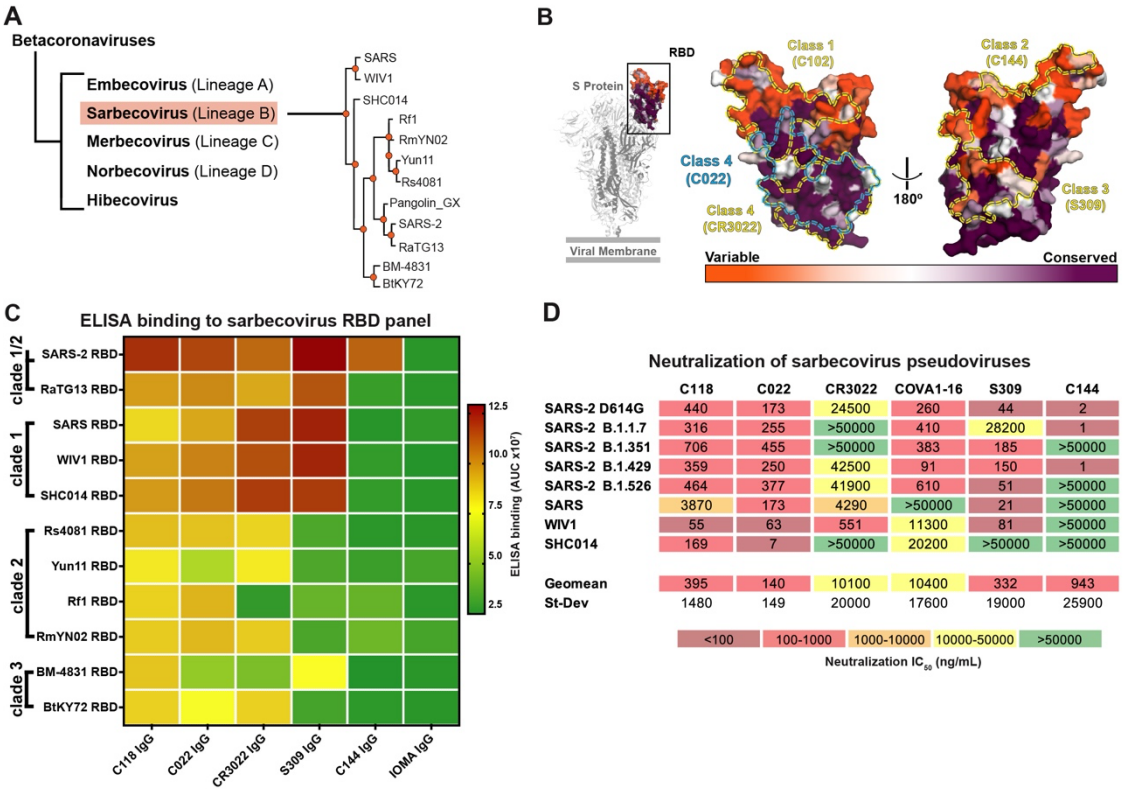

	C118	C022	CR3022	COVA1-16	S309	C144
SARS-2 D614G	440	173	24500	260	44	2
SARS-2 B.1.1.7	316	255	>50000	410	28200	1
SARS-2 B.1.351	706	455	>50000	383	185	>50000
SARS-2 B.1.429	359	250	42500	91	150	1
SARS-2 B.1.526	464	377	41900	610	51	>50000
SARS	3870	173	4290	>50000	21	>50000
WIV1	55	63	551	11300	81	>50000
SHC014	169	7	>50000	20200	>50000	>50000
Geomean	395	140	10100	10400	332	943
St-Dev	1480	149	20000	17600	19000	25900

Figure 1. C118 and C022 show diverse binding and neutralization of sarbecoviruses, see also Figures S1 and S2.

(A) Sarbecovirus (Lineage B) phylogenetic tree classified based on RBD sequence conservation.

(B) Left: Cartoon rendering of SARS-CoV-2 S trimer (PDB 6VYB) showing location of 'up' RBD (surface, orange and purple). Right: Amino acid sequence conservation of 12 RBDs calculated as described (Landau et al., 2005) plotted on a surface representation of a SARS-CoV-2 RBD structure (PDB 7BZ5). Primary RBD epitopes for the indicated representatives from defined classes of RBD-binding antibodies (class 1-4) (Barnes et al., 2020a) are indicated as yellow dotted lines (PDB 7K90, 6W41, 7JX3,7K8M). C022 epitope indicated as blue dotted line.

(C) Comparison of binding of the indicated monoclonal IgGs to a panel of sarbecovirus RBDs from ELISA data shown as area under the curve (AUC) values. Data presented are mean AUC values from two independent experiments. IOMA IgG is an anti-HIV-1 antibody serving as a negative control (Gristick et al., 2016).

(D) Neutralization IC_{50} values for the indicated IgGs against SARS-CoV-2 (D614G version of the original variant (GenBank: NC_045512)), SARS-CoV-2 variants of concern, and other ACE2-tropic sarbecovirus pseudoviruses. Geomean = geometric mean IC_{50} in which IC_{50} values >50000ng/mL were entered as 50000 ng/mL for the calculation. SD = standard deviation. IC_{50} values are means of 2-7 independent experiments.

Relative to wild-type RBD, C118, C022, CR3022 and S309 demonstrated a similar binding profile with respect to the RBD substitutions tested and exhibited a broader range of binding to the RBD mutants than did the more potent class 2 C144 antibody (Figure 1C and Figure S2A). Collectively, the ELISA binding data suggested that C022 and C118 recognize a highly-conserved epitope and are therefore likely to be class 4 anti-RBD antibodies.. We next measured neutralization potencies using an in vitro pseudovirus-based assay that quantitatively correlates with authentic virus neutralization (Schmidt et al., 2020) to evaluate SARS-CoV-2, SARS-CoV-2 RBD mutants, SARS-CoV-2 variants (Annavajhala et al., 2021; Faria et al., 2021; Rambaut et al., 2020; Tegally et al., 2020; Voloch et al., 2020; West et al., 2021; Zhang et al., 2021), and sarbecovirus strains known to infect human ACE2-expressing target cells (SARS-CoV-2, SARS-CoV, WIV1, SHC104, WIV16, Pangolin GD and Pangolin GX) (Figure 1D and Figure S2B-D). Against a panel of SARS-CoV-2 pseudotyped viruses harboring single amino acid RBD substitutions, C118 and C022 neutralized all viruses with potencies similar to 'wt' SARS-CoV-2, consistent with the results obtained in ELISA binding assays (S gene with D614 residue; GenBank: NC_045512) (Figure S2). For comparisons with SARS-CoV-2 variants of concern, the S gene we used to make 'wt' SARS-CoV-2 pseudovirus included the D614G substitution in the context of the Wuhan-Hu-1 spike (Korber et al., 2020), resulting in a 2-4–fold reduction in IC_{50}s for C022 and C118 antibodies (Figure 1D).

We found that C118 and C022 IgGs neutralized all four SARS-CoV-2 variants and all ACE2-tropic sarbecoviruses with 50% inhibitory concentrations (IC_{50} values) of <1 μg/mL, with the exception of C118, which inhibited SARS-CoV-pseudotyped viruses with an IC_{50} = 3.9 μg/mL (Figure 1D and Figure S2B-D). By contrast, the class 4 anti-RBD antibody CR3022 showed weak or no neutralization against the majority of pseudoviruses tested, with the exception of SARS-CoV (IC_{50} ~1.1 μg/mL) and WIV1 (IC_{50} ~0.6 μg/mL). The SARS-CoV-2 derived antibody COVA1-16 IgG neutralized SARS-CoV-2 variants of concern with IC_{50} values similar to C118 and C022 IgG, but showed weak neutralization for WIV1 (11.3ug/mL), SHC014 (20.2ug/mL) and no neutralization for SARS-CoV (>50ug/mL), which is consistent with previously published studies (Liu et al., 2020a; Liu et al., 2020b;

Brouwer et al., 2020). The class 3 S309 antibody showed strong neutralization potencies (IC_{50}s between 16 ng/mL and 120 ng/mL) against all viruses with the exceptions of the B.1.1.7 SARS-CoV-2 variant of concern and SHC014. The class 2 anti-RBD antibody C144 was highly potent against SARS-CoV-2 and the B.1.1.7 and B.1.429 variants (IC_{50}s between 1 ng/mL and 2 ng/mL), but did not neutralize the other SARS-CoV-2 variants or sarbecoviruses. Taken together, of the IgGs evaluated, C118 and C022 exhibited the greatest breadth of sarbecovirus neutralization (Figure 1D and Figure S2), consistent with their broad cross-reactive binding profile demonstrated by ELISA (Figure 1C and Figure S2A).

Crystal structures of C022-RBD and C118-RBD reveal class 4 RBD interactions and conservation of epitope residues

To understand the mechanism underlying the breadth of neutralization of C022 and C118, we solved structures of complexes between C118 Fab bound to SARS-CoV RBD and C022 bound to SARS-CoV-2 RBD to resolutions of 2.7Å and 3.2Å, respectively, chosen based on which complexes formed well-ordered crystals (Figure 2A,B and Table S1).

The C118-RBD and C022-RBD structures showed that both Fabs recognize an epitope that is highly-conserved among sarbecoviruses at the base of the RBD (Figure 1B), which is exposed only in 'up' RBD conformations as first described for the class 4 RBD-binding antibodies CR3022 (Huo et al., 2020; Yuan et al., 2020a; Yuan et al., 2020b) and EY6A (Zhou et al., 2020a). C022 and C118 use four of six complementarity-determining region (CDR) loops to interact with an epitope that extends towards the RBD ridge near the ACE2 binding site, and in the case of C022, includes an overlapping interacting residue ($K417_{RBD}$) (Figure 2C,D). In both structures, CDRH3 loops, CDRL2 loops, and portions of FWRL3 mediate the majority of RBD contacts and establish extensive polar and van der Waals interactions with RBD residues (Figure 2C,D), accounting for 71% of epitope buried surface area (BSA) on the RBD for the C022-RBD and C118-RBD structures, respectively (Table S2). No contacts were made in either complex with the $N343_{RBD}$ *N*-glycan (SARS-CoV-2 S numbering). SARS-CoV contains an additional potential *N*-linked glycosylation site at $N357_{RBD}$ (SARS-CoV S numbering), which if glycosylated, would not be contacted by

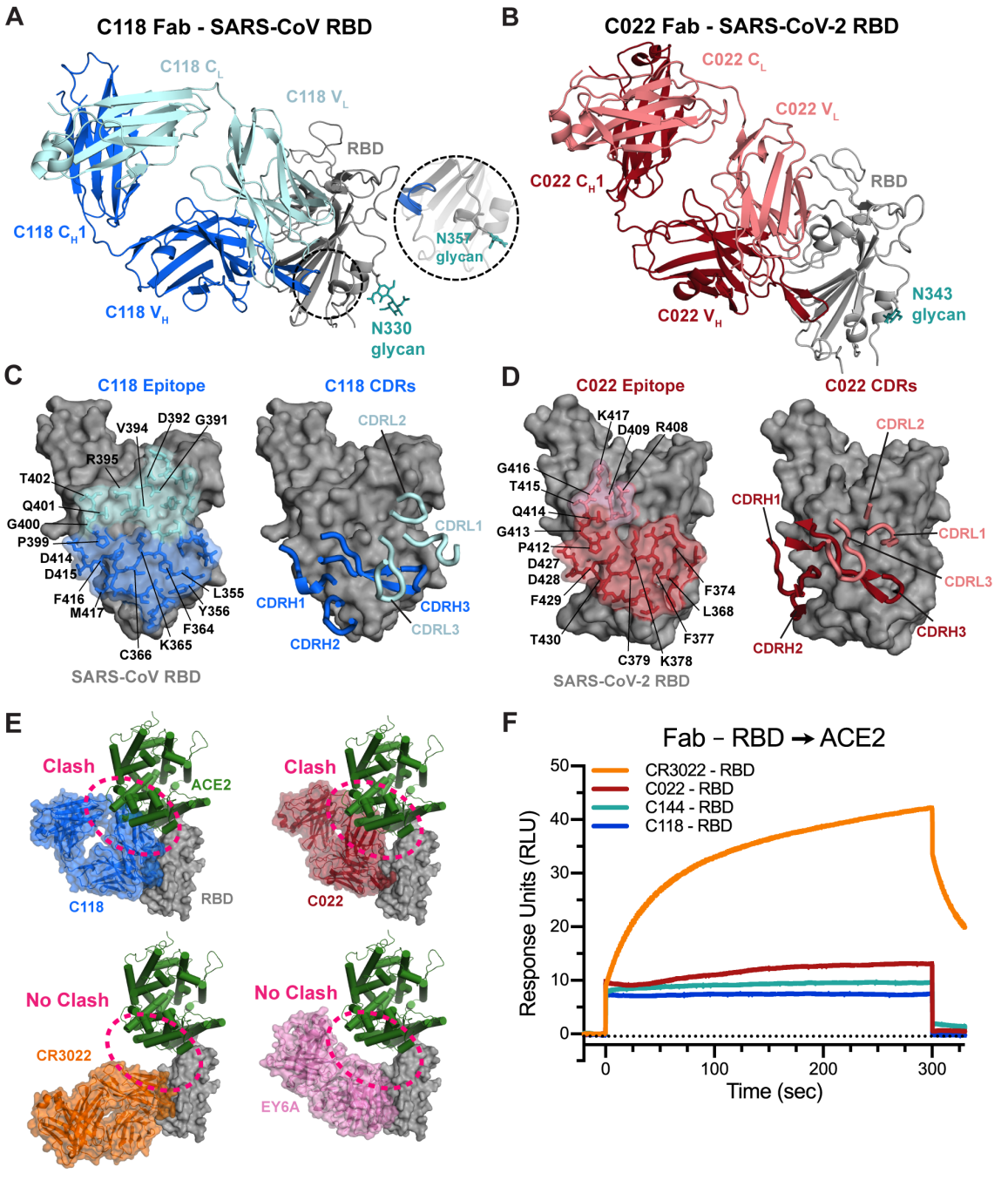

Figure 2. Crystal structures of C022 and C118 Fabs bound to RBDs reveal class 4-like RBD binding, see also Figures S1, S2 and Table S1.

(A,B) Cartoon renderings of crystal structures of (A) C0118 Fab complexed with SARS-CoV RBD, and (B) C022 Fab complexed with SARS-CoV-2 RBD. Dashed circle shows location of SARS-CoV $N357_{RBD}$ residue, with the inset showing the $N357_{RBD}$ asparagine and glycan modeled based on the SARS-CoV spike-S230 structure (PDB 6NB6).

(C,D) CDR loops and RBD epitope residues of (C) C118 Fab and (D) C022 Fab overlaid on RBDs represented as gray surfaces with stick representations of epitope residues. Framework region residues, which account for some of the contacts for both antibodies, are not shown in right panels.
(E) Comparison of Fab poses for binding to an RBD-ACE2 complex. C118 Fab (blue), C022 Fab (red), CR3022 Fab (PDB 6W41; orange), and EY6A Fab (PDB 6CZC pink) modeled onto an ACE2-RBD structure (PDB 6M0J; RBD shown as a gray surface and ACE2 shown as a green cartoon).
(F) Fab and ACE2 competition experiment by surface plasmon resonance. ACE2-Fc was immobilized on a chip and then complexes of SARS-CoV-2 with either C118, C022, CR3022, or C144 Fab flowed over. A binding event indicated no competition for RBD binding between ACE2 and the corresponding Fab.

C118, a favorable feature for cross-reactive recognition given that this potential *N*-linked glycosylation site is conserved in all S protein sequences except for SARS-CoV-2 (Figure 2A).

Overlaying the RBDs of our Fab-RBD structures with the RBD of the ACE2-RBD structure (PDB 6M0J) showed that the binding poses of both C118 and C022 placed the V_L domain of each Fab in a position that would clash with concurrent ACE2 binding, in contrast to the CR3022 and EY6A binding poses (Figure 2E). This binding orientation would sterically prevent RBD-ACE2 interactions, as has been suggested for other class 4 anti-RBD antibodies (Liu et al., 2020a; Piccoli et al., 2020a). To verify direct competition with ACE2, we conducted competition binding experiments using surface plasmon resonance (SPR). In the first setup, sACE2-Fc was coupled to a biosensor chip and a Fab-RBD complex was injected. RBD binding to immobilized sACE2-Fc was blocked in the presence of C118, C022, and C144 Fabs, which contrasts binding in the presence of CR3022 Fab (Figure 2F). Similar results were observed when SARS-CoV-2 RBD was coupled to a biosensor chip, an RBD-binding IgG was injected, and then soluble ACE2 was injected over the RBD-IgG complex (Figure S2E). Taken together, these results suggest that C118 and C022 block ACE2 binding to RBD and utilize a primary neutralization mechanism that prevents spike attachment to host cell ACE2 receptors.

Features of C118 and C022 recognition of the class 4 epitope

Class 4 RBD-binding antibodies contact a common epitope at the base of the RBD that is distant from the ACE2-binding site (Figure 3A). The epitopes of three class 4 antibodies,

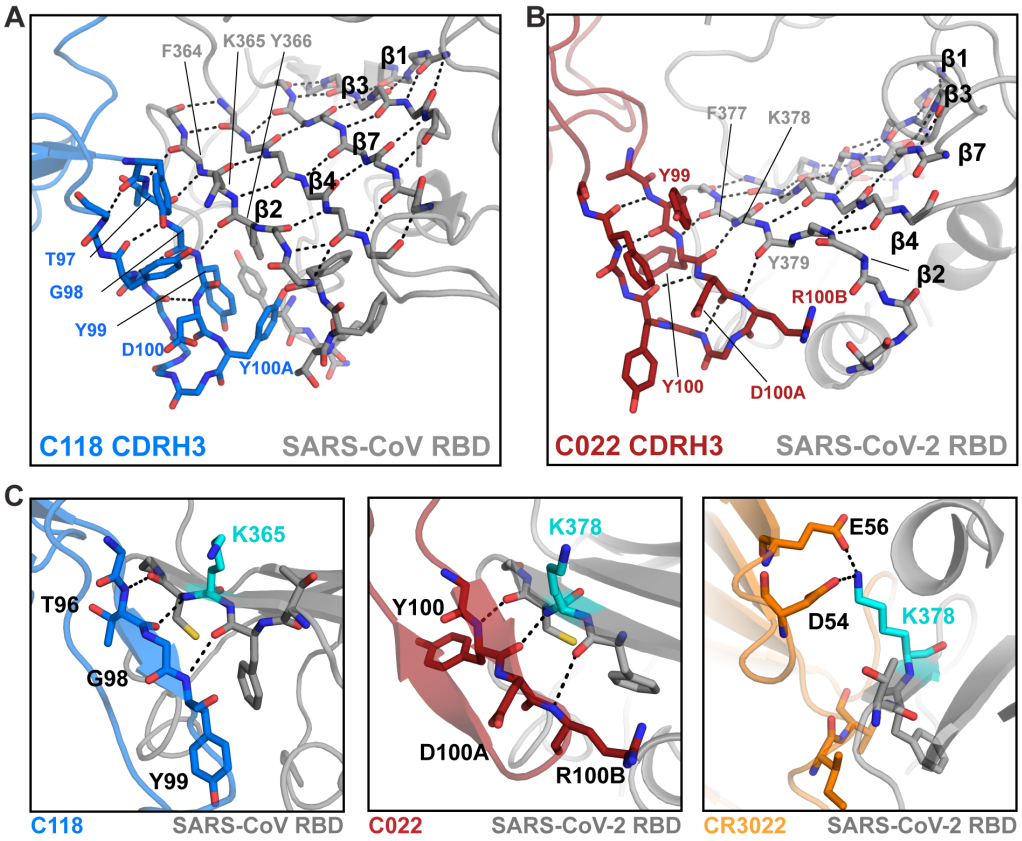

Figure 3. The C118 and C022 epitopes include a conserved RBD helix, see also Figures S3 and S4.

(A) Epitopes for ACE2 and monoclonal antibodies calculated from analyses of structures of RBD or S trimer complexes (human antibodies isolated from convalescent COVID-19 donors are C118, C022, COVA1-16, EY6A, and S2A4). RBDs shown are derived from SARS-CoV-2 except for the C118 panel, which is SARS-CoV RBD.

(B) Alignment of sequences for sarbecovirus RBDs (residue numbering for SARS-CoV-2 RBD). Secondary structure for SARS-CoV-2 RBD shown above alignment. Dots designate binding or neutralization for C118 (blue), C022 (red), or CR3022 (orange) for each strain. Diamonds designate RBD epitope residues for C118 binding to SARS-CoV (blue) and C022 (red) or CR3022 (orange) binding to SARS-CoV-2. Left boxes show binding by ELISA or neutralization of pseudovirus for each antibody for each strain; data for COVA1-16 from (Liu et al., 2020a). Circles show binding or neutralization, blank spaces designate not tested, and dashes designate no binding or neutralization. Shadings in the sequence alignment indicate conserved portions of epitope (green). Colored boxes show differing portion of epitope covering the □4 helix and following loop (pink.

(C) Cartoon representation of SARS-CoV-2 RBD (gray) showing overlapping antibody-interacting residues (green) as sticks in epitopes for C118, C022, COVA1-16, and CR3022 (corresponding to green shading in panel B).

(D) Cartoon representation of SARS-CoV-2 RBD (gray) showing α4 helix and following (sticks, pink) that differ in their contacts with C118, C022, COVA1-16, and CR3022 (pink shading in panel B).

(E) Cartoon representation of RBDs showing α4 region of RBD and C118 (left) or C022 (right) interacting loops with interacting Fab residues in light blue (C118) and light pink (C022).

C118, C022, and COVA1-16, also includes a patch reaching towards the ridge on the left side of the RBD as depicted in Figure 3A.

To compare the C118 and C022 epitopes with epitopes of other class 4 anti-RBD antibodies, we analyzed RBD residues contacted by C118, C022, COVA1-16, and CR3022 on aligned sequences of sarbecovirus RBDs (Figure 3B). Sequence conservation among sarbecoviruses at the C022 and C118 epitopes involves a majority of residues that are strictly-conserved or conservatively-substituted between SARS-CoV-2 and other RBDs (Figure 3B), likely explaining the broad cross-reactivity observed for these antibodies (Figure 1C). Comparison of the C118 and C022 epitopes showed a majority of recognized RBD residues are shared between the two antibodies (70% of C118 epitope also contacted by C022) (Figure 3B). CR3022 contacted a similar number of residues as C118 and C022, including the conserved patch at the RBD base (Figure 3B,C); however, a region from 404-417$_{RBD}$ that comprises an unstructured loop and the α4 helix above an internal RBD β-sheet contained only a single CR3022 contact residue (R408$_{RBD}$) and was not contacted by antibodies EY6A, S2A4 and S304; whereas C118, C022, and COVA1-16 showed contacts with this region (Figure 3B,D).

The α4 helix is proximal to the ACE2 receptor-binding motif and has less sequence conservation across the 12 sarbecoviruses (Figure 3B). To accommodate binding in this region, C118 uses insertions in its FWRL3 (54B-56$_{LC}$) to form a β-strand adjacent to the α4 helix, establishing both side chain and backbone interactions (Figure 3E – left panel). C022 showed similar binding in this region but used non-contiguous CDRH1, CDRH3, and CDRL2 loops (Figure 3E – right panel). C022 contacts were located more to the C-terminal end of the α4 helix than the C118 contacts and encompassed the disordered RBD loop that includes the ACE2-interacting residue K417$_{RBD}$ (K404$_{RBD}$ in SARS-CoV) (Lan et al., 2020) (Figure 3E – right panel). Additionally, C022 buried more surface area on RBD in this region than C118 (323Å^2 vs 150Å^2). Four of eight and five of nine RBD contacts for C118 and C022, respectively, were fully conserved among sarbecoviruses (Figure 3B), suggesting that interactions in this region may be possible with other sarbecoviruses. In particular, the conserved residue R408$_{RBD}$ (R395$_{RBD}$ in SARS-CoV) was contacted by both antibodies and

alone was responsible for 94Å^2 and 95Å^2 of BSA buried on the RBDs for C118 and C022, respectively. Despite both C118 and C022 engaging the α4 helix and residue R408$_{RBD}$, mutations at this position known to affect class 1 and class 4 anti-RBD antibodies (Greaney et al., 2021) had no effect on these antibodies (Figure S2A). Overall, engagement of the α4 helix region provided 16% (C118) and 36% (C022) of the BSA buried on RBD, and extended their epitopes past the cryptic epitope to bind adjacent to or overlapping with the ACE2 binding site.

Shared features of the C022 and COVA1-16 class 4 anti-RBD antibodies

The C022 epitope on RBD closely resembles the epitope of COVA1-16 (Figure 3A,B), a class 4 antibody isolated from a SARS-CoV-2 convalescent donor derived from *VH1-46/VK1-33* V-gene segments (Brouwer et al., 2020) (Figure S3). Yet, COVA1-16 showed weak neutralization (>10μg/mL) against WIV1-CoV, SHC014, and SARS-CoV pseudoviruses, which contrasts the potent C022 neutralization (Figure 1D). After superimposing the RBDs from crystal structures of SARS-CoV-2 RBD complexed with COVA1-16 (PDB 7JMW) and C022 (this study), the V_H-V_L domains of the bound Fabs were related by an root mean square deviation (RMSD) of 1.3Å (235 Cα atoms), with the majority of conformational differences occurring in the CDRH1 and CDRH2 loops (Figure S4A). Despite being derived from different V gene segments (which would affect their VH gene segment-encoded CDRH1 and CDRH2 loops), C022 and COVA1-16 recognized similar epitopes, contacting a common set of 23 RBD residues that include interactions with the RBD α4 helix (Figure 3B).

While C022 and COVA1-16 share a generally similar mode of binding, there are differences in interactions of residues encoded within their different V_H gene segments (i.e., their CDRH1 and CDRH2 loops) (Figure S4B). For example, the C022 contact with T430$_{RBD}$ was part of an extensive clasp made by an interaction between the C022 CDRH1 residue R33$_{HC}$ with backbone carbonyls of D427$_{RBD}$, D428$_{RBD}$, and F429$_{RBD}$ and with the sidechain of T430$_{RBD}$ (Figure S4C). Two of the same RBD residues (D427$_{RBD}$ and F429$_{RBD}$) interacted with an arginine from COVA1-16, but this arginine (R100B$_{HC}$) is located at the base of the

CDRH3 loop rather than within CDRH1, as is the case with C022 $R33_{HC}$. The larger separation distance from the RBD of COVA1-16 $R100B_{HC}$ allowed it to form a sidechain-backbone H-bond with $D427_{RBD}$ similar to a sidechain–backbone H-bond involving C022 $R33_{HC}$ and $D428_{RBD}$, but precluded interactions with $D428_{RBD}$ and $T430_{RBD}$ (Figure S4D). In addition, the COVA1-16 CDRH1 was shorter than the C022 CDRH1 (7 versus 9 residues) (Figure S3A), and was shifted away from the RBD relative to the C022 CDRH1. These differences, in addition to fewer LC interactions by COVA1-16, resulted in less total BSA for COVA1-16 relative to C022 (1607 $Å^2$ vs 1875 $Å^2$, respectively) despite similar contributions from CDRH3 loops (Table S2).

Interactions with RBD main chain atoms facilitate recognition of diverse RBDs

The paratopes of both C118 and C022 were dominated by their long CDRH3 loops (20 and 21 residues, respectively) (Figure 4A,B and Figure S3), which make up ~half of the buried surface areas (BSAs) of each paratope (461 $Å^2$ of 1020 $Å^2$ for C118 and 537 $Å^2$ of 969 $Å^2$ for C022) (Table S2). The C118 and C022 CDRH3s comprise two anti-parallel β-strands that extend a largely internal RBD β-sheet (β-strands β1-β4 and β7) through main chain H-bonds between the RBD β2 strand ($377\text{-}379_{RBD}$) and the first CDRH3 β-strand (CDRH3 residues 97-99 (C118) or 100-100B (C022)) (Figure 4A,B). A similar feature is also seen in the structure of the COVA1-16–RBD complex (Liu et al., 2020a), which shares a nearly identical CDRH3 sequence with C022 (Figure S4E).

C118 and C022 form extensive backbone interactions with RBD, with 10 and 9 H-bonds formed with the backbone of RBD, respectively. Extensive backbone interactions in the C118 and C022 epitopes could contribute to their breadth of binding and neutralization across sarbecoviruses, as backbone interactions would facilitate binding despite side chain substitutions, which are rare across the RBD sequences listed (Figure 3B), but could occur in other CoV RBDs. For example, the backbone H-bonds between the CDRH3s of C118 and C022 with the RBD β2 strand allow for binding despite substitution at position $K378_{RBD}$ ($K365_{RBD}$ in SARS-CoV) (Figure S2A and Figure 4C). By contrast, the class 4 antibody CR3022 uses side chain interactions (potential electrostatic interactions between $D54_{HC}$ and

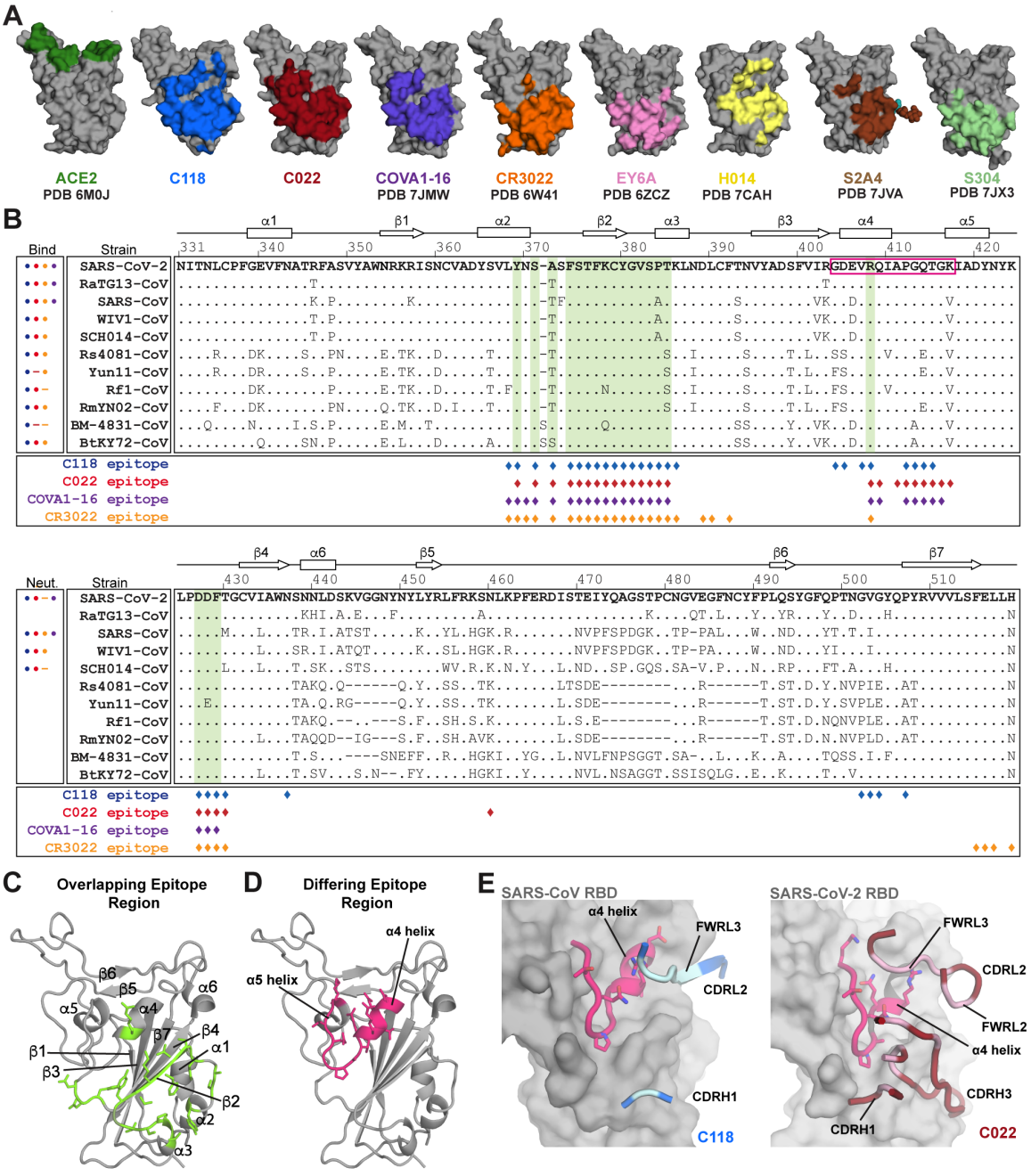

Figure 4: C118 and C022 Fabs primarily use their CDRH3s for main chain backbone contacts with the RBD β2 strand, see also Table S2.

(A) Close-up cartoon showing β-hairpin formed by C118 CDRH3 (blue sticks) and β-sheet formation with SARS-CoV RBD (grey cartoon with sticks). H-bonds shown as black dashed lines.

(B) Close-up cartoon showing β-hairpin formed by C022 CDRH3 (red sticks) and β-sheet formation with SARS-CoV-2 RBD (grey cartoon with sticks). H-bonds shown as black dashed lines.

(C) Cartoon and stick representation of C118-RBD (left), C022-RBD (middle) and CR3022-RBD (right) showing distinct interactions with residue $K365_{SARS}$/$K378_{SARS2}$ (cyan).

$E56_{HC}$ and $K378_{RBD}$); thus CR3022 is sensitive to mutation at $K378N_{RBD}$ (Figure S2A). This is consistent with CR3022 not binding to Rf1-CoV RBD (Figure 1C), which contains an asparagine at the equivalent position to SARS-CoV-2 $K378_{RBD}$ (Figure 3B), whereas C118 and C022 binding to Rf1-CoV RBD was not affected. Overall, mainchain H-bond interactions likely reduce sensitivity to RBD sidechain substitutions, making antibodies such as C118 and C022 more tolerant to differences between sarbecoviruses strains or variants.

C118-S cryo-EM structure shows increased S trimer opening

On an S trimer, the class 4 cryptic epitope is at the base of the RBD, where it faces towards the center of the trimer (Barnes et al., 2020a; Huo et al., 2020; Yuan et al., 2020b). The epitope is buried in the closed, prefusion S conformation and interacts with portions of th spike S2 subunit and neighboring 'down' RBDs. Compared to class 2 or class 3 anti-RBD antibodies that recognize their epitopes in 'up' or 'down' RBD conformations (Barnes et al., 2020a), the class 4 epitope is less accessible and requires two 'up' RBDs for antibody binding (Piccoli et al., 2020a). Additionally, class 4 antibody binding may also require RBD rotation to prevent steric clashes with neighboring 'up' RBDs, as observed for the complexes of S trimer with EY6A, S2A4, and S304 (Piccoli et al., 2020a; Zhou et al., 2020a).

Given the similar binding poses of C118 and C022 antibodies, which bind with a more acute angle with respect to the RBD than EY6A or CR3022 (Figure 2E), and the increased breadth and potency of C118 and C022 relative to other class 4 anti-RBD antibodies (Figure 1D), we sought to understand the requirements for epitope recognition on a S trimer. Thus, we solved a single-particle cryo-EM structure of C118 Fabs bound to SARS-CoV-2 S 6P trimers (Hsieh et al., 2020), finding two distinct states defined by RBDs adopting various rotational conformations (Figure 5A,B and Figure S5), as well as C118 Fab bound to dissociated S1 subunit protomers (Figure S5B). For the state 1 C118-S trimer complex structure solved to 3.4Å, we subsequently used symmetry expansion and local refinement to generate a 3.7Å map of the C118 V_HV_L – RBD interface (Figure S5B-E).

The C118 pose with respect to the RBD observed in the C118 – SARS-CoV-2 S structure was similar to the C118 – SARS-CoV RBD crystal structure (Figure S5F), demonstrating consistent recognition of the antibody epitope on both SARS-CoV-2 and SARS-CoV RBDs. Furthermore, the C118 binding pose was oriented higher on the RBD relative to other class 4 anti-RBD antibodies (Figure 5C), and was consistent with SPR competition data that suggested C118 would sterically hinder ACE2 binding to the same protomer (Figure S2E).

Despite differences in binding poses relative to other class 4 antibodies (Figure 5C), C118 binding also resulted in RBD conformations displaced further from the trimer center relative to S2E12 (a class 1 anti-RBD neutralizing antibody) (Tortorici, 2020) and ACE2 (Yan et al., 2020) (Figure 5D). On average, class 4 anti-RBD antibody binding resulted in an ~15-20Å displacement of the RBD relative to ACE2-bound conformations, which likely results in destabilization of the spike trimer. Indeed, S1 shedding induced by class 4 antibodies has been described as a possible neutralization mechanism (Huo et al., 2020; Piccoli et al., 2020a; Wec et al., 2020). The presence of C118-S1 protomer classes in our cryo-EM data suggested that C118 also induces shedding (Figure S5), but the role S1 shedding and premature S-triggering plays in C118-mediated neutralization requires further investigation.

C118 and C022 neutralization of sarbecoviruses demonstrate differential effects of avidity enhancement

Neutralization of SARS-CoV-2 and SARS-CoV by COVA1-16 was found to be mediated by avidity effects based on potent neutralization by the bivalent COVA1-16 IgG, but not the monovalent Fab (Liu et al., 2020a). To evaluate whether intra-spike crosslinking, one source of avidity enhancement for bivalent antibodies, was possible for C118 or C022 IgGs, we examined the C118-S trimer structure to ask whether the positioning of two Fabs on adjacent RBDs would be compatible with binding by a single IgG. As previously described for other anti-RBD IgGs, we compared the distance between residues near the C-termini of adjacent Fab C_H1 domains to analogous distances in crystal structures of intact IgGs, setting a cut-off of ≤65Å as potentially allowing a single IgG to include both Fabs (Barnes et al., 2020a). The measured distance for the C-termini of adjacent Fab C_H1 domains in the symmetric State 1

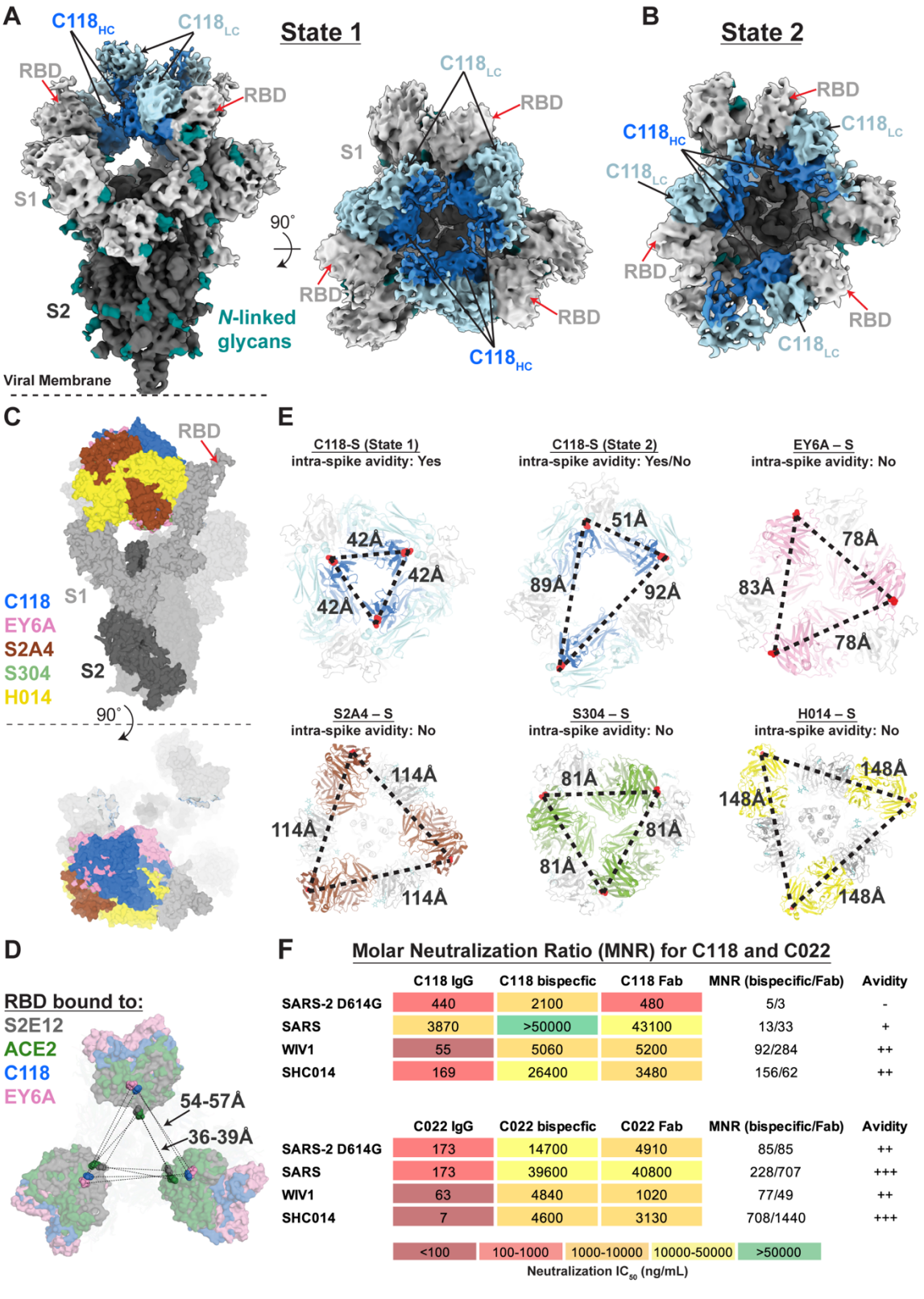

F Molar Neutralization Ratio (MNR) for C118 and C022

	C118 IgG	C118 bispecfic	C118 Fab	MNR (bispecific/Fab)	Avidity
SARS-2 D614G	440	2100	480	5/3	-
SARS	3870	>50000	43100	13/33	+
WIV1	55	5060	5200	92/284	++
SHC014	169	26400	3480	156/62	++

	C022 IgG	C022 bispecfic	C022 Fab	MNR (bispecific/Fab)	Avidity
SARS-2 D614G	173	14700	4910	85/85	++
SARS	173	39600	40800	228/707	+++
WIV1	63	4840	1020	77/49	++
SHC014	7	4600	3130	708/1440	+++

<100 | 100-1000 | 1000-10000 | 10000-50000 | >50000

Neutralization IC_{50} (ng/mL)

Figure 5. Cryo-EM structure of C118-S complex shows binding to cryptic epitope and the potential for intra-spike crosslinking, see also Figure S5 and Table S3.

(A) 3.4Å cryo-EM density for the C118 – S trimer complex (State 1). Side view (left panel) illustrates orientation with respect to the viral membrane (dashed line). Top view (right panel) shows symmetric binding at the trimer apex with C118 HC (blue) oriented in the interior.

(B) 4.4Å cryo-EM density for the C118 – S trimer complex (State 2). Top view illustrates asymmetry of complex due to RBD rotation in one protomer.

(C) Composite model of an open SARS-CoV-2 trimer bound by class 4 Fabs: C118 (this paper, blue), EY6A (PDB 6ZDH, pink), S2A4 (PDB 7JVC, brown), the class 4 anti-SARS antibody S304 (PDB 7JW0, green), and H014 (PDB 7CAK, yellow).

(D) Comparison of S trimer openness by measurements of Cα distances for $D428_{RBD}$ between adjacent 'up' RBDs in S trimers complexed with: the class 1 antibody S2E12 (PDB 7K43, gray), soluble ACE2 (PDB 7KMS, green) and the class 4 antibodies C118 (this study, blue) and EY6A (PDB 6ZDH, pink).

(E) Prediction of potential intra-spike avidity effects by measurement of Cα distances between the C-termini of adjacent C_H1 domains for the mAb-S trimer complexes described in panel C. Measurements were used to evaluate the potential for intra-spike crosslinking by an IgG binding to a single spike trimer as described (Barnes et al., 2020a). For the H014-S complex, the C_H1-C_L domains were rigid body fit into the cryo-EM density (EMD-30333) prior to measurements.

(F) IC_{50} values and molar neutralization ratios (MNRs) defined as: [IC_{50} Fab or bispecific IgG (nM)/IC_{50} IgG (nM)] (Klein and Bjorkman, 2010) for C118 and C022. IC_{50} values shown for the IgGs are from Figure 1D. IC_{50} values for all assays against SARS-CoV-2 and SARS-CoV are means of 2-7 independent experiments. Two MNRs are presented in the MNRs (bispecific/Fab) column: the MNR calculated using a bispecific IgG versus the bivalent IgG (left) and the MNR calculated using a Fab versus the bivalent IgG (right). Neutralization results with MNRs ≤5 are indicated as not demonstrating avidity effects (-), >10 are indicated as demonstrating minimal avidity (+), results with one MNR> 50 are indicated as moderate avidity (++), and MNRs demonstrating strong avidity effects (one MNR >700) are indicated as +++.

C118-S trimer structure was 41Å (Figure 5E), suggesting that intra-spike crosslinking would be possible for C118 IgGs bound to spike trimers. The asymmetric State 2 C118-S structure included distances of 50Å, 89Å, and 92Å (Figure 5E), also allowing intra-spike crosslinking between one combination of two bound RBDs, as well as the potential for inter-spike crosslinking between adjacent spikes on the virion surface. In comparison, no other class 4 anti-RBD Fab-S trimer structures showed measured distances that would be compatible with intra-spike crosslinking (Figure 5E), thus any potential avidity effects for those IgGs could only occur via inter-spike crosslinking.

To further evaluate whether avidity could also facilitate cross-reactive neutralization by the C118 and C022 antibodies, we compared neutralization of SARS-CoV-2, SARS-CoV,

WIV1, and SHC014 by the bivalent C118 and C022 IgGs and by two monovalent forms of each antibody: a 50 kDa Fab and an IgG size-matched bispecific IgG containing only one relevant Fab. The bispecific IgGs included one C118 or C022 RBD-binding Fab and a second non-RBD-binding Fab derived from the HIV-1 antibody 3BNC117 (Scheid et al., 2011). To interpret neutralization results, we calculated molar neutralization ratios (MNRs) defined as: [IC_{50} Fab or bispecific IgG (nM)/IC_{50} IgG (nM)] (Klein and Bjorkman, 2010). In the absence of avidity effects resulting from either crosslinking within a spike trimer (intra-spike crosslinking) or cross-linking between adjacent spike trimers (inter-spike crosslinking), an MNR would be 2.0, which accounts for twice as many relevant Fabs in a bivalent IgG compared to its monovalent forms.

Using pseudotyped SARS-CoV-2, SARS-CoV, WIV1, and SHC014, we derived neutralization potencies of the bivalent IgG, monovalent bispecific IgG, and Fab forms of C118 and C022 and then calculated MNRs for the bivalent IgG to bispecific IgG comparison (bispecific MNR) and for the bivalent IgG to Fab comparison (Fab MNR) (Figure 5F). Comparisons between the Fab and bispecific IgG forms of monovalent antibody allowed evaluation of potential steric affects that could increase neutralization potencies for larger IgGs compared to smaller Fabs. With the exception of the low MNRs derived from the IgG comparison with the bispecific and Fab forms of C118 against SARS-CoV-2 (MNRs of 5 and 3, respectively), we found mostly high MNRs ranging from the lowest values of 13 and 33 for the MNRs for C118 against SARS-CoV (where 11 is a minimal estimate since the C118 bispecific was non-neutralizing) to the highest values of 708 and 1444 for the C022 bispecific and Fab MNRs against SHC014. Four of the bispecific to Fab MNR comparisons showed a two-fold or higher Fab MNR than the comparable bispecific MNR, suggesting that at least some of the increased potencies of the bivalent IgGs compared with their counterpart Fabs resulted from steric effects. However, six of the eight monovalent to bivalent comparisons exhibited MNRs well over 70, suggestive of strong avidity effects. By contrast, mean MNRs derived for broadly neutralizing anti-HIV-1 Env antibodies are ≤10 (Wang et al., 2017), consistent with the low spike density on HIV-1 virions that largely prevents inter-

spike crosslinking, and the architecture of the HIV-1 Env trimer, which prohibits intra-spike crosslinking for all known HIV-1 broadly neutralizing antibodies (Klein and Bjorkman, 2010). Taken together with the analysis of the C118-S trimer structure, the observed avidity effects for C118 IgGs binding to WIV1 and SHC014 and for the related C022 IgGs binding to the four viruses tested could arise from intra-spike as well as inter-spike crosslinking.

The question as to why C118 exhibits little or no avidity effects for neutralization of SARS-CoV-2 and SARS-CoV is difficult to address since the same IgG showed strong avidity effects against WIV1 and SHC014, and C022, which binds similarly to C118, showed avidity effects in neutralization of all four pseudoviruses. These results could derive from different binding characteristics for C118 to the SARS-CoV-2 and SARS-CoV RBDs compared with C118 and C022 interactions with the other sarbecoviruses evaluated. Indeed, simulations of avidity effects demonstrated that some combinations of IgG concentration and antigen-binding affinity and kinetic constants showed no advantages of bivalent versus monovalent binding (Klein, 2009; Klein and Bjorkman, 2010). Thus the effects of avidity are a complicated function of concentration and binding constants that preclude predictions in the absence of experimental data.

Discussion

Concerns about coronaviruses having spillover potential as well as the increasing prevalence of SARS-CoV-2 variants necessitates identification of cross-reactive antibodies. Antibodies elicited against infectious viruses for which there are multiple circulating variants, either within an individual or the population, often show a trade-off between potency and breadth (Corti et al., 2010; Desrosiers et al., 2016). In the case of antibody responses against SARS-CoV-2, the cause of the current global pandemic, many strongly neutralizing antibodies have been isolated that block ACE2 receptor interactions (Barnes et al., 2020a; Dejnirattisai et al., 2021; Lee et al., 2021; Liu et al., 2020b; Piccoli et al., 2020b). However, the ACE2-binding region of the RBD also tends to accumulate amino acid changes, as evidenced by substitutions identified in the current SARS-CoV-2 variants of concern (Annavajhala et al.,

2021; Faria et al., 2021; Rambaut et al., 2020; Tegally et al., 2020; Voloch et al., 2020; West et al., 2021; Zhang et al., 2021), thus reducing the potential efficacies of vaccines and monoclonal antibody therapies. Recent studies suggest that antibodies against the S2 subunit offer the potential of greater cross-reactivity across coronaviruses, but these antibodies generally lack strong neutralization potency (Sauer et al., 2021; Shah et al., 2021; Wang et al., 2021).

The class 4 RBD-binding epitope, which is more conserved than the class 1 and class 2 RBD epitopes, represents a plausible target for the elicitation of antibodies with broad cross-reactive recognition across sarbecoviruses. Indeed, some recently described class 4 antibodies (e.g., CR3022, H014, COVA1-16, EY6A, ADI-56046) neutralize two or more sarbecovirus strains, and/or can bind RBDs from multiple sarbecoviruses (Liu et al., 2020a). However, while many class 4 antibodies show some cross-reactivity, they generally exhibit decreased potencies against heterologous sarbecovirus strains. For example, the SARS-CoV–derived CR3022 antibody does not potently neutralize SARS-COV-2 (Huo et al., 2020), and the SARS-CoV-2 – derived COVA1-16 antibody does not potently neutralize SARS-CoV, WIV1, or SHC014 (Liu et al., 2020a; Liu et al., 2020b).

Here we characterized two antibodies, C118 and C022, derived from different COVID-19 convalescent donors (Robbiani et al., 2020), which show breadth of and potent neutralization against sarbecoviruses of all three clades. The structural similarity of RBD binding poses between C022 and COVA1-16 (Liu et al., 2020a), which was derived from yet a third COVID-19 convalescent donor (Brouwer et al., 2020), suggests that these sorts of cross-reactive antibodies are commonly elicited by natural infection and that their epitope represents an attractive target for immunogen design. Of particular importance for the current pandemic, circulating variants of concern or variants of interest did not confer resistance to the C118 and C022 antibodies. In addition, C118 and C022 antibodies were not affected by naturally-occurring RBD mutations that undermine the activity of several antibodies approved for therapeutic use (Hoffmann et al., 2021; Starr et al., 2021b).

Analysis of our C118-RBD and C022-RBD complex structures revealed key details of cross-reactive recognition and broad sarbecovirus neutralization. First, C118 and C022 utilize long CDRH3s to facilitate interactions with the cryptic RBD epitope at the base of the RBD. In contrast to less potent class 4 antibodies such as CR3022 (Huo et al., 2020; Yuan et al., 2020a; Yuan et al., 2020b) and EY6A (Zhou et al., 2020a) that also contact this region, the longer CDRH3 provides the opportunity to target a highly-conserved patch of residues across sarbecoviruses with an orientation that extends the epitope upwards to the ACE2 binding site, a structural feature shared with COVA1-16 (Liu et al., 2020a). Second, the aforementioned binding poses of C118, C022, and COVA1-16, as well as overlap of the C022 epitope with the edge of the ACE2 binding site, suggested competition with ACE2 as part of their neutralization mechanisms. Indeed, competition experiments reported here for C118 and C022 and by others for COVA1-16 (Liu et al., 2020a) demonstrated competition with ACE2 for SARS-CoV-2 RBD binding. Third, C118 and C022 formed many interactions with backbone atoms of RBD residues, adding a second level of buffering against viral escape since amino acid substitutions at these positions are less likely to abrogate antibody binding. Finally, the demonstration that C118 and C022 bivalency increased potency of neutralization against some of the viruses evaluated showed the potential for these antibodies to utilize avidity effects for neutralization of sarbecoviruses. Given the requirement for two ‘up’ RBDs on a S trimer for class 4 antibody binding, bivalent binding within a single S trimer would be possible. Thus we suggest that intra-spike crosslinking would be an advantage for neutralization of sarbecoviruses, where avidity effects likely play a role.

In conclusion, class 4 antibodies that access the cryptic RBD epitope and compete with ACE2 binding are important for understanding cross-reactivity of human SARS-CoV-2 antibody responses elicited by natural sarbecovirus infection. We suggest that potent class 4 anti-RBD antibodies could be used therapeutically to avoid resistance to SARS-CoV-2 variants of concern, perhaps after in vitro selection to further improve their potencies. Structural characterization of these antibodies could also be used to inform future vaccine design efforts to produce immunogens that preferentially elicit C118 and C022-like cross-

reactive antibodies by blocking RBD epitopes recognized by class 1 and class 2 antibodies, which typically are not cross-reactive to other sarbecoviruses.

Methods

Lead Contact

All requests for further information or requests for resources and reagents should be directed to the Lead Contact, Pamela Bjorkman (bjorkman@caltech.edu).

Materials Availability

All expression plasmids generated in this study for CoV proteins, CoV pseudoviruses, human Fabs and IgGs are available upon request.

Cell lines

Cells for pseudovirus production (HEK293T) were cultured at 37°C and 5% CO_2 in Dulbecco's modified Eagle's medium (DMEM, Gibco) supplemented with 10% heat-inactivated fetal bovine serum (FBS, Sigma-Aldrich) and 5 µg/ml Gentamicin (Sigma-Aldrich).

Target cells for pseudovirus neutralization experiments ($HEK293T_{ACE2}$) were generated as described (Robbiani et al., 2020) and cultured at 37°C and 5% CO_2 in Dulbecco's modified Eagle's medium (DMEM, Gibco) supplemented with 10% heat-inactivated fetal bovine serum (FBS, Sigma-Aldrich), 5 µg/ml gentamicin (Sigma-Aldrich), and 5µg/mL Blasticidin (Gibco).

Expi293F cells (Gibco) for protein expression were maintained at 37°C and 8% CO_2 in Expi293 expression medium (Gibco), transfected using an Expi293 Expression System Kit (Gibco) and maintained under shaking at 130 rpm. All cell lines were female and were not specifically authenticated.

Bacteria

E. coli DH5 Alpha (Zymo Research) used for propagation of expression plasmids were cultured with shaking at 250 rpm at 37˚C in LB broth (Sigma-Aldrich).

Viruses

To generate pseudotyped viral stocks, HEK293T cells were transfected with pNL4-3ΔEnv-nanoluc and pSARS-CoV2-S_{trunc} (Robbiani et al., 2020) using polyethylenimine, leading to production of HIV-1-based pseudovirions carrying the SARS-CoV-2 S protein at the surface. Eight hours after transfection, cells were washed twice with phosphate buffered saline (PBS) and fresh media was added. Supernatants containing pseudovirus were harvested 48 hours post transfection, filtered and stored at -80°C. Infectivity of pseudoviruses was determined by titration on $293T_{ACE2}$ cells.

Phylogenetic trees

Sequence alignments of RBDs were made with Clustal Omega (Sievers et al., 2011). Phylogenetic trees were calculated from amino acid alignments using PhyML 3.0 (Guindon et al., 2010) and visualized with PRESTO (http://www.atgc-montpellier.fr/presto).

Graphical Abstract

Portions of the graphical abstract were produced using www.biorender.com. The remaining parts were made using Adobe Illustrator.

Protein Expression

Fabs and IgGs were expressed and purified as previously described (Scharf et al., 2015; Schoofs et al., 2019; Liu et al., 2020a) and stored at 4 °C. Bispecific IgGs (C118 or C022 plus 3BNC117, a non-coronavirus binding HIV-1 antibody (Scheid et al., 2011)) were produced by co-transfection of two heavy chain and two light chain genes that included knobs-into-holes mutations in IgG Fc and a domain cross-over in the 3BNC117 Fab to prevent incorrect light chain pairing (Schaefer et al., 2011). Antibody CDR lengths were determined using the IMGT definitions (Lefranc et al., 2015; Lefranc et al., 2009).

The following C-terminally 6xHis-tagged RBD proteins were transfected and expressed as described previously (Cohen et al., 2021): SARS-CoV-2 RBD (residues 328-533), SARS-CoV-2 RBD mutants (residues 319-541), SARS RBD (residues 318-510), SHC014 RBD (residues 307-524), WIV-1 RBD (residues 307-528), RaTG13 RBD (residues 319-541), Rs4081 RBD (residues 310-515), Yun11 RBD (residues 310-515), Rf1 RBD (residues 310-515), RmYN02 RBD (298-503), BM-4831 RBD (residues 310-530), BtKY72 RBD (residues 309-530). A trimeric SARS-CoV-2 ectodomain (residues 16-1206 of the early SARS-CoV-2 GenBank MN985325.1 sequence isolate with 6P (Hsieh et al., 2020) stabilizing mutations, a mutated furin cleavage site between S1 and S2, a C-terminal TEV site, foldon trimerization motif, octa-His tag, and AviTag) was expressed as described (Barnes et al., 2020a; Barnes et al., 2020b). A gene encoding a 6xHis-tagged soluble human ACE2 construct (residues 1-615) was purchased from Addgene (Catalog # 149268) and expressed and purified as described (Chan et al., 2020).

SARS-CoV-2 S trimer, RBDs, and soluble ACE2 were purified by Nickel-NTA and size-exclusion chromatography using a Superdex 200 column (GE Life Sciences) as described (Barnes et al., 2020a; Cohen et al., 2021). Peak fractions were identified by SDS-PAGE, and those containing S trimer, monomeric RBDs, or soluble ACE2 were pooled, concentrated, and stored at 4 °C (RBDs) or flash frozen in nitrogen and stored at -80 °C (S trimer) until use.

ELISAs

Purified RBD at 10 μg/ml in 0.1 M $NaHCO_3$ pH 9.8 was coated onto Nunc® MaxiSorp™ 384-well plates (Sigma) and stored overnight at 4ºC. The following day, plates were blocked with 3% bovine serum albumin (BSA) in TBS-T Buffer (TBS + 0.1% Tween20) for 1hr at room temperature. Blocking solution was removed from the plates, purified IgGs at 50 μg/mL were serially diluted by 4-fold with TBS-T/3% BSA and added to plates for 3 hr at room temperature. Plates were washed with TBS-T and then incubated with 1:15,000 dilution of secondary HRP-conjugated goat anti-human IgG for 45 minutes at room

temperature (Southern Biotech). Plates were washed again with TBS-T and developed using SuperSignal™ ELISA Femto Maximum Sensitivity Substrate (ThermoFisher) and read at 425 nm. ELISAs were done in duplicate, and curves were plotted and integrated to obtain the area under the curve (AUC) using Graphpad Prism v9.1.0.

Neutralization assays

SARS-CoV-2, SARS-CoV-2 variants of concern (Annavajhala et al., 2021; Faria et al., 2021; Rambaut et al., 2020; Tegally et al., 2020; Voloch et al., 2020; West et al., 2021; Zhang et al., 2021), SARS-CoV, WIV1, and SHC014 pseudoviruses based on HIV-1 lentiviral particles were prepared as described (Cohen et al., 2021; Crawford et al., 2020; Robbiani et al., 2020) using genes encoding S protein sequences with cytoplasmic tail deletions: 21 amino acid deletions for SARS-CoV-2, SARS-CoV-2 variants of concern, WIV1, and SHC014 and a 19 amino acid deletion for SARS-CoV. Plasmids expressing the spike protein found in the bat (*Rinolophus Sinicus*) coronavirus bCoV-WIV16 as well as the pangolin (*Manis javanica*) coronaviruses from Guandong, China (pCoV-GD) and Guanxi, China (pCoV-GX) have been described previously and are based on ALK02457 (Genebank), Pangolin_CoV_EPI_ISL_410721(Gisaid) and Pangolin_CoV_EPI_ISL_410542 (Gisaid) (Muecksch et al., 2021).

Relative to the SARS-CoV-2 spike gene (Wuhan-Hu-1 Spike Glycoprotein Gene, D614G mutant, designated as 'wt' in Figure 1D), the SARS-CoV-2 variants of concern included the D614G mutation and the following other substitutions: B.1.351: L18F, D80A, D215G, del242-244, R246I, K417N, E484K, N501Y, A701V; B.1.1.7: del69-70, del144, N501Y, A570D, P681H, T716I, S982A, D1118H; B.1.429: S13I, W152C, L452R, and B.1.526: L5F, T95I, D253G, E484K, A701V. For neutralization assays presented in Figure 1D, four-fold dilutions of purified IgGs (starting concentrations of 50 μg/mL) were incubated with a pseudotyped virus for 1 hour at 37˚C. Cells were washed twice with phosphate-buffered saline (PBS) and lysed with Luciferase Cell Culture Lysis 5x reagent (Promega) after incubation with $293T_{ACE2}$ target cells for 48 hours at 37˚C. NanoLuc Luciferase activity in lysates was measured using the Nano-Glo Luciferase Assay System (Promega). Relative

luminescence units (RLUs) were normalized to values derived from cells infected with pseudotyped virus in the absence of IgG. Half-maximal inhibitory concentrations (IC_{50} values) were determined using 4- or 5-parameter nonlinear regression in AntibodyDatabase (West et al., 2013).

Relative to the SARS-CoV-2 spike gene (Wuhan-Hu-1; NC_045512, D614 sequence designated as 'wt' in Figure S2), a panel of plasmids expressing RBD mutant SARS-CoV-2 S proteins in the context of pSARS-CoV-2-$S_{\Delta 19}$ have been described previously (Muecksch et al., 2021; Robbiani et al., 2020; Schmidt et al., 2020; Weisblum et al., 2020). The E484K substitution was constructed in the context of a pSARS-CoV-2-$S_{\Delta 19}$ variant with a mutation in the furin cleavage site (R683G) to increase infectivity (Muecksch et al., 2021). The IC_{50} values of this pseudotype (E484K/R683G) was compared to a wild-type SARS-CoV-2 S sequence carrying R683G in the subsequent analyses. For neutralization assays presented in Figure S2, monoclonal antibodies were four-fold serially diluted and incubated with SARS-CoV-2 pseudotyped HIV-1 reporter virus for 1 h at 37 °C (final starting concentration of 2.5 µg/ml). The antibody and pseudotyped virus mixture was added to HT1080ACE2.cl 14 cells (Schmidt et al., 2020). After 48 h, cells were washed with PBS and lysed with Luciferase Cell Culture Lysis 5× reagent (Promega). Nanoluc luciferase activity in cell lysates was measured using the Nano-Glo Luciferase Assay System (Promega) and the Glomax Navigator (Promega). Relative luminescence units were normalized to those derived from cells infected with SARS-CoV-2 pseudovirus in the absence of monoclonal antibodies. The 50% inhibitory concentration (IC_{50}) was determined using 4-parameter nonlinear regression (least-squares regression method without weighting; constraints: top = 1, bottom = 0) (GraphPad Prism).

SPR-based ACE2 binding competition experiments

Surface Plasmon Resonance (SPR) experiments were done using a Biacore T200 instrument (GE Healthcare). For Figure 2F, purified ACE2-Fc was conjugated to each of the four flow cells using primary amine chemistry at pH 4.5 (Biacore manual) to a CM5 chip (GE Healthcare) to a response level of ~1000 resonance units (RUs). C118 Fab-SARS-CoV-2

RBD, C022 Fab-SARS-CoV-2 RBD, C144 Fab-SARS-CoV-2 RBD, and CR3022 Fab-SARS-CoV-2 RBD complexes were formed in HBS-EP+ buffer (150mM sodium chloride, 10mM HEPES, 3mM EDTA, 0.05% Tween-20, pH 7.6) by incubating 10uM Fab with 1uM RBD for 2 hours at room temperature. Complexes were injected on the ACE2-Fc-CM5 chip for a contact time of 300 sec at 30µL/min and a dissociation time of 30 sec in HBS-EP+ buffer.

For Figure S2E, purified SARS CoV-2 RBD was conjugated to each of the four flow cells using primary amine chemistry at pH 4.5 (Biacore manual) to a CM5 chip (GE Healthcare) to a response level of ~700 RUs. C118, C022, C144, and CR3022 IgG (1000nM) in buffer HBS-EP+ (150mM sodium chloride, 10mM HEPES, 3mM EDTA, 0.05% Tween-20, pH 7.6) were each injected on the RBD-CM5 chip for a contact time of 600 sec at 30µL/min. A second injection of soluble ACE2 at 250nM was injected over the immobilized RBD-Fab at 30µL/min for a contact time of 300 sec and dissociation time of 30 sec in HBS-EP+ buffer. Data were analyzed and plotted using Prism 9 (Graphpad).

X-ray crystallography

Fab-RBD complexes were assembled by incubating an RBD with a 1.5x molar excess of Fab for 1 hr on ice followed by size exclusion chromatography on an S200 10/300 increase column (GE Life Sciences). Fractions containing complex were pooled and concentrated to 8mg/mL. Crystallization trials using commercially-available screens (Hampton Research) were performed at room temperature using the sitting drop vapor diffusion method by mixing equal volumes of a Fab-RBD complex and reservoir using a TTP LabTech Mosquito instrument. Crystals were obtained for C118 Fab-SARS RBD in 0.2M sodium fluoride, 20% w/v polyethylene glycol 3,350 and for C022 Fab-SARS-CoV-2 RBD in 0.05M ammonium sulfate, 0.05M Bis-Tris, 30% v/v pentaerythritol ethoxylate (15/4 EO/OH). Crystals were cryoprotected by adding glycerol directly to drops to a final concentration of 20% and then looped and cryopreserved in liquid nitrogen.

X-ray diffraction data were collected at the Stanford Synchrotron Radiation Lightsource (SSRL) beamline 12-2 on a Pilatus 6M pixel detector (Dectris). Data from single crystals were indexed and integrated in XDS (Kabsch, 2010) and merged using AIMLESS in *CCP4* (Winn et al., 2011) (Table S1). The C022-RBD structure was solved by molecular replacement in PHASER (McCoy et al., 2007) using unmodified RBD coordinates (PDB 7K8M) and coordinates from C102 Fab (PDB 7K8M) after trimming heavy chain and light chain variable domains using Sculptor (Bunkóczi and Read, 2011) as search models. Coordinates were refined with *phenix.refine* from the PHENIX package ver. 1.17.1 (Adams et al., 2010) and cycles of manual building in Coot (ver 0.8.9.1) (Emsley et al., 2010) (Table S1).

Cryo-EM Sample Preparation

C118 Fab-S trimer complex was assembled by incubating purified SARS-CoV-2 S trimer at a 1.2:1 molar excess of purified Fab per S protomer at RT for 30 min. 17 uL of complex was mixed with 0.8uL of a 0.5% w/v F-octylmaltoside solution (Anatrace) and then 3μL were immediately applied to a 300 mesh, 1.2/1.3 AuUltraFoil grid (Electron Microscopy Sciences) that had been freshly glow discharged for 1 min at 20mA using a PELCO easiGLOW (Ted Pella). The grid was blotted for 3.5s with Whatman No. 1 filter paper at 22°C and 100% humidity then vitrified in 100% liquid ethane using a Mark IV Vitrobot (FEI) and stored under liquid nitrogen.

Cryo-EM data collection and processing

Single-particle cryo-EM data were collected for the C118-S trimer complex as previously described (Barnes et al., 2020a). Briefly, for the C118-S trimer complex, micrographs were collected on a Talos Arctica transmission electron microscope (Thermo Fisher) operating at 200 kV using a 3x3 beam image shift pattern with SerialEM automated data collection software (Mastronarde, 2005). Movies were obtained on a Gatan K3 Summit direct electron detector operating in counting mode at a nominal magnification of 45,000x (super-resolution 0.4345 Å/pixel) using a defocus range of −0.7 to −2.0 μm. Movies were collected with an 3.6 s exposure time with a rate of 13.5 e^-/pix/s, which resulted in a total dose of ~60 e-/$Å^2$

over 40 frames. The 2,970 movies were patch motion corrected for beam-induced motion including dose-weighting within cryoSPARC v3.1 (Punjani et al., 2017) after binning super resolution movies by 2 (0.869 Å/pixel). The non-dose-weighted images were used to estimate CTF parameters using Patch CTF in cryoSPARC, and micrographs with poor CTF fits and signs of crystalline ice were discarded, leaving 2,487 micrographs. Particles were picked in a reference-free manner using Gaussian blob picker in cryoSPARC (Punjani et al., 2017). An initial 923,707 particle stack was extracted, binned x4 (3.48 Å/pixel), and subjected to *ab initio* volume generation (4 classes) and subsequent heterogeneous refinement. The 3D classes that showed features for a Fab-S trimer complex were 2D classified to identify class averages corresponding to intact S-trimer complexes with well-defined structural features. This routine resulted in a new particle stack of 110,789 particles, which were unbinned (0.836 Å/pixel) and re-extracted using a 432 box size. Particles were then moved to Relion v3.1 (Zivanov et al., 2018), for further 3D classification (k=6)., which revealed two distinct states of the C118-S trimer complex.

Particles from state 1 (53,728 particles) and state 2 (31,422 particles) were separately refined using non-uniform 3D refinement imposing either C3 or C1 symmetry in cryoSPARC, respectively, to final resolutions of 3.4 Å and 4.5 Å according to the gold-standard FSC (Bell et al., 2016), respectively. To improve features at the C118-RBD interface, particles from State 1 were symmetry expanded and classified for a focused, non-uniform 3D local refinement in cryoSPARC. A soft mask was generated around the C118 V_HV_L – RBD domains (5-pixel extension, 10-pixel soft cosine edge) for local refinements. These efforts resulted in a modest improvement in the RBD-C118 Fab interface (Figure S5B), with an overall resolution of 3.7 Å according to the gold-standard FSC.

Cryo-EM Structure Modeling and Refinement

Initial coordinates were generated by rigid-body docking reference structures into cryo-EM density using UCSF Chimera (Goddard et al., 2007). The following coordinates were used: SARS-CoV-2 S 6P trimer: PDB 7K4N (mutated to include 6P mutations), PDB 7BZ5, and C118 Fab variable domains: this study. These initial models were then refined into cryo-EM

maps using one round of rigid body refinement, morphing and real space refinement in Phenix (Adams et al., 2010). Sequence-updated models were built manually in Coot (Emsley et al., 2010) and then refined using iterative rounds of refinement in Coot and Phenix (Adams et al., 2010). Glycans were modeled at possible N-linked glycosylation sites (PNGSs) in Coot using 'blurred' maps processed with a variety of B-factors (Terwilliger et al., 2018). Validation of model coordinates was performed using MolProbity (Chen et al., 2010) and is reported in Table S3.

Structure Analyses

Interacting residues were determined using PDBePISA (Krissinel and Henrick, 2007) for the C118 and C022 epitopes using the following criteria: Potential H-bonds were assigned using a distance of <3.6A˚and an A-D-H angle of >90˚, and the maximum distance allowed for a van der Waals interaction was 4.0A˚. H-bonds assigned for the C022-RBD complex should be considered tentative due to the relatively low resolution of the structure (3.2Å). Epitope patches for other antibodies in Figure 4A were defined as residues containing an atom within 4Å of the partner protein as determined in PyMOL (Schrödinger, 2011). Buried surface areas (BSAs) were determined with PDBePISA (Krissinel and Henrick, 2007) using a 1.4A˚probe. Structure figures were made using PyMOL ver. 2.3.5 (Schrödinger, 2011) or UCSF Chimera ver. 1.14 (Goddard et al., 2018). Fab-RBD-ACE2 complex figures (Figure 2E) were made by aligning RBD Cα atoms of Fab-RBD (this study and PDBs 6W41 and 6ZCZ) and RBD-ACE2 structures (PDB 6M0J). As density at position $N357_{RBD}$ for our C118-SARS RBD structure precluded building of the glycan, it was modeled (Figure 2A) by aligning Cα atoms of residues 353-371 of SARS-CoV spike-S230 structure (PDB 6NB6, chain E) and overlaying the glycan at $N357_{RBD}$ from the SARS-CoV spike on the RBD model of the C118-RBD crystal structure. Sequence alignments were done using the MUSCLE server (https://www.ebi.ac.uk/Tools/msa/muscle/) (Edgar, 2004). Secondary structure was defined as described in (Huo et al., 2020).

To predict whether intra-spike crosslinking by a single IgG binding to a spike trimer might be possible, we measured the distance between residue 222_{HC} Cα atoms in the C_H1 domains

of adjacent Fabs in Fab-S structures as previously described (Barnes et al., 2020a). This distance was compared to analogous distances in crystal structures of intact IgGs (42Å, PDB 1HZH; 48Å, PDB 1IGY; 52Å, PDB 1IGT). We accounted for potential influences of crystal packing in intact IgG structures, flexibility in the V_H-V_L/C_H1-C_L elbow bend angle, and uncertainties in C_H1-C_L domain placement in Fab-S cryo-EM structures, by setting a cut-off of ≤65Å for this measured distance as potentially allowing for a single IgG to include both Fabs when binding a spike trimer.

Quantification and Statistical Analysis

All software used for structural analysis and processing is listed in Star Methods Table. At least two experimental duplicates were performed for each ELISA or pseudovirus neutralization assay. IC50s for neutralization assays reported in Figure 1 were determined by normalizing relative luminescence units (RLUs) to values derived from SARS-CoV-2 pseudovirus infected cells in the absence of IgG antibody followed by 4- or 5-parameter nonlinear regressions analyzed using AntibodyDatabase (West et al., 2013). IC_{50}s reported in Figure S2 were determined by normalizing RLUs to values derived from cells infected with SARS-CoV-2 pseudovirus in the absence of antibodies followed by a 4-parameter nonlinear regression (least-squares regression method without weighting; constraints: top = 1, bottom = 0) using GraphPad Prism. Additional statistical details of experiments can be found where appropriate in the Experimental Model and Subject Details section and in legends of each figure.

Data and Code Availability

Atomic models of C118 Fab complexed with SARS-CoV RBD and C022 Fab complexed with SARS-CoV-2 RBD have been deposited in the Protein Data Bank (PDB) (http://www.rcsb.org/) under accession codes 7RKS and 7RKU, respectively. The atomic model and cryo-EM maps generated for the C118 Fab–SARS-CoV-2 S complex have been deposited at the PDB (http://www.rcsb.org/) and the Electron Microscopy Databank (EMDB) (http://www.emdataresource.org/) under accession codes 7RKV (state 1 coordinates), EMD-24504 (state 1) and EMD-24505 (state 2). All models and maps are

publicly available as of the date of publication. Additional Supplemental Items are available from Mendeley Data at http://dx.doi.org/10.17632/kkf4zdz2x7.1

This paper does not report original code.

Any additional information required to reanalyze the data reported in this paper is available from the lead contact upon request.

Acknowledgements

We thank J. Vielmetter, P. Hoffman, and the Protein Expression Center in the Beckman Institute at Caltech for expression assistance and K. Dam for assistance with soluble ACE2 purification. Electron microscopy was performed in the Caltech Cryo-EM Center with assistance from S. Chen and A. Malyutin. We thank the Gordon and Betty Moore and Beckman Foundations for gifts to Caltech to support the Molecular Observatory. We thank J. Kaiser, director of the Molecular Observatory at Caltech, and beamline staff C. Smith and S. Russi at SSRL for data collection assistance. Use of the Stanford Synchrotron Radiation Lightsource, SLAC National Accelerator Laboratory, is supported by the U.S. Department of Energy, Office of Science, Office of Basic Energy Sciences under Contract No. DE-AC02-76SF00515. The SSRL Structural Molecular Biology Program is supported by the DOE Office of Biological and Environmental Research, and by the National Institutes of Health, National Institute of General Medical Sciences (P30GM133894). The contents of this publication are solely the responsibility of the authors and do not necessarily represent the official views of NIGMS or NIH. This work was supported by NIH (P01-AI138938-S1 to P.J.B. and M.C.N.), the Caltech Merkin Institute for Translational Research (P.J.B.), a George Mason University Fast Grant (P.J.B.), NIH R01AI078788 (to T.H.) and R01AI640511 (to P.D.B). C.O.B was supported by the Hanna Gray Fellowship Program from the Howard Hughes Medical Institute and the Postdoctoral Enrichment Program from the Burroughs Wellcome Fund. M.C.N. is an HHMI investigator.

Author Contributions

C.A.J., A.A.C., P.J.B., and C.O.B. conceived and designed experiments. Proteins were produced and characterized by A.A.C., K.H.T., C.O.B., and C.A.J. Binding and neutralization studies were done by A.A.C., and F.M. with assistance from P.N.P.G., Y.L., and F.S. SPR binding competition experiments were done by C.A.J. with assistance from J.R.K. Structural studies were performed by C.A.J. with assistance from C.O.B. Structure analysis was done by C.A.J. with assistance from C.O.B. and A.A.C. Sequence analysis was done by A.P.W. Paper was written by C.A.J., P.J.B., and C.O.B. with assistance from A.A.C., T.H., M.C.N., P.D.B., and other authors.

Declaration of interest

The Rockefeller University has filed provisional patent applications in connection with this work on which M.C.N. (US patent 63/021,387) is listed as an inventor.

References

Adams, P.D., Afonine, P.V., Bunkoczi, G., Chen, V.B., Davis, I.W., Echols, N., Headd, J.J., Hung, L.W., Kapral, G.J., Grosse-Kunstleve, R.W.*, et al.* (2010). PHENIX: a comprehensive Python-based system for macromolecular structure solution. Acta Crystallogr D Biol Crystallogr *66*, 213-221.

Annavajhala, M.K., Mohri, H., Zucker, J.E., Sheng, Z., Wang, P., Gomez-Simmonds, A., Ho, D.D., and Uhlemann, A.-C. (2021). A Novel SARS-CoV-2 Variant of Concern, B.1.526, Identified in New York. medRxiv 10.1101/2021.02.23.21252259.

Barnes, C.O., Jette, C.A., Abernathy, M.E., Dam, K.-M.A., Esswein, S.R., Gristick, H.B., Malyutin, A.G., Sharaf, N.G., Huey-Tubman, K.E., Lee, Y.E.*, et al.* (2020a). SARS-CoV-2 neutralizing antibody structures inform therapeutic strategies. Nature *588*, 682-687.

Barnes, C.O., West, A.P., Jr., Huey-Tubman, K.E., Hoffmann, M.A.G., Sharaf, N.G., Hoffman, P.R., Koranda, N., Gristick, H.B., Gaebler, C., Muecksch, F.*, et al.* (2020b). Structures of Human Antibodies Bound to SARS-CoV-2 Spike Reveal Common Epitopes and Recurrent Features of Antibodies. Cell *182*, 828-842 e816.

Bell, J.M., Chen, M., Baldwin, P.R., and Ludtke, S.J. (2016). High resolution single particle refinement in EMAN2.1. Methods *100*, 25-34.

Brouwer, P.J.M., Caniels, T.G., van der Straten, K., Snitselaar, J.L., Aldon, Y., Bangaru, S., Torres, J.L., Okba, N.M.A., Claireaux, M., Kerster, G.*, et al.* (2020). Potent neutralizing antibodies from COVID-19 patients define multiple targets of vulnerability. Science *369*, 643-650.

Bunkóczi, G., and Read, R.J. (2011). Improvement of molecular-replacement models with Sculptor. Acta Cryst *67*, 303-312.

Cao, Y., Su, B., Guo, X., Sun, W., Deng, Y., Bao, L., Zhu, Q., Zhang, X., Zheng, Y., Geng, C.*, et al.* (2020). Potent neutralizing antibodies against SARS-CoV-2 identified by high-throughput single-cell sequencing of convalescent patients' B cells. Cell 10.1016/j.cell.2020.05.025.

Chan, K.K., Dorosky, D., Sharma, P., Abbasi, S.A., Dye, J.M., Kranz, D.M., Herbert, A.S., and Procko, E. (2020). Engineering human ACE2 to optimize binding to the spike protein of SARS coronavirus 2. Science *369*, 1261-1265.

Chen, V.B., Arendall, W.B., 3rd, Headd, J.J., Keedy, D.A., Immormino, R.M., Kapral, G.J., Murray, L.W., Richardson, J.S., and Richardson, D.C. (2010). MolProbity: all-atom structure validation for macromolecular crystallography. Acta Crystallogr D Biol Crystallogr *66*, 12-21.

Cohen, A.A., Gnanapragasam, P.N.P., Lee, Y.E., Hoffman, P.R., Ou, S., Kakutani, L.M., Keeffe, J.R., Wu, H.-J., Howarth, M., West, A.P.*, et al.* (2021). Mosaic nanoparticles elicit cross-reactive immune responses to zoonotic coronaviruses in mice. Science *371*, 735-741.

Corti, D., Suguitan, A.L., Pinna, D., Silacci, C., Fernandez-Rodriguez, B.M., Vanzetta, F., Santos, C., Luke, C.J., Torres-Velez, F.J., Temperton, N.J.*, et al.* (2010). Heterosubtypic neutralizing antibodies are produced by individuals immunized with a seasonal influenza vaccine. Journal of Clinical Investigation *120*, 1663-1673.

Crawford, K.H.D., Eguia, R., Dingens, A.S., Loes, A.N., Malone, K.D., Wolf, C.R., Chu, H.Y., Tortorici, M.A., Veesler, D., Murphy, M.*, et al.* (2020). Protocol and Reagents for Pseudotyping Lentiviral Particles with SARS-CoV-2 Spike Protein for Neutralization Assays. Viruses *12*.

de Wit, E., van Doremalen, N., Falzarano, D., and Munster, V.J. (2016). SARS and MERS: recent insights into emerging coronaviruses. Nat Rev Microbiol *14*, 523-534.

Dejnirattisai, W., Zhou, D., Ginn, H.M., Duyvesteyn, H.M.E., Supasa, P., Case, J.B., Zhao, Y., Walter, T.S., Mentzer, A.J., Liu, C.*, et al.* (2021). The antigenic anatomy of SARS-CoV-2 receptor binding domain. Cell 10.1016/j.cell.2021.02.032.

Desrosiers, R.C., Wagh, K., Bhattacharya, T., Williamson, C., Robles, A., Bayne, M., Garrity, J., Rist, M., Rademeyer, C., Yoon, H.*, et al.* (2016). Optimal Combinations of Broadly Neutralizing Antibodies for Prevention and Treatment of HIV-1 Clade C Infection. PLOS Pathogens *12*, e1005520.

Edgar, R.C. (2004). MUSCLE: multiple sequence alignment with high accuracy and high throughput. Nuc Acids Res *32*, 1792-1797.

Emsley, P., Lohkamp, B., Scott, W.G., and Cowtan, K. (2010). Features and development of Coot. Acta Crystallogr D Biol Crystallogr *66*, 486-501.

Faria, N.R., Claro, I.M., Candido, D., Moyses Franco, L.A., Andrade, P.S., Coletti, T.M., Silva, C.A.M., Sales, F.C., Manuli, E.R., Agular, R.S.*, et al.* (2021). Genomic characterisation of an emergent SARS-CoV-2 lineage in Manaus: preliminary findings. https://virological.org/t/genomic-characterisation-of-an-emergent-sars-cov-2-lineage-in-manaus-preliminary-findings/586.

Fung, T.S., and Liu, D.X. (2019). Human Coronavirus: Host-Pathogen Interaction. Annu Rev Microbiol *73*, 529-557.

Goddard, T.D., Huang, C.C., and Ferrin, T.E. (2007). Visualizing density maps with UCSF Chimera. J Struct Biol *157*, 281-287.

Goddard, T.D., Huang, C.C., Meng, E.C., Pettersen, E.F., Couch, G.S., Morris, J.H., and Ferrin, T.E. (2018). UCSF ChimeraX: Meeting modern challenges in visualization and analysis. Protein Sci *27*, 14-25.

Greaney, A.J., Loes, A.N., Crawford, K.H.D., Starr, T.N., Malone, K.D., Chu, H.Y., and Bloom, J.D. (2021). Comprehensive mapping of mutations in the SARS-CoV-2 receptor-binding domain that affect recognition by polyclonal human plasma antibodies. Cell Host & Microbe *29*, 463-476.e466.

Gristick, H.B., von Boehmer, L., West, A.P., Jr., Schamber, M., Gazumyan, A., Golijanin, J., Seaman, M.S., Fatkenheuer, G., Klein, F., Nussenzweig, M.C.*, et al.* (2016). Natively glycosylated HIV-1 Env structure reveals new mode for antibody recognition of the CD4-binding site. Nat Struct Mol Biol *23*, 906-915.

Guindon, S., Dufayard, J.F., Lefort, V., Anisimova, M., Hordijk, W., and Gascuel, O. (2010). New algorithms and methods to estimate maximum-likelihood phylogenies: assessing the performance of PhyML 3.0. Syst Biol *59*, 307-321.

Haagmans, B.L., Al Dhahiry, S.H.S., Reusken, C.B.E.M., Raj, V.S., Galiano, M., Myers, R., Godeke, G.-J., Jonges, M., Farag, E., Diab, A.*, et al.* (2014). Middle East respiratory syndrome coronavirus in dromedary camels: an outbreak investigation. The Lancet Infectious Diseases *14*, 140-145.

Hoffmann, M., Arora, P., Groß, R., Seidel, A., Hörnich, B.F., Hahn, A.S., Krüger, N., Graichen, L., Hofmann-Winkler, H., Kempf, A.*, et al.* (2021). SARS-CoV-2 variants B.1.351 and P.1 escape from neutralizing antibodies. Cell 10.1016/j.cell.2021.03.036.

Hoffmann, M., Kleine-Weber, H., Schroeder, S., Kruger, N., Herrler, T., Erichsen, S., Schiergens, T.S., Herrler, G., Wu, N.H., Nitsche, A.*, et al.* (2020). SARS-CoV-2 Cell Entry Depends on ACE2 and TMPRSS2 and Is Blocked by a Clinically Proven Protease Inhibitor. Cell *181*, 271-280 e278.

Hsieh, C.-L., Goldsmith, J.A., Schaub, J.M., DiVenere, A.M., Kuo, H.-C., Javanmardi, K., Le, K.C., Wrapp, D., Lee, A.G., Liu, Y.*, et al.* (2020). Structure-based design of prefusion-stabilized SARS-CoV-2 spikes. Science *369*, 1501-1505.

Huo, J., Zhao, Y., Ren, J., Zhou, D., Duyvesteyn, H.M.E., Ginn, H.M., Carrique, L., Malinauskas, T., Ruza, R.R., Shah, P.N.M.*, et al.* (2020). Neutralization of SARS-CoV-2 by Destruction of the Prefusion Spike. Cell Host & Microbe *28*, 445-454.e446.

Kabsch, W. (2010). XDS. Acta Crystallogr D Biol Crystallogr *66*, 125-132.

Kane, M., Zang, T.M., Rihn, S.J., Zhang, F., Kueck, T., Alim, M., Schoggins, J., Rice, C.M., Wilson, S.J., and Bieniasz, P.D. (2016). Identification of Interferon-Stimulated Genes with Antiretroviral Activity. Cell Host Microbe *20*, 392–405.

Kirchdoerfer, R.N., Cottrell, C.A., Wang, N., Pallesen, J., Yassine, H.M., Turner, H.L., Corbett, K.S., Graham, B.S., McLellan, J.S., and Ward, A.B. (2016). Pre-fusion structure of a human coronavirus spike protein. Nature *531*, 118-121.

Klein, J.S. (2009). Investigations in the design and characterization of HIV-1 neutralizing molecules (Pasadena: California Institute of Technology), pp. 166.

Klein, J.S., and Bjorkman, P.J. (2010). Few and far between: how HIV may be evading antibody avidity. PLoS Pathog *6*, e1000908.

Korber, B., Fischer, W.M., Gnanakaran, S., Yoon, H., Theiler, J., Abfalterer, W., Hengartner, N., Giorgi, E.E., Bhattacharya, T., Foley, B.*, et al.* (2020). Tracking Changes in SARS-CoV-2 Spike: Evidence that D614G Increases Infectivity of the COVID-19 Virus. Cell *182*, 812-827.e819.

Kreer, C., Zehner, M., Weber, T., Ercanoglu, M.S., Gieselmann, L., Rohde, C., Halwe, S., Korenkov, M., Schommers, P., Vanshylla, K.*, et al.* (2020). Longitudinal Isolation of Potent Near-Germline SARS-CoV-2-Neutralizing Antibodies from COVID-19 Patients. Cell 10.1016/j.cell.2020.06.044.

Krissinel, E., and Henrick, K. (2007). Inference of macromolecular assemblies from crystalline state. J Mol Biol *372*, 774-797.

Lan, J., Ge, J., Yu, J., Shan, S., Zhou, H., Fan, S., Zhang, Q., Shi, X., Wang, Q., Zhang, L.*, et al.* (2020). Structure of the SARS-CoV-2 spike receptor-binding domain bound to the ACE2 receptor. Nature *581*, 215-220.

Landau, M., Mayrose, I., Rosenberg, Y., Glaser, F., Martz, E., Pupko, T., and Ben-Tal, N. (2005). ConSurf 2005: the projection of evolutionary conservation scores of residues on protein structures. Nucleic Acids Res *33*, W299-302.

Lee, B., Huang, K.-Y.A., Tan, T.K., Chen, T.-H., Huang, C.-G., Harvey, R., Hussain, S., Chen, C.-P., Harding, A., Gilbert-Jaramillo, J.*, et al.* (2021). Breadth and function of antibody response to acute SARS-CoV-2 infection in humans. PLOS Pathogens *17*, e1009352.

Lefranc, M.P., Giudicelli, V., Duroux, P., Jabado-Michaloud, J., Folch, G., Aouinti, S., Carillon, E., Duvergey, H., Houles, A., Paysan-Lafosse, T.*, et al.* (2015). IMGT(R), the international ImMunoGeneTics information system(R) 25 years on. Nucleic Acids Res *43*, D413-422.

Lefranc, M.P., Giudicelli, V., Ginestoux, C., Jabado-Michaloud, J., Folch, G., Bellahcene, F., Wu, Y., Gemrot, E., Brochet, X., Lane, J.*, et al.* (2009). IMGT, the international ImMunoGeneTics information system. Nucleic Acids Res *37*, D1006-1012.

Leist, S.R., Dinnon, K.H., Schäfer, A., Tse, L.V., Okuda, K., Hou, Y.J., West, A., Edwards, C.E., Sanders, W., Fritch, E.J.*, et al.* (2020). A Mouse-Adapted SARS-CoV-2 Induces Acute Lung Injury and Mortality in Standard Laboratory Mice. Cell *183*, 1070-1085.e1012.

Li, Q., Wu, J., Nie, J., Zhang, L., Hao, H., Liu, S., Zhao, C., Zhang, Q., Liu, H., Nie, L.*, et al.* (2020). The Impact of Mutations in SARS-CoV-2 Spike on Viral Infectivity and Antigenicity. Cell *182*, 1284-1294.e1289.

Li, W., Moore, M.J., Vasilieva, N., Sui, J., Wong, S.K., Berne, M.A., Somasundaran, M., Sullivan, J.L., Luzuriaga, K., Greenough, T.C.*, et al.* (2003). Angiotensin-converting enzyme 2 is a functional receptor for the SARS coronavirus. Nature *426*, 450-454.

Li, W., Shi, Z., Yu, M., Ren, W., Smith, C., Epstein, J.H., Wang, H., Crameri, G., Hu, Z., Zhang, H.*, et al.* (2005). Bats are natural reservoirs of SARS-like coronaviruses. Science *310*, 676-679.

Li, Z., Tomlinson, A.C., Wong, A.H., Zhou, D., Desforges, M., Talbot, P.J., Benlekbir, S., Rubinstein, J.L., and Rini, J.M. (2019). The human coronavirus HCoV-229E S-protein structure and receptor binding. Elife *8*.

Liu, H., Wu, N.C., Yuan, M., Bangaru, S., Torres, J.L., Caniels, T.G., van Schooten, J., Zhu, X., Lee, C.-C.D., Brouwer, P.J.M.*, et al.* (2020a). Cross-Neutralization of a SARS-CoV-2 Antibody to a Functionally Conserved Site Is Mediated by Avidity. Immunity *53*, 1272-1280.e1275.

Liu, H., Yuan, M., Huang, D., Bangaru, S., Zhao, F., Lee, C.-C.D., Peng, L., Barman, S., Zhu, X., Nemazee, D.*, et al.* (2021). A combination of cross-neutralizing antibodies synergizes to prevent SARS-CoV-2 and SARS-CoV pseudovirus infection. Cell Host & Microbe 10.1016/j.chom.2021.04.005.

Liu, L., Wang, P., Nair, M.S., Yu, J., Rapp, M., Wang, Q., Luo, Y., Chan, J.F.W., Sahi, V., Figueroa, A.*, et al.* (2020b). Potent neutralizing antibodies against multiple epitopes on SARS-CoV-2 spike. Nature *584*, 450-456.

Mastronarde, D.N. (2005). Automated electron microscope tomography using robust prediction of specimen movements. J Struct Biol *152*, 36-51.

McCoy, A.J., Grosse-Kunstleve, R.W., Adams, P.D., Winn, M.D., Storoni, L.C., and Read, R.J. (2007). Phaser crystallographic software. J Appl Crystallogr *40*, 658-674.

Muecksch, F., Weisblum, Y., Barnes, C.O., Schmidt, F., Schaefer-Babajew, D., Lorenzi, J.C.C., Flyak, A.I., DeLaitsch, A.T., Huey-Tubman, K.E., Hou, S.*, et al.* (2021). Development of potency, breadth and resilience to viral escape mutations in SARS-CoV-2 neutralizing antibodies. bioRxiv 10.1101/2021.03.07.434227.

Pear, W.S., Nolan, G.P., Scott, M.L., and Baltimore, D. (1993). Production of high-titer helper-free retroviruses by transient transfection. Proc National Acad Sci *90*, 8392–8396.

Pettersen E.F., Goddard T.D., Huang C.C., Couch G.S., Greenblatt D.M., Meng E.C., Ferrin T.E. (2004) UCSF Chimera--a visualization system for exploratory research and analysis. J Comput Chem *25*, 1605-12.

Piccoli, L., Park, Y.-J., Tortorici, M.A., Czudnochowski, N., Walls, A.C., Beltramello, M., Silacci-Fregni, C., Pinto, D., Rosen, L.E., Bowen, J.E.*, et al.* (2020a). Mapping neutralizing and immunodominant sites on the SARS-CoV-2 spike receptor-binding domain by structure-guided high-resolution serology. Cell 10.1016/j.cell.2020.09.037.

Piccoli, L., Park, Y.-J., Tortorici, M.A., Czudnochowski, N., Walls, A.C., Beltramello, M., Silacci-Fregni, C., Pinto, D., Rosen, L.E., Bowen, J.E.*, et al.* (2020b). Mapping Neutralizing and Immunodominant Sites on the SARS-CoV-2 Spike Receptor-Binding Domain by Structure-Guided High-Resolution Serology. Cell *183*, 1024-1042.e1021.

Pinto, D., Park, Y.-J., Beltramello, M., Walls, A.C., Tortorici, M.A., Bianchi, S., Jaconi, S., Culap, K., Zatta, F., De Marco, A.*, et al.* (2020). Cross-neutralization of SARS-CoV-2 by a human monoclonal SARS-CoV antibody. Nature *583*, 290-295.

Punjani, A., Rubinstein, J.L., Fleet, D.J., and Brubaker, M.A. (2017). cryoSPARC: algorithms for rapid unsupervised cryo-EM structure determination. Nat Methods *14*, 290-296.

Rambaut, A., Pybus, O., Barclay, W., Barrett, J., Carabelli, A., Connor, T., Peacock, T., Robertson, D.L., Volz, E., and UK, C.-G.C. (2020). Preliminary genomic characterisation of an emergent SARS-CoV-2 lineage in the UK defined by a novel set of spike mutations. virologicalorg, https://virological.org/t/preliminary-genomic-characterisation-of-an-emergent-sars-cov-2-lineage-in-the-uk-defined-by-a-novel-set-of-spike-mutations/563.

Rappazzo, C.G., Tse, L.V., Kaku, C.I., Wrapp, D., Sakharkar, M., Huang, D., Deveau, L.M., Yockachonis, T.J., Herbert, A.S., Battles, M.B.*, et al.* (2021). Broad and potent activity against SARS-like viruses by an engineered human monoclonal antibody. Science *371*, 823-829.

Robbiani, D.F., Gaebler, C., Muecksch, F., Lorenzi, J.C.C., Wang, Z., Cho, A., Agudelo, M., Barnes, C.O., Gazumyan, A., Finkin, S.*, et al.* (2020). Convergent antibody responses to SARS-CoV-2 in convalescent individuals. Nature *584*, 437-442.

Rogers, T.F., Zhao, F., Huang, D., Beutler, N., Burns, A., He, W.T., Limbo, O., Smith, C., Song, G., Woehl, J.*, et al.* (2020). Rapid isolation of potent SARS-CoV-2 neutralizing antibodies and protection in a small animal model. Science 10.1126/science.abc7520.

Sauer, M.M., Tortorici, M.A., Park, Y.-J., Walls, A.C., Homad, L., Acton, O., Bowen, J., Wang, C., Xiong, X., de van der Schueren, W.*, et al.* (2021). Structural basis for broad coronavirus neutralization. bioRxiv 10.1101/2020.12.29.424482.

Schaefer, W., Regula, J.T., Bahner, M., Schanzer, J., Croasdale, R., Durr, H., Gassner, C., Georges, G., Kettenberger, H., Imhof-Jung, S.*, et al.* (2011). Immunoglobulin domain crossover as a generic approach for the production of bispecific IgG antibodies. Proc Natl Acad Sci U S A *108*, 11187-11192.

Scharf, L., Wang, H., Gao, H., Chen, S., McDowall, A.W., and Bjorkman, P.J. (2015). Broadly Neutralizing Antibody 8ANC195 Recognizes Closed and Open States of HIV-1 Env. Cell *162*, 1379-1390.

Scheid, J.F., Mouquet, H., Ueberheide, B., Diskin, R., Klein, F., Olivera, T.Y., Pietzsch, J., Fenyo, D., Abadir, A., Velinzon, K.*, et al.* (2011). Sequence and Structural Convergence of Broad and Potent HIV Antibodies That Mimic CD4 Binding. Science *333*, 1633-1637.

Schmidt, F., Weisblum, Y., Muecksch, F., Hoffmann, H.-H., Michailidis, E., Lorenzi, J.C.C., Mendoza, P., Rutkowska, M., Bednarski, E., Gaebler, C.*, et al.* (2020). Measuring SARS-CoV-2 neutralizing antibody activity using pseudotyped and chimeric viruses. Journal of Experimental Medicine *217*.

Schoofs, T., Barnes, C.O., Suh-Toma, N., Golijanin, J., Schommers, P., Gruell, H., West, A.P., Jr., Bach, F., Lee, Y.E., Nogueira, L.*, et al.* (2019). Broad and Potent Neutralizing Antibodies Recognize the Silent Face of the HIV Envelope. Immunity *50*, 1513-1529 e1519.

Schrödinger, L. (2011). The PyMOL Molecular Graphics System (The PyMOL Molecular Graphics System).

Seydoux, E., Homad, L.J., MacCamy, A.J., Parks, K.R., Hurlburt, N.K., Jennewein, M.F., Akins, N.R., Stuart, A.B., Wan, Y.H., Feng, J.*, et al.* (2020). Analysis of a SARS-CoV-2-Infected Individual Reveals Development of Potent Neutralizing Antibodies with Limited Somatic Mutation. Immunity *53*, 98-105 e105.

Shah, P., Canziani, G.A., Carter, E.P., and Chaiken, I. (2021). The Case for S2: The Potential Benefits of the S2 Subunit of the SARS-CoV-2 Spike Protein as an Immunogen in Fighting the COVID-19 Pandemic. Frontiers in Immunology *12*.

Shi, R., Shan, C., Duan, X., Chen, Z., Liu, P., Song, J., Song, T., Bi, X., Han, C., Wu, L.*, et al.* (2020). A human neutralizing antibody targets the receptor-binding site of SARS-CoV-2. Nature *584*, 120-124.

Shu, Y., and McCauley, J. (2017). GISAID: Global initiative on sharing all influenza data – from vision to reality. Eurosurveillance *22*, 30494.

Sievers, F., Wilm, A., Dineen, D., Gibson, T.J., Karplus, K., Li, W., Lopez, R., McWilliam, H., Remmert, M., Soding, J.*, et al.* (2011). Fast, scalable generation of high-quality protein multiple sequence alignments using Clustal Omega. Mol Syst Biol *7*, 539.

Song, H.D., Tu, C.C., Zhang, G.W., Wang, S.Y., Zheng, K., Lei, L.C., Chen, Q.X., Gao, Y.W., Zhou, H.Q., Xiang, H.*, et al.* (2005). Cross-host evolution of severe acute respiratory syndrome

coronavirus in palm civet and human. Proceedings of the National Academy of Sciences *102*, 2430-2435.

Starr, T.N., Czudnochowski, N., Zatta, F., Park, Y.-J., Liu, Z., Addetia, A., Pinto, D., Beltramello, M., Hernandez, P., Greaney, A.J.*, et al.* (2021a). Antibodies to the SARS-CoV-2 receptor-binding domain that maximize breadth and resistance to viral escape. bioRxiv 10.1101/2021.04.06.438709.

Starr, T.N., Greaney, A.J., Addetia, A., Hannon, W.W., Choudhary, M.C., Dingens, A.S., Li, J.Z., and Bloom, J.D. (2021b). Prospective mapping of viral mutations that escape antibodies used to treat

COVID-19. Science *371*, 850-854.

Tegally, H., Wilkinson, E., Giovanetti, M., Iranzadeh, A., Fonseca, V., Giandhari, J., Doolabh, D., Pillay, S., San, E.J., Msomi, N.*, et al.* (2020). Emergence and rapid spread of a new severe acute respiratory syndrome-related coronavirus 2 (SARS-CoV-2) lineage with multiple spike mutations in South Africa. medRxiv 10.1101/2020.12.21.20248640.

Terwilliger, T.C., Adams, P.D., Afonine, P.V., and Sobolev, O.V. (2018). A fully automatic method yielding initial models from high-resolution cryo-electron microscopy maps. Nat Methods *15*, 905-908.

Tortorici, M.A. (2020). Ultrapotent human antibodies protect against SARS-CoV-2 challenge via multiple mechanisms. Science *370*, 950-957.

Tortorici, M.A., Czudnochowski, N., Starr, T.N., Marzi, R., Walls, A.C., Zatta, F., Bowen, J.E., Jaconi, S., Di Iulio, J., Wang, Z.*, et al.* (2021). Broad sarbecovirus neutralization by a human monoclonal antibody. Nature 10.1038/s41586-021-03817-4.

Voloch, C.M., Silva F, R.d., de Almeida, L.G.P., Cardoso, C.C., Brustolini, O.J., Gerber, A.L., Guimarães, A.P.d.C., Mariani, D., Costa, R.M.d., Ferreira, O.C.*, et al.* (2020). Genomic characterization of a novel SARS-CoV-2 lineage from Rio de Janeiro, Brazil. medRxiv 10.1101/2020.12.23.20248598.

Walls, A.C., Park, Y.J., Tortorici, M.A., Wall, A., McGuire, A.T., and Veesler, D. (2020). Structure, Function, and Antigenicity of the SARS-CoV-2 Spike Glycoprotein. Cell *181*, 281-292 e286.

Walls, A.C., Tortorici, M.A., Bosch, B.J., Frenz, B., Rottier, P.J.M., DiMaio, F., Rey, F.A., and Veesler, D. (2016). Cryo-electron microscopy structure of a coronavirus spike glycoprotein trimer. Nature *531*, 114-117.

Wang, C., van Haperen, R., Gutiérrez-Álvarez, J., Li, W., Okba, N.M.A., Albulescu, I., Widjaja, I., van Dieren, B., Fernandez-Delgado, R., Sola, I.*, et al.* (2021). A conserved immunogenic and vulnerable site on the coronavirus spike protein delineated by cross-reactive monoclonal antibodies. Nature Communications *12*.

Wang, H., Gristick, H.B., Scharf, L., West, A.P., Galimidi, R.P., Seaman, M.S., Freund, N.T., Nussenzweig, M.C., and Bjorkman, P.J. (2017). Asymmetric recognition of HIV-1 Envelope trimer by V1V2 loop-targeting antibodies. Elife *6*.

Wang, N., Li, S.-Y., Yang, X.-L., Huang, H.-M., Zhang, Y.-J., Guo, H., Luo, C.-M., Miller, M., Zhu, G., Chmura, A.A.*, et al.* (2018). Serological Evidence of Bat SARS-Related Coronavirus Infection in Humans, China. Virologica Sinica *33*, 104-107.

Wec, A.Z., Wrapp, D., Herbert, A.S., Maurer, D.P., Haslwanter, D., Sakharkar, M., Jangra, R.K., Dieterle, M.E., Lilov, A., Huang, D.*, et al.* (2020). Broad neutralization of SARS-related viruses by human monoclonal antibodies. Science *369*, 731-736.

Weisblum, Y., Schmidt, F., Zhang, F., DaSilva, J., Poston, D., Lorenzi, J.C.C., Muecksch, F., Rutkowska, M., Hoffmann, H.-H., Michailidis, E.*, et al.* (2020). Escape from neutralizing antibodies by SARS-CoV-2 spike protein variants. eLife *9*.

West, A.P., Barnes, C.O., Yang, Z., and Bjorkman, P.J. (2021). SARS-CoV-2 lineage B.1.526 emerging in the New York region detected by software utility created to query the spike mutational landscape. bioRxiv 10.1101/2021.02.14.431043;.

West, A.P., Jr., Scharf, L., Horwitz, J., Klein, F., Nussenzweig, M.C., and Bjorkman, P.J. (2013). Computational analysis of anti-HIV-1 antibody neutralization panel data to identify potential functional epitope residues. Proc Natl Acad Sci U S A *110*, 10598-10603.

Winn, M.D., Ballard, C.C., Cowtan, K.D., Dodson, E.J., Emsley, P., Evans, P.R., Keegan, R.M., Krissinel, E.B., Leslie, A.G., McCoy, A.*, et al.* (2011). Overview of the CCP4 suite and current developments. Acta Crystallogr D Biol Crystallogr *67*, 235-242.

Wrapp, D., Wang, N., Corbett, K.S., Goldsmith, J.A., Hsieh, C.L., Abiona, O., Graham, B.S., and McLellan, J.S. (2020). Cryo-EM structure of the 2019-nCoV spike in the prefusion conformation. Science *367*, 1260-1263.

Yan, R., Zhang, Y., Li, Y., Xia, L., Guo, Y., and Zhou, Q. (2020). Structural basis for the recognition of SARS-CoV-2 by full-length human ACE2. Science *367*, 1444-1448.

Yuan, M., Liu, H., Wu, N.C., Lee, C.-C.D., Zhu, X., Zhao, F., Huang, D., Yu, W., Hua, Y., Tien, H.*, et al.* (2020a). Structural basis of a shared antibody response to SARS-CoV-2. Science 10.1126/science.abd2321, eabd2321.

Yuan, M., Wu, N.C., Zhu, X., Lee, C.-C.D., So, R.T.Y., Lv, H., Mok, C.K.P., and Wilson, I.A. (2020b). A highly conserved cryptic epitope in the receptor binding domains of SARS-CoV-2 and SARS-CoV. Science *368*, 630-633.

Yuan, Y., Cao, D., Zhang, Y., Ma, J., Qi, J., Wang, Q., Lu, G., Wu, Y., Yan, J., Shi, Y.*, et al.* (2017). Cryo-EM structures of MERS-CoV and SARS-CoV spike glycoproteins reveal the dynamic receptor binding domains. Nat Commun *8*, 15092.

Zhang, W., Davis, B.D., Chen, S.S., Sincuir Martinez, J.M., Plummer, J.T., and Vail, E. (2021). Emergence of a Novel SARS-CoV-2 Variant in Southern California. Jama 10.1001/jama.2021.1612.

Zhou, D., Duyvesteyn, H.M.E., Chen, C.-P., Huang, C.-G., Chen, T.-H., Shih, S.-R., Lin, Y.-C., Cheng, C.-Y., Cheng, S.-H., Huang, Y.-C.*, et al.* (2020a). Structural basis for the neutralization of SARS-CoV-2 by an antibody from a convalescent patient. Nature Structural & Molecular Biology *27*, 950-958.

Zhou, H., Ji, J., Chen, X., Bi, Y., Li, J., Hu, T., Song, H., Chen, Y., Cui, M., Zhang, Y*., et al.* (2021). Identification of novel bat coronaviruses sheds light on the evolutionary origins of SARS-CoV-2 and related viruses. bioRxiv 10.1101/2021.03.08.434390.

Zhou, P., Yang, X.L., Wang, X.G., Hu, B., Zhang, L., Zhang, W., Si, H.R., Zhu, Y., Li, B., Huang, C.L*., et al.* (2020b). A pneumonia outbreak associated with a new coronavirus of probable bat origin. Nature *579*, 270-273.

Zivanov, J., Nakane, T., Forsberg, B.O., Kimanius, D., Hagen, W.J., Lindahl, E., and Scheres, S.H. (2018). New tools for automated high-resolution cryo-EM structure determination in RELION-3. Elife *7*.

Zost, S.J., Gilchuk, P., Case, J.B., Binshtein, E., Chen, R.E., Nkolola, J.P., Schafer, A., Reidy, J.X., Trivette, A., Nargi, R.S*., et al.* (2020a). Potently neutralizing and protective human antibodies against SARS-CoV-2. Nature *584*, 443-449.

Zost, S.J., Gilchuk, P., Chen, R.E., Case, J.B., Reidy, J.X., Trivette, A., Nargi, R.S., Sutton, R.E., Suryadevara, N., Chen, E.C*., et al.* (2020b). Rapid isolation and profiling of a diverse panel of human monoclonal antibodies targeting the SARS-CoV-2 spike protein. Nat Med 10.1038/s41591-020-0998-x.

Supplementary Materials

Supplemental Movie 1

C118 and C022 Fab bind to SARS-CoV-2 RBD in a class 4 orientation at a 'cryptic' epitope. The video shows soluble SARS-CoV-2 spike (PDB: 7BZ5) and the 'down' and 'up' conformations of the RBD domain. Next, the sequence conservation of 12 sarbecovirus RBDs is mapped onto the surface of the RBD domain. Finally, The C118-SARS-CoV RBD and C022-SARS-CoV-2 RBD structures are shown.

Supplemental Movie 1 can be accessed at Mendeley Data:

http://dx.doi.org/10.17632/kkf4zdz2x7.1

Table S1: Crystallographic data collection and validation statistics for C118-SARS RBD and C022-SARS2 RBD, (related to Figure 2).

	C118 Fab – SARS-CoV RBD	**C022 Fab – SARS-CoV-2 RBD**
PDB ID	7RKS	7RKU
Data collection[a,b]		
Space group	$P2_1$	$P6_1$
Unit cell (Å)	92.9, 90.0, 93.9	178.4 178.4 247.3
α, β, γ (°)	90.0, 113.3, 90.0	90.0 90.0 120.0
Wavelength (Å)	0.980	0.980
Resolution (Å)	46.6 -2.70 (2.80-2.70)	44.6-3.20 (3.32-3.20)
Unique Reflections	37505 (3085)	73261 (7337)
Completeness (%)	95.7 (79.5)	99.5 (96.9)
Redundancy	3.4 (2.9)	10.3 (9.8)
$CC_{1/2}$ (%)	99.8 (91.8)	99.8 (27.7)
$\langle I/\sigma I \rangle$	13.14 (2.27)	12.87 (0.56)
R_{merge} (%)	6.22 (40.1)	16.4 (492)
R_{pim} (%)	3.96 (28.0)	5.36 (165)
Wilson *B*-factor (Å^2)	59.53	125.06
Refinement and Validation		
Resolution (Å)	2.70	3.20
Number of atoms	9582	19802
Protein	9516	19696
Ligand	66	106
Waters	0	0
R_{work}/R_{free} (%)	19.5/24.7	18.8/23.1
R.m.s. deviations		
Bond lengths (Å)	0.009	0.011
Bond angles (°)	1.17	1.28
MolProbity score	2.04	2.12
Clashscore (all atom)	7.77	9.23
Poor rotamers (%)	2.09	2.04
Ramachandran plot		
Favored (%)	94.52	94.36
Allowed (%)	5.23	5.28
Disallowed (%)	0.25	0.36
Average *B*-factor (Å^2)	62.79	124.4

[a] Data collected on 12-2 beamline at the Stanford Synchrotron Radiation Lightsource (SSRL).
[b] Numbers in parentheses correspond to the highest resolution shell.

Table S2. Buried Surface Area, (related to Figure 4).

Interface Buried Surface Area (Å^2)				
Structure **PDB**	**C118 Fab/ SARS RBD** this study	**C022 Fab/ SARS2 RBD** this study	**CR3022 Fab/ SARS2 RBD** PDB 6W41	**COVA1-16 Fab/ SARS2 RBD** PDB 7JMW
Heavy Chain Paratope	750	769	593	673
FWRH1	0	12	4	0
CDRH1	197	218	271	109
FWRH2	0	0	0	0
CDRH2	92	3	113	0
FWRH3	0	0	3	0
CDRH3	461	537	202	564
FWRH4	0	0	0	0
Light Chain Paratope	272	200	432	154
FWRL1	0	0	0	0
CDRL1	0	1	239	0
FWRL2	4	48	50	34
CDRL2	121	20	62	0
FWRL3	147	130	28	120
CDRL3	0	0	0	0
FWRL4	0	0	0	0
Total Paratope	1022	969	1025	827
Heavy Chain Epitope	656	704	593	628
Light Chain Epitope	292	202	398	153
Total Epitope	948	906	990	780

Table S3. Cryo-EM data collection and refinement statistics for C118-S complex structure, (related to Figure 5).

	C118 SARS-CoV-2 S 2P (state 1)	C118 SARS-CoV-2 S 2P (state 2)
PDB	**7RKV**	**-**
EMD	**24504**	**24505**
Data collection conditions		
Microscope	Talos Arctica	
Camera	Gatan K3 Summit	
Magnification	45,000x	
Voltage (kV)	200	
Recording mode	counting	
Dose rate (e^-/pixel/s)	13.5	
Electron dose ($e^-/Å^2$)	60	
Defocus range (μm)	0.7-2.0	
Pixel size (Å)	0.836	
Micrographs collected	2,970	
Micrographs used	2,487	
Total extracted particles	923,707	
Refined particles	53,728	31,422
Symmetry imposed	C3	C1
Nominal Map Resolution (Å)		
FSC 0.143 (unmasked/masked)	4.4/3.4	7.7/4.5
FSC 0.143 local (unmasked/masked)	4.8/3.7	NA
Refinement and Validation		
Initial model used	7K4N	
Number of atoms		
Protein	28,865	
Ligand	795	
MapCC (global/local)	0.83/0.82	
Map sharpening B-factor	88	
R.m.s. deviations		
Bond lengths (Å)	0.01	
Bond angles (°)	0.81	
MolProbity score	2.56	
Clashscore (all atom)	14.1	
Poor rotamers (%)	0.6	
Ramachandran plot		
Favored (%)	93.1	
Allowed (%)	6.9	
Disallowed (%)	0	

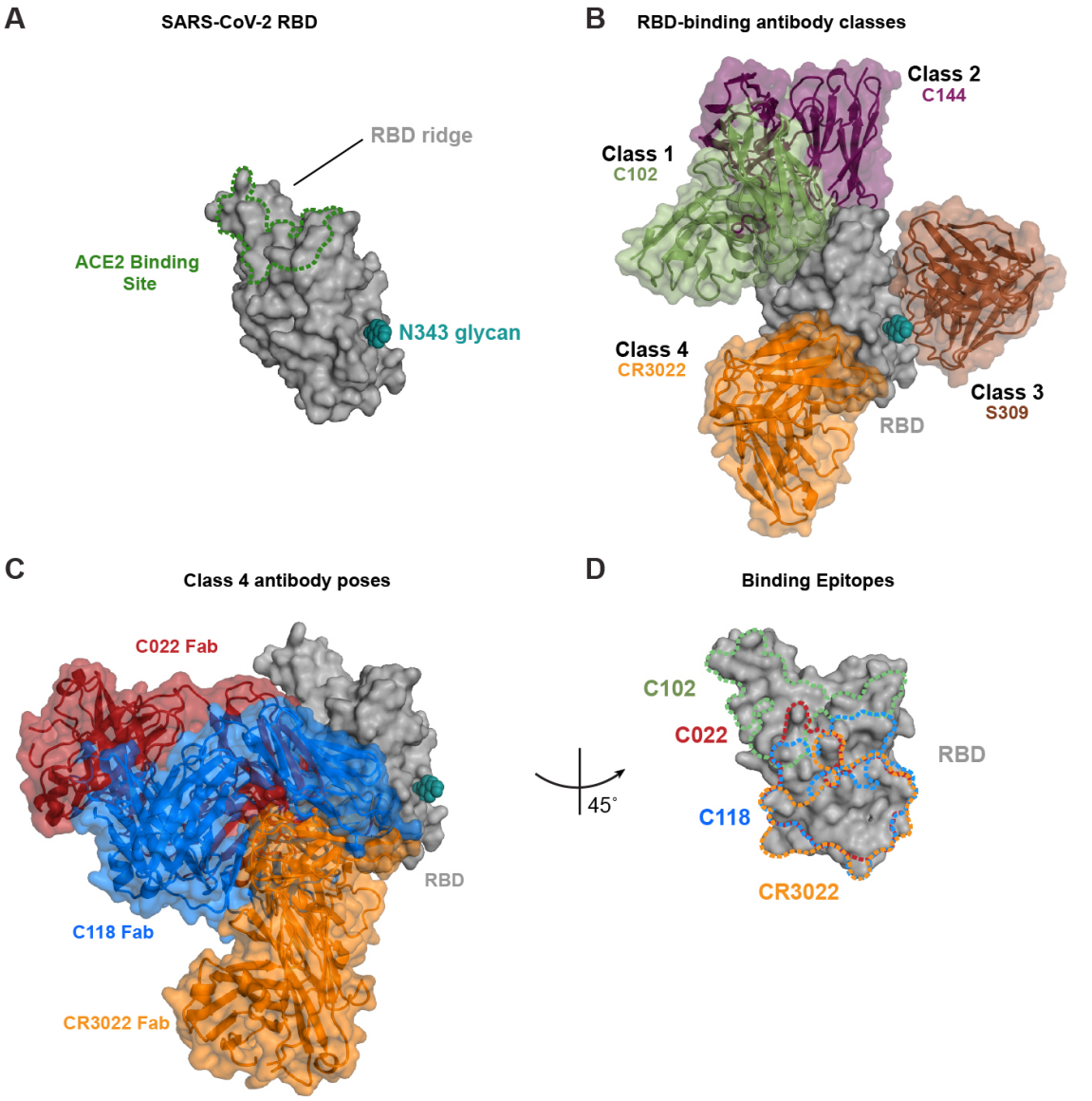

Figure S1. Epitopes of class 1 – class 4 anti-RBD antibodies, (related to Figures 1 and 2).
(A) SARS-CoV-2 RBD surface representation (grey) with N343 glycan (teal). The ACE2 binding site is represented by a green dashed line.
(B) SARS-CoV-2 RBD surface representation (grey) with overlaid bound models of V_HV_L of antibodies for class 1 (C102, green, PDB: 7K8M), class 2 (C144, purple, PDB: 7K90), Class 3 (S309, brown, 7JMX), and class 4 (CR3022, orange, PDB: 6W41).
(C) SARS-CoV-2 surface representation with overlay of bound C118 Fab (blue), C022 Fab (red), and CR3022 Fab (orange, PDB: 6W41).
(D) SARS-CoV-2 RBD surface representation (grey) at 45˚ angle from previous panels. Dotted outlines show epitopes of C102 (green), C022 (red), C118 (blue), and CR3022 (orange) mapped onto SARS-CoV-2 RBD.

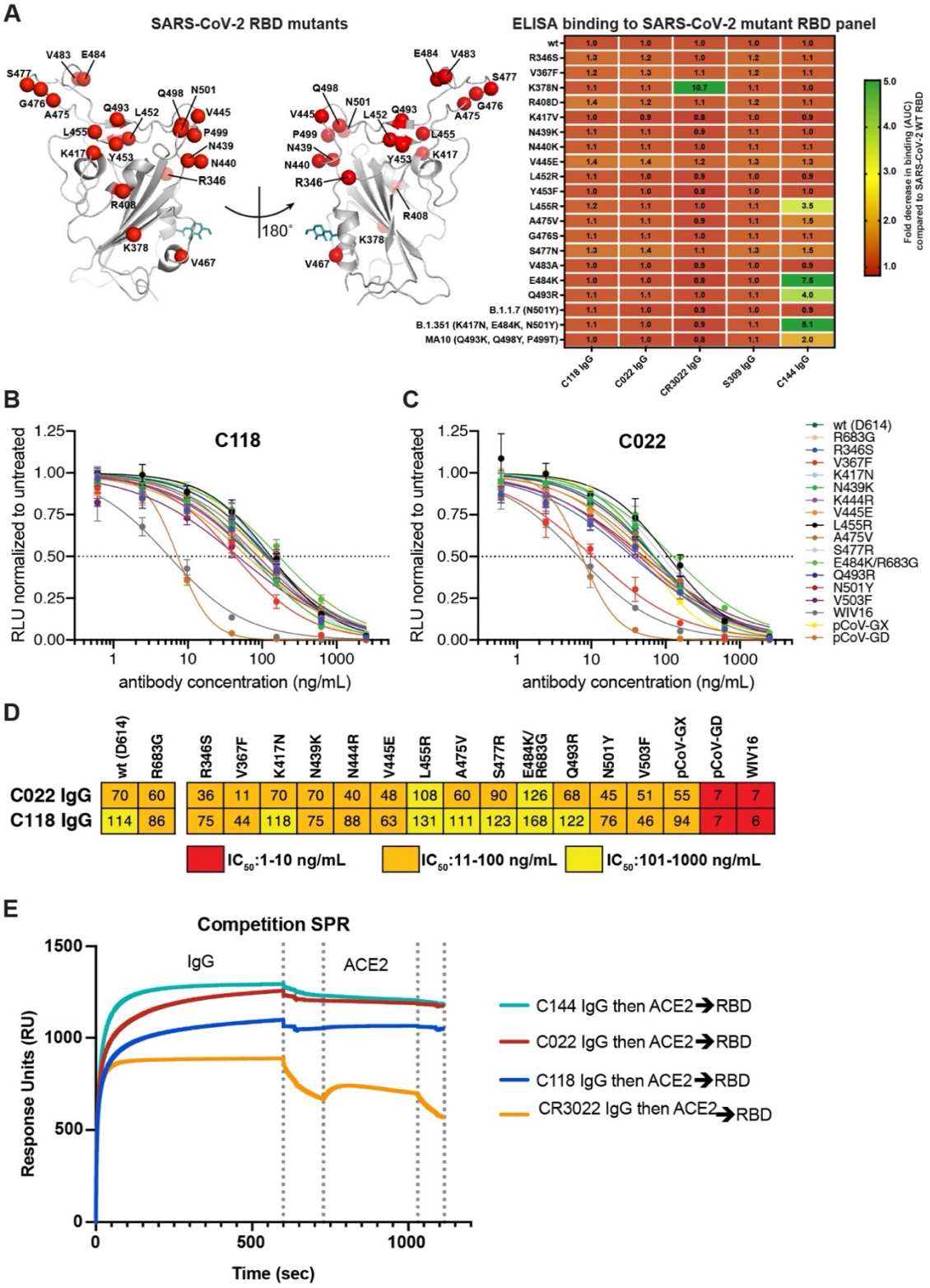

Figure S2. C118 and C022 binding, neutralization of sarbecoviruses, and direct competition with ACE2, (related to Figures 1 and Figure 2).

(A) Left: Cartoon model of SARS-CoV-2 RBD (RBD from C022-RBD structure) showing locations of point mutations as red spheres and the $N343_{RBD}$ *N*-glycan as teal sticks. Right: Comparison of binding of the indicated monoclonal IgGs to RBD mutants from ELISA data shown as AUC values normalized to antibody binding to 'wt' SARS-CoV-2 RBD. Data presented 2are normalized mean AUC values from two independent experiments.

(B-C) Normalized relative luminescence values for cell lysates of $HT1080_{ACE2}$ cells 48h after infection with SARS-CoV-2 pseudovirus carrying indicated spike variants in the presence of increasing concentrations of monoclonal IgGs C118 (B) and C022 (C). The mutants represented substitutions found in circulating SARS-CoV-2 sequences with frequencies >0.01% in GISAID (Shu and McCauley, 2017). Mean and standard deviation of two experiments, each performed in duplicate (n=4), is shown.

(D) Half-maximal inhibitory concentrations (IC_{50}) calculated from the neutralization curves in panels B and C for monoclonal IgGs C022 and C118 for neutralization of 'wt' (D614 S trimer) and the indicated mutant SARS-CoV-2 S pseudotyped viruses, as well as other sarbecovirus pseudoviruses. IC_{50} values are means of 2 independent experiments. Colors indicate IC_{50} ranges, as indicated. The E484K substitution was constructed in an R683G (furin cleavage site mutant) background to increase infectivity (Muecksch et al., 2021).

(E) SPR-based competition of soluble ACE2 against C144, CR3022, C118, or C022 IgG for SARS-CoV-2 RBD binding. SARS-CoV-2 RBD was coupled to a biosensor chip using primary amine chemistry. An IgG was injected first (seconds 0-600). Seconds 600 - 730 represent the delay required to switch samples for a subsequent injection. From seconds 730 – 1030, soluble ACE2 was injected. Buffer was injected after 1030 seconds.

A

```
                          FWR1                CDRH1          FWR2          CDRH2
C118 VH         QVQLVESGGGVVQPGRSLRLSCAASGFTFSN--YAMHWVRQAPGKGLEWVAVISYDGSNKY
C022 VH         QVQLQESGPGLVKPSETLSVTCTVSGGSISSSRYYWGWIRQPPGKGLEWIGSIYYSG-STY
COVA1-16 VH     QVQLVQSGAEVKKPGASVKVSCKASGYTFTS--YYMHWVRQAPGQGLEWMGIINSSGGSTS
                **** :**  : :*. :: ::* .** :::.  *   *:**.**:****:. *  .* ..

                                FWR3                                CDRH3
C118 VH         YADSVKGRFTISRDNSKNTLYLQMNSLRAEDTAIYYCASGYTGY----DYFVRGDYYGLDV
C022 VH         YNPSLKSRVTISVDTSKNQFSLKLSSVTAADTAVYYCARHAAAYYDRSGYYF-IEYF--QH
COVA1-16 VH     YAQKFQGRVTMTRDTSTSTVYMELSSLRSEDTAVYYCARPPRNYYDRSGYYQRAEYF--QH
                *  ..:.*.*:: *.*.. . :::.*: : ***:****     *    .*:   :*:  :
```

B

```
                          FWR1              CDRL1        FWR2         CDRL2
C118 VL         QPVLTQSPSA-SASLGASVKLTCTLSSGHSSYAIAWHQQQPEKGPRYLMKLNTDGSHSKGDG
C022 VL         DIQMTQSPSTLSASVGDSVTITCRASQSISSW-LAWYQQKPGKAPKLLIY----KASSLESG
COVA1-16 VL     DIQLTQSPSSLSASVGDRVTITCQASQDISNY-LNWYQQRPGKAPKLLIY----DASNLETG
                :  :*****: ***:*  *.:**  *.. *.: : *:**.* *.*. *:      : .   *

                                FWR3                CDRL3
C118 VL         IPDRFSGSSSGAERYLTISSLQSEDEADYYCQTWGTGILVFGGGTKLTVLLGQPKAAP
C022 VL         VPSRFSGSGSGTEFTLTISSLQPDDFATYYCQQYNNYRYTFGQGTKLEI--KRTVAAP
COVA1-16 VL     VPSRFSGSGSGTDFTFTISSLQPEDIATYYCQQYDNPPLTFGGGTKLEI--KRTVAAP
                :*.*****.**::  :******.:* * **** :..   .** **** :   .. ***
```

C

```
                                          IGHD3-22                    IGHJ1
Germline                          ATTACTATGATAGTAGTGGTTATTA       GCTGAATACTTCCAGCACTGG
COVA1-16      TGTGCGAGGCCCCCTCGAAATTACTATGATAGGAGTGGTTATTATCAGAGGGCTGAATACTTCCAGCACTGG
C022        CTGTGCGAGACATGCGGCAGCA-TACTATGATAGAAGTGGTTATTATTTCATC---GAATACTTCCAGCACTGG
```

Figure S3. Comparison of C022, C118, and COVA1-16 V_HV_L sequences, (related to Figure 3).
(A,B) Alignment of C118, C022, and COVA1-16 (A) V_H and (B) V_L domains. Framework regions (FWRs) and complementarity determining regions (CDRs) assigned using the IMGT definition (Lefranc et al., 2015). Conserved residues (*), residues with similar properties (:), residues with weakly similar properties (.).
(C) Alignment of portions of the C022 and COVA1-16 V_H domain nucleotide sequences to germline gene segment sequences for *IGHD3-22* (sand) and *IGHJ1* (teal).

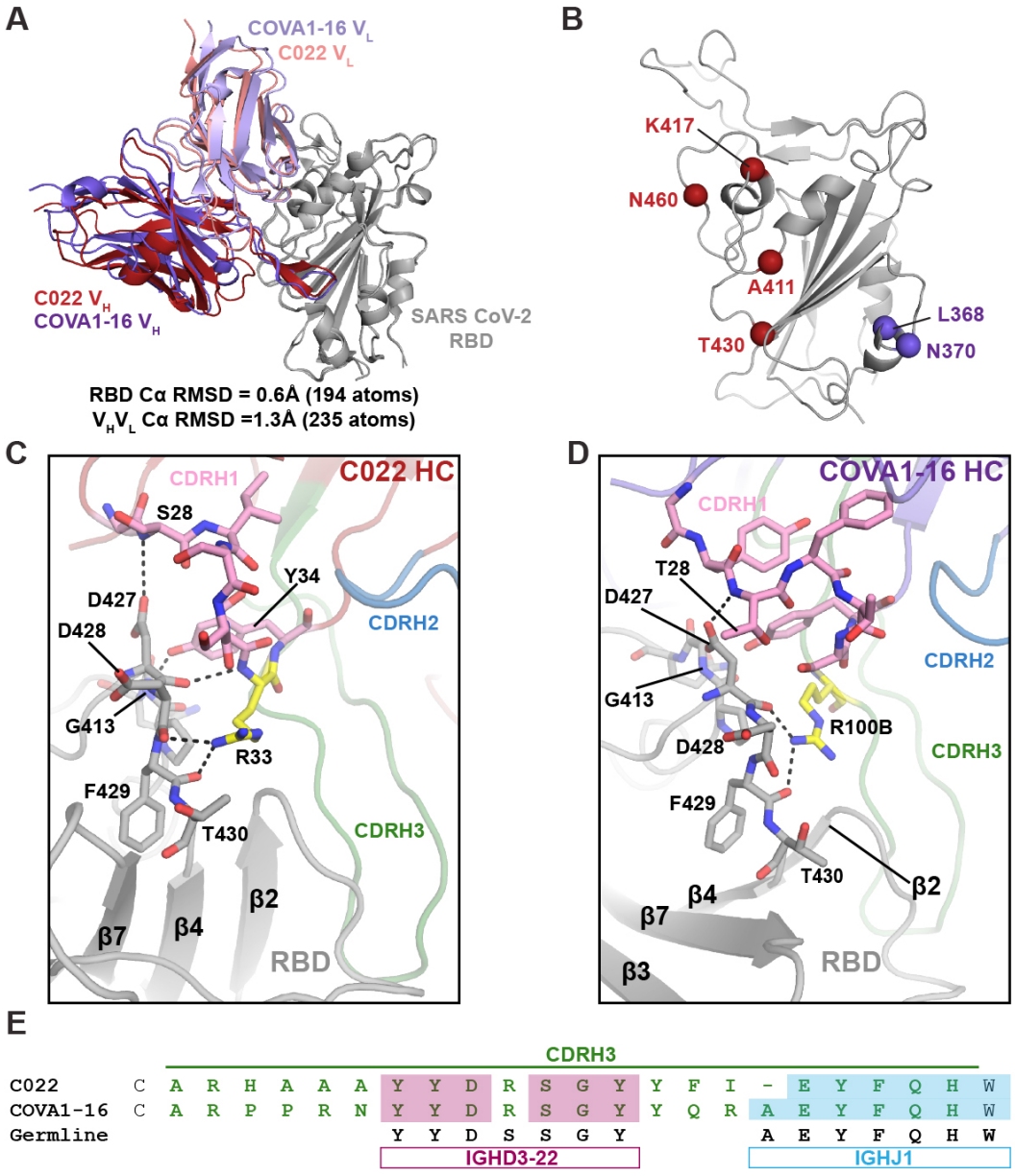

Figure S4. Comparison of C022 and COVA1-16 antibody binding, (related to Figure 3).
(A) Cartoon representation of superposition of RBDs from C022-RBD and COVA1-16-RBD (PDB 7JMW) crystal structures aligned by their Cα atoms.
(B) SARS-CoV-2 RBD cartoon model showing differences between C022 (red) and COVA1-16 (purple) epitopes. (C,D) Interacting residues of SARS-CoV-2 RBD with the CDRH1 regions from (D) C022 Fab and (E) COVA1-16 Fab (PDB 7JMW). Colors: Oxygens (red), nitrogens (blue). Carbon atoms of critical arginines from each paratope are highlighted in yellow.
(E) Alignment of CDRH3 amino acid sequences for C022 and COVA1-16 and germline-encoded amino acids derived from *IGD3-22* (mauve) and *IGJ1* (blue) gene segments. Identities between C022 or COVA1-16 with *IGHD3-22* and *IGHJ1* amino acid sequences shown as shaded boxes and residues within the CDRH3 loop are green.

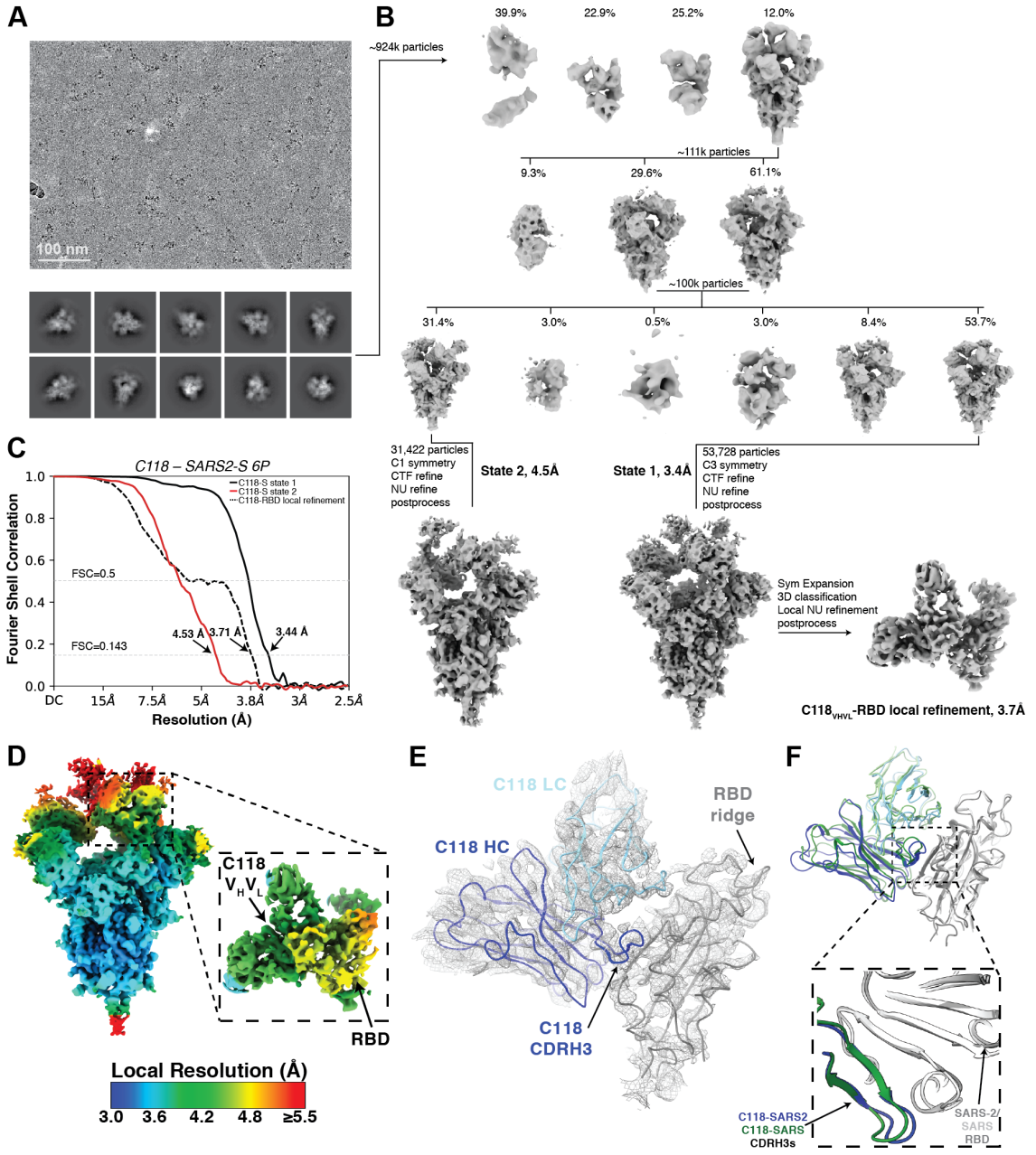

Figure S5. Details for cryo-EM C118-S reconstructions, (related to Figure 5).
(A) C118-S 6P representative micrograph (top) and 2D class averages (bottom). Scale bar = 100 nm.
(B) Data processing pipeline for C118-S structure and focused refinement of C118-RBD portion of the structure.
(C) Gold Standard FSC for final reconstruction of C118-S reconstructions. Resolutions at FSC=0.143 are shown for each volume.
(D) Local resolution estimates for C118-S map and C118-RBD focused map calculated in cryoSPARC.
(E) Ribbon representation of C118-RBD rigid body-refined model into cryo-EM density contoured at 8σ (gray mesh).
(F) Overlay of C118-RBD (SARS-CoV-2) from Fab-S cryo-EM structure (blue and gray cartoon) and C118-RBD (SARS-CoV) (green and light gray). CDRH3 interactions are highlighted.